Electrothermal instabilities induced by a metastable electronic state in PbTe(Ga)

B. A. Akimov, N. B. Brandt, A. V. Albul, and L. I. Ryabova

M. V. Lomonosov Moscow State University, 119899 Moscow, Russia
(Submitted February 26, 1996; accepted for publication April 1, 1996)
Fiz. Tekh. Poluprovodn. **31**, 197–200 (February 1997)

The electrothermal instabilities in high-resistance single crystals of PbTe(Ga) irradiated by infrared light are described phenomenologically. Instabilities show up in the form of periodic oscillations in the current in the sample circuit and in its temperature in sufficiently high electric fields. For observation of these phenomena it is important that the energy spectrum of the semiconductor contain metastable electronic states lying about 20 meV below the bottom of the conduction band. © *1997 American Institute of Physics.* [S1063-7826(97)00202-0]

INTRODUCTION

One of the most interesting members of the family of modified alloys of the lead chalcogenides[1] is PbTe(Ga). Recently new, extremely important experimental data have been obtained on the properties of this compound[2–7] and models have been proposed for the spectrum of impurity states.

When PbTe is doped with gallium, within a certain range of gallium impurity ($1-3\times10^{19}$ cm^{-3}), a dielectric state, which is not typical of the narrow gap semiconductors, is realized. Here the charge carrier concentration is close to the intrinsic concentration and is $10^{12}-10^{13}$ cm^{-3} at liquid-nitrogen temperature, while $n<10^{9}$ cm^{-3} at liquid-helium temperature. The temperature dependences of the resistance R obtained when the samples are shielded from background radiation and when they are illuminated by infrared light differ sharply (by nine orders of magnitude) for $T<T_c=80$ K. The relaxation times for nonequilibrium electrons are $\tau\simeq10^{-3}$ s at 77 K and $\tau>10^{5}$ s at 4 K. At low temperatures the ''frozen'' concentration of nonequilibrium electrons is as high as $n\simeq3\times10^{17}$ cm^{-3}.

Measurements of the photoconductivity spectrum[6] and of the photoconduction kinetics[7] have been used to obtain a spectrum of impurity states in PbTe(Ga) which, to a first approximation, provides a qualitative description of the available data and yields an estimate for certain characteristic energies in the spectrum (see a sketch of this spectrum in Ref. 7). For the purposes of the present paper, this system can be regarded as having three levels. The ground state of the gallium impurity lies about 70 meV below the bottom of the conduction band and stabilizes the Fermi level in PbTe(Ga). Photoionization of the ground state causes the formation of the metastable state, which lies approximately 20 meV below the bottom of the conduction band. These two impurity levels, together with the conduction band, form the above-mentioned three level system, which mainly determines the photoconduction kinetics.[7] The basic assumption for the studies conducted in this paper is our assumption that a conductor with this type of level system can serve as a model for studies of self-oscillations. We have also proposed the following method for realizing these processes.

If light is used for continuous excitation of electrons into metastable states and an electric field sufficient to cause Joule breakdown[8] is applied to the sample, then periodic oscillations in the current and temperature will develop in the sample. When the current in the sample increases, its temperature will also increase. When a certain critical temperature is reached where a key role is played by relaxation from the metastable state into the ground state, the concentration of electrons in the levels will be exhausted, causing a drop in the current, and heating of the sample will cease. Since heating of the sample begins anew after this cycle, because of the accumulation of electrons in the metastable states due to the illumination, the process repeats itself and can be repeated periodically. In this paper we perform experiments with variations in the following conditions: electric field, illumination power, temperature of the surroundings, and heat transfer. As a result, the oscillations in the current and temperature have been clarified and are analyzed further. In addition, a new type of instability that cannot be described in terms of a thermal breakdown has been observed in single crystal PbTe(Ga).

TEST SAMPLES AND EXPERIMENTAL TECHNIQUE

In these studies we have used several series of PbTe(Ga) single crystals grown by the Czochralski, Bridgman, and vapor methods. Galvanomagnetic measurements and studies of the photoconduction kinetics and spectra of these samples have been done previously.[6,7] The crystals were cut by electroerosion and the sample surfaces were prepared, etched, and had contacts soldered to them by the same methods.[7] In the present work we used samples with fixed dimensions of $0.3\times0.8\times3.0$ mm^3. In order to avoid inaccuracies associated with volume-nonequilibrium states, the voltage U at the contacts and the total currents I through the sample are given in the following characteristics. No fundamental qualitative differences associated with the different methods of growing the samples showed up. A sample was placed in a shielded chamber together with the load resistance and was supplied with dc current from a separate supply. This chamber contained a miniature infrared source. The transient processes were recorded using an S9-8 digital storage oscilloscope.

In order to examine the nature of the observed instabilities in more detail, we have performed experiments with parallel control of the changes in the current and temperature.

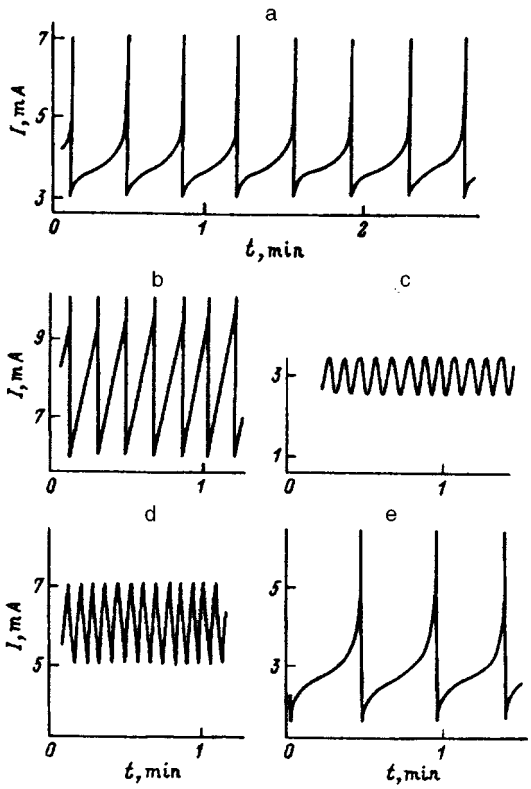

FIG. 1. Characteristic form of the observed thermoelectric instabilities (oscillations in the current I) in PbTe(Ga) single crystals. The conditions under which curves a–e were obtained are given in the text.

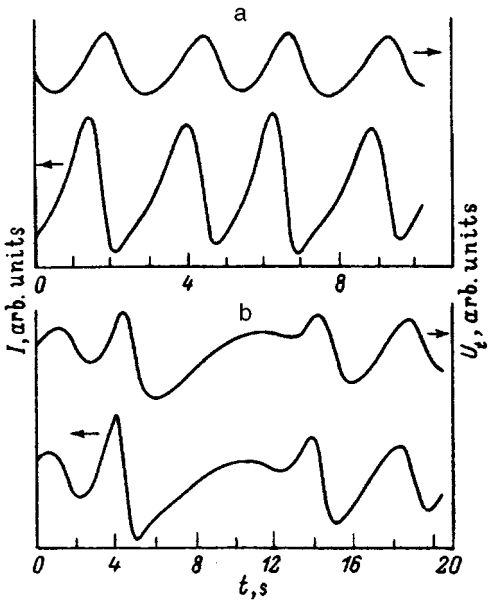

FIG. 2. Forms of the oscillations in the current I in the sample circuit and in the sample temperature characterized by the thermocouple voltage U_t with illumination (see text).

The sample was suspended in the chamber on current leads at a distance of 1 cm from the holder. A thin (100 μm) differential thermocouple was attached to the side face of the sample and its cold junction was positioned in parts that were well cooled in helium. The signal from the thermocouple was passed through an R3003 voltage comparator to channel A of the S9-8 oscilloscope. The signal from a load resistance R_l in the sample circuit that was proportional to the current (for all conditions $R_l \ll R$) was fed to channel B. Data from the oscilloscope was fed in digital form to a computer for subsequent analysis.

EXPERIMENTAL RESULTS

We first present a brief description of the recorded instabilities. The form of the periodic oscillations in the current at $T=4.2$ K and a voltage of $U=35$ V on the sample is shown in Fig. 1a. Figures 1b–1e show the variation in the shape of the oscillations with increases in the (b) helium pressure in the chamber (increased heat transfer); (c) temperature of the surroundings (to 35 K); (d) illumination level; and (e) voltage on the sample (to 45 V). The oscillatory process cannot be observed at temperatures above 42 K, at voltages below 30 V, and at too low or too high illumination levels (with a heat source below 1.6 mW or above 2.8 mW).

Some examples of combined traces of current and temperature oscillations are shown in Fig. 2. Under the conditions for heat transfer from the sample described above, the oscillations were close to sinusoidal in form and the average sample temperature rose. Since it was not possible to measure the sample temperature sufficiently accurately with this design, the changes in T are estimates in these experiments. The amplitude of the oscillations corresponds to heating of the sample by several degrees with an increase in the average temperature of the sample to 15 K. A shift in the phase of the oscillations, which can also be associated with the mass and inertia of the thermocouple junction, is observed. As the illumination level and electric field are varied, it is also possible to observe a more complicated periodic process which is related to the fact that ahead of the main current discharge one can observe at least one weaker oscillation (Fig. 2b).

These data provide qualitative confirmation of the above-mentioned possibility of electrothermal instabilities in PbTe(Ga).

During the experiments it was found that a distinctive oscillatory process can develop in the sample even without continuous illumination. This process can be induced in the following way: a voltage U_c of some magnitude is applied to the sample. This voltage was $U_c=24$ V, while the oscillations shown in Fig. 2a took place with $U=40$ V. Subsequently the illumination is turned on and the sample current increases to a certain magnitude. Then, after a time $\Delta t \simeq 10$ s, the illumination is turned off. If a weak voltage were applied to the sample, the current through the sample would decrease over a long time interval, as shown in Ref. 7. However, when the voltage U_c is applied to the sample, at a certain level (on the order of 2 mA), the relaxation of the current disrupts into an oscillatory process which essentially terminates the relaxation, since this process can obviously continue for an unlimited time. The shape of the oscillations in the current and temperature is shown in Fig. 3. The temperature oscillations take place around some average value (7 K) which is much lower than the same magnitude in Fig. 2. It should be noted that these oscillations are observed within a very narrow range of voltages applied to the sample, $U=23.5-24.5$ V,

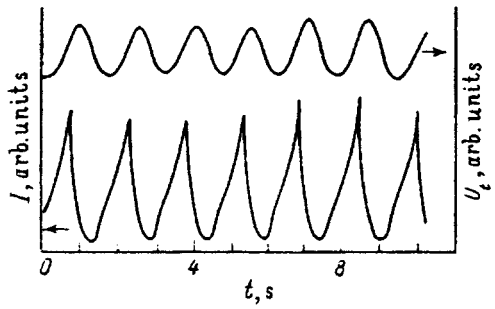

FIG. 3. Forms of the oscillations in the current I in the sample circuit and in the sample temperature characterized by the thermocouple voltage U_t without illumination (see text).

and their period varies by almost a factor of 2 (from 2.8 s to 1.5 s) within this range. The nature of these oscillations differs substantially from that of the instabilities observed before in p-type PbTe(Ga).[9]

DISCUSSION OF THE RESULTS

At present, it is difficult to carry out a detailed quantitative analysis of the observed instabilities. It is appropriate to cite some initial data for such an analysis.

The thermal activation energy for conduction, E_a, in PbTe(Ga) for $T<80$ K is estimated from the $\ln R(1/T)$ curve to be $E_a \sim 70$ meV. The magnitude W_1 of the barrier which determines the relaxation time for the frozen photoconductivity during heating of the samples can be estimated from measurements of the characteristic times for the steady-state photoconductivity as functions of the temperature or from an analysis of the variation in the static characteristics $\ln R(1/T)$ taken with illumination at temperatures of 40–80 K. The basic criteria for the existence of single-electron metastable states in PbTe(Ga) are the previously discussed[6,7] thermally stimulated currents ''induced by impurity photoconductivity'' and certain other data.[4,5]

The current-voltage characteristics in high resistance PbTe(Ga) samples are determined by conductivity along the impurity band of metastable states, as well as by field and thermal scattering of carriers into the conduction band. The conductivity of the sample under these conditions is a function of the field E and temperature T, which in turn are determined by Joule heating of the system. Under these conditions impurity breakdown or impurity and Joule breakdown may develop in the system. Temperature and field heating of the electrons may cause the barrier W_1 to be overcome and lead to a transition of these electrons into the ground state. In this sort of system Joule breakdown differs fundamentally from ordinary breakdown, since during thermal carrier generation the number of centers is depleted.

Joule breakdown has been studied before in $Pb_{1-x}Sn_xTe$(In).[8] The variation in the shape of the oscillations as the external conditions are changed (Fig. 1) is in qualitative agreement with theory. In the theory of thermal breakdown one introduces as a parameter the critical temperature $T_0^{(c)}$ of the surrounding medium at which breakdown can be observed. This critical temperature is determined by the conduction activation energy E_a, i.e.,

$$T_0^{(c)} = E_a / 8kT, \tag{1}$$

which allows us to estimate the activation energy of the electrons from the metastable states. If the critical temperature is taken to be the temperature at which the observed instabilities disappear, then the activation energy is $E_a \simeq 25$ meV. Naturally, a determination of this energy on the basis of this effect or from a study of thermally stimulated currents carries a large error. Nevertheless, the data obtained here correlate well with the optical measurements of Khokhlov and Belogorokhov.[3] The far-infrared lines observed in the photoconductivity spectrum there (with energies on the order of 20 meV) can be tentatively attributed to transitions of electrons from the metastable states into the conduction band.

The nature of the oscillations observed without illumination (Fig. 3) is not clear at present; these data show that structure of the spectrum of the metastable levels in PbTe(Ga) is more complex and the possible types of instabilities may be of interest for further study.

We wish to thank A. M. Gas'kov, E. I. Slyn'ko, and S. A. Belokon' for providing the samples.

This work was supported by the Russian Fund for Fundamental Research.

[1] B. A. Akimov, A. V. Dmitriev, D. R. Khokhlov, and L. I. Ryabova, Phys. Status Solidi A **137**, 9 (1993).
[2] S. P. Grishechkikna, A. A. Zhuravlev, K.-P. Mollmann, and K. H. Herrmann, Fiz. Tekh. Poluprovodn. **25**, 677 (1991) [Sov. Phys. Semicond. **25**, 409 (1991)].
[3] A. I. Belogorokhov, E. I. Slyn'ko, and D. R. Khokhlov, Piz'ma Zh. Tekh. Fiz. **18**, 30 (1992) [Sov. Tech. Phys. Lett. **18**, 594 (1992)].
[4] A. N. Vasil'ev, T. N. Voloshok, Yu. P. Gaidukov, and N. P. Danilova, Pis'ma Zh. Éksp. Teor. Fiz. **58**, 970 (1993).
[5] A. N. Vasil'ev, B. A. Volkov, T. N. Voloshok, and S. V. Kuvshinnikov, Pis'ma Zh. Éksp. Teor. Fiz. **61**, 768 (1995).
[6] B. A. Akimov, A. V. Albul, V. Yu. Il'in, M. Yu. Nekrasov, and L. I. Ryabova, Fiz. Tekh. Poluprovodn. **29**, 2015 (1995) [Semiconductors **29**, 1051 (1995)].
[7] B. A. Akimov, A. V. Albul, and L. I. Ryabova, Fiz. Tekh. Poluprovodn. **29**, 2158 (1995) [Semiconductors **29**, 1125 (1995)].
[8] B. A. Akimov, N. B. Brandt, B. S. Kerner, V. N. Nikiforov, and S. M. Chudinov, Solid State Commun. **43**, 31 (1982).
[9] Yu. G. Troyan, F. F. Sizov, and V. M. Lakeenkov, Ukr. Fiz. Zh. **32**, 467 (1987).

Translated by D. H. McNeill

Resonant interaction of electrons with a high frequency electric field in two-barrier structures

I. V. Belyaeva, E. I. Golant, and A. B Pashkovskiĭ

''Potok'' Scientific Research Institute, 141120 Fryazino, Russia
(Submitted July 21, 1995; accepted for publication April 4, 1996)
Fiz. Tekh. Poluprovodn. **31**, 201–208 (February 1997)

The frequency dependences of the small-signal dynamic conductivity of symmetric and nonsymmetric two-barrier heterostructures are calculated in a one-electron approximation. Special attention is focused on the case of electron tunnelling through the upper minibands. In the approximation of high-barrier power (width), an analytic expression is obtained for the dynamic conductivity of a two-barrier resonance-tunnel structure that agrees with a rigorous calculation. It is shown that (a) the dynamic conductivity increases as the fourth power of the barrier width, (b) quantum transitions with an even change in the level number are forbidden, and (c) the dynamic conductivity is inversely proportional to the cube of the frequency if the separation between the levels varies with frequency in a way such that the resonance condition is always satisfied. The maximum possible intensity of the radiating transitions of two-barrier heterostructures are calculated as a function of the quantum numbers of the working levels under conditions such that the supply current density and the characteristic time for breakup of the coherence by phonon scattering are constant. It is shown that the intensity increases significantly if, for example, the fourth level of the structure, rather than the ground state, is used as the working level. [S1063-7826(97)00302-5]

1. INTRODUCTION

In the many papers on resonance-tunnel structures[1–5] considerable attention has been devoted to studies of the dynamic conductivity σ.

In the small-signal approximation the conductivity at frequency ω is determined by the difference in the electron fluxes J coming out of a two-barrier resonance-tunnel structure as absorbed ($J(\varepsilon+\hbar\omega)$) and emitted ($J(\varepsilon-\hbar\omega)$) photons with energy $\hbar\omega$:[6,7]

$$\sigma(\varepsilon,\omega)=\frac{2\hbar\omega}{aE^2}[J(\varepsilon+\hbar\omega)-J(\varepsilon-\hbar\omega)], \tag{1}$$

where $2E$ is the amplitude of the alternating field of frequency ω, a is the size of the localization region of the rf field, and ε is the electron energy. There is special interest in determining the negative dynamic conductivity σ in the THz frequency range, where a unipolar superlattice laser has been recently created for the first time.[8]

The characteristics of a resonance-tunnel structure are to a great extent determined by the method for injecting electrons into the interior of the structure, which is usually done by applying a voltage which biases the system of quasilevels (minibands) of the structure downward, so that one of the levels ends up sufficiently close to the bottom of the conduction band of the input contact of the resonance-tunnel structure, where conditions for intense overflow of electrons to this level are ensured. The applied voltage, however, substantially disrupts the symmetry of the resonance-tunnel structure, which leads to a reduction in the maximum tunnel transparency (transmission coefficient) T compared to the $T=1$ for complete symmetry of the structure. This limits the efficiency of direct injection, especially into the higher minibands of the resonance-tunnel structure. In order to avoid this limitation, an experimental study has been made[9] of a method based on using an injector which accelerates the electrons to the required energy. The possibility of coherent tunnelling of electrons in a resonance-tunnel structure with an injector, including over the higher levels, was demonstrated. On this basis it has been theoretically predicted[10] that injecting electrons into the second miniband of a two-barrier resonance-tunnel structure can provide sufficient negative dynamic conductivity for operation of an infrared (IR) laser.

In this article we develop an earlier approach[10,11] to study the dynamic conductivity of a two-barrier resonance-tunnel structure which arises when electrons pass over the upper resonant levels of the structure.

2. CALCULATING THE DYNAMIC CONDUCTIVITY WHEN ELECTRONS ARE INJECTED INTO THE HIGHER MINIBANDS OF A TWO-BARRIER RESONANCE-TUNNEL STRUCTURE

It has been shown[12] that when an electron with energy ε moves through a quantum-well structure with a nonmonotonically varying static transmission coefficient $T(\varepsilon)$, the probability of absorption or emission of a photon $\hbar\omega$ by the electron is greatest if the energy of the electron undergoing a collision with the photon is close to the energy $\mathscr{E}_m$ corresponding to the maximum of $|T(\varepsilon)|$. Thus, the absolute value of the conductivity increases sharply at a frequency $\omega=|\mathscr{E}_m-\varepsilon|/\hbar$. However, with nonresonant passage of electrons through a two-barrier resonance-tunnel structure the magnitude of the negative dynamic conductivity is limited by the fact that, because of the low transmission coefficient $T(\varepsilon)$, relatively few electrons enter the structure and interact with the rf field. Thus, the idea naturally arises, and is confirmed by a rigorous quantum-mechanical calculation,[10] that the probability of interaction with the rf field increases sub-

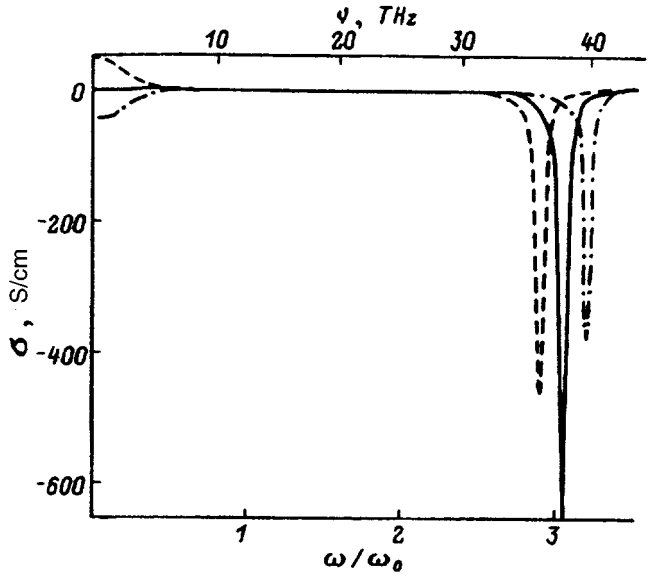

FIG. 1. Active conductivity σ of a two-barrier, resonance- tunnel structure as a function of the normalized frequency ω/ω_0 ($\omega_0=\varepsilon_0/\hbar$) for passage of a monoenergetic electron flux with a concentration $n=10^{17}$ cm^{-3} through the second resonance level. The parameters of the structure are: $a=95$ Å, $\varphi_b=1.04$ eV, $b=11$ Å. The electron energies ε are: $\mathscr{E}_2=4.05\varepsilon_0$ (smooth curve), $3.9\varepsilon_0$ (dashed curve), $4.2\varepsilon_0$ (dot-dashed curve); $\varepsilon_0=51.24$ meV.

stantially if the electrons pass through the two-barrier resonance-tunnel structure along the second resonant level, rather than along the first, while the frequency of the oscillations in the field corresponds to the separation between the levels. Here the magnitude of the negative dynamic conductivity increases sharply and can become significantly larger than the static value (see Fig. 1).

High negative dynamic conductivities can, in principle, be obtained using higher resonant levels, as well as just the first and second. We shall consider this question for the example of the simplest symmetric two-barrier structure[11] of thickness a with thin (δ-shaped) barriers of height φ_b and thickness b in the absence of a constant electric field. Figure 2 shows a plot of the active conductivity $\sigma(\varepsilon)$ when monoenergetic electrons pass through the eighth resonant level of a structure with $a=275$ Å, $\varphi_b=1.04$ eV, and $b=11$ Å calculated using the method of Ref. 11. (For this structure the frequency of the transitions from the first to the second resonant level is $\nu=\omega/2\pi\simeq 5$ THz.) The frequencies corresponding to transitions to even levels are denoted in Fig. 2a by dashed lines. Along with the peaks and the dashed lines, the quantum numbers of the levels to which the transitions take place are also indicated. It should be noted that for this structure the calculation is strictly an approximation, since the calculation ignores such important features of the band structure of the semiconducting material as the nonparabolic dispersion and the presence of the valleys L and X. It is evident that the conductivity is resonant in character, both for transitions between the second and first levels and for transitions between the eighth and odd resonant levels. The probability of transitions to even levels is low (we can say that these transitions are forbidden). For transitions between the eighth and seventh levels the maximum conductivity is

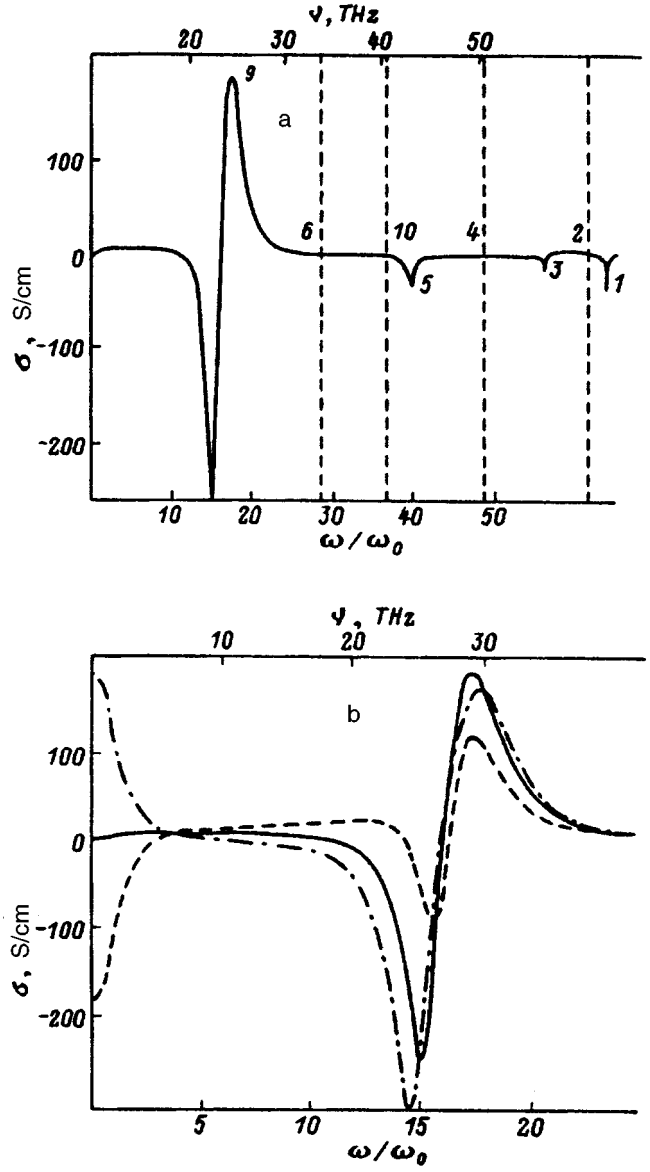

FIG. 2. Active conductivity σ of a two-barrier, resonance- tunnel structure as a function of the normalized frequency ω/ω_0 ($\omega_0=\varepsilon_0/\hbar$) for passage of a monoenergetic electron flux with a concentration $n=10^{17}$ cm^{-3} through the eighth resonance level. The parameters of the structure are: $a=275$ Å, $\varphi_b=1.04$ eV, $b=11$ Å. The electron energies ε are: (a) $\mathscr{E}_8=64.8\varepsilon_0$, (b) $\mathscr{E}_8$ (smooth curve), $64.2\varepsilon_0$ (dashed curve), $65.4\varepsilon_0$ (dot-dashed curve); $\varepsilon_0=6.91$ meV.

observed at an energy which does not coincide exactly with resonant passage through the eigthth level, $\mathscr{E}_8$, but is lower (Fig. 2b). This is explained by the fact that in this case transitions from the eighth level to the broad ninth level become important, along with those to the seventh level. In this case, conditions are created such that the difference in the number of transitions to the seventh and ninth levels is greater when $\varepsilon<\mathscr{E}_8$ than when $\varepsilon=\mathscr{E}_8$. For transitions to lower-lying resonance levels the maximum in the conductivity is observed at an electron energy equal strictly to $\mathscr{E}_8$. (It should be noted that the width of the eighth level, $\Gamma_8=21.3$ meV, is much greater than the width of the first level, $\Gamma_1=0.053$ meV.)

It is clear that for this structure at frequencies corresponding to transitions to allowed (in this case, odd) levels

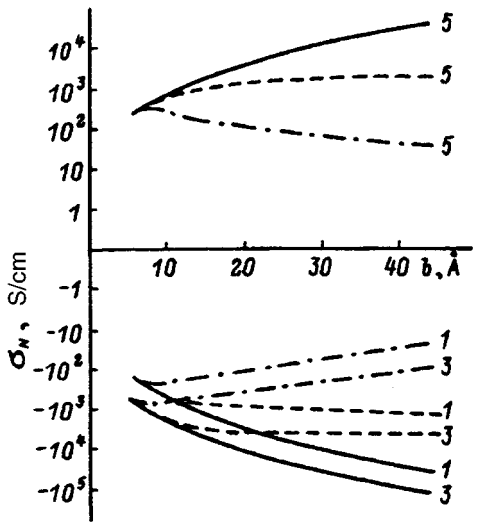

FIG. 3. Active conductivity σ_N of a two-barrier, resonance- tunnel structure ($a=275$ Å, $\varphi_b=1.04$ eV) as a function of barrier thickness b for passage of a monoenergetic electron flux through the fourth resonance level. Smooth curves are $\sigma_N(b)$ when the thicknesses of the two layers are changed, the dashed curves are $\sigma_N(b_2)$ for $b_1=$const, and the dot-dashed curves are $\sigma_N(b_1)$ for $b_2=$const. The numbers on the curves denote the quantum numbers of the levels to which the transitions take place.

the maximum conductivity is observed for transitions between neighboring levels. The probability of transitions to the next allowed levels is much smaller, while as the difference in the quantum numbers of the levels increases, the probability of a transition to them then increases again.

It is interesting to examine how the nonsymmetry of the structure (difference in the power of the first and second barriers) affects the magnitude of the resonant high-frequency conductivity. Figure 3 shows plots of σ_N for electrons passing through the fourth resonance level as functions of the thickness b_2 of the second barrier for a fixed width b_1 of the first and *vice versa*. It should be noted that in the case of a nonsymmetric structure, as in the case of a symmetric structure, the maximum conductivity is observed at a frequency close, but not equal, to $\omega_{NL}=|\mathscr{E}_N-\mathscr{E}_L|/\hbar$. For comparison the figure shows plots of $\sigma_N(b)$, where the thicknesses of both barriers increase simultaneously. (The change in the thickness of each barrier b is equal to half the change in the thickness of the second barrier in the first case: $b=(b_1+b_2)/2$.)

It is clear from Fig. 3 that as the thickness of the second barrier is increased, σ_N initially rises rapidly (almost as in a symmetric structure) and then approaches a roughly constant value. An utterly different picture is seen when the thickness of the first barrier is increased: at first the conductivity rises slightly and then it falls off monotonically. This behavior can be explained as follows: When the thickness of the second barrier is increased, the amplitude of the electron wave function at first increases and then, when the second barrier becomes thick enough and essentially does not let any electrons through, the growth in the amplitude of the wave function ceases. In the limit, with increasing thickness of the second barrier, a barrier$-\langle$section in high frequency field$\rangle-\langle$infinite wall$\rangle$ situation develops. The conductivity behaves accordingly: at first, it increases and then it remains essentially constant. Here, as the calculations show, most of the electrons that have interacted with the rf field leave to the left (are reflected from the wall). In the case where the thickness of the first barrier is increased, even fewer of the electrons pass into the two-barrier resonance-tunnel structure and, after a certain time, the amplitude of the wave functions decreases, so that the magnitude of the conductivity decreases accordingly. Here, of course, most of the electrons that have interacted with the rf field leave to the right (are reflected from the first barrier).

3. THE APPROXIMATION OF HIGH-"POWER" BARRIERS

In order to explain this behavior, it is appropriate to derive an analytic expression for the dynamic conductivity. Let us assume that a weak uniform electric field that varies in time as $E(t)=E(e^{i\omega t}+e^{-i\omega t})$ is applied to the structure. For definiteness we assume that the electrons move from left to right. Taking into acount the above assumptions, the time-dependent Schrödinger equation will then have the form

$$i\hbar\frac{\partial\Psi}{\partial t}=-\frac{\hbar^2}{2m^*}\frac{\partial\Psi}{\partial x^2}+\alpha\delta(x)\Psi+\alpha\delta(x-a)\Psi+H(x,t)\Psi,$$
$$H(x,t)=-qE[x[\theta(x)-\theta(x-a)]+a\theta(x-a)]\times(e^{i\omega t}+e^{-i\omega t}). \tag{2}$$

Here q and m^* are the electron charge and mass, $\alpha=\varphi_b b$, and $\theta(x)$ is the unit step function. If the ground state wave function Ψ_0 normalized to a single electron has the form

$$\Psi_0(x)=\begin{cases}\exp ikx+D\exp ikx & x<0,\\ A\sin kx+B\cos kx & 0<x<a,\\ C\exp[ik(x-a)] & x>a,\end{cases} \tag{3}$$

then in the small-signal approximation the correction Ψ_1 to it is given by[7]

$$\Psi_1=\Psi_+(x)e^{-i(\omega_0+\omega)t}+\Psi_-(x)e^{-i(\omega_0-\omega)t},$$

where $\omega_0=\varepsilon/\hbar$, ε is the energy of the electrons incident on the structure, and $k=(2m^*\varepsilon/\hbar^2)^{1/2}$ is their wave vector. The functions $\Psi_\pm$ for this structure have the form

$$\Psi_\pm(x)=\begin{cases}D_\pm\exp(-ik_\pm x) & x<0,\\ A_\pm\sin k_\pm+B_x\cos k_\pm x+\chi_\pm(x) & 0<x<a,\\ C_\pm\exp[ik_\pm(x-a)]+P_\pm\exp[ik(x-a)] & x>a,\end{cases} \tag{4}$$

where $k_\pm=[2m^*(\omega_0\pm\omega)/\hbar]^{1/2}$, $P_\pm=\mp qEa\Psi_0(a)/\hbar\omega$, and $\chi_\pm(x)$ are the particular solutions of the equation

$$\hbar(\omega_0\pm\omega)\chi_\pm(x)=-\frac{\hbar^2}{2m^*}\frac{\partial\chi_\pm}{\partial x^2}-qEx\Psi_0(x). \tag{5}$$

In this case (see Ref. 11) we have

$$\chi_\pm(x)=\mp\frac{qEx}{\hbar\omega}\Psi_0(x)+\frac{qE}{m^*\omega^2}\Psi_0'(x). \tag{6}$$

The coefficients $A_\pm$, $B_\pm$, $C_\pm$, and $D_\pm$ can be found by using the conditions for matching the wave function and its

derivatives at the barriers at each instant of time,[11] while the system of equations for finding them has the following matrix form:

$$\begin{pmatrix} 1 & 0 & -1 & 0 \\ ik_{\pm}-y & k_{\pm} & 0 & 0 \\ 0 & \sin k_{\pm}a & \cos k_{\pm}a & -1 \\ 0 & -k_{\pm}\cos k_{\pm}a & k_{\pm}\sin k_{\pm}a & ik_{\pm}-y \end{pmatrix} \times \begin{pmatrix} D_{\pm} \\ A_{\pm} \\ B_{\pm} \\ C_{\pm} \end{pmatrix} = \begin{pmatrix} f_1 \\ f_2 \\ f_3 \\ f_4 \end{pmatrix}, \tag{7}$$

where

$$f_1=\chi_{\pm}(0), \qquad f_2=-\chi'_{\pm}(0),$$
$$f_3=P_{\pm}-\chi_{\pm}(a), \qquad f_4=(y-ik)P_{\pm}+\chi'_{\pm}(a),$$
$$y=2m^*\alpha/\hbar^2.$$

The solution of Eq. (7) is simple but rather cumbersome and is inconvenient for analytic studies; however, under certain conditions it can be greatly simplified. It is known that in a two-barrier, resonance-tunnel structure the transmission coefficient has a distinctly resonant character and in structures with thin barriers the magnitude of the wave vector which determines the resonance levels at which the transmission coefficient equals 1 is found by solving the transcendental equation[13]

$$\tan ka=-\frac{k\hbar^2}{\alpha m^*}=-\frac{2k}{y}, \tag{8}$$

Under resonant tunnelling conditions the coefficients of the unperturbed wave function and the function f in Eq. (7) have the form

$$A=\frac{y}{k}+i, \qquad B=1,$$

$$C=\left(\frac{y}{k}+i\right)\sin ka+\cos ka, \qquad D=0;$$

$$f_1=\frac{qE}{m^*\omega^2}(ik+y), \qquad f_2=\frac{qE}{\hbar\omega}\left(\pm 1+\frac{2\omega_0}{\omega}\right),$$

$$f_3=-\frac{qE}{m^*\omega^2}[(ik+y)\cos ka-k\sin ka],$$

$$f_4=\frac{qE}{\hbar\omega}\left(\pm 1+\frac{2\omega_0}{\omega}\right)\left[\left(\frac{y}{k}+i\right)\sin ka+\cos ka\right].$$

Let us assume that the monoenergetic flux of electrons passes through the resonance level with quantum number N, and that the frequency of the electric field corresponds to transitions at the resonance level with quantum number L. The determinant of the system of equations (7) is

$$\Delta=(2k_{\pm}^2-y^2)\sin k_{\pm}a-2k_{\pm}\cos k_{\pm}a + 2ik_{\pm}(k_{\pm}\cos k_{\pm}a+y\sin k_{\pm}a). \tag{9}$$

For $y\gg k_{\pm}$ and a wave vector of magnitude corresponding to a resonance level, the determinant becomes small and equal to $\Delta\approx 2ik_{\pm}^2(-1)^{L+1}$, while for transitions that are not to a resonance level we have $\Delta\approx k_{\pm}y$. Thus, for narrow resonance levels, only the probability of transitions between the two levels is important. On the other hand, in the case of broad levels with large quantum numbers, transitions to the lower and to the upper level are important (see Fig. 2). The determinants for finding $C_{\pm}$ and $D_{\pm}$ are given by

$$\Delta_{D\pm}=f_1[k_{\pm}(ik_{\pm}-y)\cos k_{\pm}a+k_{\pm}^2\sin k_{\pm}a] - f_2[ik_{\pm}-y)\sin k_{\pm}a+k_{\pm}\cos k_{\pm}a] + f_3k_{\pm}(ik_{\pm}-y)+k_{\pm}f_4, \tag{10}$$

and

$$\Delta_{C\pm}=-f_1k_{\pm}(ik_{\pm}-y)+k_{\pm}f_2 - f_3[k_{\pm}(ik_{\pm}-y)\cos k_{\pm}a+k_{\pm}^2\sin k_{\pm}a] + f_4[k_{\pm}\cos k_{\pm}a-(ik_{\pm}-y)\sin k_{\pm}a]. \tag{11}$$

For $y\gg k_{\pm}$ we have

$$\Delta_{D\pm}\approx\frac{qE}{m^*\omega^2}(ik+y)(ik_{\pm}-y)k_{\pm}(\cos k_{\pm}a-\cos ka), \tag{12}$$

and

$$\Delta_{C\pm}\approx\frac{qE}{m^*\omega^2}(ik+y)(ik_{\pm}-y)k_{\pm}(\cos k_{\pm}a\cos ka-1). \tag{13}$$

Using Eq. (8), for transitions with an even change in the quantum number of the level it is clear that

$$|\cos k_{\pm}a-\cos ka|\approx|\cos k_{\pm}a\cos ka-1|\approx 2,$$

while for an odd change,

$$|\cos k_{\pm}a-\cos ka|\approx|\cos k_{\pm}a\cos ka-1|\approx 0,$$

This well−known parity selection rule is explained by the symmetry properties of the wave functions and perturbations.

Thus, given that $ak_{\pm}\approx\pi L$, for monoenergetic electrons with concentration n for transitions between resonance levels the active conductivity of a two-barrier resonance-tunnel structure has the form

$$\sigma\approx\pm\frac{8q^2m^*\alpha^4n}{\pi L\hbar^6\omega^3}[1-(-1)^{N-L}]. \tag{14}$$

A more rigorous calculation incorporating terms which do not include y in the expressions for $\Delta_{C_{\pm}}$ and $\Delta_{D_{\pm}}$ yields the formula

$$\sigma\approx\pm\frac{q^2n}{\pi L}\left[\frac{8\alpha^2}{\hbar^3\omega^3}\left(\frac{m^*\alpha^2}{\hbar^3}+2\omega_0\pm\omega\right)\right][1-(-1)^{N-L}], \tag{15}$$

which, in contrast with Eq. (14), has a relative error on the order of $(k/y)^3$, as opposed to $(k/y)^2$. We emphasize that the two formulas have been derived under the assumption that transitions occur only between two levels.

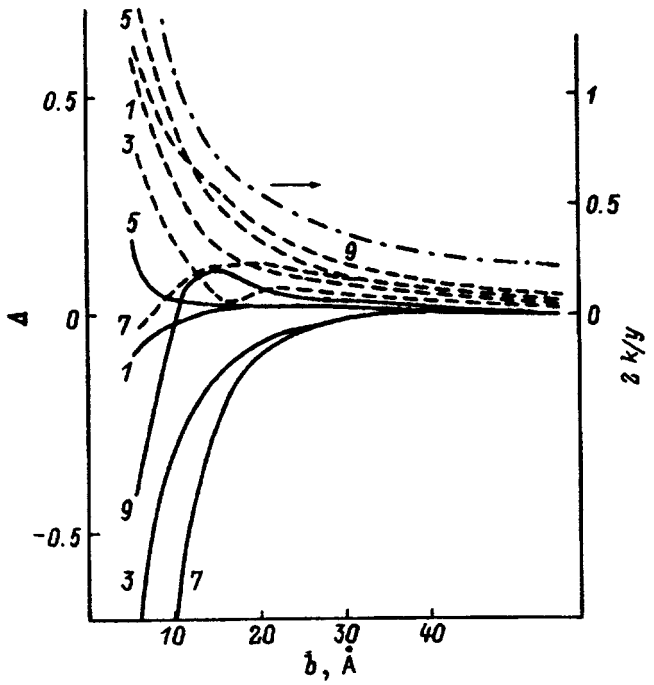

FIG. 4. Relative error $\Delta=(\sigma-\tilde{\sigma})/\sigma$ as a function of barrier thickness b when the resonance active conductivity $\tilde{\sigma}$ is calculated using Eq. (15) (smooth curves) and (14) (dashed curves), as well as the parameter $2k/y$ (dot-dashed curve) for passage of electrons through the eighth level of a two-barrier structure of width $a=275$ Å (barrier height $\varphi_b=1.04$ eV). The numbers denote the quantum numbers of the levels to which the transitions take place.

Let us investigate how accurately these formulas describe the magnitude of the conductivity in real structures with a ratio k/y that is moderately low. Figure 4 shows the relative errors in the magnitude of the active conductivity [calculated according to Eqs. (14) and (15)] plotted as functions of the barrier thickness when electrons pass through the eighth resonance level of a structure with width $a=275$ Å. Also shown in this figure is the dependence of the parameter $2k/y$ on the barrier thickness. It is clear that for thin barriers ($b<20$ Å, $2k/y>0.5$), with transitions between levels $8\rightarrow 7$ the conductivity is better fit by Eq. (14). This is explained by the fact that in a structure with thin barriers, transitions to the ninth resonance level, as well as those to the seventh resonance level, are important; thus, both formulas are inaccurate and the cruder approximation (14) is better.

It should be noted that the maximum possible value of the conductivity for $8\rightarrow 7$ transitions, which, as a rigorous calculation shows, occur at a frequency $\omega<(\mathscr{E}_8-\mathscr{E}_7)/\hbar$ (see Fig. 2b), is given better by Eq. (15). For thicker barriers (20 Å $< b <$ 40 Å, $0.25<2k/y<0.5$), Eq. (15) is significantly more accurate than Eq. (14). When the structure thickness is increased further, as might be expected, the calculations according to Eqs. (14) and (15) are essentially the same and provide a very accurate fit to the conductivity.

4. ESTIMATE OF THE MAXIMUM INTEGRAL CONDUCTIVITY OF TWO-BARRIER RESONANCE-TUNNEL STRUCTURES

It might seem possible to obtain arbitrarily high resonance conductivities of a two-barrier, resonance-tunnel structure by increasing the barrier thickness; however, the feasibility of increasing the conductivity by using thicker barriers is limited by a narrowing of the level into which the electrons are injected. This leads to a rise in the average time an electron spends in the well and, therefore, to an enhancement in scattering processes which destroy the coherence of the electrons' passage.

It is interesting to find the dependence of the conductivity on the quantum numbers L and N of the working levels by limiting the power of the barriers to the maximum condition for maintenance of coherence.

According to Eq. (14), the monoenergetic conductivity σ is directly proportional to the fourth power of the barrier power α. At the same time, it can be shown that the width of the Mth quasilevel (the Mth energy miniband), Γ_M, which is determined by tunnelling through identical δ-barriers, is inversely proportional to α^2:

$$\Gamma_M=\left(\frac{\hbar^2\pi M}{m^*}\right)^3\frac{1}{\alpha^2a^4}. \tag{16}$$

The width of the quantum well a is determined by the frequency ω and the quantum numbers of the working levels as

$$a=\left[\frac{\pi^2}{2m^*\omega}(N^2-L^2)\right]^{1/2}, \tag{17}$$

so that the conductivity of the two-barrier, resonance-tunnel structure is expressed in terms of $\tau_M=\hbar/\Gamma_M$, the tunnel lifetime of an electron in the Mth miniband, as

$$\sigma=\pm\frac{256\omega}{\pi^3m^*}(q\tau_M)^2I\frac{M^6}{N^3L_3}F(N,L),$$

$$\frac{\omega\tau_M}{2\pi}>\frac{(N^2-L^2)}{M^3}K^2, \tag{18}$$

where $F(N,L)=N^2L^2/(N^2-L^2)^4$, and $K=NL/I$ is the quantum number of the level to which the electrons move under the action of the rf field.

In order for this model of the coherent passage of electrons through a two-barrier, resonance-tunnel structure to be correct, it is necessary that the characteristic tunnelling time $\tau_M=\hbar/\Gamma_M$ exceed the time for the scattering processes which destroy the coherence of the electron wave function. This time τ_P is less than the characteristic time for transitions excited by phonon scattering since the coherence can also be destroyed by collisions which leave an electron in the same energy subband.[14] Strictly speaking, the more rigorous condition $\tau_P<\tau_L$ (a restriction on the narrower lower level), which ensures coherence of the entire tunnelling process involving photons should be imposed; however, if we assume that scattering processes in the miniband into which the current is injected are dominant, then during injection into the upper level ($I=N$) it is appropriate to consider the weaker restriction on the upper level: $\tau_P<\tau_N$.

For a qualitative analysis we assume that τ_P is independent of the energy while the barrier power α is chosen as large as possible, so that $\hbar/\Gamma_M=\tau_P$. Here in Eq. (18) for $I=L$ (injection into the lower level, positive conductivity) it is necessary to set $M=L$ (limit on the lower level), while for $I=N$ (injection into the upper level, negative conductivity),

$M=L$ or $M=N$, depending on whether the restriction on the scattering has been imposed on level L or M.

For instrument applications there is interest in the integral conductivity G:

$$G=S\int_0^\infty f(\varepsilon)\frac{\sigma(\varepsilon)}{a}\,d\varepsilon, \tag{19}$$

where S is the perpendicular cross-sectional area of the two-barrier, resonance-tunnel structure, and $f(\varepsilon)$ is the distribution function of the electrons with respect to the transverse (perpendicular to the barrier) energy ε of the flux incident on the structure. For sufficiently narrow quasilevels, given that $\Gamma_L/\Gamma_I n(\mathscr{E}_I)$ electrons participate in the resonance interaction, where $n(\mathscr{E}_I)$ is their average concentration in the flux incident on the two-barrier, resonance-tunnel structure (in the energy interval Γ_I near $\mathscr{E}_I$), Eq. (6) implies that

$$G\simeq[\Gamma_L/\Gamma_I n(\mathscr{E}_I)]\sigma(\mathscr{E}_I)/a. \tag{20}$$

The static transmission coefficient is assumed equal to unity.

Let us assume that in addition to the change in the height of the injection level $\mathscr{E}=\hbar\omega I/(N^2-L^2)$, the height of the injector and the concentration of electrons in it vary in such a way that the density of the supply current, $J_0=qv(\mathscr{E}_I)n(\mathscr{E}_I)$, is held constant. Here the electron concentration $n(\mathscr{E}_I)$ is inversely proportional to the transverse electron velocity $v(\mathscr{E}_I)=(2\mathscr{E}_I/m^*)^{1/2}$:

$$n(\mathscr{E}_I)=\frac{J_0}{qv(\mathscr{E}_I)}=J_0/\{q[2(\hbar\omega/m^*)I/(N^2-L^2)]\}^{1/2}. \tag{21}$$

Substituting Eqs. (1) and (8) in Eq. (7) and noting that $\Gamma_L/\Gamma_I=L^3/I^3$ according to Eq. (20), we obtain

$$G=\pm S\frac{256}{\pi^4}qJ_0\omega\frac{\tau_P^2}{\hbar}\frac{M^6}{N^3I^3}F(N,\,L). \tag{22}$$

It is interesting that G does not depend explicitly on the effective electron mass m^*, but the active properties of the apparatus are determined to a great extent by the quantity Ga^2/S, which is directly proportional (ignoring the effect of the variable space charge) to the specific resistivity $SR=Ga^2/S(\varepsilon\omega)^2$ (here ε is the absolute dielectric constant of the semiconductor). This quantity determines the intensity of radiative transitions (per unit area) over the entire structure, which equals $Ga^2E_1^2/(2\hbar S)$, and also the conditions for lasing, both in a laser as such,[10] with $-Ga^2/S>\sigma_S w$ (σ is the positive conductivity for ohmic losses, and w is the width of the optical waveguide), and in a laser based on a resonance-tunnel time-of-flight diode,[15] with $-Ga^2/S>SR_S(\varepsilon\omega)^2$ (R_S is the ohmic resistance of the passive and contact layers of the diode).

Using Eqs. (3) and (9), we obtain

$$Ga^2/S=\pm\frac{256}{\pi^3}qJ_0\frac{\tau_P^2}{2m^*}\frac{M^6}{N^3I^3}F(N,L)(N^2-L^2). \tag{23}$$

It can be shown rigorously, given the properties of the function $F(N,L)$ [see Eq. (4)], that the maximum absolute value of Ga^2/S, like the maximum absolute values of G and σ, is attained for transitions between neighboring levels with $N=L+1$, in agreement with the above numerical calculations. In this case

$$|Ga^2/S|_{L+1,L+1}\sim L^2(L+1)^2/(2L+1)^3,$$

$$|Ga^2/S|_{L+1,L}\sim[L/(L+1)]^6(Ga^2/S)_{L+1,L+1},$$

$$|Ga^2/S|_{L,L}\sim[L/(L+1)]^3(Ga^2/S)_{L+1,L+1},$$

where the first subscript denotes the injection level and the second, the level whose width is limited by scattering. Corresponding graphs are shown in Fig. 5. It is evident that the operating efficiency of the apparatus at the edge of the coherent regime increases substantially as the working level L is raised.

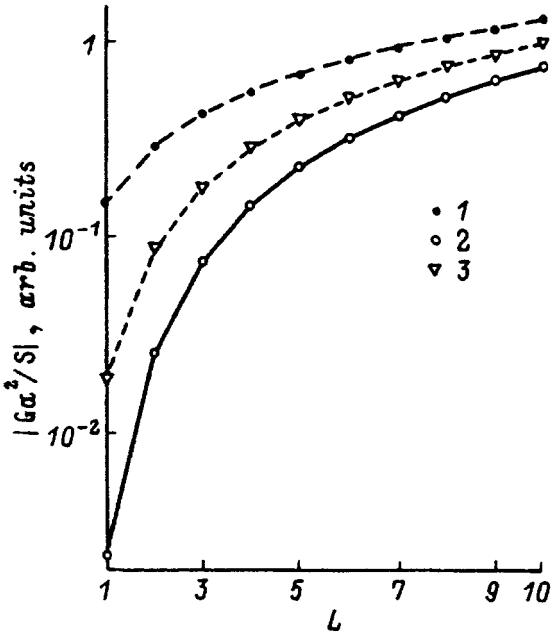

FIG. 5. Maximum attainable value of $|Ga^2/S|$ as a function of the quantum number L of the lower working level. Injection into the upper level: (*1*) limitation in the upper level, (*2*) limitation in the lower level, (*3*) injection and limitation in the lower level.

Clearly, $|Ga^2/S|$ is largest when τ_P limits the width of the upper miniband, while the processes which destroy the coherence in the narrower lower subband are disregarded. Here, using $5\rightarrow4$ transitions, instead of $2\rightarrow1$, makes it possible to increase the intensity of the radiative processes, which is proportional to $|Ga^2/S|$, by a factor of roughly 50. A still larger difference in the intensity of the transitions, by roughly two orders of magnitude, can be expected when L is increased from 1 to 4 if we use the more rigorous condition $\hbar\Gamma_L\geqslant\tau_P$, which ensures coherence of the wave function, both in the upper and in the lower subbands.

5. CONCLUSIONS

The solution of the time-dependent Schrödinger equation in the small-signal approximation has been used to analyze the frequency dependences of the active dynamic conductivity of a two-barrier, resonance-tunnel structure in the THz range. It has been shown that the conductivity of the structure is greatest when operating in neighboring energy levels.

The dependence of the conductivity on the barrier thickness (''power'') has been calculated. Differences in the behavior of the conductivity when the thicknesses of the first and second barriers are increased have been pointed out and explained. Simple analytic expressions for the conductivity of a two-barrier resonance-tunnel structure have been obtained under the assumption of high barrier powers α and found to match very precisely the corresponding rigorous solution of the Schrödinger equation for $\alpha > 4\hbar[\hbar(\omega_0 \pm \omega)/2m^*]^{1/2}$.

The expressions for the conductivity derived here imply, in particular, that:

1) the conductivity increases as the fourth power of the barrier thickness;

2) transitions with an even change in the quantum numbers of the levels are forbidden;

3) the conductivity decreases in inverse proportion to the quantum number of the level;

4) the conductivity is inversely proportional to the cube of the frequency;

5) the maximum attainable (when limited by scattering) integral conductivity, as well as the intensity of radiative quantum mechanical transitions proportional to it, increase substantially with the quantum number of the level into which electrons are injected.

We thank A. S. Tager for interest in this work and for useful comments.

This work has been supported by the Russian Fund for Fundamental Research, Grant No. 94-02-04449, and the Scientific Council of the program ''Physics of Solid State Nanostructures,'' Grant No. 1-050.

[1] R. F. Kazarinov and R. A. Suris, Fiz. Tekh. Poluprovodn. **6**, 148 (1972) [Sov. Phys. Semicond. **6**, 96 (1972)].
[2] W. H. Frensley, Superlattices Microstruct. **4**, 491 (1988).
[3] L. Y. Chen and C. S. Ting, Phys. Rev. B **43**, 2097 (1991).
[4] V. Kislov and A. Kamenev, Appl. Phys. Lett. **59**, 1500 (1991).
[5] J. P. Loehr, J. Singh, R. K. Mains, and G. I. Haddad, Appl. Phys. Lett. **59**, 2070 (1991).
[6] A. B. Pashkovskiĭ, Pis'ma Zh. Tekh. Fiz. **19**(9), 1 (1993) [Tech. Phys. Lett. **19**, 533 (1993)].
[7] E. I. Golant, A. B. Pashkovskiĭ, and A. S. Tager, Fiz. Tekh. Poluprovodn. **28**, 740 (1994) [Semiconductors **28**, 436 (1994)].
[8] J. Faist, F. Capasso, D. L. Sivco, C. Sirtori, A. L. Hutchinson, and A. Y. Cho, Science **264**, 533 (1994).
[9] P. England, J. R. Hayes, E. Colas, and M. Helm, Solid–State Electron. **32**, 1213 (1989).
[10] E. I. Golant, A. B. Pashkovskiĭ, and A. S. Tager, Pis'ma Zh. Tekh. Fiz. **20**(11), 74 (1994) [Tech. Phys. Lett. **20**, 886 (1994)].
[11] E. I. Golant and A. B. Pashkovskiĭ, Fiz. Tekh. Poluprovodn. **28**, 954 (1994) [Semiconductors **28**, 553 (1994)].
[12] E. I. Golant, Ya. B. Martynov, A. B. Pashkovskiĭ, and A. S. Tager, Pis'ma Zh. Tekh. Fiz. **20**, 11 (1994) [Tech. Phys. Lett. **20**, 814 (1994)].
[13] V. M. Galitskii, B. M. Karnakov, and V. I. Kogan, *Problems in Quantum Mechanics* [in Russian], Nauka, Moscow (1981).
[14] J. Faist, F. Capasso, C. Sirtori, D. L. Sivco, A. L. Hutchinson, S. N. G. Chu, and A. Y. Cho., Appl. Phys. Lett. **63**, 1354 (1993).
[15] E. I. Golant, A. B. Pashkovskiĭ, and A. S. Tager, Pis'ma Zh. Tekh. Fiz. **21**, 16 (1995) [Tech. Phys. Lett. **21**, 171 (1995)].

Translated by D. H. McNeill

Transport of hydrogen in films of graphite, amorphous silicon, and nickel oxide

I. E. Gabis

Scientific Research Institute of Physics, State University at St. Petersburg, 198904 St. Petersburg, Russia
(Submitted February 20, 1996; accepted for publication April 8, 1996)
Fiz. Tekh. Poluprovodn. **31**, 209–215 (February 1997)

A new concentration pulse method is used to study the transport of hydrogen in three semiconducting materials deposited in the form of films on nickel substrates. The most probable models for the transport are proposed. In graphite hydrogen diffuses in the form of molecules and its diffusion is accompanied by reversible capture; transport occurs along microscopic voids between scales of graphite. Valence unsaturated bonds at the boundaries of the scales serve as capture centers. Diffusion in amorphous silicon is also accompanied by capture, but takes place in an atomic form along interstices; valence unsaturated Si-bonds serve as capture centers. In nickel oxide, as in graphite, diffusive transport takes place in the form of molecules, but capture of hydrogen on valence unsaturated bonds has not been observed. A comparative analysis is made of the properties manifested by these materials for oxygen in order to establish their correlation with the structure and electronic properties of the semiconductors. [S1063-7826(97)00402-X]

Research on the transport of hydrogen in semiconductor materials is an important scientific and applied problem. The overwhelming majority of data on the interaction of hydrogen with solids, however, has been obtained on metals, and one of the most powerful experimental techniques, the hydrogen permeation technique,[1,2] applies specifically to metals. The main problem in using it for semiconductors lies in the need to prepare a thin, vacuum-tight barrier of the test material which will not be destroyed as the temperature is varied. In contrast with the classical hydrogen permeation technique, the concentration pulse method which we have developed[3,4] can be used for detailed studies of the kinetics of hydrogen transport through double-layer membranes. The above-mentioned difficulty can be avoided by depositing a layer of semiconductor material on a metal and studying the interaction of hydrogen with the resulting system over the entire transport path.

In this paper we briefly describe the results of a study of the transport of hydrogen in films of graphite, amorphous silicon, and nickel oxide deposited on nickel substrates which have been presented in detail elsewhere,[5–7] discuss the most probable models on a phenomenological level, and make a comparative analysis of the properties which show up with hydrogen. The test materials were semiconductors that have widely differing properties and important practical applications. Graphite may be used as a structural material in controlled thermonuclear fusion reactors. The hydrogen passivation of unsaturated bonds is of interest for reducing the density of states in the bandgap of semiconductor devices based on amorphous and crystalline silicon and for improving the device characteristics. Oxide coatings can be used to actively inhibit hydrogen saturation processes which are often an undesirable factor in materials operating in hydrogenic environments.

EXPERIMENTAL APPARATUS

The experiments were carried out in an automated experimental system which combined the techniques of hydrogen permeation, desorption with linear heating, and a gaseous chemical reactor with analysis of the reaction products through a microscopic leak. The gas analyzer is a time-of-flight mass spectrometer with mass selection. The system was controlled with a computer. Slave systems were organized for controlling the sample temperature, turning on the dissociator, and controlling the hydrogen pressure and mass selector. The latter made it possible to simultaneously record several components of the gas mixture. This apparatus has been described in detail elsewhere.[8]

RESEARCH TECHNIQUE

Besides standard variants of the hydrogen permeation and desorption with linear heating techniques, we have used the concentration pulse method described in Ref. 3. This method is based on analyzing a pulsed flux of hydrogen which penetrates through a membrane. In particular, this method can be used to study the kinetics of transport in two-layer diffusive systems, choose among several models, and determine the magnitudes of the kinetic constants which influence the process.

In the regions near the surface of a membrane, one side of which will be called the inlet side in the following, discussion, rectangular concentration pulses of hydrogen are created with a spacing of 2 meanders. After a certain time, a penetrating flux is established and detected. The shape of these pulses is highly distorted because dispersion of the hydrogen concentration waves. By expanding them in a Fourier series it is possible to determine the frequency dependence of the amplitude and phase of the penetrating flux. In the case of a layered system, the latter will, in turn, depend on the mechanism for hydrogen transport, on the diffusion coefficient in the layers, and on the boundary conditions. An analysis of the experimental data leads to a choice of one model out of several possibilities and to numerical values for the kinetic parameters of the model.

Concentration pulses were created on the inlet side of the membrane by turning a hydrogen dissociator on and off

along the coating-free nickel surface. In separate experiments it was established that this procedure yields high-quality concentration pulses.

THE SAMPLES

All the test films were deposited on the surface of carefully degassed nickel membranes of diameter 38 mm, welded into tubular stainless-steel holders. The side of the sample with the film on it was the outlet side with respect to the permeating flow.

Graphite films were obtained by high-temperature decomposition of acetylene on the nickel surface. The procedure for depositing a carbon film was studied beforehand and developed on ribbon samples placed in a gaseous reactor.[9] Deposition on the membrane involved a single, short-duration (less than 400 s) interaction of acetylene with the nickel surface heated to temperatures of 640–740 °C, after which the volume with the sample was evacuated and the sample cooled. The short pyrolysis time prevents a significant amount of carbon from dissolving in the substrate. In the subsequent studies of hydrogen transport through the resulting two-layer system, the sample temperature did not exceed 450 °C, a temperature at which the solubility of carbon in nickel is negligible[10] and which guaranteed the stability of the test sample.

The films were ~ 0.4 μm thick. Auger analysis with ion etching was used to establish the absence of any impurities in the carbon. Electron microscopy of the surface revealed a scaly structure with a characteristic scale size of about 50 μm. Peaks corresponding to graphite showed up in x-ray structural measurements.

Amorphous silicon was deposited on a heated nickel surface by rf plasma decomposition of SiH_4. This technique makes it possible to control the density of states in the band gap (the band gap is $\Delta E \simeq 1.75$ eV), reducing it to below 10^{16} $eV^{-1} \cdot cm^{-3}$ through the formation of Si–H valence bonds.[11] These states bond with the valence saturated bonds intrinsic to amorphous silicon. The test films were intrinsic semiconductors. Their thickness was 0.5 μm.

The possible recrystallization of silicon was considered during the experiments. Recrystallization, which took place under our conditions at a temperature of ~ 550 °C, led to irreversible changes in the sample properties. The magnitudes of the steady-state fluxes and the rates at which they were approached were increased by several factors. As a result, the upper bound of the range of temperatures to be studied was found to be 500 °C.

An oxide coating was formed by processing one of the membrane surfaces for 20 h in air at a temperature of 800 °C. Here the second surface faced a vacuum. X-ray structural analysis showed that an essentially single-phase layer of the oxide NiO with a thickness of about 0.2 μm was formed in close contact with the substrate. Electron microscopy revealed a grainy structure with a characteristic grain size of ~ 3 μm.

TRANSPORT MODELS

One of the purposes of this study was to determine the mechanism for transport of hydrogen through the semiconducting films, i.e., to choose the most probable of the many possible phenomenological models. Here we describe the models that were considered. They are based on the boundary value problems for two-layer membranes. C_j is the hydrogen concentration, D_j is the diffusion coefficient, and $j=1, 2$, with 1 referring to nickel and 2, to the semiconductor film.

The first layer was of nickel, through which hydrogen diffuses in accordance with Fick's law,

$$\frac{\partial C_1}{\partial t} = D_j \frac{\partial^2 C_1}{\partial x_1^2}, \qquad x_1 \in [0, l_1]. \tag{1}$$

On the free entrance surface of the nickel boundary conditions of the first kind are satisfied:

$$C_1(l_1, t) = C_{l_1}(t). \tag{2}$$

We examined two variants for transport of hydrogen through the test materials: in molecular or in dissociated form. The conditions at the boundary between the materials were represented by an equation of continuity for the flux,

$$D_1 \frac{\partial C_1}{\partial x_1}(0, t) = m D_2 \frac{\partial C_2}{\partial x_2}(l_2, t), \tag{3}$$

where m is a coefficient equal to 1 for atomic diffusion and to 2 for molecular diffusion through the film and the boundary condition of the first kind for the concentrations is

$$\frac{C_1^m(0,t)}{C_2(l_2,t)} = \frac{\Gamma_1^m}{\Gamma_2}, \tag{4}$$

where Γ_1 and Γ_2 are the equilibrium solubilities of hydrogen in the nickel and in the semiconductor layer.

On the surface of the semiconductor that faced the vacuum we considered a boundary condition of the first kind,

$$C_2(0, t) = 0 \tag{5}$$

or of the third kind,

$$D_2 \frac{\partial C_2}{\partial x_2}(0, t) = b C_2^m(0, t), \tag{6}$$

where b is the constant for associative loss into the vacuum from the solution in the semiconductor.

Three variants of hydrogen transport through the semiconductor were examined:

1) diffusion according to Fick's law,

$$\frac{\partial C_2}{\partial t} = D_2 \frac{\partial^2 C_2}{\partial x_2^2}, \qquad x_2 \in [0, l_2]; \tag{7}$$

2) diffusion with reversible capture,

$$\begin{aligned} &\frac{\partial C_2}{\partial t} = D_2 \frac{\partial^2 C_2}{\partial x_2^2} - k_t C_2 + k_d C_t, \qquad x_2 \in [0, l_2], \\ &\frac{\partial C_t}{\partial t} = k_t C_2 - k_d C_t, \end{aligned} \tag{8}$$

where k_t and k_d are the rates of capture in traps and of discharge from them, and C_t is the concentration of hydrogen in the traps;

TABLE I. Characterization of diffusion processes.

Characteristic	Graphite	*a*-Si	NiO
Temperature, °C	250–400	300–500	450–590
Diffusion	Molecular	Atomic	Molecular
D_0, cm^2/s	3.8×10^{-9}	2.9×10^{-8}	6×10^{-11}
E_D, eV	0	0.35	0
Capture	on dangling bonds		absent
k_{t0}, s^{-1}	0.5	0.055	-
E_t, eV	0	0	-
k_{d0}, s^{-1}	3×10^3	340	-
E_d, eV	0.55	0.45	-

Note: E_D is the activation energy for the diffusion process, D_0 is the corresponding preexponential factor; E_t and E_d are the activation energies for the capture of hydrogen at a trap and for escape from traps [see Eq. (8)]; k_{t0} and k_{d0} are the corresponding preexponential factors.

3) the case of high permeability of the semiconductor layer; the boundary condition at the outlet side is written in the form of a balance between the diffusion and associative loss fluxes from the dissolved state in the nickel into the vacuum at rate b^*,

$$b^*C_1^2(0)=D_1\frac{\partial C_1(x_1,t)}{\partial x_1}(0,\,t). \tag{9}$$

EXPERIMENTAL RESULTS AND DISCUSSION

The following is a discussion, on a qualitative level, of the most probable mechanisms for the transport of hydrogen through the test materials established as a result of the present investigation. The quantitative results are given in Table I.

Graphite. Hydrogen is transported in the form of molecules and diffusion is accompanied by reversible capture. This corresponds to the system of diffusion equations (8) and the boundary conditions (3) and (4) with $m=2$. The low value of the diffusion coefficient (see the table) and its nonactivation character (activation energy $E_D=0$) show that transport appears to proceed along microscopic voids between the scales of graphite.

The scaly structure of a graphite film means that the actual path length followed by the diffusant particles is much longer than the film thickness, which may explain the low diffusion coefficient in the direction perpendicular to the surface. Additionally, free movement of an H_2 molecule along the intercrystalline voids is also improbable, since it is inhibited by unsaturated π-bonds in the base planes of the graphite scales. Because they overlap the electron cloud of the molecule, elastic repulsion must occur and the diffusant may follow a twisting trajectory along a microcavity. Evidently, this circumstance, along with the structural factor, also leads to low diffusion coefficients for hydrogen molecules in graphite.

Transport of molecules over internal microscopic void is accompanied by capture. Apparently, the traps are dangling bonds along the perimeter of graphite scales and the capture reaction is just an adsorption, but not on the outer surface of a graphite film that becomes the gaseous phase, but on inner centers that are energetically favorable. A semiempirical molecular orbital method has been used[12] to calculate the potential energies during adsorption of hydrogen on different planes of graphite. These calculations imply that when a hydrogen atom approaches the base graphite plane, an energy barrier of height ~1.5 eV develops with a potential well beyond it, whose bottom, however, lies above the energy level of the hydrogen atom outside the solid. Thus, adsorption onto the base graphite plane is energetically unfavorable. The favorable adsorption sites lie on the boundaries along the perimeter of the planes: they lie 3–4 eV below the level of a hydrogen atom, and there is no energy barrier for adsorption.

The absence of capture or the existence of small activation energy for it indicate that the adsorption of hydrogen on σ-bonds inside the microscopic voids has a weak activation character. In this situation the activation energy of roughly 0.55 eV for the reverse reaction, escape from a trap, characterizes the energy that binds a hydrogen atom to the trap.

As a semimetal, graphite has a sufficiently high concentration of charge carriers ($\sim10^{19}$ cm^{-3})[13] in the temperature range under consideration to lead to dissociation of a hydrogen molecule and adsorption of the atoms on neighboring σ-bonds. A hydrogen molecule inside the microcavities is always immediately adjacent to graphite, which enhances the probability of this sort of reaction. Taking the analogy with adsorption from the gaseous phase, we can say that the molecule, in effect, moves constantly along the surface of the adsorbate and experiences the effect of its electron cloud.

This model gives a satisfactory explanation of the magnitude of the diffusion of hydrogen in a graphite film, as well as of its weak temperature dependence. Confirmation of its validity can be found elsewhere.[14,15] In a review[14] the large scatter in the values of the diffusion coefficient for hydrogen in compact graphites obtained by various authors has been attributed to the different structures of the materials that were studied. Clearly, the different methods for preparing the graphite and the resulting different structures should lead to differences in the configuration and sizes of the microcavities along which hydrogen molecules may move. A correlation has been obtained[15] between the measured hydrogen diffusion coefficients and the ''degree of structural ordering'' in the samples.

The references in a review[16] have been divided into two classes according to the temperature intervals over which the measurements have been made. Our measurements of the diffusion coefficient are in satisfactory agreement with data from the low-temperature studies ($T<500$ °C).

Amorphous silicon. The diffusion of hydrogen in this material is also accompanied by capture [Eq. (8)], but the hydrogen is atomic [$m=1$ in the boundary conditions (3) and (4)]. It may be assumed that the capture centers are the valence unsaturated bonds intrinsic to amorphous silicon.

Our data on the hydrogen diffusion are in good agreement with data[17] for amorphous silicon and with the calculations[18] given in a review.[19] That review[19] also cites data which indicate the possible capture of hydrogen in silicon. However, the overall scatter in the data for the hydrogen diffusion coefficient in silicon cited there is up to five orders of magnitude, so the agreement with some of them may be a coincidence.

The diffusion of deuterium in layered samples with hydrated and deuterated amorphous silicon has been studied[20] by analyzing SIMS concentration profiles. The resulting values of the diffusion coefficient are 4–5 orders of magnitude lower. SIMS does not resolve hydrogen that is diffusively mobile and captured on free Si-bonds, while our data show that there is substantially more of the latter (units and tens of at. % captured on traps as opposed to tens and hundredths of at. % of diffusively mobile hydrogen). Thus, the reported values[20] appear to reflect changes in the profiles of the concentration of hydrogen on dangling Si bonds, rather than diffusion.

The magnitude of the preexponential factor for the diffusion coefficient of hydrogen in amorphous silicon was several orders of magnitude smaller than in metals (for them a ''normal'' value of 10^{-3} cm^2/s is typical[21]). Evidently, the mechanism for diffusive transport in the semiconductor is different. Hydrogen is present in the lattice of metals in the form of a screened proton which perturbs the equilibrium density of the electron fluid and the elastic interactions in the ion core.[22] In this semiconductor this sort of screening is improbable because of a lack of intrinsic current carriers: we estimate, on the basis of the magnitude of the permeating flux and the data given in the table, that the concentration of diffusively mobile hydrogen in the silicon layer is $\sim 10^{18}-10^{19}$ cm^{-3}, while the concentration of free electrons is 1–2 orders of magnitude lower.[23] The covalent, as opposed to metallic, bonds in the silicon lattice (distances on the order of several coordination spheres can be arbitrarily viewed as a lattice[23]) should lead to large energy expenditures in the elastic deformation caused by introduction of the impurity.

One variant that explains the low preexponential factor D_0 is discussed in the book by Vavilov *et al.*[24] on the mechanism for diffusive migration of hydrogen atoms along Si bonds. Here the equilibrium position is the central site on a line joining neighboring silicon atoms. It appears that a diffusive jump into a neighboring equilibrium position can occur if there is an electron vacancy, i.e., a hole, there. In this case the probability of a jump would be proportional to the probability of encountering a hole immediately adjacent to the diffusant, i.e., proportional to the concentration of intrinsic current carriers relative to the concentration $N_0 \simeq 10^{23}$ cm^{-3} of silicon atoms. Thus, the preexponential factor D_0 would be $D_0 = D_N N_c / N_0$, where $D_n \simeq 10^{-3}$ cm^2/s is the normal value of the diffusion preexponential factor,[21] and $N_c \simeq 10^{18}-10^{19}$ cm^{-3} is an estimate[25] for the effective density of states in the conduction band.

Although this mechanism for hydrogen diffusion in silicon explains the small value of the preexponential factor, it is nonetheless unlikely. The doubled length of the Si–H bond, equal to $\sim$0.3 nm, exceed the length of the Si–Si bond, ($\sim$0.27 nm), which should lead to repulsion of the silicon atoms when hydrogen is introduced on the line joining them. The idea of repulsion has been confirmed elsewhere.[24]

The model in which the equilibrium position of a hydrogen atom is in the interstices, as in metals, is more realistic. The energy expended in a diffusion jump in this case is determined mainly by elastic relaxation of the lattice as the diffusant crosses the ''narrowest'' site. The lattice of silicon is considerably ''looser'' than that of metals, but because of the lack of free current carriers and the covalent chemical bonds, elastic relaxation of the injected perturbation is difficult. Because of this circumstance, migration of the diffusant is also difficult. In order for a jump to take place from one equilibrium position into another, current carriers must be present in the immediate neighborhood to facilitate local elastic relaxation. Thus, the measured diffusion of hydrogen in amorphous silicon can be represented as the product of the normal (intrinsic) diffusive migration times the local screening probability, which leads to the same estimate for D_0 as with the mechanism involving migration over Si bonds discussed above.

There is still an objection to this model: the activation energy for diffusion in this case should include the energy for generating free current carriers, $\sim$0.8 eV, but it is at least a factor of 2 smaller than this value. However, hydrogen injected into an interstice, which elastically deforms the nearest surroundings, should be a trap for electrons. This has been confirmed experimentally by data presented in a review[25] which indicate that the density of states near the bottom of the conduction band rises when the concentration of hydrogen injected during fabrication of a film increases beyond some optimal level. The concentration of electrons captured in these levels, on the other hand, should have a temperature dependence which differs from that of the equilibrium concentration determined by heat removal (transfer) from the valence band.

An alternative reason for the low value of D_0 in amorphous silicon may also be that hydrogen can migrate only along special diffusion paths which have a low concentration. However, low preexponential factors for the diffusion coefficient have also been obtained in several crystalline semiconductors. Data from studies[15,26] of hydrogen diffusion in graphites at temperatures above 700 °C, which corresponds to transport in the single-particle form through the graphite lattice, i.e., migration along interstices, show that here also the preexponential D_0 is three to five orders of magnitude smaller than normal. We can assume, therefore, that the low preexponential factor D_0 is related to a specific mechanism for diffusive transport of hydrogen in semiconductors which differs from that for migration in metals.

Nickel oxide. Here, as in graphite, diffusive transport takes place in the form of molecules [$m=2$ in Eqs. (3) and (4)], but capture of hydrogen on valence unsaturated bonds has not been observed, despite the special attention which has been devoted to this problem.

Attempts to compare the experimental results with the model which gave the best agreement for graphite, where diffusion along the semiconducting layer was accompanied by reversible capture [Eqs. (8)], yielded negligible capture rates, i.e., degenerated to classical diffusion.

We may assume that, as in graphite, the resulting diffusion coefficient corresponds to transport of molecules over microscopic voids between NiO grains. In fact, nonactivated

transport of such a large injected impurity as the hydrogen molecule over a nickel oxide lattice appears unlikely.

COMPARISON OF THE RESULTS

By comparing the properties of the three test materials with respect to hydrogen it is possible to evaluate the influence of the structure and electronic characteristics of the solid on the diffusion and adsorption of hydrogen.

Diffusion. Graphite and nickel oxide have polycrystalline structures. Hydrogen diffuses in these materials as molecules and has a zero or very low activation energy, which indicates that the hydrogen moves along microscopic voids. The low diffusion coefficients show that this transport is not a Knudsen flow, but is a more complicated process. A comparison of graphite and nickel oxide, which consist of microcrystals of substantially different shapes and sizes, indicates that the determining factor is apparently not the configuration of the microscopic voids, but the presence of electron clouds from valence unsaturated bonds at the boundaries of the crystals. In amorphous silicon deposited on nickel there are no microcrystals or grain boundaries, so diffusion takes place through the volume of the semiconductor with the hydrogen dissociated.

Thus, we conclude that the structure of the material determines the form of hydrogen transport through semiconductors and the predominant diffusion mechanism: the presence of microscopic voids between grains provides the hydrogen with a channel for transport in the molecular form which turns out to predominate.

Adsorption. It is known that for metals adsorption is a collective interaction of the electron subsystem and ion core with a hydrogen molecule during which the molecule dissociates and a covalent-metallic chemical bond[22] is formed with the surface. Adsorption of hydrogen on semiconducting materials should be more localized than on metals in the sense that a hydrogen atom is held on the surface by a local covalent-ionic bond.

There is, however, a much more important difference associated with the huge difference in the concentrations of free current carriers in metals and semiconductors, which affects the probability of dissociative adsorption. Let us compare the transport of hydrogen over films of graphite and nickel oxide. Both these materials have a polycrystalline structure which, although it is not the same in terms of either the size or shape of the grains, is identical in the sense that both materials have microscopic voids along which H_2 molecules diffuse. In the region of the microscopic void of graphite and NiO there are valence unsaturated bonds which interact differently with hydrogen in these materials. Thus, as they migrate along the grain boundaries of nickel oxide, H_2 molecules are not adsorbed on the valence unsaturated bonds, while at the same time, the interaction with graphite proceeds at an appreciable rate.

Thus, by comparing nickel oxide and graphite, each of which has dangling bonds, we find that the presence of these bonds alone is not sufficient to dissociate hydrogen molecules; evidently, a high concentration of electrons in the conduction band is also necessary. In order for a hydrogen molecule to dissociate, it must interact with the electron subsystem of the solid. At very low free-electron concentrations, such as in nickel oxide, this interaction does not occur and adsorption is not observed even when active adsorption centers are present. The free electron concentration in graphite is substantially higher than in NiO and has been estimated[13] to be $10^{17}-10^{18}$ cm^{-3}. This is very low compared to metals, but is apparently high enough for adsorption of hydrogen on graphite.

The low concentration of free electrons in graphite compared to that in metals would also seem to lead to a low probability of dissociation and adsorption for hydrogen. But adsorption on a metal surface takes place (or does not) during a single collision of a molecule with the surface, while in graphite, an H_2 molecule inside a film and moving over the micropores is always immediately next to graphite scales and is being acted on by them, which leads to appreciable rates of adsorption.

[1] F. Waelbroeck, *Influence of bulk and surface phenomena on the hydrogen permeation through metals*, Jülich (1984).
[2] I. E. Gabis, T. N. Kompaniets, and A. A. Kurdyumov, in *Interaction of Hydrogen with Metals* [in Russian], A. P. Zakharov, ed., Moscow (1987), p. 177.
[3] I. E. Gabis and A. V. Ermakov, FKhMM, No. 4, 64 (1989).
[4] I. E. Gabis, Author's Abstract of Doctoral Dissertation, St. Petersburg (1995).
[5] I. E. Gabis, A. A. Kurdyumov, N. A. Tikhonov, and A. V. Samsonov, Pis'ma Zh. Tekh. Fiz. **20** (4), 88 (1994) [Tech. Phys. Lett. **20**, 300 (1994)].
[6] I. E. Gabis, A. A. Kurdyumov, and A. A. Samsonov, Pis'ma Zh. Tekh. Fiz. **21** (5), 1 (1995) [Tech. Phys. Lett. **21**, 315 (1995)].
[7] I. E. Gabis T. N. Kompaniets, V. A. Kurakin, A. A. Kurdyumov, and V. A. Piven', FKhMM, No. 4, 18 (1991).
[8] I. E. Gabis, A. A. Kurdyumov, and N. A. Tikhonov, Vestn. SPbGU, ser. 4, vyp. 2, N. 11, 77 (1993).
[9] I. E. Gabis, A. A. Kurdyumov, and N. A. Tikhonov, Vestn. SPbGU, ser. 4, vyp. 3, N. 18, 93 (1993).
[10] E. Fromm and E. Gebhard, *Gases and Carbon in Metals* [Russian translation], Moscow (1980).
[11] A. M. Danishevskii, V. Latinis, O. I. Kon'kov, E. I. Terukov, and M. M. Mezdrogina, Semiconductors **27**, 495 (1993).
[12] J. P. Chen and R. N. Yang, Surf. Sci. **216**, 481 (1989).
[13] E. M. Baitinger, *Electronic Structure of Condensed Carbon* [in Russian], Sverdlovsk (1988).
[14] K. Morita, K. Chisuka, and Y. Hasebe, J. Nucl. Mater. **162-164**, 990 (1989).
[15] M. J. Saeki, Nucl. Mater. **131**, 32 (1985).
[16] E. A. Denisov, T. N. Kompaniets *et al.*, J. Nucl. Mater. **212-215**, 1448 (1994).
[17] J. W. Corbett, D. Peak *et al.*, A. S. I. NATO, ser. B **136**, 61 (1986).
[18] A. Capizzi and A. Mitiga, Appl. Phys. Lett. **5**, 918 (1987).
[19] M. Aucoutrier and J. Chevalier, Ann. Chim. Fr. **14**, 117 (1989).
[20] G. J. Clark, C. W. Wite, D. D. Allred, B. R. Appleton, C. W. Magee, and D. E. Carlson, Appl. Phys. Lett. **31**, 582 (1977).
[21] V. P. Zhdanov, Ya. Pavlichek, and É. Knor, Poverkhnost', No. 10, 41 (1986).
[22] V. N. Ageev, O. P. Burmistrova, N. D. Potekhina, and S. M. Solov'ev, in *Interaction of Hydrogen with Metals* [in Russian], A. P. Zakharov, Ed., Moscow (1987), p. 18.
[23] N. Mott and E. Davis, *Electronic Processes in Non-crystalline Materials*, Oxford (1982).
[24] V. S. Vavilov, V. F. Kiselev, and B. N. Mukashev, *Defects in Silicon and on its Surface* [in Russian], Moscow (1990).
[25] M. Brodsky, Ed., *Amorphous Semiconductors*, Springer Verlag, N. Y. (1982).
[26] H. Atsumi, S. Tokura, and M. Miyake, J. Nucl. Mater. **155-157**, 241 (1988).

Translated by D. H. McNeill

Tunnel excess current in nondegenerate barrier ($p-n$ and $m-s$) silicon-containing III–V structures

V. V. Evstropov and Yu. V. Zhilyaev

A. F. Ioffe Physicotechnical Institute, Russian Academy of Sciences, 194021 St. Petersburg, Russia

M. Dzhumaeva and N. Nazarov

Physicotechnical Institute, Turkmenistan Academy of Sciences, 744000 Ashkhabad, Turkmenistan

(Submitted March 26, 1996; accepted for publication April 8, 1996)
Fiz. Tekh. Poluprovodn. **31**, 216–222 (February 1997)

Data are scaled from a study of the forward current in three types of barrier structure: $p-n$ homostructures $p-n$-GaP/n-Si, $p-n$-GaAs$-n$-GaP/n-Si, and $p-n$-GaAs$-n$-GaAs/n-Si; heterostructures n-GaP/p-Si, p-GaP/n-Si, n-GaAsP/p-Si, and n-GaAs/p-Si; and Au$-n$-GaP/n-Si surface-barrier structures. Epitaxial layers of GaP and GaAs were created on Si-substrates by gaseous phase epitaxy in a chloride system. Temperature measurements show that the forward current has a tunnel character, although the width of the space charge region greatly exceeds the tunneling length. A model is proposed for nonuniform tunneling along dislocations that intersect the space charge region. This type of tunneling is taken into account by introducing a phenomenological ''dilution'' factor for the barrier. The model makes it possible to calculate the dislocation density in device structures from the current-voltage characteristic. © *1997 American Institute of Physics.* [S1063-7826(97)00502-4]

1. INTRODUCTION

One of the areas of current interest in semiconductor electronics is the development of a reproducible technology for epitaxial growth of GaP and GaAs layers on Si-substrates for the purpose of creating different micro- and optoelectronic devices based on them.[1–5] Heterostructures of this type can be used to combine the unique electrical, photoelectric, and luminescence properties of GaAs and GaP with the advantages of high quality silicon wafers in monolithic structures.

The creation of homogeneous-band $p-n$-structures of GaP and GaAs on Si-substrates and of anisotypic GaP/Si and GaAs/Si heterostructures by gaseous phase epitaxy in a chloride system, as well as of surface-barrier $m-s$-structures based on epitaxial layers of n-GaP on Si-substrates, has been reported.[5–10] All the III–V layers were nondegenerate, i.e., the current carriers obeyed Boltzmann statistics. These data show that the current flows in all these structures have one feature in common: the current manifests a tunneling character, even at room temperature, despite the large width of the space charge region compared to the tunneling length.

The purpose of this paper is to scale data from studies of current flow in three types of barrier structures based on GaP and GaAs on Si-substrates: epitaxial $p-n$-structures, anisotypic heterostructures, and surface-barrier structures. The scaling is based on a model of tunneling facilitated by dislocations in which the tunneling transition probability and the characteristic tunneling length are substantially increased due to local dilution of the barrier along the flow path by a dislocation which intersects the space charge region.

First, a brief overview of the data from a study of the tunnel excess forward current is presented separately for each type of structure (Sec. 3). Then the similarities and differences in the mechanisms for current flow in the three types of structure are discussed (Sec. 4). Then the dislocation mechanism for the tunnel excess current flow through a wide (compared to the characteristic tunneling length) barrier is discussed (Sec. 5).

2. TEST SAMPLES

The anisotypic n-GaP/p-Si, p-GaP/n-Si, n-$GaAs_{0.25}P_{0.75}$/p-Si, and n-GaAs/p-Si heterostructures had epitaxial layer thicknesses of 3–4 μm. The GaP epitaxial $p-n$ structures on Si-substrates had n- and p-type layers with thicknesses of 3–4 and 2–3 μm, respectively. The concentration of the principal equilibrium carriers in the n-GaP, n-GaAsP, and n-GaAs layers was $n_0 \simeq 10^{17}$ cm^{-3} and in the p-GaP layers, $p_0 \simeq 5\times 10^{16}$ cm^{-3}. The epitaxial $p-n$ structures of GaAs on Si-substrates came in two forms: first, a buffer epitaxial layer of GaP grown by gaseous phase epitaxy in a chloride system, where the thickness of the buffer layer was of order 6 μm, and second, with a buffer layer of GaAs obtained by molecular beam epitaxy with a thickness of order 1.7 μm. The functional n- and p-type GaAs layers were created by gaseous phase epitaxy in a chloride system and had thicknesses of 5 and 3 μm, respectively. The concentration of the principal equilibrium carriers in the n-type GaAs layers was $n_0 \simeq 5\times 10^{16}$ cm^{-3} and in the p-type GaAs layers, $p_0 \simeq 10^{17}$ cm^{-3}. The Au–n-GaP/n-Si surface-barrier structures were obtained by thermal sputtering of gold to a thickness of 100–150 Å on the surface of an epitaxial n-GaP layer.

3. PRINCIPAL RESULTS

For the test structures the dependence of the current on voltage (forward branches) can be written as essentially exponential with a small addition in the form of ''bumps'' (Fig.

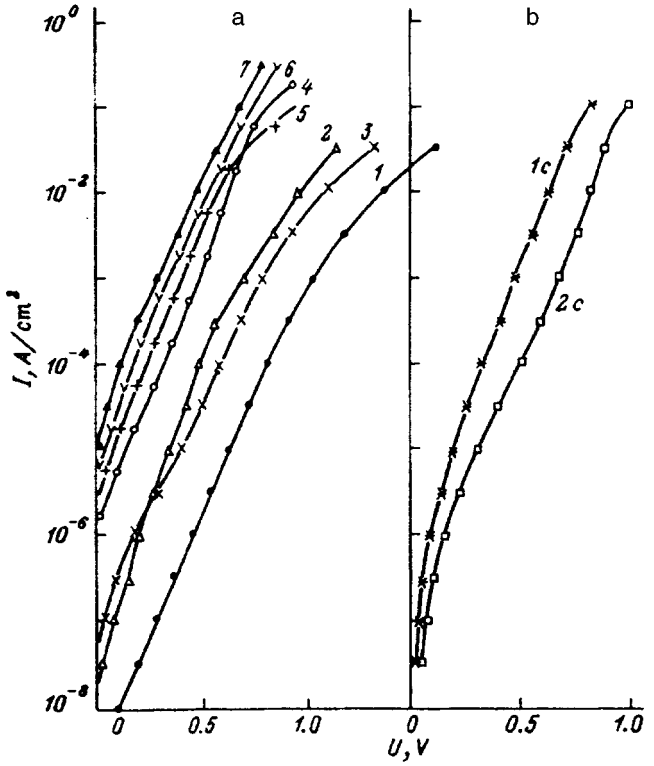

FIG. 1. The straight branches of the current-voltage characteristics for three types of barrier structures at 300 K: (a) homo-$p-n$- and hetero-$p-n$-structures, (b) surface-barrier $m-s$-structures. The numbers on the curves correspond to the sample numbers in Tables I and II.

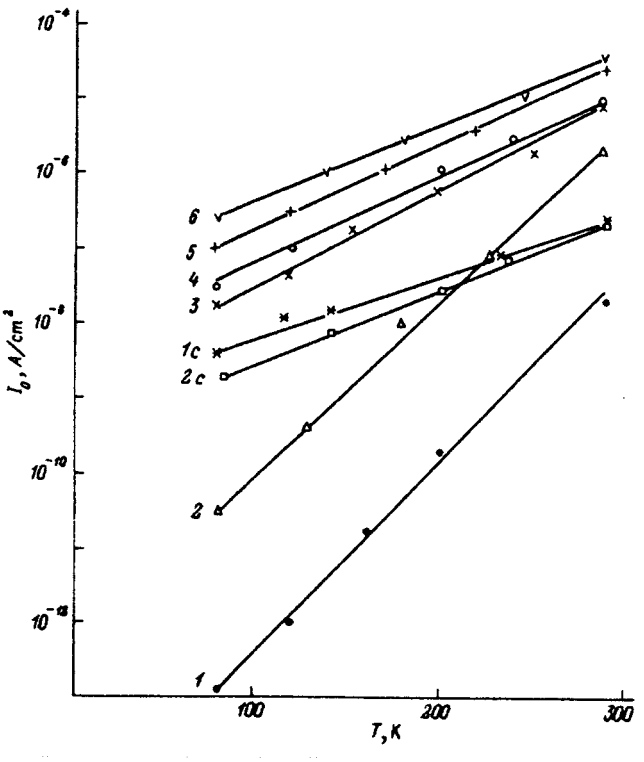

FIG. 2. Temperature dependence of the preexponential factor I_0 for the three types of structure. The numbers on the curves correspond to the sample numbers in Tables I and II.

1a and 1b), so that in analyzing the experimental data for all three types of structure the current-voltage characteristic was approximated by the expression

$$I = I_0 \exp eU/\varepsilon, \tag{1}$$

where the temperature dependence of the preexponential factor I_0 is given by the exponential (Fig. 2)

$$I_0 = I_{00} \exp aT$$

for all three types of structure.

3.1 The anisotypic heterostructures (samples *4–7* in Tables I and II) are characterized by a tunnel excess current flow mechanism.[6] The parameters in Eq. (1) at room temperature are: characteristic energy $\varepsilon = 60-85$ meV and preexponential factor $I_0 = 10^{-6}-10^{-5}$ A/cm^2. ε does not depend on temperature or increases slowly with temperature (Fig. 3b). The value of ε extrapolated to $T=0$ lies in the interval $\varepsilon_0 = 33-80$ meV (Table II). The preexponential factor I_0 increases slowly (not thermally activated) with temperature (Fig. 2), the temperature coefficient $a = \Delta \ln I_0/\Delta T \simeq 2.3-2.5\times10^{-2}$ K^{-1}, and I_{00} lies in the range $I_0 \simeq (10^{-8}-10^{-9})$ A/cm^2 (Table II).

3.2. A tunnel excess mechanism for current flow is also typical of the homogeneous-band $p-n$ structures of GaP and GaAs deposited on Si.[7–9] At room temperature $\varepsilon = 45-70$ meV and $I_0 = 5\times10^{-8}-10^{-9}$ A/cm^2, i.e., less than for the heterojunctions (samples *1–3* in Tables I and II).

The characteristic energy increases slowly with temperature (Fig. 3a). The value of ε extrapolated to absolute zero temperature lies in the range $\varepsilon_0 = 30-70$ meV (Table II), i.e., is roughly the same as in the heterojunctions. The preexponential factor I_0 increases slowly with temperature (Fig. 2). $I_{00} = 10^{-9}-3\times10^{-13}$ A/cm^2 for the $p-n$ junction and $I_{00} = 10^{-15}$ A/cm^2 for the $p-n$ junction (Table II) in GaAs.

3.3. For the Au$-n$-GaP/n-Si surface-barrier structures (samples *1c* and *2c* in Tables I and II) $\varepsilon = 55-70$ meV and $I_0 \simeq 10^{-7}$ A/cm^2 at room temperature, i.e., midway between the hetero- and homojunctions. As the temperature is lowered, I_0 decreases (Fig. 2). Extrapolating I_0 to $T=0$ gives $I_{00} \simeq 10^{-9}$ A/cm^2 and the temperature coefficient $a = 2.2\times10^{-2}$ K^{-1} (Table II). ε is essentially independent of temperature (Fig. 3c).

TABLE I. Principal parameters of the current-voltage characteristics at room temperature.

Samples	Structure type	I_0, A/cm^2	ε, meV	β
	Homo-$p-n$-structures			
1	$p-n$-GaP/n-Si	10^{-9}	70	2.7
2	$p-n$-GaAs/n-GaP/n-Si	10^{-8}	45	1.7
3	$p-n$-GaAs/n-GaAs/n-Si	6×10^{-8}	70	2.6
	Anisotypic hetero-$p-n$-structures			
4	n-GaP/p-Si	2×10^{-6}	65	2.5
5	p-GaP/n-Si	10^{-6}	60	2.2
6	n-GaAsP/p-Si	3×10^{-6}	85	3.6
7	n-GaAs/p-Si	10^{-5}	–	–
	Surface-barrier $m-s$-structures			
1*c*	Au–n-GaP/n-Si	2×10^{-7}	55	2.1
2*c*	Au–n-GaP/n-Si	10^{-7}	70	2.4

TABLE II. Parameters characterizing the temperature dependence of the straight branch of the current–voltage characteristic.

Samples	Structure type	ε_0, meV	β_∞	a, K^{-1}	I_{00}, A/cm^2
	Homo-$p-n$-structures				
1	$p-n$-GaP/n-Si	60	2	6.1×10^{-2}	10^{-15}
2	$p-n$-GaAs/n-GaP/n-Si	31	2	5.4×10^{-2}	3×10^{-13}
3	$p-n$-GaAs/n-GaAs/n-Si	73	2	3.0×10^{-2}	$(1–10)\times10^{-10}$
	Anisotypic hetero-p-n-structures				
4	n-GaP/p-Si	65	2	2.5×10^{-2}	$(3–10)\times10^{-10}$
5	p-GaP/n-Si	33	2	2.5×10^{-2}	$(1–10)\times10^{-9}$
6	n-GaAsP/p-Si	80	2	2.3×10^{-2}	$(3–10)\times10^{-9}$
7	n-GaAs/p-Si	–	2	–	–
	Surface-barrier $m-s$-structures				
1c	Au–n-GaP/n-Si	55	1	2.1×10^{-2}	10^{-9}
2c	Au–n-GaP/n-Si	70	1	2.2×10^{-2}	$(3–8)\times10^{-10}$

Approximate values are given for β_∞.

4. COMPARISON OF PARAMETERS

It is clear from Fig. 2 and Table I that for the homogeneous $p-n$-junctions the lowest value of I_0 occurs for the phosphide-gallium structures and the highest, for the arsenide-gallium structures with a buffer layer of GaAs. This agrees with the idea that as the width of the band gap increases, the tunneling probability decreases, since there is an increase in the height of the potential barrier to be overcome. In the heterostructures I_0 changes little compared to its variation in the homogeneous structures (Fig. 2, Table I). This agrees with the idea that for heterostructures the main contribution to current transport is from silicon. For the same reason, I_0 is greater in the heterostructures than in the homogeneous structures, which is consistent with the above mentioned idea of the effect of the band width on the tunneling probability. Thus, the tunnel excess current is lowest in the phosphide-gallium $p-n$ homostructures. In some of the structural types that were studied, ε increases as the temperature is raised (Fig. 3), but in all the structures $\beta=\varepsilon/kT$ decreases (Fig. 4a–4c). A crude extrapolation to an infinite temperature yields β_∞ (Table II). In the $p-n$ homo- and heterostructures $\beta_\infty\simeq2$, while in the surface-barrier structures $\beta_\infty\simeq1$. In all three types of structure, I_0 increases with rising temperature, and extrapolating the function $I_0(1/T)$ to an infinite temperature yields a value that is of the same order of magnitude for all the structures: $10^{-4}-10^{-5}$ A/cm^2 (Fig. 4). In the homo- and heterostructures, I_0 decreases with increasing temperature coefficient $a=\Delta\ln I_0/\Delta T$ (Fig. 2).

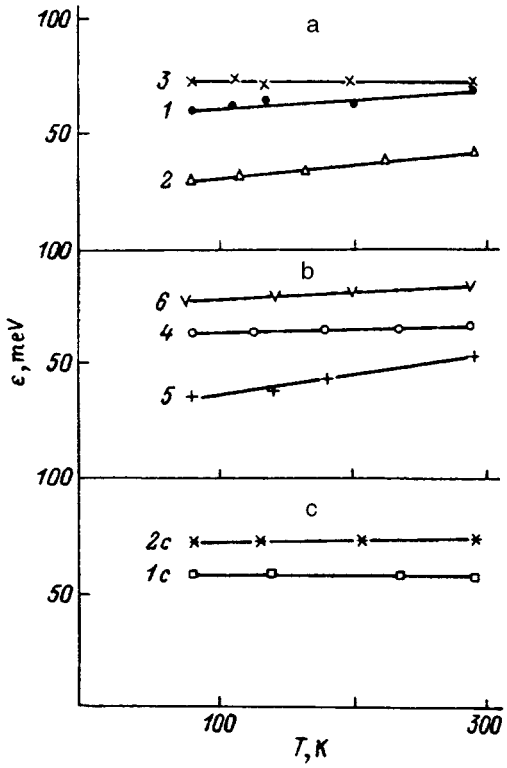

FIG. 3. Temperature dependence of the characteristic energy ε for the three types of structure. The numbers on the curves correspond to the sample numbers in Tables I and II.

5. DISCUSSION OF THE RESULTS

5.1. In all the structures examined here, the forward current therefore, has the same functional dependence on voltage and temperature, which is evidence of a tunneling character, although the epitaxial layers (neutral interiors) of the barrier structures were nondegenerate and had concentrations on the order of $10^{16}-10^{17}$ cm^{-3}.

The tunneling features of the current-voltage characteristics show up most clearly at low temperatures, as is indicated by the temperature variation in ε (Fig. 3) and the weak (not thermally activated) temperature dependence of I_0 (Figs. 2 and 4). The observed difference in I_0 for the three types of structures is consistent with the different heights of the potential barriers to be overcome. The lowest potential barrier exists in the heterojunctions (and is determined by the width of the bandgap of silicon E_g^{Si}) and the highest, in the homogeneous band $p-n$-junctions based on GaP (determined by E_g^{GaP}).

5.2. The characteristic energy ε. That the layers constituting the structure are nondegenerate implies that the width of the space charge region, W, is substantially greater than the characteristic tunneling length (sometimes called the tunneling de Broglie wavelength), λ, in all three structures; i.e., all the structures were wide-gap structures with respect to the

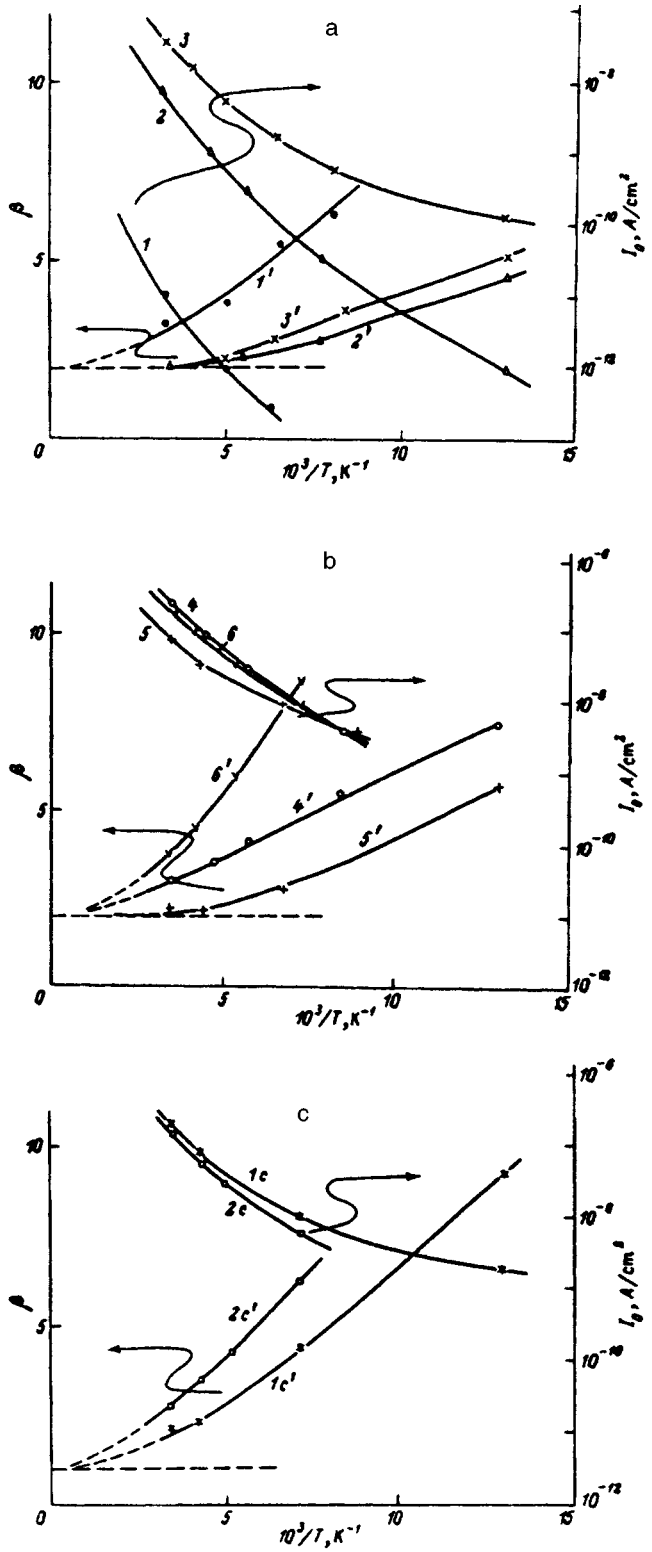

FIG. 4. The parameters I_0 and β as functions of the reciprocal of the temperature for the three types of barrier structure: (a) homo-$p-n$, (b) hetero-$p-n$, and (c) $m-s$. The numbers on the curves correspond to the sample numbers in Tables I and II. The curves labelled with numbers without primes show the temperature dependence of I_0 and those with primes, β. The dashed line indicates the level of β_∞.

tunneling effect. In fact, W can be estimated using the formula

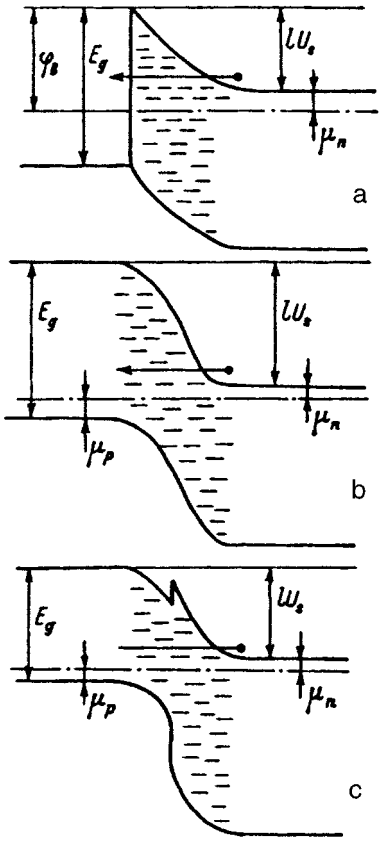

FIG. 5. Energy diagrams of barriers for the three types of structure: (a) $m-s$, (b) homo-$p-n$, (c) hetero-$p-n$.

$$W \simeq \left[\frac{2\varkappa_0}{e} \left(\frac{\varkappa}{N} \right)_{\text{eff}} (U_s - U) \right]^{1/2}, \tag{2}$$

where $\varkappa_0$ is the dielectric constant, $\varkappa_0$ is the dielectric constant of the interior of the semiconductor, e is the electronic charge, and

$$\left(\frac{\varkappa}{N} \right)_{\text{eff}} = \begin{cases} \varkappa / n_n, & \text{(3a)} \\ \varkappa \left(\dfrac{1}{n_n} + \dfrac{1}{p_p} \right), & \text{(3b)} \\ \dfrac{\varkappa_n \varkappa_p}{n_n \varkappa_n + p_p \varkappa_p} \dfrac{(n_n + p_p)^2}{n_n p_p}, & \text{(3c)} \end{cases}$$

where n_n, p_p, and $\varkappa_n$, $\varkappa_p$ are the concentrations of the principal carriers and the relative dielectric constants, respectively, in the interiors of the n- and p-type barrier structures, and eU_s is the height of the potential barrier (Fig 5). Equation (3a) is for Schottky barriers, Eq. (3b) is for $p-n$ homojunctions, and Eq. (3c) is for $p-n$ heterojunctions.

$$eU_s \simeq \begin{cases} \varphi_b - \mu_n \simeq \dfrac{2}{3} E_g^{\text{GaP}} - \mu_n, & \text{(4a)} \\ E_g^{\text{GaP}} - \mu_n - \mu_p, \quad E_g^{\text{GaAs}} - \mu_n - \mu_p, & \text{(4b)} \\ E_g^{\text{Si}} - \mu_p^{\text{Si}} - \mu_n^{\text{GaP,GaAs}}, & \text{(4c)} \end{cases}$$

where the chemical potentials $\mu_n \simeq kT \ln N_c/n_n$ and $\mu_p \simeq kT \ln N_v/p_p$. Equation (4a) is for Schottky barriers, Eq. (4b) is for the $p-n$ homojunctions, and Eq. (4c) is for the

$p-n$ heterostructures. An estimate of the thickness of the space charge region gives $W \simeq 0.2-0.5$ μm. In addition, an estimate of the tunneling length,

$$\lambda = \hbar / \sqrt{2m^* e(U_s - U)}, \tag{5}$$

where m^* is the effective electron mass, gives $\lambda = 1$ nm. The inequality $W \gg \lambda$ means that the proposed tunneling has an enhanced probability for a tunneling transition. This can be caused[11–14] by a spatially extended system of levels in the bandgap, which ensures so-called multistep, rather than single-step, tunneling (Fig. 5), which, according to our ideas, can be represented by a single effective one-step and favored (and, therefore, extended) tunnel transition by introducing a scaling coefficient r (the barrier ''dilution'' coefficient), which enhances λ. The required spatial extent of the system of energy levels in the bandgap is ensured by dislocations which intersect the space charge region of the barrier structure. In the structures studied here, this sort of dislocation can be nucleated on the heteroboundary and extend to the space charge layer.

The introduction of a phenomenological dilution scaling coefficient, which increases the tunneling length, also enhances the tunneling probability, which shows up experimentally as a rise in the characteristic energy ε compared to its theoretical value ε_t. In fact, the current I is proportional to the probability P of tunneling through the barrier,[15] while the probability is determined by the ratio of the width of the barrier to the de Broglie tunneling wavelength, i.e., $P \simeq \exp(-W/\lambda)$, which after substitution of Eqs. (2) and (5) gives

$$I \sim \exp[-e(U_s - U)/\varepsilon_t], \tag{6}$$

where the theoretical value

$$\varepsilon_t = \frac{\hbar e}{2}\left[\frac{1}{\varkappa_0 m^*}\left(\frac{N}{\varkappa}\right)_{\text{eff}}\right]^{1/2}$$

and does not exceed $\varepsilon_t \simeq 10$ meV, which is less than the experimental values (Table I). Thus, the phenomenological barrier dilution coefficient $r = \varepsilon/\varepsilon_t = 5-10$.

5.3. The temperature variation $\varepsilon(T)$. We note that in some samples the excess current is not a purely tunneling current but a thermotunneling current. The thermal character shows up, in particular, through a stronger (tending to exponential) dependence of I_0 on $1/T$ (Figs. 4a–4c) at high temperatures. Another thermal feature, which is enhanced at higher temperatures, is the temperature dependence of ε (Fig. 3). This dependence can be approximated[16] by

$$\varepsilon(T) = \varepsilon_0 \coth(\varepsilon_0/\beta_\infty kT). \tag{7}$$

In the high-temperature limit ($T \to \infty$) Eq. (7) approaches the linear form $\varepsilon(T) = \beta_\infty kT$ (thus, the characteristic coefficient becomes temperature independent, since $\beta = \beta_\infty$) and corresponds to the Bethe thermal emission current in surface-barrier structures ($\beta_\infty = 1$) (extrapolation in Fig. 4c) and to the Shockley-Nois Saa thermal injection current in $p-n$ junctions (β_∞) (extrapolation in Figs. 4a and 4c). In the low-temperature limit ($T \to 0$) Eq. (7) gives a characteristic energy that is independent of temperature: $\varepsilon(0) = \varepsilon_0 n$. A functional dependence on the temperature of the form (7) has been derived theoretically for a model of thermionic current flow in narrow Schottky barriers[11] and in nonideal (with surface states at a heteroboundary interface) anisotypic heterojunctions.[12] In order to achieve agreement with experiment, the formula from Refs. 11 and 12 has been generalized[16] by introducing the parameter β_∞. This has been confirmed in our study.

5.4. The temperature coefficient a. The temperature coefficient a can be calculated proceeding from Eq. (6),

$$I_0 \sim \exp[-eU_s(T)/\varepsilon(T)]. \tag{8}$$

If $\varepsilon(T) = \varepsilon_0$ in the range of temperatures studied here and is essentially temperature independent, then a is entirely determined by the temperature dependence $U_s(T)$.

The linear temperature dependence $U_s(T)$ is derived from Eq. (4), with allowance for the fact that $E_g(T) = E_g(0) - \alpha T$ (in the range studied here):

$$a = \begin{cases} \dfrac{1}{\varepsilon_0}\left(\dfrac{2}{3}\alpha + k \ln \dfrac{N_c}{n_n}\right), \\ \dfrac{1}{\varepsilon_0}\left(\alpha + k \ln \dfrac{N_c}{n_n} + k \ln N_v p_p\right), \end{cases} \tag{9}$$

where the upper expression is valid for Schottky barriers and the lower, for $p-n$ homo- and heterostructures; $eU_s(0) = E_g(0)$ for $p-n$ structures and $eU_s(0) = (2/3)E_g(0)$ for Schottky barriers. Assuming for an estimate that $\alpha \simeq 0.4$ meV/K (the temperature coefficient for the gap width) and $N_c \simeq N_v \simeq 10^{18}$ cm^{-3}, we obtain $a \simeq (0.5-2.0) \times 10^{-2}$ K^{-1}.

The somewhat higher experimental values of a (Table II) are caused by the thermotunneling and not just tunneling nature of the current in the extrapolated segment, so that ε is not a constant, as assumed in the calculation, but rises with T and, thereby increases a.

5.5. The low-temperature preexponential factor I_{00}. If we adhere to the assumption that the tunnel excess current originates in dislocations, then it can be estimated using the formula

$$I = e\rho\nu P, \tag{10}$$

where ρ is the density of dislocations, and $\nu \simeq 10^{13}$ s^{-1}.

In fact, the number of attempts at tunneling per unit time is $\nu = 10^{13}$ s^{-1}, the number of successful attempts is νP, the current through a single dislocation tube is $e\nu P$, and the current density through the entire structure is $\rho e \nu P$. Equations (6) and (10) imply that

$$I = e\rho\nu \exp[-eU_s(T)/\varepsilon(T)]\exp[eU/\varepsilon(T)] \tag{11}$$

and, therefore,

$$I_{00} = e\rho\nu \exp\left[-\frac{eU_s(0)}{\varepsilon(0)}\right]. \tag{12}$$

It is difficult to verify the relationship between I_{00} and $\varepsilon(0)$ using Eq. (12) in these experiments because an ad-

equate method for approximating the bumpy $I-U$ characteristic with a single exponent has not been developed, so there is an uncertainty in the value of ε.

The experimental values of ε were determined over a limited range of voltages so they may be higher than the average. The smallest deviations should occur in the wider-gap semiconductors, since the range of measured voltages in the exponential part of the current-voltage characteristic is larger for them, so that there are more possibilities of introducing a correction for the ''bump.'' Despite these difficulties in determining ε exactly, agreement with Eq. (12) is observed, for example, for the $p-n$ structures, surface-barrier structures, and certain samples of hetero-$p-n$ structures if the density of dislocations is assumed to be $\rho \simeq 10^7$ cm^{-3}.

CONCLUSIONS

The experimental data[5–10] scaled in this paper, as well as the voluminous data which have been scaled before,[17,18] show that the forward current in barrier structures ($p-n$ and $m-s$ homo- and heterostructures) can originate in tunneling even in wide-gap ($W>\lambda$) structures. This kind of tunnel excess current is caused by dislocations (extended defects), which lie in the space charge region and create a spatially extended system of levels in the band gap and thereby facilitate tunneling through the barrier created by the space charge region.

In this paper we have shown that this kind of enhanced tunneling can be taken into account phenomenologically by introducing a free scaling coefficient for the barrier dilution, r, which increases the tunneling length along the path of a dislocation tube by a factor of r compared to the de Broglie tunneling length outside a tube.

Thus, the entire straight branch of the current-voltage characteristic and its temperature dependence can be described using just one phenomenological dilution parameter. In the present experiments $r=5-10$ and the proposed dislocations are formed on the layer-substrate (III–V/Si) heterostructure and extend to the space charge region.

We consider it our pleasant duty to thank L. M. Fedorov, D. V. Sergeev, and A. N. Topchii for help in preparing the samples and A. M. Strel'chuk for useful discussions.

[1] T. Katoda and M. Kishi, J. Electron. Mater. **9**, 783 (1980).
[2] S. F. Fang, S. Adomi, S. Lyer, H. Morkoc, and H. Zabel, J. Appl. Phys. **68**, R31 (1990).
[3] A. Georgakila, P. Panayotatos, J. Stolmones, and J. L. Christou, J. Appl. Phys. **71**, 2679 (1992).
[4] V. M. Andreev and O. V. Sulima, Élektronnaya Promyshennost', No. 11, 24 (1990).
[5] V. V. Evstropov, Yu. V. Zhilyaev, R. Nazarov, V. V. Roslin, L. M. Fedorov, and Yu. Shernyakova, Pis'ma Zh. Tekh. Fiz. **19**, 61 (1993) [Tech. Phys. Lett. **19**, 24 (1993)].
[6] V. V. Evstropov, Yu. V. Zhilyaev, N. Nazarov, D. V. Sergeev, and L. M. Fedorov, Zh. Tekh. Fiz. **63**, 41 (1993) [J. Tech. Phys. **38**, 10 (1993)].
[7] V. V. Evstropov, Yu. V. Zhilyaev, N. Nazarov, D. V. Sergeev, L. M. Fedorov, and Yu. M. Shernyakov, Fiz. Tekh. Poluprovodn. **27**, 1319 (1993) [Semiconductors **27**, 729 (1993)].
[8] V. V. Evstropov, Yu. V. Zhilyaev, N. Nazarov, D. V. Sergeev, and L. M. Fedorov, Fiz. Tekh. Poluprovodn. **27**, 688 (1993) [Semiconductors **27**, 379 (1993)].
[9] V. V. Evstropov, Yu. V. Zhilyaev, N. Nazarov, Yu. G. Sadof'ev, A. N. Topchiĭ, N. N. Faleov, L. M. Fedorov, and Yu. M. Shernyakov, Fiz. Tekh. Poluprovodn. **29**, 385 (1995) [Semicond. **29**, 195 (1995)].
[10] A. V. Bobrov, V. V. Evstropov, Yu. V. Zhilyaev, M. G. Mynbaeva, and N. Nazarov, V. V. Roslin, L. M. Fedorov, and Yu. Shernyakova, Pis'ma Zh. Tekh. Fiz. **19**, 30 (1993) [Tech. Phys. Lett. **19**, 144 (1993)].
[11] R. Stratton, in *Tunnelling Phenomena in Solids* [Russian transl., Mir, Moscow (1973), p. 106].
[12] A. Ya. Shik, Fiz. Tekh. Poluprovodn. **17**, 1295 (1983) [Sov. Phys. Semicond. **17**, 818 (1983)].
[13] A. R. Riben and D. L. Feucht, Solid–State Electron. **9**, 1055 (1966).
[14] A. R. Riben and D. L. Feucht, Int. J. Electron. **20**, 583 (1966).
[15] S. M. Sze, *The Physics of Semiconductor Devices*, Wiley, N.Y. (1969).
[16] V. V. Evstropov and A. M. Strel'chuk, Fiz. Tekh. Poluprovodn. **30**, 92 (1996) [Semiconductors **30**, 52 (1996)].
[17] A. Milnes and D. Feucht, *Heterojunctions and Metal-semiconductor Junctions*, Academic, N.Y. (1972).
[18] B. L. Sharma and R. K. Purohit, *Semiconductor Heterojunctions*, Pergamon, Oxford (1974).

Translated by D. H. McNeill

Photosensitivity of porous silicon-silicon heterostructures

E. V. Astrova, A. A. Lebedev, A. D. Remenyuk, and Yu. V. Rud'

A. F. Ioffe Physicotechnical Institute, Russian Academy of Sciences, 194021 St. Petersburg, Russia

V. Yu. Rud'

St. Petersburg State Technical University, 195251 St. Petersburg, Russia
(Submitted March 26, 1996; accepted for publication April 8, 1996)
Fiz. Tekh. Poluprovodn. **31**, 223–225 (February 1997)

Data from experimental studies of the photoelectric properties of heterostructures of porous and single-crystal silicon are presented. Rectifying heterostructures with photosensitivities of up to 1 mA/W at 300 K in the spectral range 1.2–2.3 eV are obtained. Oscillations in the photocurrent due to interference of the light in the porous silicon layers are observed. The refractive index of porous silicon is estimated. The polarization dependence of the photosensitivity of the heterostructures is studied. © *1997 American Institute of Physics.* [S1063-7826(97)00602-9]

Studies of the physical properties of porous silicon become important because of the observed possibility of fundamentally transforming the basic parameters of the principal material in semiconductor electronics, silicon, by the relatively simple action of anodic etching.[1–5] We have used for the first time photoactive absorption polarization spectroscopy[6] to study porous silicon in heterostructures formed by a junction of porous and single-crystal silicon.

EXPERIMENT

The test samples consisted of mirror layers of porous silicon on a polished substrate of p-type silicon with a specific resistivity of 2 $\Omega\cdot$cm and a (100) orientation prepared by conventional techniques.[2] The thickness d of the porous silicon layer was controlled by the etching regime, was measured by a microscope on a section that had been etched in KOH, and ranged from 1 to 10 μm for different samples. Current leads were connected to the layer of porous silicon and to the silicon wafer by means of transient melting of indium.

The photosensitivity was measured at 300 K by irradiating the side with the porous silicon layer in both natural and polarized light. A tungsten lamp and an SPM-2 monochromator with a quartz prism were used. When the samples were irradiated on the side of the original silicon, there was essentially no photoresponse. The photoluminescence measurements were made similarly to those described in Ref. 2.

RESULTS AND DISCUSSION

The test samples had a rectifying current-voltage characteristic with a forward direction corresponding to a negative potential on the porous silicon layer. The current-voltage characteristic for one of the samples at 300 K is shown in Fig. 1. With a forward bias the current I depends linearly on the voltage V,

$$I=(V-V_c)/R,$$

with a cutoff voltage $V_c\simeq 1.5$ V and a residual resistance R ranging from 2 to 10 MΩ. Thinner layers of porous silicon correspond to lower R. Breakdown sets in for a reverse bias V_r exceeding 300 V. The saturation current is $2-6\times10^{-8}$ A.

When the structures are irradiated on the porous silicon side, a photovoltaic effect is observed with a negative charge on the porous silicon layer and a voltage sensitivity $S_u=20-50$ V/W and a short circuit current sensitivity $S_i=0.5-1$ mA/W. Since the magnitude of the effect is independent of the distance between the illuminated segment and the contact, the effect can be attributed to separation of photoinduced charge carriers in the electric field at the silicon-porous silicon interface.

Figure 2 shows a typical spectral dependence of the quantum efficiency of the photoresponse, η, defined as the ratio of the short circuit photocurrent to the number of photons incident normal to the porous silicon surface. The long wavelength limit of the spectrum coincides with the absorption edge of silicon and η depends exponentially on $h\nu$. The short wavelength limit is apparently caused by intrinsic absorption in the porous silicon.[5] For thinner layers of porous silicon this limit is shifted toward higher photon energies (to $\sim$3 eV for thicknesses $d\simeq 1$ μm).

In the high photoresponse region the spectrum contains about 20 peaks and minima in η. The average distance between neighboring peaks for a 4-μm-thick layer is $\sim$90 meV. The refractive index n was estimated using the formula $n=\lambda_m\lambda_{m-1}/2d(\lambda_m-\lambda_{m-1})$, where λ_m is the wavelength corresponding to a peak response, and m denotes the interference order. The values of the refractive index obtained for different samples lie in the range 1.6–1.8, which corresponds to published values.[7,8] The presence of a rich interference pattern in the photosensitivity spectra of the silicon-porous silicon heterostructures is evidence that the porous silicon layers are highly uniform.

In addition to a photosensitivity spectrum, Fig. 2 shows the photoluminescence spectrum of the same sample. It can be seen that photoluminescence is observed in the spectral range of the peak photosensitivity. At 300 K the photoluminescence spectrum contains no oscillations, but only steps, whose positions do not match the extrema in the photosensitivity spectrum. This indicates that the fine structure in the

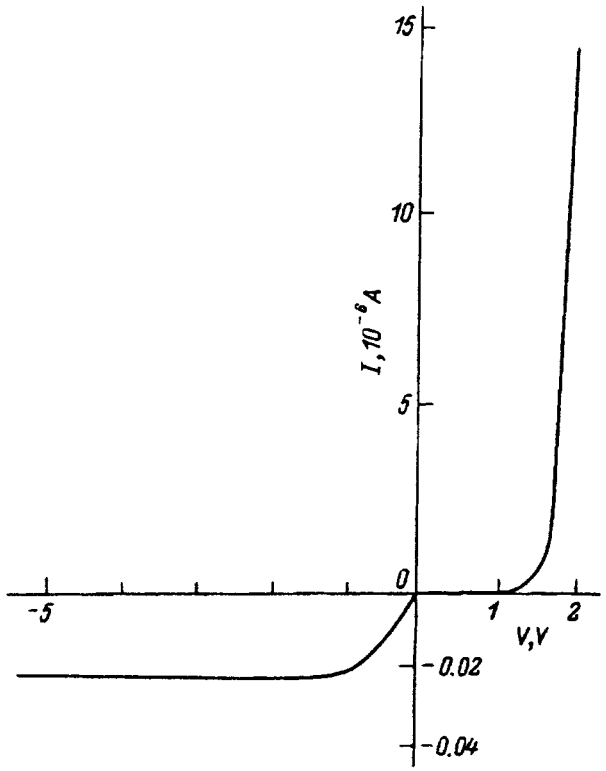

FIG. 1. Steady-state current-voltage characteristic of a junction between porous and single-crystal silicon at 300 K. $d=5$ μm.

photoluminescence spectra of porous silicon does not originate in interference.[9,10]

When the same heterostructures were illuminated by linearly polarized light, the photoresponse quantum efficiency was independent of the direction of polarization of the light relative to the principal crystallographic axes of the substrate of the heterostructure over the entire photosensitive region for normal incidence of the light on the layer surface. With oblique incidence of the light on the porous silicon layer, the photoresponse for light, whose electric vector **E** lay in the plane of incidence (i^p), exceeded that corresponding to **E** perpendicular to the plane of incidence. Figure 3 shows the spectral dependence of the photoresponse for both polarizations incident at an angle of 75°. Figure 3 also shows that the interference pattern and spectral range of the photosensitivity are similar to those when the structures are illuminated with unpolarized light. The difference in the magnitudes of the photoresponse for the different polarizations lies within the difference in the intensities of the light passing into the sample and is caused by different reflectivities. The inset in Fig. 3 shows the angular dependences of the reflectivities r^p and r^s at the air-porous silicon interface for the two polarizations with a refractive index of 1.8.[11] It is clear from the inset that the difference between r^p and r^s at 75° is large enough to explain the difference in the photoresponse. Therefore, in contrast with the photoluminescence of porous silicon, which manifests partial polarization,[12,13] photoactive absorption is isotropic.

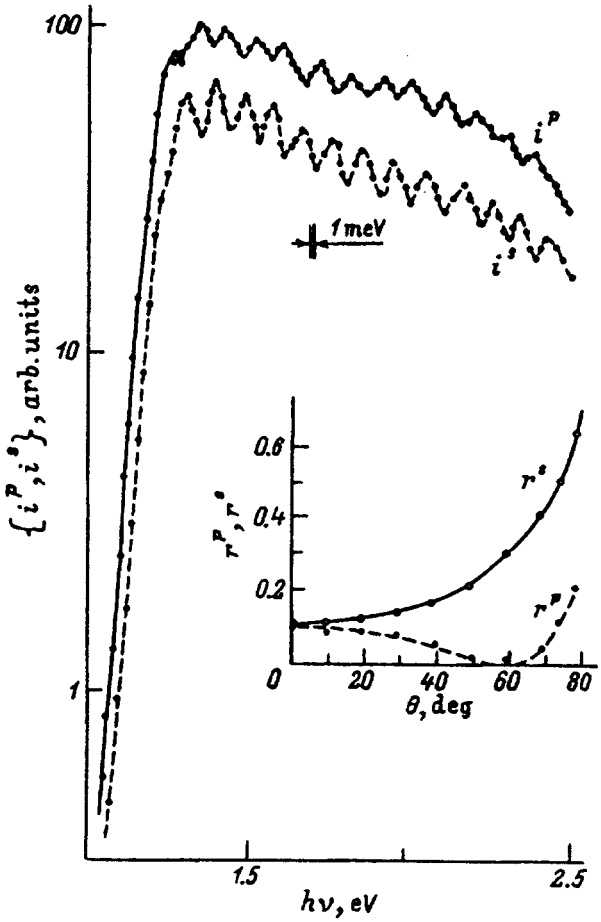

FIG. 3. Spectral dependence of the photocurrents i^p and i^s for a silicon-porous silicon heterojunction with light incident at 75° at 300 K. The inset shows the reflectivities (r^p and r^s) at the air-porous silicon interface for the two polarizations as a function of the angle of incidence θ.

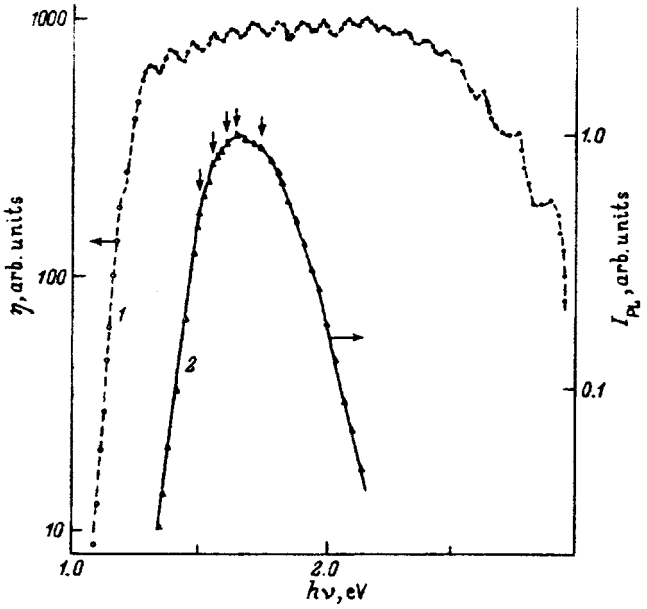

FIG. 2. Spectral dependences in a silicon-porous silicon heterostructure: (*1*) relative quantum efficiency of photoconversion η at 300 K; unpolarized light; angle of incidence 0°; illumination on porous silicon side; (*2*) photoluminescence (I_{PL}) at 300 K.

CONCLUSIONS

The present studies of the photosensitivity spectrum of a porous silicon-silicon heterostructure show that the photosensitivity of the structure is related to separation of photoinduced charge carriers at the silicon-porous silicon interface. High photosensitivity is observed in the window between the absorption edges of silicon and porous silicon. The fine structure in the photosensitivity spectrum is related to interference of light. The refractive index of luminescent porous silicon has been determined. Polarization measurements show that photoactive absorption is isotropic in this structure.

[1] L. T. Canham, Appl. Phys. Lett. **57**, 1046 (1990).
[2] E. V. Astrova, A. A. Lebedev, A. D. Remenyuk, and Yu. V. Rud', Japan. J. Appl. Phys. **34**, 251 (1995).
[3] C. Tsai, K.-H. Li, D. S. Kinosky, R. Z. Quian, T. C. Hsu, J. T. Irby, S. K. Banerjee, A. F. Tasch, and J. C. Campbell, Appl. Phys. Lett. **60**, 1700 (1992).
[4] S. M. Prokes, Appl. Phys. Lett. **62**, 3244 (1993).
[5] E. V. Astrova, A. A. Lebedev, A. D. Remenyuk, and Yu. V. Rud', Fiz. Tekh. Poluprovodn. **29**, 1649 (1995) [Semiconductors **29**, 858 (1995)].
[6] Yu. V. Rud', Izv. Vyssh. Uchebn. Zaved. No. 8, 68 (1986).
[7] E. V. Astrova, S. V. Belov, and A. A. Lebedev,, Fiz. Tekh. Poluprovodn. **28**, 332 (1994) [Semiconductors **28**, 203 (1994)].
[8] C. Mazzoleni and L. Pavesi, Appl. Phys. Lett. **67**, 2983 (1995).
[9] N. S. Averkiev, V. M. Asnin, I. I. Markov, A. Yu. Silov, V. I. Stepnov, A. B. Churilov, and N. E. Mokrousov, Pis'ma Zh. Éksp. Teor. Fiz. **55**, 657 (1992).
[10] E. V. Astrova, A. A. Lebedev, A. D. Remenyuk, and Yu. V. Rud', Pis'ma Zh. Tekh. Fiz. **20** (7), 33 (1994) [Tech. Phys. Lett. **20**, 532 (1994)].
[11] G. S. Landsberg, *Optics* [in Russian], Nauka, Moscow (1976), p. 474.
[12] A. N. Starukhin, A. A. Lebedev, B. S. Razbirin, and L. M. Kapitonova, Pis'ma Zh. Tekh. Fiz. **18** (16), 33 (1992) [Sov. Tech. Phys. Lett. **18**, 450 (1992)].
[13] S. V. Gaponenko, V. K. Kononenko, E. P. Petrov, I. N. Germanenko, A. P. Stupak, and Y. H. Xie, Appl. Phys. Lett. **67**, 3019 (1995).

Translated by D. H. McNeill

Quantum dot injection heterolaser with ultrahigh thermal stability of the threshold current up to 50 °C

M. V. Maksimov, N. Yu. Gordeev, S. V. Zaĭtsev, P. S. Kop'ev, I. V. Kochnev, N. N. Ledentsov, A. V. Lunev, S. S. Ruvimov, A. V. Sakharov, A. F. Tsatsul'nikov, Yu. M. Shernyakov, and Zh. I. Alferov

A. F. Ioffe Physicotechnical Institute, Russian Academy of Sciences, 194021 St. Petersburg, Russia

D. Bimberg

Technische Universität Berling, D-10623 Berling, Germany
(Submitted April 2, 1996; accepted for publication April 9, 1996)
Fiz. Tekh. Poluprovodn. **31**, 226–229 (February 1997)

Gaseous phase epitaxy from metal organic compounds is used to obtain a low-temperature injection laser with an active region based on $In_{0.5}Ga_{0.5}As/GaAs$ quantum dots. Optimizing the growth conditions and geometric parameters of the structure has made it possible to increase the range of ultrahigh thermal stability in the threshold current (the characteristic temperature is $T_0=385$ K) up to 50 °C. © *1997 American Institute of Physics.* [S1063-7826(97)00702-3]

One of the most promising areas of modern semiconductor physics is the production and study of the properties of structures with dimensionalities of less than 2: quantum wires and quantum dots. These structures can be used to improve fundamentally the characteristics of most devices in opto- and microelectronics. Thus, it has been shown that the thermal stability of the threshold current in quantum dot lasers is substantially higher than the upper limit predicted theoretically for quantum well-lasers.[1–5] Until now, however, ultrahigh stability in the threshold current has only been realized well below room temperature and this has substantially limited the possibilities for practical applications of quantum dot lasers.

In this paper we study the effect of structure geometry, growth conditions, and after-growth annealing on the operating characteristics of GaAs-(Al,Ga)As injection lasers with an active region based on InGaAs quantum dots produced by gaseous phase epitaxy from metal-organic compounds. It is shown for the first time that the range of ultrahigh thermal stability in the threshold current (the characteristic temperature is $T_0=385$ K) can be extended to 50 °C.

The laser epitaxial heterostructures were grown on a gaseous phase epitaxy system using metal-organic compounds of elements from group III and hydrides of elements from group V. The system was equipped with a horizontal reactor and resistive heating. Growth took place at a reduced pressure. A reduced pressure makes it possible to enhance the uniformity of the composition, thicknesses, and doping levels of the epitaxial layers compared to growth at atmospheric pressure. Hydrogen subjected to multistep cleaning was used as the carrier gas in this system. The sources of the main components of the solid solutions were trimethyl gallium, trimethyl aluminum, ethyldimethyl indium, and arsine, while the sources of the dopant donor impurity was silane and of the dopant acceptor impurity, bicyclopentadienyl magnesium. Growth took place with excess arsine. The ratio of the elements from groups V and III was 75. The epitaxial heterostructure was grown on a gallium-arsenide substrate doped with silicon and in a (100) orientation. A schematic illustration of the laser structure is shown in Fig. 1a. The buffer zone, lower emitter, waveguide, and lower 8-nm-thick GaAs layer were grown at a temperature of 750 °C. The temperature was then lowered to 490 °C and a layer of $In_{0.5}Ga_{0.5}As$ quantum dots was deposited. The average amount of deposited InGaAs was three monolayers. The dots grew in GaAs layer of thickness 8 nm. The temperature was then again raised to 750 °C and the waveguide, upper emitter, and contact layer were grown. This laser structure, therefore, includes a layer of quantum dots enclosed in a narrow (16 nm) quantum well, which, in turn, is bounded by wide-gap $Al_{0.3}Ga_{0.7}As$ barriers.

In the case of the samples for studies by transmission electron microscopy and photoluminescence, $In_{0.5}Ga_{0.5}As$ quantum dots were grown under the same conditions and were embedded halfway into the interior of a 2000-Å-thick GaAs layer surrounded on both sides by a rather narrow (250 Å) $Al_{0.5}Ga_{0.5}As$ barrier. The transmission electron microscope studies were carried out on a JEOL JEM 1000 microscope (acceleration voltage 1 MV). The photoluminescence was excited by the 514.5-nm line of an Ar laser and a germanium photodetector was used for detection. ''Shallow mesa''-type strip lasers with a wide strip (width $W=40$ μm) were made for electroluminescence studies. The operating characteristics were measured with pulsed excitation (pulse duration 200 ns, repetition rate 5 kHz) at temperatures in the range 80–380 K.

The dots were formed by morphological transformation of an elastically stressed $In_{0.5}Ga_{0.5}As$ layer.[6] A high-resolution transmission electron microscope image of the cross section of a quantum dot along the [011] direction is shown in Fig. 1b. Figure 1c shows a high-resolution image of a quantum dot looking in the substrate plane (view from above). It follows from Figs. 1b and 1c that the quantum dot has the shape of a pyramid with a square base (20×20

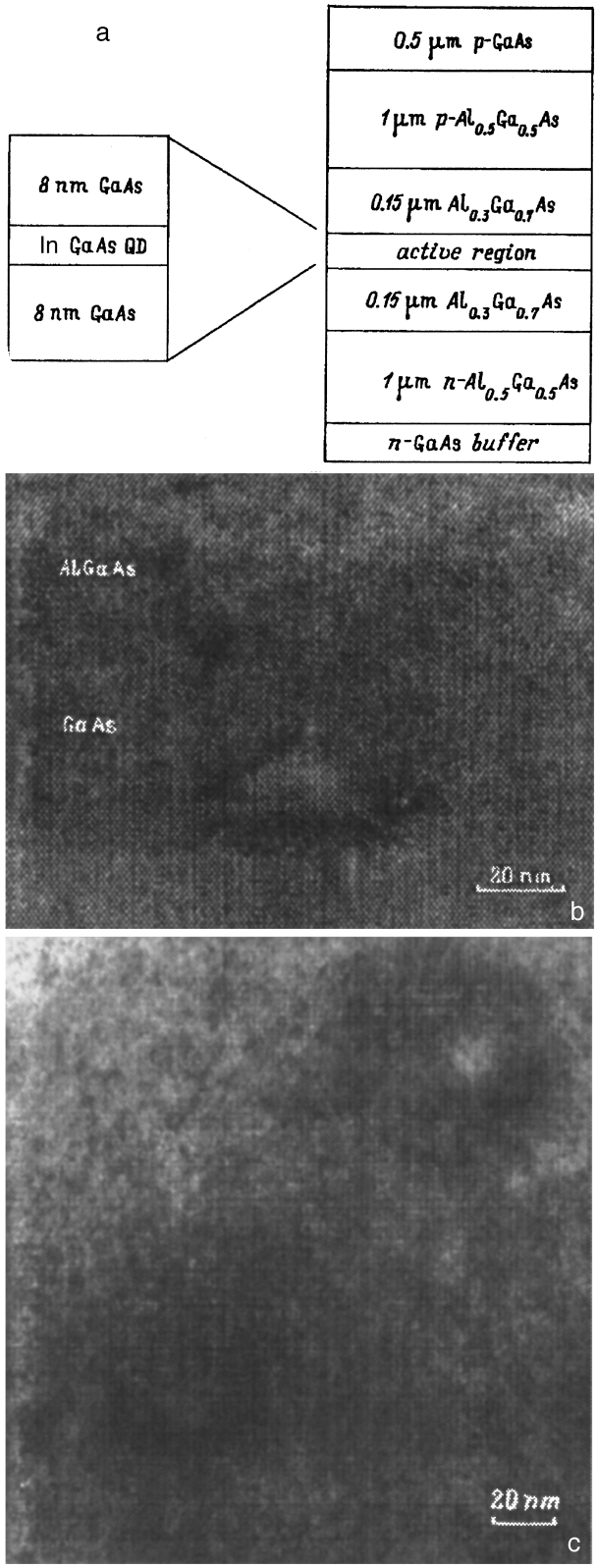

FIG. 1. Schematic illustration of an $In_{0.5}Ga_{0.5}As$ quantum dot (QD) laser structure (a), high-resolution transmission electron microscope images of a quantum dot in the cross section (b) and in the plane of the substrate (view from above) (c).

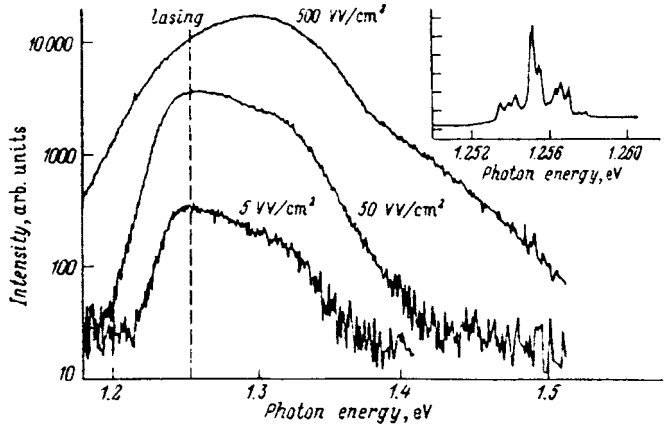

FIG. 2. Photoluminescence spectra for different excitation power densities of an $In_{0.5}Ga_{0.5}As$ quantum dot laser structure after removal of the upper emitter and contact layer by chemical etching. The dashed line indicates the lasing wavelength. The measurement temperature was 300 K. The inset shows the laser output spectrum for a current of 1.5 times threshold.

nm^2) with sides oriented along the [010] and [001] directions and a height of ~8 nm. The characteristic size of the quantum dots can be varied by varying the amount of deposited InGaAs, as well as the time at which growth is cut off after deposition; this makes it possible to vary the position of the peak in the photoluminescence spectrum in the range 1.00–1.36 μm at 300 K.

Annealing the quantum dots, which is unavoidable for high temperature (750 °C) growth of the upper emitter layers of AlGaAs in laser structures, leads to a shift in the photoluminescence line to shorter wavelengths. According to the electron microscopy data under trans-illumination, this stems from a reduction in the amount of In in the quantum dots owing to diffusion of In into the surrounding region. At the same time, the shape and size of the quantum dot profile do not change.

Figure 2 shows photoluminescence spectra of a laser structure whose upper contact layer was removed by chemical etching. The photoluminescence spectrum for weak pumping (5 W/cm^2) consists of an intense line with a peak at ~1.25 eV and a half-width of 60 meV, which is typical of samples with quantum dots and which is determined by the statistical size distribution of the dots. At high-excitation power densities a feature shows up at 1.32 eV, which is associated with a heavy exciton in the so-called wetting layer. At still higher excitation powers the luminescence of the ground state is observed to saturate and the photoluminescence peak shifts to shorter wavelengths.

The inset in Fig. 2 shows the laser output spectrum of a quantum dot structure. The spectral location of the laser line (shown by a dotted line in Fig. 2) corresponds to the peak of the photoluminescence line for current densities close to the threshold; i.e., lasing takes place through zero-dimensional states of the quantum dots. For long strips of length $L \simeq 1600$ μm at 300 K the threshold current density was 390 A/cm^2, while the differential quantum efficiency was 45%. For short strips ($L \simeq 500$ μm), the differential quantum efficiency rose to 60%, while the threshold current density increased to 760 A/cm^2. The temperature dependence of the laser wavelength is consistent with that of the gap width in aAs (Fig. 3); i.e., the mechanism for lasing does not change up to room temperature.

It is known that for relatively high temperatures (180-

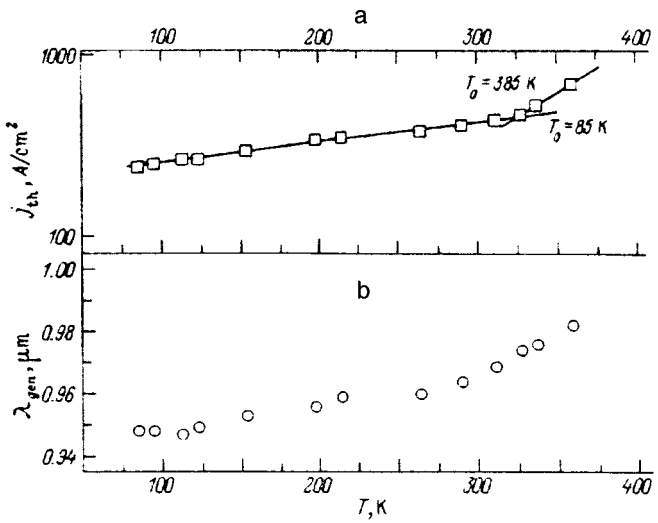

FIG. 3. The threshold current density J_{th} (a) and lasing wavelength λ_{gen} (b) as functions of temperature. The strip width is $W=40$ μm and the strip length is $L=1500$ μm.

220 K) the activated loss of carriers from quantum dots leads to a substantial reduction in their concentration and to a corresponding rise in the threshold current density.[3,4] This effect can be avoided when the points lie within a sufficiently narrow (16 nm) quantum well (Fig. 1a). Here the region of ultrahigh temperature stability in the threshold current density for this type of laser is extended to 330 K (Fig. 3a). As can be seen from Fig. 3a, in the temperature range 80–330 K the change in the threshold current density corresponds to a characteristic temperature $T_0=385$ K, which substantially exceeds the theoretical limit $T_0=285$ K predicted for lasers with an active region based on two-dimensional structures (quantum wells).[1] Extending the region of ultrahigh temperature stability to above room temperatures (50 °C) opens up extensive possibilities for practical applications of quantum dot lasers.

In summary, we have shown that with an optimal choice of the structure geometry, quantum dot lasers produced by gaseous phase epitaxy from metal organic compounds have a low density and ultrahigh thermal stability for the threshold current up to 50 °C.

This work was supported by the Russian Fund for Fundamental Research (RFFI), the Soros Foundation, and grant INTAS-94-1028.

[1] Y. Arakawa and H. Sakaki, Appl. Phys. Lett. **40**, 939 (1982).
[2] N. Kirstaedter, N. N. Ledentsov, M. Grundmann, D. Bimberg, V. M. Ustinov, S. S. Ruvimov, M. V. Maximov, P. S. Kop'ev, Zh. I. Alferov, U. Richter, P. Werner, U. Gossel, and J. Heydenreich, Electron. Lett. **30**, 1416 (1994).
[3] Zh. I. Alferov, N. Yu. Gordeev, S. V. Zaitsev, P. S. Kop'ev, I. V. Kochnev, V. V. Komin, I. L. Krestnikov, N. N. Ledentsov, A. V. Lunev, M. V. Maksimov, S. S. Ruvimov, A. V. Sakarov, A. F. Tsatsul'nikov, Yu. M. Shernyakov, and D. Bimberg, Fiz. Tekh. Poluprovodn. **30**, 357 (1996) [Semiconductors **30**, 200 (1996)].
[4] Zh. I. Alferov, N. A. Bert, A. Yu. Egorov, A. E. Zhukov, P. S. Kop'ev, A. O. Kosogov, I. L. Krestnikov, N. N. Ledentsov, A. V. Lunev, M. V. Maksimov, A. V. Sakarov, V. M. Ustinov, A. F. Tsatsul'nikov, Yu. M. Shernyakov, and D. Bimberg, Fiz. Tekh. Poluprovodn. **30**, 351 (1996) [Semiconductors **30**, 196 (1996)].
[5] V. M. Ustinov, A. Yu. Egorov, A. E. Zhukov, N. N. Ledentsov, M. V. Maksimov, A. F. Tsatsul'nikov, N. A. Bert, A. O. Kosogov, P. S. Kop'ev, D. Bimberg, and Zh. I. Alferov, *Proc. Material Research Society, Fall Meeting*, Boston, USA (1995), paper EE3.6.
[6] V. A. Shchukin, N. N. Ledentsov, P. S. Kop'ev, and D. Bimberg, Phys. Rev. Lett. **75**, 2968 (1995).

Translated by D. H. McNeill

Optical properties of submonolayer CdSe-(Zn,Mg)(S,Se) structures

I. L. Krestnikov, M. V. Maksimov, S. V. Ivanov, N. N. Ledentsov, S. V. Sorokin, A. F. Tsatsul'nikov, O. G. Lyublinskaya, B. V. Volovik, P. S. Kop'ev, and S. M. Sotomayor Torres[1)]

A. F. Ioffe Physicotechnical Institute, Russian Academy of Sciences, 194021 St. Petersburg, Russia

(Submitted April 2, 1996; accepted for publication April 9, 1996)
Fiz. Tekh. Poluprovodn. **31** 230–234 (February 1997)

The optical properties of structures with submonolayer inclusions of CdSe in a Zn(S,Se) matrix are studied. The submonolayer coating consists of a group of nanosized (40 Å) islands with a height of one monolayer. The exciton oscillator strength of multiple submonolayer CdSe–ZnSSe structures is substantially increased compared to the case of a uniform quantum well of comparable thickness and composition. In submonolayer structures lasing takes place immediately next to the energy of the ground state of the heavy exciton, in contrast with ordinary quantum wells of ZnCdSe, where it is strongly shifted to longer wavelengths by the energy of a single optical phonon. This effect results from the removal of the momentum selection rules during radiative recombination of excitons in submonolayer structures. © *1997 American Institute of Physics.* [S1063-7826(97)00802-8]

1. INTRODUCTION

In the last few years considerable attention has been devoted to the creation of semiconductor lasers based on II–VI compounds and the group III nitrides which operate in the blue-green optical range. A clear understanding of the mechanisms for lasing in these semiconductors is extremely important for fabricating long-lived laser structures with low threshold currents.

It has been shown that excitons are not important in the mechanism for lasing in III–V compounds, because many-particle effects screen the Coulomb interaction between electrons and holes and prevent the formation of excitons.[1] In fact, in calculating the gain spectra of III–V semiconductor lasers it is necessary to include only band-band transitions and the observed lasing energy can be explained by a renormalization of the band width due to the high carrier density. The situation changes, however, on going to the II–VI compounds because of smaller Bohr radius (r_B) and higher bond energy for excitons. The exciton density, at which the screening effects must be taken into account, can be estimated from the Mott condition,[2] which gives a reciprocal cubic dependence on r_B. Thus, for example, $r_B = 32$ Å for ZnSe, which is a factor of 5 smaller than for GaAs, and the critical exciton density in ZnSe is $\sim 5\times 10^{18}$ cm^{-3}. This is two orders of magnitude higher than in GaAs. The exciton binding energy in ZnSe is 21 meV, which is comparable to the energy of thermal motion, even at room temperature. In quantum wells the exciton binding energy increases to 30 meV or more, the exciton radius decreases, and screening is further suppressed due to the reduction in size. Thus, the stability of excitons is further increased. Therefore, excitons are preserved up to the power densities for laser pumping at room temperature, as has been confirmed by studies of laser excitation spectra in which exciton characteristics have been observed.[2–4] Exciton effects thus play an important role in lasing in II–VI compounds. However, as Gross *et al.*[5] have shown, when the pump power density or temperature is raised, the effective exciton temperature and, therefore, their momentum, increase. Hot excitons, i.e., those with large wave vectors, cannot recombine radiatively, because momentum must be conserved. Thus, mechanisms for the relaxation of exciton momentum are required; these may include inelastic exciton-exciton scattering and exciton-⟨LO-phonon⟩ scattering.[6] In the first case, lasing should begin at energies lower than the energy of the exciton ground state by an amount equal to the exciton binding energy and in the second case, it should begin at energies lower by an amount equal to the energy of an LO-phonon, as is confirmed by experiment. Even in very high-quality structures, the shift is 30 to 60 meV. The need for an additional many-particle interaction reduces the gain and this leads to higher threshold currents, heating of the structures, and their rapid degradation.

We have shown previously[7] that at low temperatures and pump power densities, hot excitons can undergo luminescence because of their localization on fluctuations in the composition and because of the thickness of a quantum well. At high temperatures or high pump power densities, this effect does not show up because of the low density of localized centers.

According to theoretical calculations that have been confirmed by numerous experimental data,[8,9] when two phases with different values of the components of the surface friction tensor are present on a crystal surface, the formation of an ordered group of two-dimensional islands of similar size and shape is always energetically favorable in the initial stages of growth. This effect is caused by elastic relaxation of the intrinsic stresses of the crystal surface at the boundaries of the two-dimensional domains (islands).

In this paper we propose to introduce localizing centers deliberately, employing a group of CdSe islands with a height of one monolayer formed by deposition of submonolayer coatings of CdSe on a Zn(S,Se) surface for this purpose. In this case the excitons are localized in the direction of

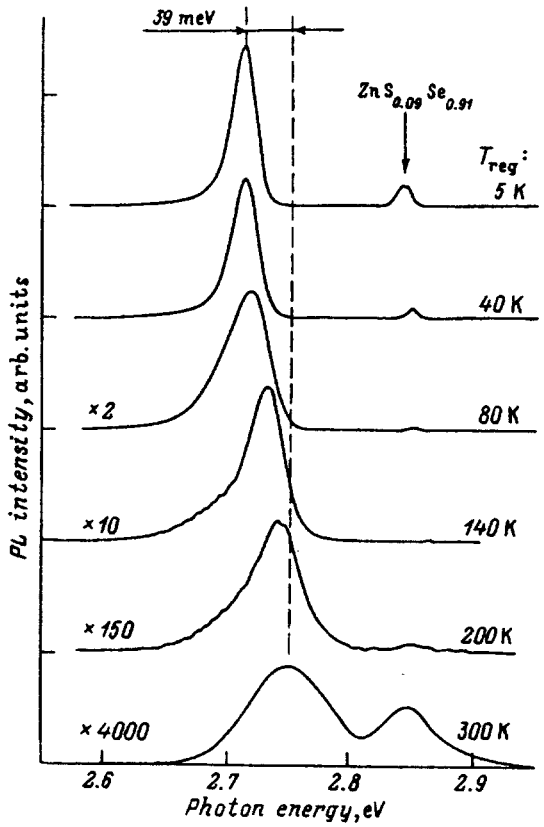

FIG. 1. Temperature dependence of the photoluminescence spectra for a sample with a single submonolayer. For each temperature the gap width is reduced to the width corresponding to 80 K. The excitation power density is 1 W/cm^2.

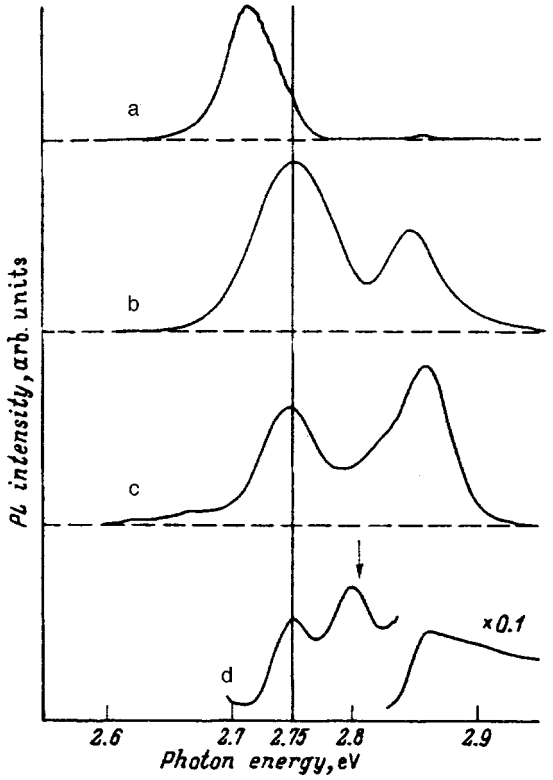

FIG. 2. Photoluminescence spectra (PL) (a–c) and photoluminescence excitation spectra with a detection energy of 2.684 eV (d) of a sample with a single submonolayer. The spectra were taken with: (a) $T_{reg}=80$ K, $P_{ex}=1$ W/cm^2; (b) $T_{reg}=300$ K, $P_{ex}=1$ W/cm^2; (c) $T_{reg}=80$ K, $P_{ex}=100$ kW/cm^2; (d) $T_{reg}=80$ K, $P_{ex}=1$ mW/cm^2. The arrow denotes the calculated energy of transitions involving a light hole.

growth and in the plane of the substrate, which eliminates the momentum selection rules. We have studied the optical properties of these structures and demonstrated the possibility, in principle, of using them as active regions for lasers.

2. EXPERIMENT

Epitaxial layers were grown with the aid of a molecular beam epitaxy system (ÉP-1203) on GaAs substrates with (100) orientation with and without use of an epitaxial GaAs buffer layer. The sources for the base molecular beams were elementary Zn (6N), Se (6N), Mg (5N), and Cd (6N), and zinc sulfide (5N). Photoluminescence spectra were taken by placing the sample in a cryostat in a flow of gaseous helium at temperatures of 5–300 K. The excitation sources were a halogen lamp, light from which passed through the monochromator, a cw He–Cd laser with an output wavelength of 325 nm and a pump power density $P_{ex}=1$ W/cm^2, and a pulsed nitrogen laser with an output wavelength of 337 nm and a pump power density of up to $P_{ex}=100$ kW/cm^2. The detection system consisted of an MDR-23 monochromator with a cooled photomultiplier operating in the photon counting regime for cw excitation or in a synchronous detection regime for pulsed excitation.

3. RESULTS AND DISCUSSION

Figure 1 shows the temperature dependence of the photoluminescence spectra of a sample with a single submonolayer of CdSe in a ZnSSe matrix (9% ZnS). The average amount of deposited CdSe determined from the growth rate was $\sim 1/3$ ML. The spectra in Fig. 1 are reduced to a temperature of 80 K, i.e., are shifted in energy according to the temperature dependence of the gap width. (The magnitude of the shift was determined from optical reflection spectra.) The peak at an energy of 2.844 eV corresponds to edge emission from the wider band ZnSSe matrix. As the detection temperature (T_{reg}) is increased, the emission from the submonolayer (2.711→2.750 eV) shifts by 39 meV to higher energies. The same effect, i.e., a shift in the emission peak from 2.711 to 2.750 eV, is produced by raising the pump power density (Fig. 2). This behavior can be explained by the fact that ''large'' and ''small'' islands are participating in the formation of the radiation. According to a calculation and some published data,[10] an energy of 2.711 eV corresponds to the emission from an exciton in a quantum well of CdSe with a thickness of 1 ML. This means that the lateral dimensions of the large islands substantially exceed the radius of an exciton and there is no additional quantization in the lateral plane. As the temperature is raised, the probability of thermal ejection of carriers from large islands, whose density is low, into the ZnSSe barrier region increases. As a result, the probability of capture and recombination of nonequilibrium carriers through small islands increases because of transport. When the pump power density is raised, all the states in the

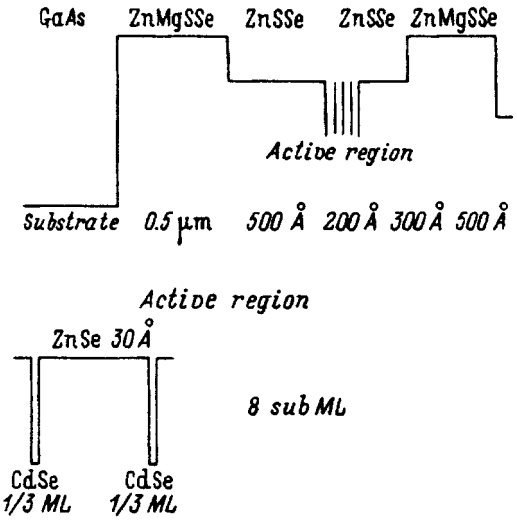

FIG. 3. A schematic representation of a structure with a short-period submonolayer superlattice.

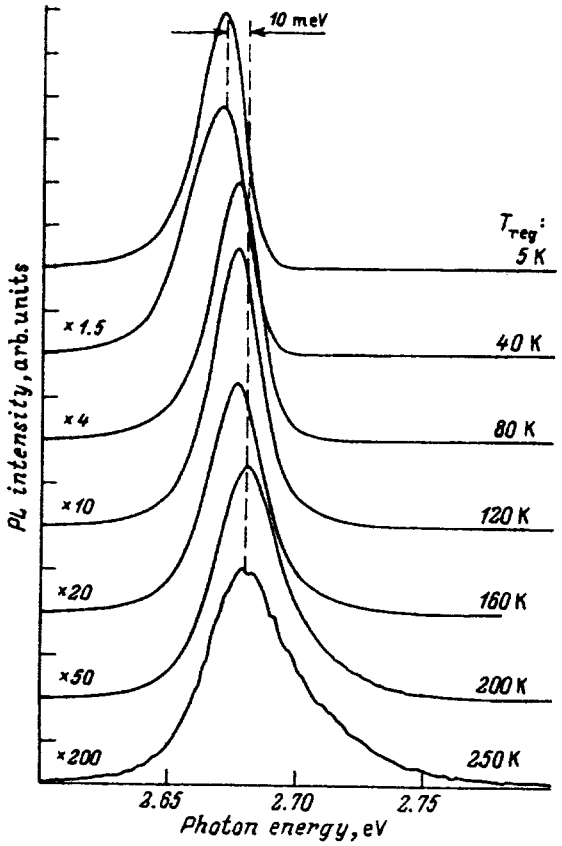

FIG. 4. Temperature dependence of photoluminescence spectra (PL) for a sample with a short-period submonolayer superlattice. For each temperature the gap width has been reduced to that corresponding to 80 K. The excitation power density is $P_{ex}=1$ W/cm^2.

large islands are filled and the intensity of the luminescence from them becomes negligible compared to that from the small islands, whose density is much higher. Thus, at low temperatures and pump power densities, we see emission from only the large islands (i.e., actually from quantum wells with a thickness of 1 ML), while as the temperature or pump power density are raised, the small islands will radiate. Their dimensions can be estimated from the quantum-well energy: in a one dimensional model with infinitely high barriers, a shift in energy by 40 meV corresponds to 35 Å. From the half- height of the peak we estimate the spread in lateral dimensions to be ~10 Å. Figure 2 shows a photoluminescence excitation spectrum of a line from large islands measured at 80 K (detection energy 2.684 eV). In this spectrum the small islands show up in the form of a peak at 2.750 eV. We attribute the peak at 2.797 eV to an electron-light hole transition in the small islands. In fact, a calculation for a 1-ML- thick quantum well and including size quantization in the plane of the islands for light holes yields fair agreement with experiment (the calculation is indicated by an arrow).

For a direct comparison of a submonolayer structure and a structure with a quantum well, we have grown a sample with multiple submonolayers, as shown schematically in Fig. 3. The reference structure had exactly the same geometry, but in this case the active region consisted of a uniform quantum well of ZnCdSe with a thickness of 70 Å containing 25% CdSe. The overall thickness of the CdSe, calculated from the composition of the solid solution, is 8 Å in the submonolayer, short-period superlattice and 18 Å in the quantum-well structure.

Figure 4 shows the temperature dependence of the photoluminescence spectra of the structure with multiple submonolyaers (as in Fig. 2, all the spectra are reduced to 80 K). The peak of the photoluminescence spectrum for this sample is shifted by 70 meV to lower energies relative to the peak of the photoluminescence spectrum of the sample with a single monolayer (Fig. 1). We may assume that the high stress from the CdSe island (the lattice mismatch between the ZnSe and CdSe is ~6%) propagates through the ZnSe with its thickness of 30 Å and the CdSe islands in the next layer grow predominantly directly above the previous layers. Here the wave functions in the islands from neighboring layers overlap, which leads to a reduction in the ground-state energy. This sort of effect has been observed in an InAs/GaAs system.[11]

The optical reflection (R) spectra shown in Fig. 5 and their second derivatives with respect to energy (d^2R/dE^2) for structures with submonolayers and with quantum wells reveal a sharp rise in the oscillator strength in the case of a structure with submonolayers. This is especially noticeable in the plot of the second derivative. Thus, the amplitude of the feature associated with the submonolayers, which for an identical lineshape is roughly proportional to the exciton oscillator strength, is four times higher than for the quantum well, and the difference would be by a factor of ten when taken per CdSe molecule. This is also confirmed by the idea of the formation of quantum-well islands, since according to theoretical calculations and experimental data, the oscillator strength for structures with a dimensionality of less than 2 (i.e., for quantum wires and dots), must be substantially greater. If a submonolayer deposit leads to the formation of a uniform quantum well of supersmall thickness, then the oscillator strength should fall due to the strong delocalization of the electron and hole wave functions and, therefore, due to

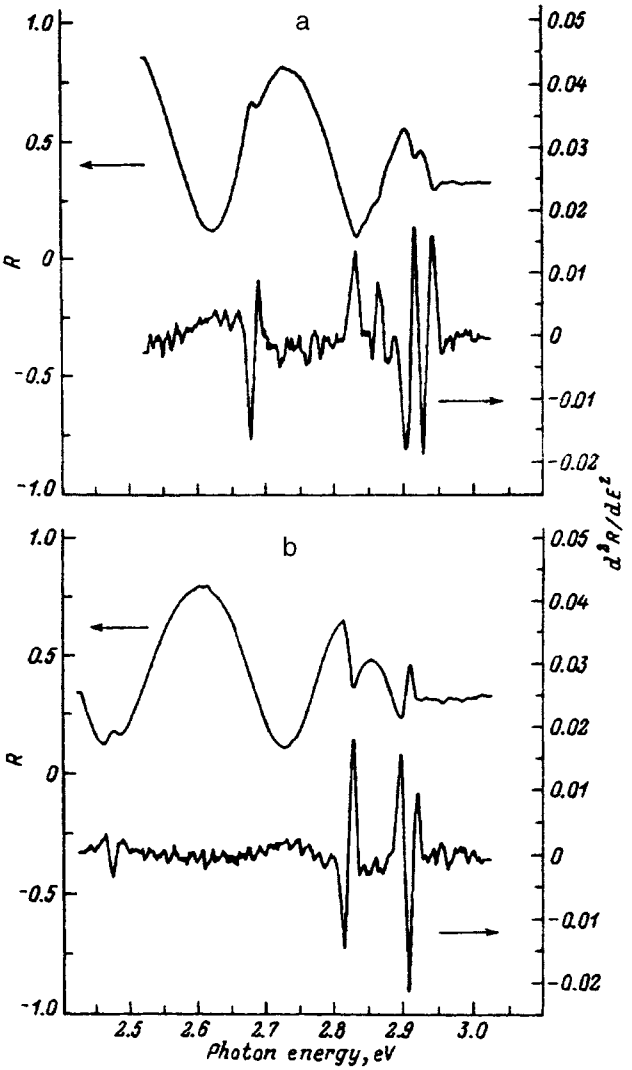

FIG. 5. Optical reflection spectra and their second derivatives for samples with a submonolayer superlattice (a) and quantum wells (b). The detection temperature is $T_{reg}=80$ K.

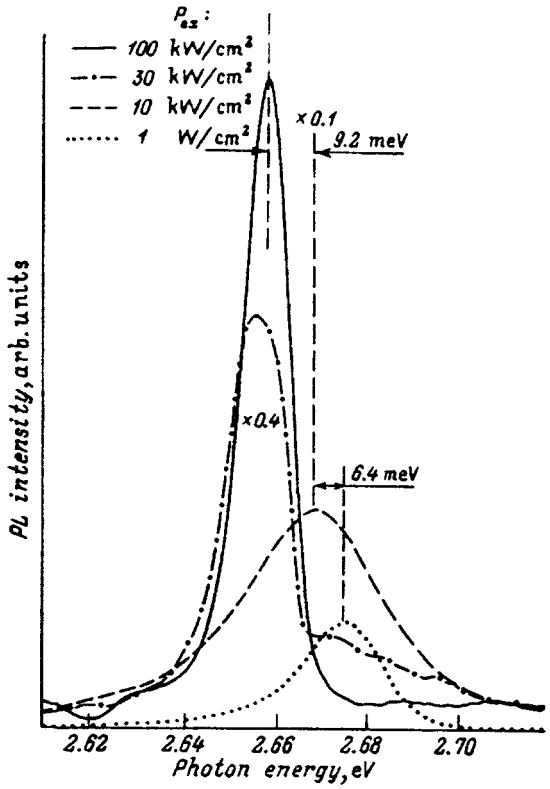

FIG. 6. The dependence of photoluminescence spectra (PL) on pump power density for a sample with a short-period submonolayer superlattice. Excitation with light from a cw He–Cd laser at $P_{ex}=1$ W/cm^2 and a pulsed N_2 laser at $P_{ex}=10$–100 kW/cm^2. The detection temperature is $T_{reg}=80$ K.

the strong reduction in their overlap for $k=0$. In a model of a uniform wide well with a thickness of ~ 200 Å and a small average content of Cd, the oscillator strength should also be small, since for thicknesses of 50–200 Å the oscillator strength falls off rapidly as the well width is increased.[12] Thus, agreement with experiment is attained only in the model of a group of quantum-well islands.

Figure 6 shows the dependence of the photoluminescence spectra on the pump power density for a structure with multiple submonolayers. For excitation power densities below 10 kW/cm^2 the shape of the spectrum is essentially unchanged as the pump power is raised; the small shift to longer wavelengths is caused by slight heating of the sample. Further increases in the pump power density leads to the appearance of stimulated emission at the low-energy edge (for 30 and 100 kW/cm^2). Here the difference in energy between the photoluminescence peak and the peak in the stimulated emission is only 9 meV, while for quantum wells this shift is in the range 30–60 meV, according to published data. That the shift is so small in our case is probably attributable to the fact that localized excitons,which can recombine radiatively at any lattice temperature, take part in the optical gain. The limitations imposed by the momentum selection rules, which are important in three- and two-dimensional cases, are eliminated here.

4. CONCLUSIONS

In this paper we have shown that:

– depositing submonolayer coatings of CdSe on a ZnSe (ZnSSe) surface leads to the formation of a group of nanosized CdSe islands with characteristic lateral dimensions of 30–40 Å.

– in short-period submonolayer structures a sharp rise in the oscillator strength for exciton transitions is observed compared to the case of the equivalent uniform quantum well.

– lasing in structures with submonolayers begins immediately adjacent to the energy of the exciton ground state because the momentum selection rules are eliminated.

– a qualitatively new possibility has been demonstrated for lowering the threshold current and increasing the laser energy in semiconductor lasers based on II–VI compounds, as well as in other wide-band semiconductors with high exciton stability.

This work was supported by the Samsung Electronics Corporation, Grant No. INTAS-94-481, and the Russian Fund for Fundamental Research, Grant N 95-02-04056.

[1)]Nanoelectronics Research Centre, Department of Electronics and Electrical Engineering, University of Glasgow, United Kingdom.

[1] W. D. Johnston Jr., Phys. Rev. B **6**, 1455 (1972).
[2] H. Haug and S. Koch, Phys. Status Solidi B **82**, 531 (1977).
[3] J. Ding, M. Hageroot, T. Ishihara, H. Jeon, and A. V. Nurmikko, Phys. Rev. B **47**, 10528 (1993).
[4] Y. Kawakami, B. Cavenett, K. Ichino, S. Fujita, and S. Fujita, Japan, J. Appl. Phys. **32**, L730 (1993).
[5] E. F. Gross, S. A. Permogorov, and B. N. Razbirin, Fiz. Tverd. Tela **8**, 1483 (1966) [Sov. Phys. Sol. State **8**, 1180 (1966)].
[6] C. B. Guillaume, J. M. Deveber, and F. Salvan, Phys. Rev. **177**, 567 (1969).
[7] N. N. Ledentsov, S. V. Ivanov, V. M. Maksimov, I. V. Sedova, I. G. Tabatadze, and P. S. Kop'ev, Fiz. Tekh. Poluprovodn. **29**, 65 (1995) [Semiconductors **29**, 34 (1995)].
[8] V. I. Marchenko, Pis'ma Zh. Eksp. Teor. Fiz. **33**, 381 (1981).
[9] O. L. Alehard, D. Vanderbilt, R. D. Meade, J. D. Joannopoulos, Phys. Rev. Lett. **61**, 1973 (1988).
[10] S. J. Hwang, W. Shan, J. J. Song, Z. Q. Zhu, and T. Yao, Appl. Phys. Lett. **64**, 2267 (1994).
[11] A. Yu. Egorov, A. E. Zhukov, P. S. Kop'ev, N. N. Ledentsov, M. V. Maksimov, V. M. Ustinov, A. F. Tsatsul'nikov, N. A. Bert, A. O. Kosogov, D. Bimberg, and Zh. I. Alferov, Fiz. Tekh. Poluprovodn. **30**, 1682 (1996) [Semiconductors **30**, 881 (1996)].
[12] V. Voiotis, R. Grousson, P. Lavallard, and R. Planel, Phys. Rev. B **52**, 10725 (1995).

Translated by D. H. McNeill

Electron and hole spectra and selection rules for optical transitions in $Ge_{1-x}Si_x$/Ge heterostructures

V. Ya. Aleshkin and N. A. Bekin

Institute of Microstructure Physics, Russian Academy of Sciences 603600 Nizhniĭ Novgorod, Russia
(Submitted November 20, 1995; accepted for publication January 15, 1996)
Fiz. Tekh. Poluprovodn. **31**, 235–242 (February 1997)

The electron and hole spectra in strained $Ge_{1-x}Si_x$/Ge heterostructures grown on a (111) plane have been investigated. It is shown that the structure of the conduction band in these structures can be determined by investigating the polarization of their photoluminescence. The selection rules for indirect optical transitions have been found. © *1997 American Institute of Physics.* [S1063-7826(97)00902-2]

INTRODUCTION

Silicon-based materials are of great interest because of their wide applications in electronics and because of the rapid development of silicon technology. In particular, the heterostructures $Ge_{1-x}Si_x$/Ge and $Ge_{1-x}Si_x$/Si have been studied intensively in recent years.

Since the lattice constants of Ge and Si differ by approximately 4%, at least one of the materials in such heterostructures is deformed. In addition, structures with thin layers, in which the elastic deformation energy is less than the formation energy of a dislocation at a heterostructure, can be dislocation-free structures. It is now well known that in $Ge_{1-x}Si_x$/Ge and $Ge_{1-x}Si_x$/Si heterostructures the potential wells for holes are layers with the smaller fraction of Si in a wide range of deformations and for any orientation of the growth plane (see, for example, Refs. 1–5. However, the structure of the conduction band in these heterostructures is still not completely understood in a wide range of their parameters. This is explained by the fact that several valleys, whose position depends on the deformation, x, and on the thickness of the layers (because of the quantum-size effects), are present in the conduction bands of Ge and Si and of the solid solution. Even for the currently intensively studied $Ge_{1-x}Si_x$/Si systems, grown pseudomorphically on Si, the data indicating which layer is a potential well for electrons for the deformation x close to 1 are ambiguous and contradictory.[1,6,7]

In the present work, we will calculate the electron and hole spectra in $Ge_{1-x}Si_x$/Ge heterostructures grown on the (111) plane, and we will determine the selection rules for interband dipole transitions in this system. We found that, depending on the deformation and composition of the solid solution, the bottom of the conduction band in Ge can lie below or above the bottom of the conduction band of the solid solution. We will show that the type of valley at the absolute minimum of the conduction band in these heterostructures can be determined by investigating the polarization dependences of the photoluminescence.

Despite the indirect structure of the gaps in Ge, Si, and their solid solution, $Ge_{1-x}Si_x$/Ge heterostructures can be direct-gap structures.[8] Direct-gap band structure can be obtained when the bottom of the conduction band lies at a point of the Brillouin zone where the quasimomentum in the bulk material is perpendicular to the heterostructures. In this case, an electron in structures with thin layers loses this quasimomentum in a collision with the heterostructure. This is manifested formally in that the Brillouin zone for electrons in structures with quantum wells which are not coupled by tunneling is two-dimensional. A momentum perpendicular to the heterostructures is not present in it. This is manifested in short-period superlattices as a folding of the Brillouin zone. As a result, the minimum of the conduction band lies at the center of the zone.

ENERGY BAND GAPS

The energy band gaps must be determined in order to find the electron and hole spectra in a heterostructure. We shall take these band gaps from Ref. 4. We note that for $x<0.3$ and lattice constants 5.43 Å$<a<$5.65 Å the valence energy band gaps calculated in Ref. 5 are approximately 30% smaller and the values measured in Ref. 2 are approximately 6% larger than in Ref. 4. According to Ref. 4, the average energy in the valence band in the solid solution $Ge_{1-x}Si_x$ is determined by the expression

$$E_{av}=(90.9a_{\parallel}-1073.6)x. \tag{1}$$

Here and below the energy is expressed in meV. The quantity $a_{\parallel}$, expressed in Å, equals the distance between the closest atoms in the growth plane, multiplied by $\sqrt{2}$. We assumed that $a_{\parallel}=5.43$ Å in undeformed silicon and $a_{\parallel}=5.65$ Å in undeformed germanium. We also assumed that the structure is pseudomorphic ($a_{\parallel}$ is the same for both materials of the heterojunction).

Quadratic interpolation[9] was used for $a_{\parallel}$ in the undeformed solid solution:

$$a_{\parallel}=5.65-0.24x(1-x)-0.22x^2, \text{ Å}. \tag{2}$$

The average energy E_{av} of the valence band is understood to be the average energy of the maxima of the three valence bands (heavy, light, and spin split-off bands).

The positions E_{hh}, E_{lh}, and E_{sh} of the tops of the heavy, light, and spin-split-off hole bands are determined from the formulas

$$E_{hh}=E_{av}+\frac{\Delta}{3}-\frac{\delta E}{2}, \tag{3}$$

 1063-7826/97/020132-07$10.00

$$E_{lh}=E_{av}-\frac{\Delta_0}{6}+\frac{\Delta E}{4}+\frac{1}{2}\sqrt{\Delta_0^2+\Delta_0\delta E+\frac{9}{4}(\delta E)^2}, \tag{4}$$

$$E_{sh}=E_{av}-\frac{\Delta_0}{6}+\frac{\delta E}{4}-\frac{1}{2}\sqrt{\Delta_0^2+\Delta_0\delta E+\frac{9}{4}(\delta E)^2}, \tag{5}$$

$$\delta E=2\sqrt{3}d\varepsilon_{xy}, \tag{6}$$

where ε_{xy} is the xy component of the deformation tensor, d is one of the deformation constants, Δ_0 is the spin-orbit splitting,

$$\varepsilon_{xy}=\frac{1}{3}\left(1-\frac{a_\parallel}{a_0}\right)\left(1+2\frac{C_{11}+2C_{12}-2C_{44}}{C_{11}+2C_{12}+4C_{44}}\right),$$

C_{ij} are the elastic moduli, and a_0 are the lattice constants in the undeformed crystal. The x, y, and z axes are directed along [100], [010], and [001] directions, respectively. We call the holes with the large mass in the [111] direction heavy holes.

The band gap in the undeformed solid solution was studied experimentally in Ref. 10. We shall employ for the difference in the energies of the L and Δ valleys and the top of the valence band (E_g^L and E_g^Δ, respectively) the expressions obtained by us (temperature $T=4.2$ K):

$$E_g^L=740+1270x, \tag{7}$$

$$E_g^\Delta=931+18x+206x^2. \tag{8}$$

We assume that they are valid in the entire range of x. This is completely justified for Eq. (8), since it approximates well the experimentally measured quantity E_g^Δ in a wide range of x ($0.15<x<1$). We recall that the bottom valleys in the undeformed solid solution are L valleys for $x<0.15$ and Δ valleys for $x>0.15$. Because of the small range of values of x where experimental data are available for E_g^L, the use of Eq. (7) can result in substantial errors for x close to 1.

To calculate the splitting of the bands and the changes in the band gap as a result of the deformation, we used the constants of the deformation potential of pure Ge and Si calculated theoretically in Ref. 4. Linear interpolation in x was used to calculate all parameters of the solid solution.

Deformation results in the splitting of energy of the minima of the L valleys. We call the valley where the rotation axis of the constant-energy surface is directed along [111] a $1L$ valley and we call the three remaining valleys $3L$ valleys. The position of their minima is given by the expressions

$$E_{1L}=E_L+2\Xi_u^L\varepsilon_{xy}, \tag{9}$$

$$E_{3L}=E_L-\frac{2}{3}\Xi_u^L\varepsilon_{xy}, \tag{10}$$

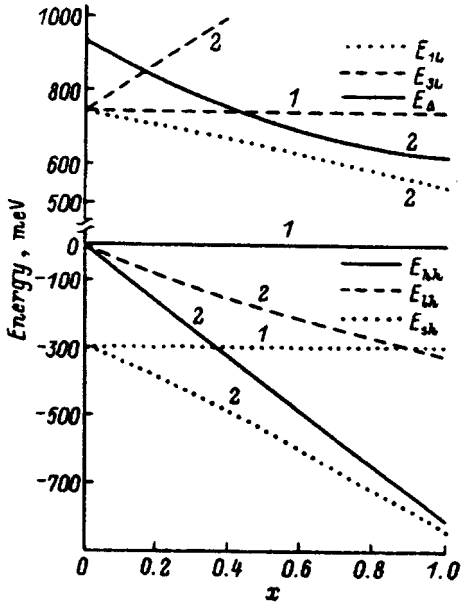

FIG. 1. Positions of the band extrema in the solid solution $Ge_{1-x}Si_x$ versus x (lines with index 2) for a structure grown pseudomorphically on germanium ($a_\parallel=5.65$ Å). The positions of the band extrema in germanium (lines with index 1) are also shown in the figure.

$$E_L=E_{av}+E_g^L+\left(\Xi_d^L+\frac{\Xi_u^L}{3}-a\right)(\varepsilon_{xx}+\varepsilon_{yy}+\varepsilon_{zz})+\frac{\Delta_0}{3}. \tag{11}$$

A deformation in the (111) plane or along the [111] direction does not lift the degeneracy of the minima of the Δ valleys. We can therefore write the following expression for the corresponding energy E_Δ:

$$E_\Delta=E_{av}+E_g^\Delta+\left(\Xi_d^\Delta+\frac{\Xi_u^\Delta}{3}-a\right)(\varepsilon_{xx}+\varepsilon_{yy}+\varepsilon_{zz})+\frac{\Delta_0}{3},$$

$$\varepsilon_{xx}=\varepsilon_{yy}=\varepsilon_{zz}=\frac{4C_{44}}{C_{11}+2C_{12}+4C_{44}}\left(\frac{a_\parallel}{a_0}-1\right). \tag{12}$$

In Eqs. (9)–(12) $\Xi_{u,d}^L$ and $\Xi_{u,d}^\Delta$ are constants in the deformation potential of the L and Δ valleys, respectively, and a is the constant in the deformation potential of the valence band.

The energies of the extrema of the energy bands in a solid solution grown pseudomorphically on a germanium substrate ($a_\parallel$ equals the lattice constant a_{Ge} of germanium) are plotted in Fig. 1 as a function of x. It is clearly seen that the energy band gap of the top of the valence band for the heavy holes is larger than for the light holes. This difference is attributable to the splitting of the valence band of the solid solution by the deformation. This assertion is true for any 5.43 Å $<a<$5.65 Å. Indeed, the germanium layers in this case can be compressed only in the growth plane. For such

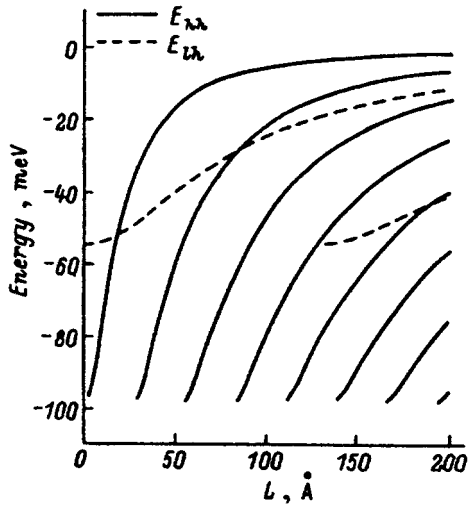

FIG. 2. Energies of the tops of the quantum-well subbands of the valence band versus the germanium thickness in a $Ge_{0.88}Si_{0.12}$/Ge heterostructure grown pseudomorphically on germanium ($a_{\parallel}=5.65$ Å). The solid curves correspond to heavy holes and the dashed curves correspond to light holes.

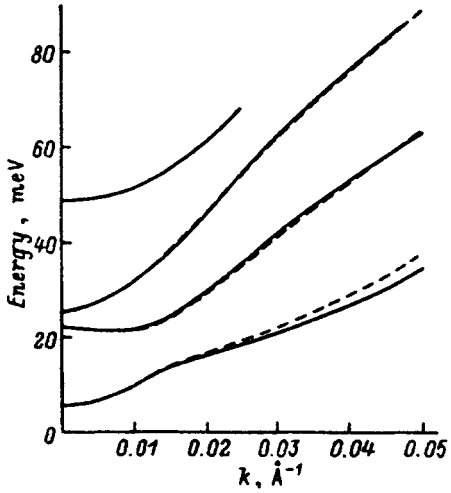

FIG. 3. Hole energies versus the wave vector along the germanium layer in a $Ge_{0.88}Si_{0.12}$/Ge heterostructure grown pseudomorphically on germanium. The solid lines correspond to the wave vector oriented along [112] and the dashed lines correspond to the wave vector oriented in a direction obtained from [112] by rotating around [111] by an angle of $\pi/6$. The Ge layer is 100 Å thick.

layers the top of the heavy-hole band lies above the top of the light-hole band, since the constant d_{Ge} of the deformation potential of the valence band in Eq. (6) is less than zero. As we have already mentioned, the average energy of the valence band is lower in the solid solution than in germanium. If the deformation of the solid solution is of a different sign than in germanium, then in $Ge_{1-x}Si_x$ the top of the light-hole band lies above the top of the heavy-hole band ($d_{\mathrm{GeSi}}<0$), and therefore the band gap of the heavy-hole band is larger. It is also larger in the case where the deformation is of the same sign in both layers, since the deformation splitting of the valence band in this case is larger in germanium than in the solid solution. The latter circumstance is explained by the fact that, first, in this case $a_{\parallel}<a_{\mathrm{GeSi}}<5.65$ Å (a_{GeSi} characterizes the undeformed solid solution) and therefore germanium is more strongly deformed and, second, $|d_{\mathrm{GeSi}}|<|d_{\mathrm{Ge}}|$.

It is also obvious that for the $Ge_{1-x}Si_x$/Ge heterostructures grown pseudomorphically on germanium the absolute minimum of the conduction band lies in the $1L$ valley of the solid solution.

HOLE SPECTRA

The hole spectra were found by numerically integrating the Schrödinger equation with the Luttinger Hamiltonian allowing for deformation.[11] The boundary conditions for the wave functions were chosen by analogy with Ref. 12.

Figure 2 shows the energies of the tops of the quantum-well subbands of the valence band as a function of the thickness of the germanium layer in a $Ge_{1-x}Si_x$/Ge heterostructure grown pseudomorphically on germanium. We see from the figure that for thin germanium layers ($L<20$ Å) the first light-hole subband lies closer to the conduction band and for thick germanium sublayers ($L>20$ Å) the first heavy-hole subband lies closer to the conduction band. This occurs because of the deformation, the result of which is that the top of the heavy-hole band in a solid solution lies below the top of the light-hole band (i.e., the well is deeper for heavy holes). For this reason, as L decreases, the heavy-hole levels are expelled more rapidly from the quantum wells.

The symmetry group of the Hamiltonian describing the motion of holes in a heterostructure is a D_{3d} symmetry group. It contains a sixfold inversion axis, which is parallel to the direction of quantization of the motion. The hole spectrum is parity degenerate with respect to reflection in the growth plane.[13] The symmetry group of hole isoenergy surfaces is therefore a D_{6h} group and these surfaces are invariant with respect to rotation by an angle of $\pi/3$ around the [111] axis. Figure 3 shows the energies of holes in the quantum-well levels on the wave vector along the geramanium layer in a $Ge_{1-x}Si_x$/Ge heterostructure grown pseudomorphically on germanium. The solid lines correspond to the wave vector directed along $[\bar{1}12]$ and the dashed line corresponds to the wave vector directed in a direction which is obtained from $[\bar{1}12]$ by rotation around [111] by an angle of $\pi/6$. The Ge layer is 100 Å thick. We see from the figure that the hole spectra are nonparabolic and almost isotropic. The characteristic energy scale for nonparabolicity is the splitting between the subbands. The fourth level with $k\approx 0.025$ Å^{-1} goes into the continuous spectrum.

Near the point $p=0$, where p is the hole quasimomentum in the growth plane, the hole dispersion relation has the form $\varepsilon=p^2/2m$. The mass m depends on the deformation, on the thickness L of the germanium layer, and on x in the solid solution. Using perturbation theory with the hole kinetic energy along the layer as the perturbation parameter, we derive the following formula for the heavy-hole mass m_{hh} in the first subband of an infinitely deep well with $p=0$:

$$m_0/m_{hh}=A+\frac{D}{\sqrt{12}}+64\left(2B^2+\frac{D^2}{3}\right)\sum_{l=1}^{\infty}\left\{\frac{l^2}{(4l-1)^2}\right.$$

$$\left.\times\frac{1}{\pi^2\left[\left(A-\frac{D}{\sqrt{3}}\right)-4l^2\left(A+\frac{D}{\sqrt{3}}\right)\right]-4\sqrt{3}m_0dL^2\varepsilon_{xy}/\hbar^2}\right\}, \tag{13}$$

where A, B, and D are constants which determine the hole spectrum,[11] and m_0 is the free-electron mass.

The curves of m_{hh} in the first quantum-well subband versus the germanium layer thickness are shown in Fig. 4 for two $Ge_{1-x}Si_x$/Ge heterostructures. The curves were obtained by solving the Schrödinger equation numerically. The lattice constant of one of these structures is $a_\parallel=5.65$ Å, which corresponds to an undeformed germanium layer. For the other constant $a_\parallel=5.637$ Å, which corresponds to a minimum of the elastic energy in a multilayer structure with equal germanium and solid-solution thicknesses. In the calculation, the solid-solution layers were assumed to be tunneling-nontransparent layers. We see from the figure that deformation of the germanium layers decreases m_{hh} and decreasing the thickness L of the germanium layers increases m_{hh}. It is interesting to compare the values of m_{hh} shown in Fig. 4 with those obtained from Eq. (13). According to Eq. (13), in an infinitely deep well m_{hh} does not depend on L in an undeformed germanium. For $a_\parallel=5.65$ Å, we obtain from Eq. (13) $m_{hh}=0.059m_0$. For a structure with $a_\parallel=5.637$ Å, we obtain from Eq. (13) $m_{hh}=0.059m_0$ for $L=20$ Å and $m_{hh}=0.0574m_0$ for $L=250$ Å. Therefore, the values of m_{hh} obtained from Eq. (13) for $L>200$ Å agree to within 20% with the values calculated by solving the Schrödinger equation.

ELECTRON SPECTRA

As we have already mentioned, the bottom of the conduction band in the Ge and solid-solution layers can lie in different valleys. In addition, the bottom of the conduction band in the Ge layer can lie above or below the bottom of the conduction band in the solid-solution layer. This is attributable to the fact that, depending on the fraction of silicon in the solid-solution layer and the lattice constant in the growth plane (deformation), the Δ, $1L$, and $3L$ valleys can be arranged differently with respect to one another, both within a layer and in neighboring layers.

First, we ignore the quantum-size effects. As $a_\parallel$ varies from 5.43 Å to 5.65 Å, the $3L$ valleys in the germanium layers lie no higher than the $1L$ valley. Furthermore, the Δ valleys in the germanium layer always lie above the Δ valleys in the solid-solution layer. It is convenient to analyze the structure of the conduction band for different values of $a_\parallel$ and x, taking into consideration only the bottom valleys in each material (see Fig. 5). We see from Fig. 5 that in the regions 1, 2, and 4 the bottom of the conduction band in the germanium layer lies below the bottom of the conduction band in the solid-solution layer (type-1 modulation of the bands) and the reverse arrangement (type 2) occurs in the regions 3 and 5. We note that in the regions 1, 2, and 4, the bottom of the conduction band in the germanium layer is located at the minima of the $3L$ valleys.

It should be noted that Fig. 5 is more likely of an illustrative, qualitative nature, i.e. it shows which situations in the conduction band are in principle possible for different parameters of the heterostructure. As we have already mentioned, this is due to the error in the quantities (8) and especially (7), as well as the uncertainty in the deformation-potential constants and the band gaps (1) employed.

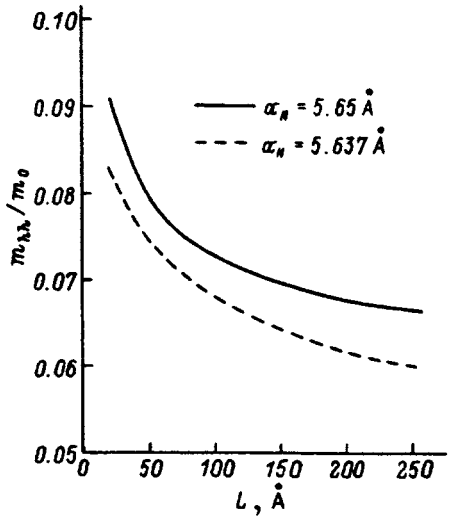

FIG. 4. Heavy-hole mass m_{hh} at the bottom of the first quantum-well subband versus the thickness of the germanium layer in a $Ge_{0.88}Si_{0.12}$/Ge heterostructure for different values of $a_\parallel$.

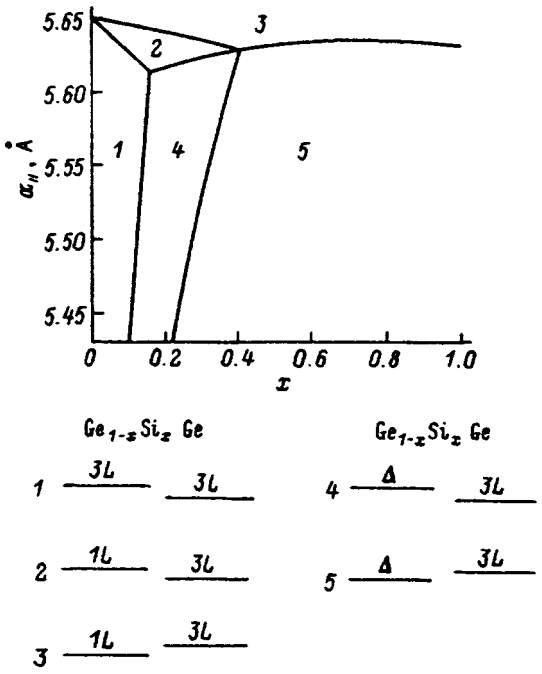

FIG. 5. Boundaries of the regions in the $(a_\parallel, x)$ plane where the bottom valleys of the conduction band in the germanium and solid-solution layers are arranged identically with respect to one another. The relative arrangement of the bottom bands in germanium and the solid solution for each region is shown in the bottom half of the figure. Size quantization was disregarded.

Furthermore, in the case of strong deformations (up to 4%) the nonlinear deformation effects which we have ignored are probably important. In reality, the boundaries of the regions in Fig. 5 can therefore have a different arrangement. Additionally, some regions can be absent or, vice versa, other regions with a different structure (in the sense which we are considering) of the conduction band can exist. Therefore, the situation with respect to the conduction band must be studied experimentally.

In Ge or solid-solution layers of finite thickness, size quantization increases the energy of the conduction band minima. As a result, the boundaries of regions 1–5 change and, in general, some of them vanish or new ones appear.

Calculations employing the data of Ref. 4 and the difference of the L-valley energies [Eq. (7)] show that a $1L$ valley in the solid solution lies lower in Ge for any values of x and $a_\parallel$. For this reason, $Ge_{1-x}Si_x$/Ge can be a direct-gap structure in momentum space, but then the electrons and holes will be localized in different layers (type-2 modulation of the bands). This situation corresponds to region 3 in Fig. 5.

Let us examine the dependence of the electron energies on the two-dimensional momenta in the case where germanium is a quantum well. In this case, as one can see from Fig. 5, the bottom of the conduction band is formed by $3L$ valleys. Let us choose a coordinate system in which the x, y, and z axes are the crystallographic directions [112], [110], and [111], respectively. Consider the valley whose constant-energy surface in the volume of the semiconductor possesses a rotation axis along [111]. For it, the tensor w_{ij} of the reciprocals of the effective masses possesses the following nonzero components:

$$w_{xx}=\frac{1}{9m_\perp}+\frac{8}{9m_\parallel},\quad w_{yy}=\frac{1}{m_\perp},$$

$$w_{zz}=\frac{1}{9m_\parallel}+\frac{8}{9m_\perp},\quad w_{xz}=w_{zx}=-\frac{2\sqrt{2}}{9}\left(\frac{1}{m_\perp}-\frac{1}{m_\parallel}\right),$$

where $m_\parallel$ and $m_\perp$ are, respectively, the longitudinal and transverse masses in the L valleys. We give the following expressions for the effective masses in the solid solution:[5]

$$m_\parallel=(1.76-0.18x+0.12x^2)m_0,$$

$$m_\perp=(0.1+0.03x)m_0. \qquad (14)$$

The constant energy surface of two-dimensional electrons in the valley considered is an ellipse. One of its semiaxes is also the projection of the rotation axis of the constant-energy ellipsoid, which corresponds to the valley in the bulk material, onto the (111) plane. For an infinitely deep well or in the case where $m_\parallel$ and $m_\perp$ are the same in the quantum well and the barrier, the dispersion relation in the nth quantum-well subband can be written in the form

$$E_m(p_x,p_y)=E_n(0,0)+\frac{p_x^2}{2m_x}+\frac{p_y^2}{2m_y}, \qquad (15)$$

where

$$\frac{1}{m_x}=w_{xx}-\frac{w_{xz}^2}{w_{zz}},\quad \frac{1}{m_y}=w_{yy}, \qquad (16)$$

and w_{ij} corresponds to the material of the quantum well.

In deep subbands which are located far from the edge of the quantum well, the electron wave function is localized mainly in the quantum well and the dispersion is approximated well by relations (15) and (16), where the components of the tensor w_{ij} are used for the quantum-well material. In the shallow subbands which are located close to the edge of the quantum well, an electron is very likely to be located in the barrier and its dispersion is described by relations (15) and (16) with the components of the tensor w_{ij} for the barrier. We see from Eq. (14) that the masses in the dispersion relation (15) should be virtually independent of the silicon content in the solid solution. The effective masses [Eq. (14)] are also virtually independent of the deformation.[5] For pure germanium $m_x\approx 1.59$ and $m_y\approx 0.1$.

SELECTION RULES FOR OPTICAL TRANSITIONS

It was shown in the preceding section that the bottom of the conduction in a $Ge_{1-x}Si_x$/Ge heterostructure can lie in the $3L$, $1L$, or Δ valley. This raises the following question: Is it possible to determine by studying interband optical transitions the valley in which the bottom of the conduction band in a heterostructure lies? We shall show that the answer is affirmative if the top of the valence band is formed by the heavy-hole subband.

We shall study a symmetric structure. We call a structure symmetric if it contains a symmetry plane at the center of the germanium layer. The symmetry group of the hole wave vector in such structures is D_{3d}. The heavy-hole wave functions transform according to a double-valued representation $L_4^+ + L_5^+$ and the light-hole wave functions transform according to L_0^+ (the designations are taken from Ref. 14). The momentum component along the [111] axis transforms according to the L_1^- representation, and its two components in the (111) plane transform according to the L_3^- representation.

$hh-1L$ TRANSITIONS

The $hh-1L$ transitions should be observed in heterostructures for which $a_\parallel$ and x lie in region 3 in Fig. 5. The wave-vector group of the $1L$ electrons is D_{3d} and the wave functions of these electrons transform according to the representation L_0^+. The phonon wave functions with a wave vector corresponding to the $1L$ point of the Brillouin zone transform according to the following representations:[15] $LO-L_1^+$, $TO-L_3^-$, $TA-L_3^+$, and $LA-L_2^-$. We employ the standard designations for phonons: The letters L and T correspond to longitudinal and transverse phonons and the letters O and A correspond to optical and acoustic phonons. Using the standard method,[14,15] we find the following selection rules for dipole transitions between the heavy-hole subband and the $1L$ valley with the participation of phonons. Just as in bulk germanium, transitions with the participation of LO and TA phonons are parity forbidden. Transitions with the participation of TO phonons are allowed with any polarization of the light. Transitions with the participation of LA phonons are allowed only for photons with nonzero projection of the electric field vector **E** onto the (111) plane. Transitions with the participation of LA phonons are forbid-

den in the case where the electric field vector of the light wave is parallel to the [111] direction. It can be shown that the $hh-1L$ transition with LA-phonon participation and $\mathbf{E} \parallel [111]$ is also forbidden in an asymmetric structure.

For structures with quantum layers the minimum of the energy of the $1L$ valley and the maximum of the valence band are located at the same point of the Brillouin zone. However, the optical dipole transitions with no scattering from light- and heavy-hole subbands into the $1L$ valley are forbidden. The point is that the electron and hole wave functions are even under inversion (indicated by the superscripts $+$ in the representations) and dipole transitions are forbidden between states with the same parities. Strictly speaking, these arguments are invalid for transitions in which the number of the quantum-well level changes (for example, for transitions from the second quantum-well hole subband into the first subband of the $1L$ valley). This is explained by the fact that the wave functions in the quantum-well subbands with even numbers are odd under inversion; i.e. the electron and hole wave functions in even subbands transform according to the representations L_0^- and $L_4^- + L_5^-$, respectively. We note that in this case the selection rule for the transitions with LO- and TA-phonon participation is also lifted.

$hh-3L$ TRANSITIONS

The regions 1, 2, and 4 in Fig. 5 correspond to $hh-3L$ transitions. The wave-vector group of the $3L$ valleys is C_{2h}. The electron wave functions transform according to the representations $B_1^+ + B_2^+$ (see *Appendix*). The wave functions of phonons with wave vectors corresponding to the $3L$ point of the Brillouin zone transform according to the following representations: $LO-A_1^+$, $TO-A_1^- + A_2^-$, $TA-A_1^+ + A_2^+$, and $LA-A_1^-$. Here dipole transitions with LA- and TO-phonon participation are allowed for any polarization of the light.

Therefore, the $hh-3L$ transitions with LA-phonon participation are allowed for photons with $\mathbf{E} \parallel [111]$ and $hh-1L$ transitions are forbidden. It is interesting to determine the intermediate states through which these allowed transitions occur. It turns out that they proceed through the states $L_4^- + L_5^-$ and $B_1^- + B_2^-$. The intermediate state $L_4^- + L_5^-$ originated from the state Γ_8 of the conduction band in bulk germanium, and the intermediate state $B_1^- + B_2^-$ originated from the $L_4^- + L_5^-$ state of the valence band. The transition through the latter state is most likely, since it is closest in energy to the initial state in the valence band. Radiative transitions with LA-phonon participation in bulk germanium proceed mainly through an intermediate Γ_7^- state in the conduction band.[16] In a heterostructure, transitions occurring through the intermediate state L_0^-, which originate from Γ_7^-, under the influence of electric-field components lying in the $\langle 111 \rangle$ plane correspond to these transitions. A transition through the L_0^- state is more likely than through the state $B_1^- + B_2^-$, since for it the difference in the energies of the initial and intermediate states is smaller. Therefore, the intensity of the $hh-3L$ transitions with LA-phonon participation and $\mathbf{E} \parallel [111]$ is lower than that of transitions occurring under the influence of $\mathbf{E} \perp [111]$.

$hh-\Delta$ TRANSITIONS

The region 5 in Fig. 5 corresponds to these transitions. The wave-vector symmetry group of the Δ valleys is σ. The electron wave functions transform according to the representation $B_1 + B_2$ (see *Appendix*). The wave functions of the TO and TA phonons transform according to the A_2 representations, and the wave functions of the LA and LO phonons transform according to the A_1 representation. The symmetry allows optical transitions with the participation of any phonons and arbitrary polarization of the light wave. However, in bulk germanium[15] and the solid solution, when the bottom of the conduction band lies in the Δ valleys, optical transitions are observed only with the participation of TA and TO phonons.[1,10] The absence of transitions with longitudinal-phonon participation cannot be attributed to the selection rules, i.e. to the symmetry.[15] Therefore, only transitions with transverse-phonon participation are observed in a $Ge_{1-x}Si_x$/Ge heterostructure in which the bottom of the conduction band lies in the Δ valleys.

CONCLUSIONS

Summarizing the results presented above, we shall formulate a method for determining from optical investigations of $Ge_{1-x}Si_x$/Ge heterostructures the states, together with the valley to which they belong, that form the bottom of the conduction band. If the bottom of the conduction band is formed by states from Δ valleys, then radiative transitions with the emission of TO phonons prevail. When the bottom of the conduction band is formed by states from a L valley, radiative transitions with LA-phonon emission predominate.[17] The TO-phonon energies corresponding to the Ge–Ge, Ge–Si, and Si–Si bonds are well known.[1] The transitions from Δ valleys can therefore be distinguished from the transitions from L valleys by comparing the energies of phonon-free transitions with the transitions with phonon participation. To distinguish transitions from $1L$ valleys and transitions from $3L$ valleys, it is necessary to investigate the polarization of the radiation. Transitions with LA-phonon participation and $\mathbf{E} \parallel [111]$ are forbidden for a $1L$ valley and are weakened for $3L$ valleys.

Of course, there are also more direct methods for determining the type of bottom valley of the conduction band. For example, one method is to measure the electron mass along layers in observations of cyclotron resonance. However, such measurements require structures of very high quality. The

TABLE I. C_{2h}.

	E	Q	C_2	QC_2	σ	$Q\sigma$	I	QI
A_1^+	1	1	1	1	1	1	1	1
A_2^+	1	1	−1	−1	−1	−1	1	1
A_1^-	1	1	1	1	−1	−1	−1	−1
A_2^-	1	1	−1	−1	1	1	−1	−1
B_1^+	1	−1	i	$-i$	i	$-i$	1	$-i$
B_2^+	1	−1	$-i$	i	$-i$	i	1	−1
B_1^-	1	−1	i	$-i$	$-i$	i	−1	1
B_2^-	1	−1	$-i$	i	i	$-i$	−1	1

TABLE II. σ.

	E	Q	σ	$Q\sigma$
A_1	1	1	1	1
A_2	1	1	-1	-1
B_1	1	-1	i	$-i$
B_2	1	-1	$-i$	i

requirements for structural quality for observing luminescence are much lower, and therefore the approach proposed here may be more acceptable.

We wish to thank Yu. A. Romanov, L. K. Orlov, V. I. Gavrilenko, N. G. Kalugin, and M. D. Moldavskaya for helpful discussions. This work was performed with the financial support of the Russian Fund for Fundamental Research (Grants 93-02-1.1721, 95-02-05863), the International Science Foundation, and the Russian government (Grant R8H300).

APPENDIX

The characters of the irreducible representations of the double groups C_{2h} and σ. The designations of the symmetry elements are taken from Ref. 18.

[1] D. J. Robbins, L. T. Canham, S. J. Barnet, A. D. Pitt, and P. Calcott, J. Appl. Phys. **71**, 1407 (1992).
[2] H. Yaguchi, K. Tay, K. Takemasa, K. Onabe, R. Ito, and Y. Shiraki, Phys. Rev. B **49**, 7394 (1994).
[3] L. K. Orlov, O. A. Kuznetsov, R. A. Rubtsova, A. L. Chernov, V. I. Gavrilenko, O. A. Mironov, V. V. Nikonorov, I. Yu. Skrylev, and S. V. Chistyakov, Zh. Éksp. Teor. Fiz. **98**, 1028 (1990) [Sov. Phys. JETP **71**, 573 (1990)].
[4] C. G. van de Walle and R. M. Martin, Phys. Rev. B **34**, 5621 (1986).
[5] M. M. Rieger and V. Vogl, Phys. Rev. B **48**, 14276 (1993).
[6] S. Fukatsu and Y. Shiraki, Appl. Phys. Lett. **63**, 2378 (1993).
[7] T. Baier, U. Mantz, K. Tronke, R. Sauer, F. Schäffler, and H.-J. Herzog, Phys. Rev. B **50**, 15191 (1994).
[8] T. P. Pearsall, J. Berk, L. C. Feldmann, J. M. Bonar, and J. P. Mannaerts, Phys. Rev. Lett. **58**, 729 (1987).
[9] J. P. Dismukes, L. Ekstrom, and R. J. Paff, J. Phys. Chem. **68**, 3021 (1964).
[10] J. Weber and M. I. Alonso, Phys. Rev. B **40**, 5683 (1989).
[11] G. L. Bir and G. E. Pikus, *Symmetry and Deformation Effects in Semiconductors* [in Russian], Nauka, Moscow, 1972, p. 393.
[12] V. Ya. Aleshkin and N. A. Bekin, Zh. Éksp. Teor. Fiz. **105**, 1396 (1994) [JETP **78**, 751 (1994)].
[13] V. Ya. Aleshkin and Yu. A. Romanov, Zh. Éksp. Teor. Fiz. **95**, 149 (1989) [Sov. Phys. JETP **68**, 85 (1989)].
[14] F. Bassani, G. Parraviccini, and G. Pastori, *Electron States and Optical Transitions in Solids*, Franklin Press, 1975 [Russian transl., Nauka, Moscow, 1982, p. 65].
[15] R. S. Knox and A. Gold, *Symmetry in the Solid State*, W. A. Benjamin, N. Y., 1964 [Russian transl., Nauka, Moscow, 1970, p. 390].
[16] G. L. Bir and G. E. Pikus, Fiz. Tverd. Tela (Leningrad) **17**, 696 (1975) [Sov. Phys. Solid State **17**, 448 (1975)].
[17] N. G. Kalugin, L. K. Orlov, and O. A. Kuznetsov, JETP Lett. **58**, 200 (1993).
[18] L. D. Landau and E. M. Lifshitz, *Quantum Mechanics: Non-Relativistic Theory*, Pergamon Press, N.Y., 1977, 3rd edition [Russian orig., Nauka, Moscow, 1989, p. 418].

Translated by M. E. Alferieff

Mechanical properties of pure and doped InP single crystals determined under local loading

Yu. S. Boyarskaya, D. Z. Grabko, M. I. Medinskaya, and N. A. Palistrant

Institute of Applied Physics, Academy of Sciences of Moldova, 277028 Kishinev, Moldova
(Submitted November 3, 1995; accepted for publication April 11, 1996)
Fiz. Tekh. Poluprovodn. **31**, 243–246 (February 1997)

The mechanical properties of pure and doped (Fe, Zn, Sn) InP single crystals have been investigated in the temperature range 293–600 K. It is shown that impurity hardening (increase in microhardness) is much more pronounced at high temperatures than at room temperature because of the retardation of moving dislocations by impurities, which is strongest at high temperatures. Appreciable scratch hardness anisotropy on the (001) face of the experimental crystals at 293 K was observed. It decreases rapidly as the temperature increases in the interval 293–600 K. It is shown that the [110] and [$\bar{1}$10] directions on the (001) face of the experimental crystals are nonequivalent. The observed phenomena are explained by the different contributions of the two mechanisms of plastic deformation: slip and twinning in the process of scratch formation along the $\langle 100\rangle$ and $\langle 110\rangle$ directions, and along the [110] and [$\bar{1}$10] directions. © *1997 American Institute of Physics.* [S1063-7826(97)01002-8]

1. INTRODUCTION

InP is a semiconductor material which is very promising for a wide practical applications. This makes a comprehensive investigation of its physical properties necessary. Among the many works devoted to the study of this compound, comparatively few are concerned with the mechanical properties. Deformation of InP single crystals by uniaxial compression showed that at temperatures below 730 K there is no plastic deformation of the material, only brittle fracture is observed.[1] Under a concentrated load on these crystals, however, it was found that dislocations appear near the deformation location even at room temperature.[2] For this reason, local loading is a promising method for studying the mechanical properties of InP at temperatures ranging from room temperature up to $T\sim 700$ K. On this basis we set as our goal in the present work to investigate the mechanisms of plastic deformation of pure and doped InP single crystals in the temperature range 293–600 K under the action of a concentrated load.

2. EXPERIMENTAL PROCEDURE

Pure and doped InP single crystals were grown by the Czochralski method. Their characteristics are presented in Table I.

The investigations were performed on the (001) face, which was subjected, after preparation, to chemical polishing in order to remove a defective layer near the surface. Deformation of the face (microindentation and scratch generation) was performed with the aid of a PMT-3 microhardness tester. The indentor consisted of a diamond pyramid with a square base (Vickers pyramid). The load P on the indentor was varied in the range 10–40 g. The indentation microhardness (H) was calculated by the standard formula,[3] and the hardness determined by the sclerometric method (H_s) was found from the relation

$$H_s = P/b^2, \tag{1}$$

where b is the scratch width.

TABLE I. Characteristic features of the experimental samples.

Crystal	Carrier density, cm^3
InP	4.1×10^{16}
InP:Fe	2.1×10^{8}
InP:Zn	2.7×10^{18}
InP:Sn	2.2×10^{17}

The microhardness measurements were performed for two orientations of the indentor: the diagonals d of the imprint parallel to the $\langle 100\rangle$ directions and $d \parallel \langle 110\rangle$. In the sclerometric investigations the indentor moved along these crystallographic directions.

The dislocation structures arising near the imprints and scratches were investigated by the method of selective etching. The etcher consisted of a solution of CrO_3 (1 g) in HCl (30 ml).

The acoustic emission (AE) accompanying the deformation process was detected with the aid of a specially assembled apparatus.[3] This apparatus makes it possible to record the number N of AE signals arising during the formation of twins and cracks, and it is insensitive to the development of dislocation structures around imprints and scratches. The experiments were conducted in the temperature range 293–600 K. The error in measuring H and H_s was $\sim 5\%$. The variance in the values of N was $\sim 25\%$. This rather large variance stems, in part, from the fact that the AE method is sensitive to the nonuniformity of the defect structure along the surface of the sample.

TABLE II. Microhardness of pure and doped InP crystals, $d \parallel \langle 100 \rangle$, $P = 40$ g.*

	$T = 293$ K		$T = 600$ K	
Crystal	H, kg/mm^2	$\lvert\Delta H\rvert/H_0$, %	H, kg/mm^2	$\lvert\Delta H\rvert/H_0$,%
InP	365	–	80	–
InP:Fe	360	1.4	110	37.5
InP:Zn	380	4.1	170	12.5
InP:Sn	380	4.1	160	100.0

*$\Delta H = H - H_0$, where H and H_0 are the microhardness values for doped and pure crystals, respectively.

3. EXPERIMENTAL RESULTS AND DISCUSSION

The data presented in Table II attest to the fact that at room temperature doping has a very weak effect on the microhardness. The change in the microhardness falls within the limits of measurement error.

However, the picture changes substantially at a deformation temperature of 600 K (Table II). In this case, substantial hardening is observed; the relative changes in H reach $\sim 100\%$. This situation can be explained as follows. The hardening observed in InP to accompany doping is attributed ordinarily to the retardation of moving dislocations by impurities.[4] In InP, just as in other III–V semiconductor compounds, dislocations are virtually immobile at room temperature.[4–6] Therefore, the retardation effect is strong only at high temperatures. The effect of the temperature on the impurity hardening of InP crystals was previously observed in uniaxial compression experiments.[4] It was shown that the increase of the upper yield point due to doping is greater at higher temperatures.

It follows from Table II that the greatest increase in microhardness occurs in the case of doping with zinc (acceptor impurity). This observation agrees well with the results of Ref. 4, where it was found that Zn in InP single crystals retards all basic types of dislocations (α, β, and screw dislocations). Another impurity (S, donor impurity) decreases the velocity only of β and screw dislocations; the velocity of α dislocations was found to be even higher.

The results for only one orientation of the indentor are presented in Table II. Similar data were obtained for the other orientation $d \parallel \langle 110 \rangle$. The microhardness anisotropy, i.e., the difference in the values of $H_{\langle 100 \rangle}$ and $H_{\langle 110 \rangle}$, is very small. For example, at room temperature the anisotropy coefficient InP$\sim$2% ($K = H_{\langle 100 \rangle} - H_{\langle 110 \rangle}/H_{\langle 110 \rangle}$,%) for pure InP and $\sim$13% for doped samples.

TABLE III. Microhardness anisotropy of pure and doped InP crystals in sclerometric investigations.

	$T = 293$ K			$T = 600$ K		
	H_s, kg/mm^2			H_s, kg/mm^2		
Crystal	$\langle 100 \rangle$	$\langle 110 \rangle$	K_s, %	$\langle 100 \rangle$	$\langle 110 \rangle$	K_s,%
InP	96	196	104	88	104	18
InP:Fe	104	192	80	70	102	45.7
InP:Zn	93	168	80.6	106	106	0
InP:Sn	91	161	77	105	163	55

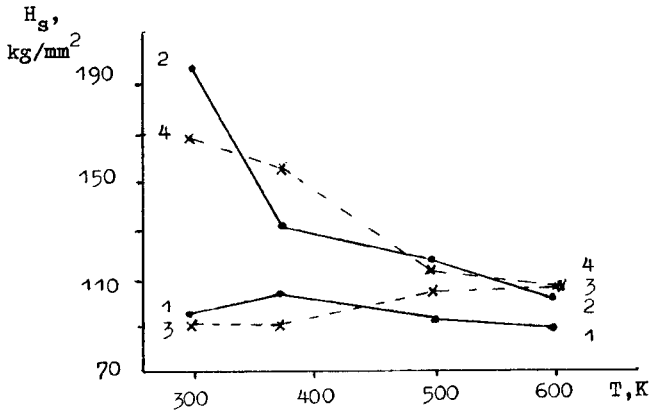

FIG. 1. Temperatures dependences of the scratch hardness for InP (*1*, *2*) and InP:Zn (*3*, *4*). The directions of indentor motion are $\langle 100 \rangle$ (*1*, *3*) and $\langle 110 \rangle$ (*2*, *4*).

However, the microhardness anisotropy was found to be appreciable in investigations by the sclerometric method (Table III).

In Table III, the $\langle 100 \rangle$ and $\langle 110 \rangle$ directions indicate the direction of motion of the indentor during scratch generation. $K_s = (H_s^{\langle 110 \rangle} - H_s^{\langle 100 \rangle})/H_s^{\langle 100 \rangle}$ is the scratch hardness anisotropy factor.

It follows from Table III that at room temperature the anisotropy of H_s reaches 80–100%. In this case $H_s^{\langle 100 \rangle} < H_s^{\langle 110 \rangle}$, while in the microindentation case the picture is reversed — $H_{\langle 100 \rangle} > H_{\langle 110 \rangle}$.[1)] The different character of the hardness anisotropy for these two methods of deformation was also observed for other crystals.[3,8] The nature of this phenomenon was studied in detail in Refs. 3 and 8.

One can see from Table III that as the deformation temperature increases from 293 to 600 K, the H_s anisotropy decreases substantially and in some cases (InP:Zn) it even vanishes. This result is rather unexpected, since previous investigations of scratch hardness anisotropy on the (111) face in InP showed that K_s remains virtually constant in the temperature range 293–673 K.[5] For this reason, additional investigations were performed to clarify the reasons for the strong effect of the temperature on the H_s anisotropy, which we observed. The temperature dependences of the microhardness which were obtained by moving an indentor in the $\langle 100 \rangle$ and $\langle 110 \rangle$ directions are presented in Fig. 1. We see that for the $\langle 110 \rangle$ directions the standard temperature dependence of the microhardness is observed — this parameter decreases with increasing temperature. However, the picture is different for the $\langle 100 \rangle$ directions. In this case, a sharp drop of H_s with increasing temperature does not occur at first, and a weak maximum is observed (Fig. 1, curve *1*) or H_s increases with increasing temperature (Fig. 1, curve *3*). As a result of such different behavior of the microhardness for the $\langle 110 \rangle$ and $\langle 100 \rangle$ directions, either a sharp decrease (Fig. 1, curves *1*, and *2*) or vanishing (Fig. 1, curves *3*, and *4*) of H_s anisotropy is observed.

The large difference in the temperature dependences $H_s(T)$ for the $\langle 100 \rangle$ and $\langle 110 \rangle$ directions suggests that the character of the plastic deformation for these two directions is different. It is well known[1] that plastic deformation in InP

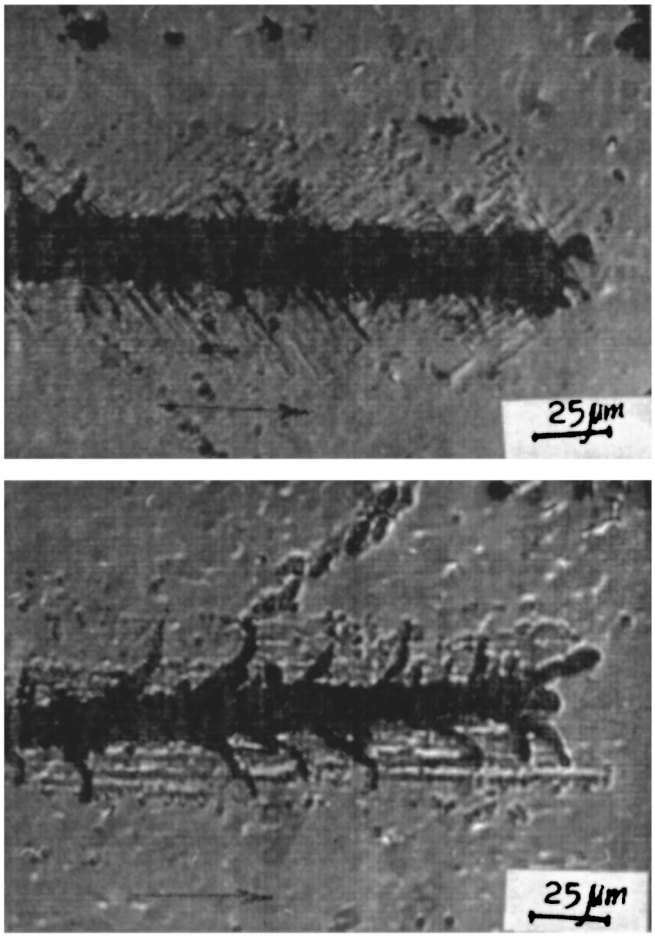

FIG. 2. InP. Dislocation zones of scratches generated along ⟨100⟩ (a) and ⟨110⟩ (b) at $P=20$ g. The arrows indicate the direction of indentor motion. The scratches were generated at room temperature. The zones are revealed after annealing at 623 K for 6 h followed by etching.

can proceed by slipping and twinning. In the deformed zones, which arise when the indentor moves in both directions, we observed twins and dislocation rows oriented along the locations where the {111} slip planes characteristic of InP emerge on the investigated face (Fig. 2). As to which type of mechanism of plastic deformation that contributes here may depend on the scratch direction. If this is so, then the number of acoustic emission signals detected during the motion of an indentor should be different for the ⟨100⟩ and ⟨110⟩ directions (see Sec. 2). The data presented in Table IV confirm this assumption.[2)]

TABLE IV. Number of acoustic emission signals detected during scratch generation ($P=13$ g, scratch length 480 μm) on the (001) face of the experimental InP crystals. $T=293$ K.

	N	
Crystal	⟨100⟩	⟨110⟩
InP	390	250
InP:Zn	500	320
InP:Sn	390	250

It follows from Table IV that twinning makes a larger contribution to scratch generation along ⟨100⟩ than along ⟨110⟩. The fact that at room temperature $H_s^{\langle 110\rangle}$ is much higher than $H_s^{\langle 100\rangle}$ (Table III) could be due, in part, to the fact that twinning is more difficult in the case of indentor motion along ⟨110⟩ than along ⟨100⟩. Therefore, a new factor producing scratch hardness anisotropy is observed: the different contributions of a particular mechanism of plastic deformation during indentor motion along different directions on the face being investigated. Thus far, H anisotropy in both semiconductors and other crystals has been attributed only to the specific nature of their slip elements, especially the arrangement of the extruded material in front of a scratch tip.[3,6,8–10]

It is well known that the [110] and [$\bar{1}$10] directions on the (001) face of III–V semiconductor compounds are not equivalent.[11,12] Therefore, it was interesting to determine whether or not they differ with respect to hardness and the parameters of the acoustic emission that accompanies deformation. Such investigations, as far as we know from the literature, have still not been conducted on these materials.

Rectangular dislocation etch pits were detected on the (001) face of InP:Sn crystals. According to Ref. 11, the [110] direction is oriented along the long side of the rectangle. Using this orienter, it was found that $H_s^{[\bar{1}10]}=130$ kg/mm^2 and $H_s^{[110]}=150$ kg/mm^2. The values of N were found to be different: $N_{[\bar{1}10]}=220$ and $N_{[110]}=290$.

Therefore, these results confirm the nonequivalence of the directions [110] and [$\bar{1}$10]. Etch pits which are as sharp as those in In:P:Sn were not obtained in other investigated crystals. However, a difference in the scratch hardness (ΔH_s) and in the number of AE pulses (ΔN) for the [110] and [$\bar{1}$10] directions was observed for them also. For example, $\Delta H_s=30$ kg/mm^2 and $\Delta N=100$ for InP and 10 kg/mm^2 and 110, respectively, for InP:Zn.

4. CONCLUSIONS

1. Impurity hardening of InP single crystals (Fe, Zn, and Sn as dopants) is much more pronounced at high temperatures ($\sim$600 K) than at room temperature, because of the retardation of moving dislocations by impurities, which is more pronounced at high temperatures.

2. Strong scratch hardness anisotropy (H_s) was observed on the (001) face of pure and doped InP crystals in sclerometric investigations at room temperature: For indentor motion along ⟨110⟩ H_s is approximately two times larger than $H_s^{\langle 100\rangle}$.

3. It was found that the temperature dependences of $H_s^{\langle 110\rangle}$ and $H_s^{\langle 100\rangle}$ differ sharply. The first parameter decreases with increasing T, as is characteristic of microhardness. The second parameter changes, only slightly, and for some samples it even increases with T. As a result, the H_s anisotropy decreases at $T\sim 600$ K or even vanishes (InP:Zn).

4. The pronounced H_s anisotropy at $T=293$ K and the inadequate behavior of $H_s^{\langle 110\rangle}$ and $H_s^{\langle 100\rangle}$ with increasing T are explained by the fact that two mechanisms of plastic deformation make different contributions — slipping and twinning during scratch generation that accompanies inden-

tor motion along ⟨100⟩ and ⟨110⟩. The experiments on the detection of acoustic emission (AE) accompanytin scratch generation confirm this explanation.

5. Sclerometric investigations and AE detection confirm [110] and [$\bar{1}$10] nonequivalence on the (001) face of III–V compounds, previously revealed by other methods.

[1)]The H_s anisotropy on the (001) face of InP:Fe was observed previously in Ref. 7.

[2)]The fact that $N_{\langle 100\rangle} > N_{\langle 110\rangle}$ cannot be attributed to crack development, since more intense crack formation was observed for scratches along ⟨110⟩ than for scratches along ⟨100⟩. Figure 2 illustrates this situtation.

[1] G. T. Brown, B. Cockayne, and W. R. Nacevan, J. Mater. Sci. **15**, 1469 (1980).

[2] S. G. Simashko *et al.*, in *Preparation and Investigation of New Materials in Semiconductor Technology* [in Russian], Shtiintsa, Kishinev, 1980.

[3] B. S. Boyarskaya, D. Z. Grabko, and M. S. Kats, *Physics of Microindentation Processes* [in Russian], Kishinev, 1986, p. 294.

[4] I. Yonenaga and K. Sumino, J. Appl. Phys. **74**, 917 (1993).

[5] S. G. Simashko, N. V. Bezhan, and V. D. Martynenko, Fiz. Tverd. Tela (Leningrad) **19**, 1619 (1977) [Sov. Phys. Solid State **19**, 946 (1977)].

[6] M. I. Val'kovskaya, B. M. Pushkash, and É. E. Maronchuk, *Plasticity and Brittleness of Semiconductor Materials During Microhardness Tests* [in Russian], Kishinev, 1972, p. 235.

[7] D. Z. Grabko, V. S. Panfilov, and Z. E. Maronchuk, in *Indium Phosphide in Semiconductor Electronics* [in Russian], Shtiintsa, Kishinev, 1988.

[8] Yu. S. Boyarskaya, *Deformation of Crystals During Microhardness Tests* [in Russian], Kishinev, 1972, p. 235.

[9] C. A. Brookes and F. Green, Proc. Roy. Soc. (London) A **368**, 37 (1979).

[10] C. A. Brookes, Phil. Mag. A **43**, 529 (1981).

[11] D. B. Holt, J. Mater. Sci. **23**, 1131 (1988).

[12] É. E. Maronchuk, in *Deformation of Crystals Under a Concentrated Load* [in Russian], Shtiintsa, Kishinev, 1978, p. 110.

Translated by M. E. Alferieff

Unusual absorption ''band'' in the infrared spectrum of silicon annealed at high temperature and then rapidly cooled

N. S. Zhdanovich

A. F. Ioffe Physicotechnical Institute, Russian Academy of Sciences 194021 St. Petersburg, Russia
(Submitted February 7, 1996; accepted for publication April 11, 1996)
Fiz. Tekh. Poluprovodn. **31**, 247–249 (February 1997)

An unusual absorption ''band'' with a giant half-width has been detected in the infrared absorption spectra of silicon obtained by zone melting and subjected to cyclic heat treatment at 1250 °C with rapid cooling after each anneal and with partial removal of the thermal oxide in each cycle. A model explaining the observed features of the spectrum in terms of the transformation, occurring during heat treatment of impurity nanoprecipitates contained in the initial silicon and in terms of the microblock structure of the material is proposed. [S1063-7826(97)02402-2]

The technological process of fabricating silicon semiconductor devices ordinarily includes a series of high-temperature heat treatments (HT) with partial removal of the thermal oxide after each treatment. To model this process approximately and to study the effect of such HTs on internal oxidation and other processes in silicon, which are important for device quality, the following experiment was performed. Plane-parallel plates, each about 1 mm thick and several centimeters long, were cut in the axial direction from the 26-mm-diameter silicon ingot obtained by zone melting. Each plate was polished on both sides using the factory technology. Two plates were annealed for 4 h in an oxygen stream at 1250 °C. Next, a boat with one of the plates was removed as quickly as possible from the furnace into air, and the second plate was cooled together with the furnace. Oxide was removed from part of the surface on both sides of each plate and an infrared (IR) transmission spectrum of the transmission in the range 2–25 μm was recorded in this section. The transmission was measured using a comparison sample, consisting of an unannealed plate of the same thickness from the same ingot. The absorption coefficient $\alpha(\lambda)$ was calculated from the transmission for each wavelength λ. Next, the annealing was repeated, but the oxide was removed from a larger area of the surface than the first time, after which the transmission spectra were recorded in the same sections of the plates as after the first anneal and in the newly exposed sections. These operations were repeated. Figure 1 illustrates the topography of the sample surface and the sequence of operations.

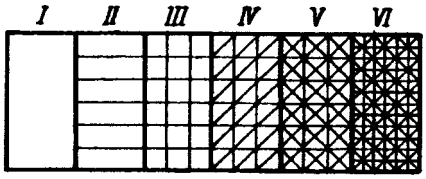

FIG. 1. Schematic diagram of the working sample. Thermal oxide was removed from both sides of the plate after each anneal — zone I, after the second and all subsequent anneals— zone II, after the third and all subsequent anneals— zone III, and so on.

An unusual absorption band was observed in the spectra of all sections (zones I–VI in Fig. 1) of a plate which was quenched after each anneal (Fig. 2). The band is so wide that without a substantial compression of the λ scale it could be completely missed. A peak near 9 μm due to interstitial oxygen is seen against the background of this band. It was found that as silicon is gradually removed from the surface of the sample, the intensity of this peak decreases, i.e., the oxygen responsible for the peak is concentrated in the surface regions of the plates. In the process of annealing, oxygen penetrates into the sample from the surrounding atmosphere and diffuses into the volume of the silicon. The diffusion coefficient (D) in the near-surface layer containing an elevated (relative to the volume of the sample) amount of interstitial oxygen after heat treatment was estimated to be 1.1×10^{-9} cm^2/s, which agrees well with the value 0.9×10^{-9} cm^2/s obtained from the temperature dependence of D presented in

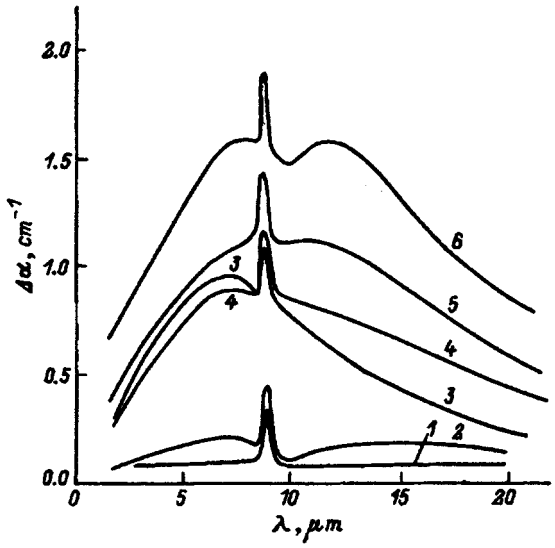

FIG. 2. Absorption (α_1) in silicon subjected to a heat treatment cycle at 1250 °C with slow (*1, 2*) or fast (*3–6*) cooling, relative to the absorption (α_0) in the unannealed material, $\Delta\alpha=\alpha_1-\alpha_0$. *1, 3* — zone I after the first six anneals; *2* — zone I after the seventh anneal; *4* — zone V after the fifth and sixth anneals; *5* — zone VI after the sixth anneal; *6* — zone I after the eighth anneal.

Ref. 1 . This is apparently the most accurate dependence, since in Ref. 1 agreement between the data obtained by different authors was also achieved in different temperature intervals with D varying over eleven orders of magnitude.

The absorption band with a giant half-width is a volume effect. The absolute absorption at the maximum apparently depends primarily on the postanneal cooling rate and increases with this rate. No appreciable variation of the intensity of this absorption as a function of the number of anneals is observed — for curves *3* and *4* in Fig. 2, except for the maximum of the peak near 9 μm, the experimental points obtained in the first six anneals are essentially indistinguishable. The differences in the curves *3* and *6*, which refer to the same zone but with different anneals, are most likely due to an intermediate anneal with slow cooling and (or) higher quench rate after the eighth anneal. The observed effect is easily reversible. For example, after the seventh anneal, which is accompanied by slow cooling (the first six anneals were accompanied by quenching), the intensity of the band decreases almost to zero (curve *2*), but the next anneal with quenching restores the magnitude of this absorption (curve *6*).

As one can see from Fig. 2, the shape of the band and the position of the maximum are different in different zones of the working plate which has undergone quenching. For example, as the light probe is moved along the axis of the ingot (from zone I to zone VI), the band transforms into a superposition of strongly overlapping components (curves *3–5*). This change in the shape of the band is especially clearly seen after an intermediate anneal with slow cooling. In this case, as a result of the next anneal with quenching, two maxima appear in the spectrum from the section of the plate (zone I) where one maximum was observed after the first six anneals with quenching (compare curves *3* and *6*). In the spectrum where such a splitting is most clearly observed, these maxima lie near 8 and 12 μm.

All observations presented above, taken collectively, suggest that the appearance of an absorption band with a giant half-width in the IR spectrum is most likely due to the presence of nanoprecipitates of silicon oxide and carbide (or, possibly, nitride), which are optically inactive before heat treatment, in the initial silicon and (or) their transformation during treatment. We are not dealing here with the precipitation of particles of a second phase, as often is the case with silicon during heat treatment — in that case the absorption bands have a much smaller half-width than the band studied here. Moreover, such formations in silicon have a tendency to dissipate at temperatures of the order of 1250 °C and higher. The situation at hand most likely concerns weakly ordered and very small clusters of Si–O and Si–C (or Si–N) bonds with an unusually wide variance in the bond angles and, possibly, bond lengths. Only in this case could the superposition of a set of narrower bands with maxima in a wide range of λ, which correspond to different variants of the incorporation of these bonds into the silicon matrix, give a result similar to the observed effect. X-Ray diffractometry of the silicon investigated apparently supports this assumption. The rocking curve for this material was found to be broadened compared with the standard curve for the silicon employed in semiconductor technology, suggesting a possible microblock structure in the experimental material. In this case the interval of λ where the absorption peaks of built-in impurity formations are distributed can indeed be very wide. If the assumptions made above are correct, then the ease with which the band with the giant half-width, which accompanies the alternation of anneals with fast and slow cooling (Fig. 2, curves *2* and *6*), appears and disappears, could indicate that these formations are extremely small. Unfortunately, I have no information about the origin and past history of the plates employed in the experiments; such information undoubtedly would be helpful for the present discussion.

The fact that one of the maxima lies near 8 μm makes it possible to attribute the shorter wavelength component of the band to absorption on Si–O bonds. The absorption band with a maximum at 1230 cm^{-1}, which is most often observed in the spectra of silicon after heat treatment and is due to SiO_2 precipitates, lies in this region (see, for example, Ref. 2). It should be noted that in studying the state of oxygen in silicon with different heat treatments, the base of the interstitial oxygen peak at 9 μm in many spectra contains additional absorption extending over a long distance on both sides in λ (see, for example, Ref. 3). This additional absorption has not yet been explained. It has not been ruled out that it could be due to processes which are similar to those which led in our investigations to the appearance of an absorption band with a giant half-width.

The longer wavelength component with a maximum near 12 μm is very likely due to clusters of Si–C bonds.[4] The change in the ratio of these components in the spectra from different zones of a quenched plate could then reflect a difference in the content and (or) state of O and C in different parts of the ingot. The increase in the long-wavelength component after an intermediate anneal with slow cooling could be due to the formation of nuclei, in the process of such cooling, for more intense subsequent formation of clusters of Si–C bonds, which are observed after annealing with quenching. The simultaneous formation of Si–O and Si–C clusters is apparently associated with a compensation of internal mechanical stresses in the sample. The incorporation of clusters of Si–O bonds in silicon produces compressive stresses in the crystal, and the simultaneous incorporation of Si–C bonds should decrease these stresses and the internal energy of the system. Processes of this kind have been observed, for example, to accompany the implantation of oxygen ions in silicon plates.[5] Clusters of Si–N bonds can also serve, in principle, for compensating the mechanical stresses due to Si–O bonds, especially since the absorption maximum on the stretching vibrations of Si–N bonds in silicon nitride also lies near 12 μm. Although the nitrogen content in ordinary commercial silicon is much lower than the oxygen and carbon content (see, for example, Ref. 6), the lack of information about the initial material does not allow us to rule out this possibility completely.

Despite the fact that the considerations stated here are not strictly proved and all the observed facts discussed above are hypothetical, it seems appropriate to publish these observations even at this stage of the work since the observed effect is unusual and since there is no real possibility of obtaining additional information.

I wish to thank M. P. Shcheglov for performing the x-ray diffraction measurements and V. I. Sokolov for his attention and assistance at the first stage of this work.

[1] G. D. Watkins, J. W. Corbett, and R. S. McDonald, J. Appl. Phys. **53**, 709 (1982).
[2] S. M. Hu, J. Appl. Phys. **51**, 5945 (1980).
[3] K. Tempelhoff, F. Spigelbeig, R. Gleichmann, and D. Wruck, Phys. Status Solidi A **56**, 213 (1979).
[4] A. R. Been and R. C. Newman, J. Phys. Chem. Solids **32**, 1211 (1971).
[5] V. I. Sokolov, I. L. Shul'pina, S. A. Goncharov, and N. S. Zhdanovich, Élektron. Tekhn. Ser. 6, Materialy, No. 7(216), 6 (1991).
[6] T. Nozaki, Y. Yatsurugi, N. A. Kiyama, Y. Endo, and Y. Makide, J. Radioanalyt. Chem. **19**, 109 (1974).

Translated by M. E. Alferieff

Numerical modeling of microplasma instability

B. I. Datsko

Institute of Applied Problems of Mechanics and Mathematics, Ukrainian National Academy of Sciences, 290601 L'vov, Ukraine

(Submitted November 9, 1995; accepted for publication April 17, 1996)
Fiz. Tekh. Poluprovodn. **31**, 250–254 (February 1997)

The basic features of current flow in the form of microplasma pulses have been confirmed by numerical modeling. It is shown that a microplasma can appear spontaneously in the presence of a local inhomogeneity in the space-charge region of a $p-n$ structure, and the increase in the temperature of the structure as a result of Joule heating leads to microplasma suppression. The kinetics, shape, and duration of the microplasma pulses were studied numerically as a function of the applied voltage and the parameters of the semiconductor structure.
 [S1063-7826(97)01102-2]

1. INTRODUCTION

Experiments show that localized regions of high current density, which are called microplasmas, are formed during avalanche breakdown of reverse-biased $p-n$ junctions. It is ordinarily assumed that microplasmas are formed because of weak inhomogeneities in the space-charge region (SCR) of a $p-n$ junction, which produce a strong electric field in local regions of the junction. However, many properties of microplasmas, primarily hysteresis which occurs upon the appearance and disappearance of microplasmas, cannot be explained on the basis of this mechanism. Microplasmas form with very weak currents on the initial section of avalanche breakdown, when the average value of the avalanche multiplication factor M does not exceed 10^2-10^3, while the avalanche multiplication factor in microplasmas is in the range[1,2] 10^7-10^9. These properties were explained theoretically in Ref. 3, where it is shown that microplasma formation is associated with an increasing dependence of the impact ionization rate on the nonequilibrium carrier density and the spreading of the current along quasineutral n and p regions of the structure. In Ref. 3 it was shown that a microplasma can also be excited in $p-i-n$ structures in which the $p-n$ junction is ideally uniform over its entire area and the existing structural nonuniformities are only nuclei of spontaneous formation of microplasmas, whose properties and parameters are essentially independent of the parameters of the nonuniformities. The theoretical results obtained in Ref. 3 were later confirmed in Ref. 5, where the results of an experimental investigation of Si-based $p-i-n$ structures are described. Nonetheless, the spontaneous switching on and off of microplasmas was not explained in Ref. 3.

In the present paper, we examine a theoretical model which makes it possible to explain microplasma instability. Specifically, we show on the basis of a qualitative and numerical investigation of the proposed mathematical model that the self-heating of a $p-n$ structure can cause spontaneous switching on and off of microplasmas.

2. MATHEMATICAL AND PHYSICAL MODEL OF SPONTANEOUS SWITCHING ON AND OFF OF MICROPLASMAS

According to Ref. 3, microplasma formation is described by a system of two equations: a balance equation for the electron density averaged over the thickness of the SCR

$$\frac{\partial n}{\partial t}=D\Delta_{\perp}n+n\nu_i(n,V_i)-\frac{n}{\tau_n}+G_T \tag{1}$$

and the equation of continuity of the total current in the quasineutral n or p regions of the structure

$$C\,\frac{\partial V_i}{\partial t}=\sigma\widetilde{W}\Delta_{\perp}V_i-j+(V-V_i)\rho^{-1}, \tag{2}$$

where ν_i is the average (over the thickness of the SCR) rate of ionization by the charge carriers, V_i is the voltage drop across the SCR of the $p-n$ junction, $j=env_n$ is the avalanche current density, D and v_n are, respectively, the diffusion coefficient and drift velocity of electrons in the SCR, $\tau_n=w/v_n$ is the time of flight of the carriers through the SCR, w is the thickness of the SCR, C is the specific capacitance of the $p-n$ structure, $\Delta_{\perp}\equiv\partial^2/\partial x^2+\partial^2/\partial y^2$, the z axis is orieneted along the normal to the plane of the $p-n$ junction, $\widetilde{W}$ is the effective thickness to which current spreads in the quasineutral p or n regions, σ is the conductivity of the quasineutral region, $\rho=\widetilde{W}/\sigma$, V is the total voltage drop across the $p-n$ structure, and G_T is the rate of thermal and tunneling generation in the SCR.[1)]

In the investigation of microplasma properties performed on the basis of models (1) and (2) the possible Joule heating of the structure, was disregarded. On the other hand the very high current density in the microplasma channel gives rise to in a substantial heating of the $p-n$ structure in the region of the microplasma. For sufficiently high current densities j the Joule heating of the lattice

$$\Delta T=T-T_i=jVR_T \tag{3}$$

can be of the order of $\Delta T=20-100$ K.[1,2] Here T_i is the heat-transfer temperature, and R_T is the thermal resistivity of the structure. Changes in the avalanche breakdown param-

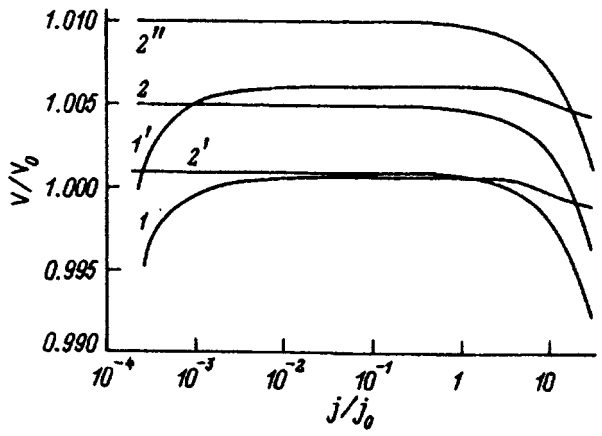

FIG. 1. Characteristic form of the zero-isoclines of the system (1), (2). *1*, *1′*—Local coupling curves [zero-isoclines of Eq. (1)] for different temperatures with uniform heating of the $p-n$ structure (*1*—$T=T_i$, *1′*—$T=1.1T_i$); *2*, *2′*, *2″*—contour lines of the states [zero-isoclines of Eq. (2)] with different voltages on the $p-n$ structure. [The results of the numerical modeling of Eqs. (5) and (6) with the parameters indicated in the text].

eters with increasing temperature of the semiconductor caused the microplasma parameters to be temperature-dependent, since the impact ionization factor of electrons and holes in the microplasma channel decreases.[1,2]

Therefore the rate of ionization ν_i in Eq. (1) is actually a function not only of n and V_i, but also of the lattice temperature T. For this reason, the system (1) and (2) must be supplemented with an equation describing the temperature distribution in the plane of the $p-n$ junction, and the decreasing temperature dependence of the impact ionization rate ν_i must be included in Eq. (1). The temperature distribution in the plane of the $p-n$ junction can be described with the aid of a simplified heat-conduction equation, averaged over the thickness of the SCR,

$$\tau_T \frac{\partial T}{\partial t}=\lambda^2\Delta_\perp T-(T-T_i)+\widetilde{C}V_i n, \tag{4}$$

where τ_T and λ are the thermal relaxation time and length, $\widetilde{C}=ev_nR_T$, R_T is the thermal resistivity of the sample, and T_i is the effective temperature of the heat reservoir (substrate). For simplicity, the temperature dependence of the thermal conductivity was disregarded and the relation (3), which describes uniform heating of the lattice, was taken as the source.

Since the characteristic length and time of temperature propagation are much longer than the characteristic length and time of the propagation of the carrier density in the SCR,[6] an approximate scenario of the effect of a temperature increase on microplasma behavior can be obtained even on the basis of a qualitative analysis of the system. Specifically, treating the temperature as a parameter of the system (1), (2), and (4), we can analyze the evolution of the zero-isoclines of the system of equations (1) and (2) for the case of uniform heating of $p-n$ structure.[6]

The characteristic form of such zero-isoclines for models describing current flow in reverse-biased $p-n$ junctions is shown in Fig. 1. According to Ref. 6, conditions for the formation of narrow spike structures, which are microplasmas, are realized in such systems with parameters corresponding to the intersection of the zero-isoclines on the descending section (curves *1* and *2*). As noted above, a temperature increase results in higher breakdown voltages; i.e., the point of intersection of the zero-isoclines will move increasingly farther into the stable region. This situation is illustrated in Fig. 1 (curve *1′*), which shows the evolution of the local coupling curve with uniform heating of the structure. A nonuniform state in the form of a microplasma can exist in this zone of the parameters (between the positions *1* and *1′*), together with a stable uniform state corresponding to a uniform distribution of the avalanche current.[6] As the temperature increases further, the points of intersection of the local-coupling curves and the contour lines of the state can end up in a region where stable, inhomogeneous solutions do not exist, and then an abrupt transition of the system into a uniform state (switching off of the microplasma, which is accompanied by a jump in the current in the current-voltage characteristic of the $p-n$ structure) should occur.

Therefore, the presence of local nonuniformities, which give rise to a local decrease of the breakdown voltage, leads at some voltage $V=V_{cr}$ to switching on of microplasmas. At the same time, the self-heating of the structure, which primarily influences the mean free path of the charge carriers, results in a suppression of instabilities and switching off of the microplasma.

The fact that self-heating is potentially capable of preventing the development of an instability is also confirmed by qualitative estimates and existing experimental microplasma switching data in which an increase in the breakdown voltage due to self-heating was noted.[1,2] This hypothesis is also confirmed by the experimental fact that, as a rule, microplasmas are generally not observed in germanium structures at room temperature, but they appear when these structures are cooled to liquid-nitrogen temperature, and in $p-i-n$ structures, where negative differential resistance (NDR) arises at a low critical current density, the existence of stationary current filaments becomes possible with intense cooling.

3. NUMERICAL MODELING OF MICROPLASMA INSTABILITY

For numerical modeling it is convenient to write the system of equations (1), (2), and (4) in the one-dimensional case in the form

$$\tau_n \frac{\partial j}{\partial t}=l^2 \frac{\partial^2 j}{\partial x^2}+\nu_i(V_i,T)\nu_i(j)jk_1-j+k_2j_t, \tag{5}$$

$$\tau_V \frac{\partial V_i}{\partial t}=L^2 \frac{\partial^2 V_i}{\partial x^2}-B_j-V_i+V, \tag{6}$$

$$\tau_T \frac{\partial T}{\partial t}=\lambda^2 \frac{\partial^2 T}{\partial x^2}-(T-1)+C_pV_ij, \tag{7}$$

where the temperature T is measured in units of T_i, and the current density j and voltage V_i are measured in units of j_0 and V_0, respectively, for which the following condition is satisfied:[2)]

$$\zeta=\frac{\partial \ln \nu_i}{\partial \ln j}=\frac{j_t}{j-j_i}. \tag{8}$$

This condition determines the point of the maximum of the Λ-shaped local-coupling curve (transition from positive to negative differential resistance for the SCR of the $p-n$ structure). The coefficients in the dimensionless equations are determined by the following expressions: $\tau_n=w/v_0, \tau_V=\rho/C$, $l=\sqrt{D\tau_n}$, $L=\widetilde{W}$, and $B=j_0V_0^{-1}\rho$. The functions k_1 and k_2 simulate local nonuniformities. A large number of mechanisms, which give rise to a decrease of the breakdown voltage, could be associated with the nonuniformities. In practice, however, they all result in a change of the character of the I-V characteristic in a local region as compared with the uniform part of the $p-n$-junction.[3)] We have therefore chosen for the numerical experiments, functions which change only slightly the voltage dependence of the current for the SCR of the structure.

For ν_i we used the model expression

$$\nu_i(V_i,T,j)=\nu(j)\exp[V_0(1-\{\exp[-\beta(1-T)]/V_i^2\})], \tag{9}$$

$$\nu_i=a+b\ \exp\left(1-\frac{c}{j}\right). \tag{10}$$

In this expression the dependence of ν_i on V_i and T is standard and a weakly growing dependence $\nu_i(j)$ is characteristic of a wide class of $p-n$ junctions.[1,2,5,8]

The system of equations (5), (6), and (7) was solved numerically, taking account of Eqs. (9) and (10), with the following coefficients: $\tau_n=2\times10^{-11}$ s, $\tau_V=3\times10^{-11}$ s, $\tau_T=2.5\times10^{-5}$ s, $l^2=2\times10^{-11}$ cm^2, $L^2=4\times10^{-5}$ cm^2, $\lambda^2=2.5\times10^{-5}$ cm^2 $C_p=1/20$, $j_t=10^{-4}$, $B=3\times10^{-4}$, $a=1$, $b=1$, $c=10$, $\beta=0.12$,

$$k_1=1-0.1\ \exp[-x^2/(0.01L)^2],$$

$$k_2=10-\exp[-x^2/(0.01L)^2].$$

The following parameters characteristic for Si-based semiconductor structures were used for the calculation: $D=1$ cm^2/s, $v_0=10^6$ cm/s, $\omega=2\times10^{-5}$ cm, $\widetilde{W}=4.5\times10^{-3}$ cm, $C=2\times10^{-8}$ F/cm^2, $\rho=1.5\times10^{-3}$ $\Omega\cdot$cm^2, $j_0=10$ A/cm^2, $V_0=50$ V, $R_t=0.03$ K$\cdot$cm^2/W, $\alpha=4\times10^{-4}$ K^{-1}, $T_i=300$ K.

Numerical modeling of the systems (5), (6), and (7) confirmed the results of the qualitative analysis made above. When the external voltage reached the value (in units of V_0) $V=V_{cr}=1.005$ (Fig. 1), a strongly nonuniform solitary state of current flow appears spontaneously over a time of the order of τ_V in a region of localization of the nonuniformity of the order of Δx (Fig. 2, curve *1*). Local heating of the lattice in the region of microplasma localization results in a decrease in amplitude over a time of the order of τ_T and switching off of the microplasma and a transition into a state of uniform current flow over a time of the order of τ_V (Fig. 2, curve *2*). It should be noted that as a result of the temperature dependence, even local blocking of the current, which is caused by a local decrease of the voltage in the region of the microplasma, i.e., the thermal current in such a region becomes less than in the rest of the $p-n$-junction, is possible. Since a high-density current does not flow in the structure,

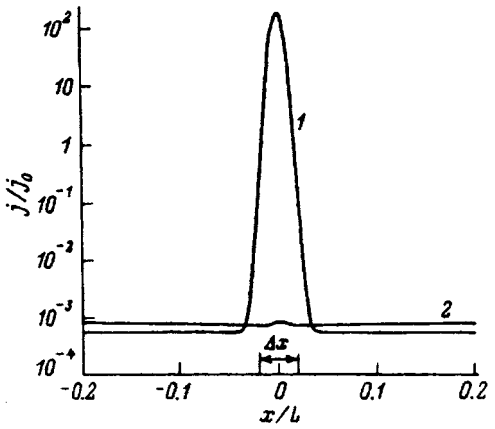

FIG. 2. Current density distribution $j(x)$ in a $p-n$-structure with the microplasma state switched on (curve 1) and off (curve 2).

the lattice cools down and the system returns to the state in which spontaneous microplasma formation is again possible. The formation of a new microplasma in the region of nonuniformity again leads to heating of the structure and to subsequent vanishing of the microplasma (over a time of the order of τ_T); i.e., a current in the form of microplasma pulses of the telegraph signal type flows through the $p-n$ junction (Fig. 3a). The dynamics of the maximum current density oscillations is shown in Fig. 3b. This picture also has been observed in an experimental study of microplasmas.[1] The vertical sections correspond to the switching on and off of microplasmas, the horizontal sections correspond to cooling, and the sloping sections correspond to heating of the lattice and decrease of the current flowing through a microplasma. In general, such pulses can exhibit very diverse shapes (from rectangular to triangular) and a random character (the pulse duration and the pauses between the pulses satisfy an exponential distribution). The shape of the pulses depends mainly on the shape of the I–V characteristic for the transit region, which later can acquire a single-valued character because of heating, and also on the load resistance. The pulse shape can be changed from triangular to rectangular by optimizing these two characteristics. The random nature of the pulses is explained by the random fluctuations of the ionization function, which is of a statistical nature. But since the embedded nonuniformities and defects can also have a random nature, the random ''telegraph'' signal can also be obtained in a model of switching on and off of nonuniformities due to heating. Since the instability region of the current flowing through a microplasma is 0.1–2 V,[4)] in the indicated range there can exist at temperature-propagation distances several nonuniformities the interaction between which upon switching on and off can produce a random telegraph signal. This is also indicated by experimental observations which show that microplasmas were observed to interact when they were separated by large distances.[1]

Furthermore, it was noted in the numerical investigations that a sufficiently large temperature gradient is capable of displacing the microplasma from the uniformity on which it

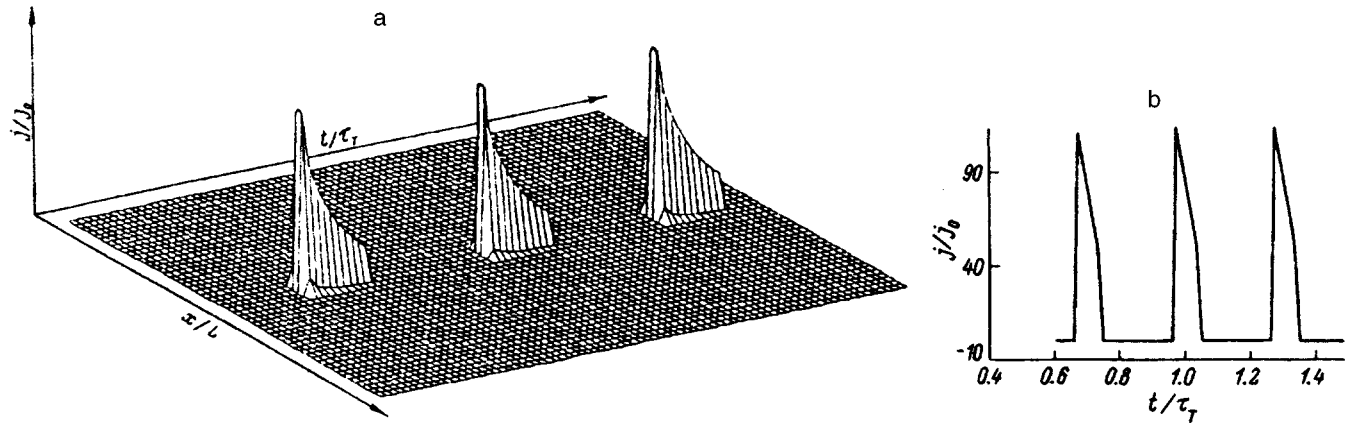

FIG. 3. Dynamics of the current flow in the form of microplasma pulses. a—Spatial distribution of the current, b—dynamics of the variation of the current density at the center of a microplasma.

was formed. Therefore, a nonperiodic heating and cooling of the lattice near a local region can occur when only one microplasma arises on a nonuniformity. In turn, this process can cause nonperiodic microplasma pulses.

I thank V. V. Gafiĭchuk for helpful discussions during the preparation of this paper.

[1)]A detailed derivation of Eqs. (1) and (2) is presented in Ref. 5.

[2)]In switching from the current-carrier density n to the current density j, the velocity v_n of the current carriers is assumed to be saturated: $v_n = v_0$.

[3)]The change in the I–V characteristic for a reverse-biased $p-n$-junction as a function of the doping level and thickness of the SCR is presented, for example, in Ref. 7.

[4)]This fact also agrees well with the proposed model. As the voltage V on the structure increases, the point of intersection of the zero-isoclines will move increasingly farther into the unstable region (Fig. 1, curve 2″), and at some value $V = V_T$ the self-heating of the structure will no longer be capable of suppressing the instability.

[1] I. V. Grekhov and Yu. N. Serezhkin, *Avalanche Breakdown of p–n Junctions in Semiconductors* [in Russian], Énergiya, Leningrad, 1980.
[2] R. V. Konakova, P. Kordash *et al.*, in *Prediction of the Reliability of Semiconductor Avalanche Diodes* [in Russian], edited by Yu. A. Tkhorik, Naukova dumka, Kiev, 1986.
[3] V. V. Gafiĭchuk, B. I. Datsko, B. S. Kerner, and V. V. Osipov, Fiz. Tekh. Poluprovodn. **24**, 724 (1990) [Sov. Phys. Semicond. **24**, 455 (1990)].
[4] V. A. Vashchenko, B. S. Kerner, V. V. Osipov, and V. F. Sinkevich, Fiz. Tekh. Poluprovodn. **24**, 1705 (1990) [Sov. Phys. Semicond. **24**, 1065 (1990)].
[5] V. V. Gafiĭchuk, B. I. Datsko, B. S. Kerner, and V. V. Osipov, Fiz. Tekh. Poluprovodn. **24**, 1282 (1990) [Sov. Phys. Semicond. **24**, 806 (1990)].
[6] B. S. Kerner and B. V. Osipov, Usp. Fiz. Nauk **157**, 201 (1989) [Sov. Phys. Usp. **32**, 101 (1989)].
[7] P. L. Hower and K. G. Reddi, IEEE Trans. **ED-17**, 320 (1970).
[8] S. Sze, *Physics of Semiconductor Devices*, Wiley, N.Y., 1981, 2nd edition [Russian translation, Mir, Moscow, 1984].

Translated by M. E. Alferieff

Oscillations of a ballistic hole current through uniaxially compressed semiconductor layers

N. Z. Vagidov, Z. S. Gribnikov, and A. N. Korshak

Institute of Semiconductor Physics, Ukrainian National Academy of Sciences, 252650 Kiev, Ukraine
(Submitted April 4, 1996; accepted for publication April 17, 1996)
Fiz. Tekh. Poluprovodn. **31**, 255–267 (February 1997)

The oscillations of the ballistic hole current through a thin base of a p^+pp^+ diode compressed uniaxially in the direction of the current are investigated theoretically. As a result of compression, the hole dispersion relation contains sections with negative effective mass along the indicated direction. The current oscillations are caused by the instability of the stationary ballistic current-carrier distribution, which contains an extensive quasineutral plasma region in which the mobile component of the charges consists of drifting carriers with negative effective mass. In many cases, the current oscillations possess a harmonic character, whose frequency is determined by the length of the base and by the voltage, amounting to hundreds of gigahertz for long (~ 1 μm), weakly doped bases and several terahertz for short (<0.1 μm), strongly doped bases. Criteria for a quasiclassical approach to the problem, which was used in the numerical modeling of the vibrational processes described here, are found. This approach is justified if the ballistically injected carriers are distributed in a sufficiently wide band of transverse momenta. © *1997 American Institute of Physics.* [S1063-7826(97)01202-7]

1. INTRODUCTION

In the present paper we theoretically analyze the generation of oscillations of a ballistic current by the current carriers with negative effective mass (NEM). We examine a specialized version of this theory when the carriers are holes in anisotropically compressed cubic semiconductors with diamond or zinc blende lattices.[1] This generation mechanism has recently been observed elsewhere,[2,3] and it was previously discussed for the model structures and specific structures with a different nature of the NEM.[4–7] Anisotropically compressed hole semiconductors are of special interest because they can be very easily verified experimentally.

The paper is organized as follows. In Sec. 2 a preliminary discussion is given of most aspects of this work and qualitative estimates of the parameter ranges required for the effect to occur are made. In the main section, Sec. 3, we present a description of a calculation of the nonstationary ballistic current of holes with a dispersion relation $E_1(p)$ corresponding to the lower subband. In the calculations it is assumed that the current is carried through the thin bases of p^+pp^+ diodes with different base lengths l, different carrier densities n_0, different light-hole masses (m) and heavy-hole masses (M), and different degrees of compression. The calculations were performed in the quasiclassical approximation, in which the existence of the next hole subband $E_2(p)$ is completely ignored. The working voltage ranges $V_a \in (V_c, V_k)$, in which the current oscillations exist, are found and the dependences of the frequency and amplitude of the current oscillations on the voltage V_a in the range (V_c, V_k) are calculated.

Two groups of substantially different parameters of the samples are examined. The first group corresponds to low temperatures at which there is no interaction between the holes and the optical phonons. In this case the diode bases are comparatively weakly doped and must be long enough (>0.5 μm) to keep the frequencies of the current oscillations that arise relatively low (up to 1 THz). Conversely, the second group of parameters corresponds to much stronger doping of the base, large deformations, and higher applied voltages. Such parameters require thin bases. Since the required voltages V_a are such that the interaction with optical phonons is unavoidable, we take some latitude in the choice of temperatures (right up to room temperature and above). The frequencies of the oscillations for this group increase to 10 THz and even higher.

The ballistic nature of transport in diodes belonging to the first group can be ensured automatically by attaining the chosen parameters. In the second case, however, the chosen parameters with a uniform random distribution of impurities are not, by themselves, guaranteed to be ballistic. Therefore, the calculations for the second group are model based. The oscillation frequencies predicted in these calculations can be realized in practice with a layered structure of a base with modulated doping, which decreases hole scattering by the charged impurity but preserves the screening action of the impurity.

The limits of the classical approach employed in Sec. 3 are investigated in Sec. 4; i.e., the conditions under which transitions into a state with the dispersion $E_2(p)$ can be ignored. In contrast to Sec. 3, where all results are obtained numerically, the criteria of Sec. 4 are obtained as a result of an analytical analysis.

Section 5 is devoted to a final discussion of the results obtained and an assessment of the possibilities.

2. PRELIMINARY DISCUSSION

2.1. Hole dispersion relation under uniaxial compression. Uniaxial deformation radically restructures the energy spectrum of holes in semiconductor crystals with diamond or zinc blende lattices.[1] As a result of compression of a crystal

along an axis of the type [100] [or as a result of uniform tension in the (100) plane], the points of degeneracy of the valence bands shift from the positions $\mathbf{p}_{1,2}=0$ in both directions along the [100] axis and occupy the new positions $(p_x)_{1,2}=\pm p_c$, $p_y=p_z=0$ (the p_z axis is oriented along [100]), and p_c^2 is proportional to the deformation. The new positions of the points of degeneracy of the valence bands are of interest to us, because sections of NEM, $\partial^2 E/\partial p_x^2<0$, in the dispersion relation $E_1(\mathbf{p})$ for the bottom valence band (see Fig. 1) appear near them. These sections exist only for sufficiently low values of p_y and p_z, i.e., in some solid angle around the [100] axis.

The hole dispersion in the uniaxially compressed crystal is given by the relation[1]

$$E_{1,2}(\mathbf{p})=Ak^2+a\epsilon\mp[E(\mathbf{k})+E(\mathbf{k},\hat{\epsilon})+E(\hat{\epsilon})]^{1/2}, \tag{1}$$

where $\mathbf{k}=\mathbf{p}/\hbar$, $\hat{\epsilon}=\{\epsilon_{ik}\}$ is the deformation tensor, $\epsilon=\epsilon_{xx}+\epsilon_{yy}+\epsilon_{zz}$,

$$E(K)=B^2k^4+C^2(k_x^2k_y^2+k_x^2k_z+k_y^2k_z^2),$$

$$E(\hat{\epsilon})=\frac{b^2}{2}[(\epsilon_{xx}-\epsilon_{yy})^2+(\epsilon_{yy}-\epsilon_{zz})^2+(\epsilon_{zz}-\epsilon_{xx})^2]$$
$$+d^2(\epsilon_{xy}^2+\epsilon_{xz}^2+\epsilon_{yz}^2),$$

$$E(\mathbf{k},\hat{\epsilon})=Bb[3(k_x^2\epsilon_{xx}+k_y^2\epsilon_{yy}+k_z^2\epsilon_{zz})-k^2\epsilon]$$
$$+2Dd(k_xk_y\epsilon_{xy}+k_xk_z\epsilon_{xz}+k_yk_z\epsilon_{yz}),$$

A, B, C, and D are parameters describing the hole dispersion in the absence of deformation, and $C^2=D^2-3B^2$; these parameters are related to the well-known Luttinger parameters[8] $\gamma_{1,2,3}$ by the relations $A=\hbar^2\gamma_1/2m_0$, $B=\hbar^2\gamma_2/m_0$, and $D=\sqrt{3}\hbar^2\gamma_3/m_0$; here m_0 is the free-electron mass. An isotropic dispersion relation with $\epsilon_{ik}=0$ is obtained in the case $C=0$ (or $\gamma_2=\gamma_3$). The parameters a, b, and d in Eq. (1) are deformation potentials.[1] In what follows, we examine the case of compression along the x axis, and $\epsilon_{xy}=\epsilon_{xz}=\epsilon_{yz}=0$ and $\epsilon_{yy}=\epsilon_{zz}$, so that it is sufficient to know only a and b. In this case $E(\hat{\epsilon})=b^2(\epsilon')^2$ and $E(\mathbf{k},\hat{\epsilon})=Bb\epsilon'(2k_x^2-k_\perp^2)$, where $\epsilon'=\epsilon_{xx}-\epsilon_{yy}$ and $k_\perp^2=k_y^2+k_z^2$. We consider only the isotropic case ($C=0$), which corresponds to large spin-orbit splitting of the valence band. We then can write

$$E_{1,2}(k)=Ak^2+a\epsilon\mp[B^2k^k+b^2(\epsilon')^2+Bb\epsilon'(2k_x^2-k_\perp^2)]^{1/2}. \tag{2}$$

We see from Eq. (2) that

$$p_c^2=-b\,\frac{\epsilon' m_0}{\gamma_2}, \tag{3}$$

and the minus sign corresponds to a negative value of ϵ', i.e., compression. Differentiating expression (2) twice, we obtain an expression for the reciprocal of the effective mass m_{xx}^{-1} near the point of degeneracy ($|\delta k_x|,|k_\perp|\ll k_c$):

$$\frac{\partial^2 E}{\partial p_x^2}=\frac{2}{\hbar^2}\left[A\mp B\,\frac{6k_ck_\perp^2}{[4\delta k_x^2+3k_\perp^2]^{3/2}}\right], \tag{4}$$

where $\delta k_x=k_x-k_c$. For $\delta k_x=1$ it follows from Eq. (4) that

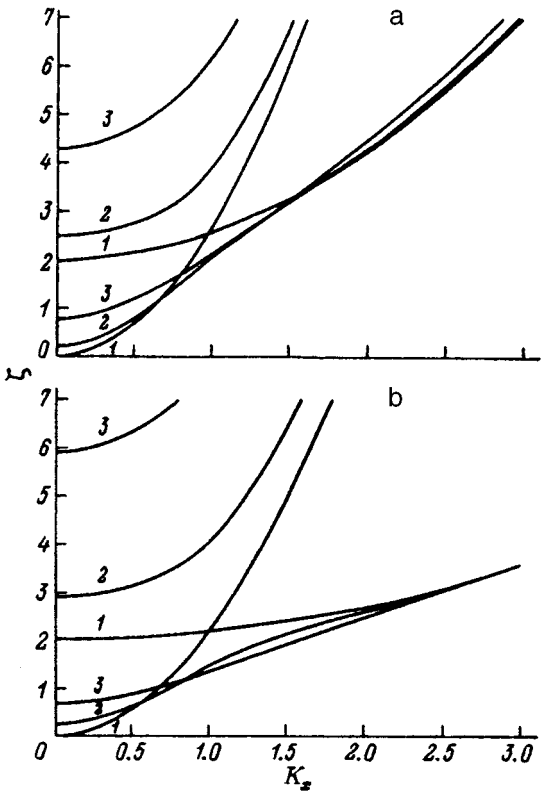

FIG. 1. The dispersion relations $E_{1,2}(p_x)$ of the valence subbands in the case of compression along the x axis. The plots were constructed in the coordinates ζ,κ defined in the text. a—p-Ge; the parameters $A/B=1.552$; values of $k_\perp$, cm^{-1}: *1*—0, *2*—0.5, *3*—1; b—p-InAs; parameters $A/B=1.173$; values of $k_\perp$, cm^{-1}: *1*—0, *2*—0.7, *3*—1.4.

$$\frac{\partial^2 E}{\partial p_x^2}=\frac{2}{\hbar^2}\left[A\mp B\,\frac{2k_c}{\sqrt{3}|k_\perp|}\right], \tag{5}$$

i.e., the differential effective mass is negative for the bottom branch $E_1(k)$ with

$$|k_\perp|<\frac{2}{\sqrt{3}}\,k_c\,\frac{B}{A}. \tag{6}$$

Obviously, Eq. (6) is only an approximate equation, since $B\simeq A$, and the right side of relation (6) is close to k_c. In reality, the limit for $|k_\perp|$ is somewhat smaller. Curves of the quantities

$$\zeta_{1,2}=\widetilde{E}_{1,2}/Bk_c^2=(A\kappa^2/B\mp)(\kappa^4+1-2\kappa_x^2+\kappa_\perp^2)^{1/2}+1$$

versus κ_x for fixed values of $\kappa_\perp^2$ are constructed in Fig. 1; here $\widetilde{E}_{1,2}=E_{1,2}-a\epsilon+Bk_c^2$ and $\kappa=\mathbf{k}/k_c$. These curves make it possible to study the NEM sections where they occur and also their disappearance at sufficiently large values of $\kappa_\perp^2$.

Besides the sections of NEM which we require, the spectra of the valence bands $E_{1,2}(\mathbf{k})$ in uniaxially compressed semiconductors are characterized by another feature which is important to us—at energies $E\leqslant Elc=(A+B)k_c^2$ [energy is measured from the bottom of the band $E_1(\mathbf{k})$] the holes become appreciably lighter: The density of states in each of them is much smaller than in the heavy-hole band without deformation. In fact, at the bottom of the band $E_1(\mathbf{k})$ the

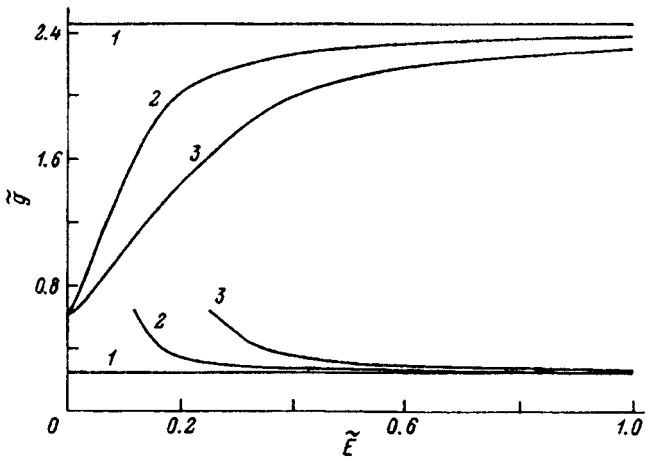

FIG. 2. Density of states $\tilde{g}$ versus $\tilde{E}$, where $\tilde{g}(\tilde{E})=2\pi^2\hbar^2 \times (\gamma_2/m_0)^{3/2} g(\tilde{E})/\sqrt{\tilde{E}-\tilde{E}(0)}$, $\tilde{E}(0)$—energy of the bottom of the corresponding subband. E_c, eV: *1*—0, *2*—0.15, *3*—0.31.

longitudinal mass equals the light-hole mass, $m_l=m$, and the transverse mass $m_t=4m/(1+3m/M)$ and density of states mass $m_g=2^{4/3}m(1+3m/M)^{-2/3}$. For $4m \ll M$ these masses are all much smaller than the heavy mass M. At the bottom of the band $E_2(k)$ the longitudinal mass $M_l=M$ (heavy-hole mass), the transverse mass $M_t=4m/(3+m/M)$ and the density of states mass $M_g=2^{4/3}M^{1/3}m^{2/3}(3+m/M)^{-2/3}$. The masses M_t and M_g are also much smaller than the mass M for $m \ll M$.

The decrease in the hole mass near low energies $E \leqslant E_c$ indicates a substantial improvement in the conditions of ballistic transport. In the well-known, study Heiblum *et al.*[9] investigated experimentally the ballistic transport of light holes injected into GaAs by a tunneling contact and verified that their mean free paths are small (compared with the analogous electronic length) because of intense scattering into the heavy-hole band. In the case of an uniaxially compressed semiconductor, the situation should change substantially, because for $E<a\epsilon+Bk_c^2$ the $E_2(k)$ band is absent, and because the holes in each band become ''lighter.'' The curves of the density of states in the bands $E_1(p)$ and $E_2(p)$ for fixed values of m and M and for several values of p_c^2, including the case $p_c=0$, are shown in Fig. 2. All energies are measured from a common zero point, which is assumed to be the bottom of the $E_1(p)$ band.

2.2. Oscillations of the ballistic current and the ballistic condition. The estimates in the preceding section show that uniaxially compressed semiconductors are suitable for investigating the ballistic transport of holes with negative effective mass (NEM); this is the topic of discussion in the next sections. A characteristic feature of this study is that it does not contain a description of stationary distributions of the hole density p and the electric potential V, because such stationary distributions in the most interesting range of voltages on the p^+pp^+ diode, which we defined by its limits (V_c, V_k), are unstable for $V_k>V_c$, and the stable regime in the indicated range is a regime of oscillations of the ballistic current around some average value. [We note that unstable stationary distributions, which are characterized in the range (V_c, V_k) by a wide central quasineutral region filled with current carriers with NEM, are described in detail in the preceding studies[3,10,11] for other mechanisms for obtaining carriers with NEM.]

As shown in Refs. 2–7, 10, and 11, the range (V_c, V_k) in which the current oscillations occur is relevant if the thickness l of the base of the ballistic n^+nn^+ (or p^+pp^+) diode is greater than some critical value l_c, which is estimated to be [10,11]

$$l_c=\frac{\pi}{e}\left[\frac{\kappa_d b|\epsilon'|}{n_0(1-m/M)}\right]^{1/2}. \tag{7}$$

Here κ_d is the permittivity, and n_0 is the density of the ionized impurity (in our case acceptors), which is assumed to uniformly dope the base. In the picture under consideration the doping of the base is mandatory.

In most investigated cases the oscillations of the ballistic current (for $l>l_c$ and $V_c<V_a<V_k$) are nearly harmonic; i.e., they are described by a single frequency f, which increases with decreasing length of the sample. Since the condition $l>l_c$ must be satisfied, the frequency f could be increased, first, by increasing the doping and, second, by means of small deformations. A decrease of the deformation means that E_c decreases and therefore the lower limit V_c of the active voltage interval also decreases, since

$$eV_c \simeq E_c=(A+B)k_c^2=\frac{2b|\epsilon'|}{1-m/M}. \tag{8}$$

Decreasing the voltage, in turn, decreases the frequency f. Furthermore, by varying the length l or the voltage V_a, we cannot proceed as we please, since we must satisfy with an adequate margin the ballistic condition $l<l_b$, where l_b is the mean free path of the carriers with energy $E \simeq E_c$: $l_b=E_c\tau(p_c)/p_c=p_c\tau(p_c)/2m$. We represent the momentum relaxation time $\tau(p_c)$ in the form $\tau(p_c)=\tau_l \times (p_c)\tau_p(p_c)/[\tau_l(p_c)+\tau_p(p_c)]$, where $\tau_l(p_c)$ is the scattering by impurity ions with density n_0 and $\tau_p(p_c)$ is the scattering time on phonons. Suppose that there is no scattering by phonons and only scattering by impurities is present. In this case, just as in the case of the elementary dispersion, $\tau_l(p_c)\sim E_c^{3/2}/n_0$; i.e., $l_b\sim E_c^2/n_0$. Since according to Eq. (7), $l_c\sim(E_c/n_0)^{1/2}$, the condition $l_b>l_c$ has the form

$$E_c^{3/2}>\alpha n_0^{1/2}, \tag{9}$$

where α is a constant of the material. This condition can always be satisfied by adjusting E_c and (or) n_0. Actually, however, we always have an upper limit on the values of E_c, determined by the threshold for the formation of numerous dislocations and imperfections. The existence of a threshold value of E_c also indicates the existence of a threshold density $n_0^{\max}$, which cannot be exceeded because of the unavoidable destruction of ballisticity. The latter circumstance means that there exists a lower limit on l and an upper limit on the frequency of the generated current oscillations: $f<f_{\max}$.

Disregard of the scattering by phonons is justified only when $E_c<\hbar\omega_0$, where ω_0 is the frequency of a longitudinal optical phonon (it is assumed that the small anisotropy of the deformation of the semiconductor, which gives rise to appre-

ciable changes in the spectrum of the valence bands at energies $E \leqslant E_c$, does not cause a large change in the phonon spectrum), and only in the case of lattice temperatures which are so low that the absorption of optical phonons can be ignored. In this case, only scattering by acoustic phonons remains, which for the actual values of E_c and n_0 can be disregarded. In this case, we must also impose the condition $eV_a \leqslant \hbar\omega_0$. The top $E_c < \hbar\omega_0$ for a possible deformation, which is much lower than the fracture threshold, indicates the existence of a maximum density, which is determined by the condition $\alpha(n_0^{(1)})^{1/2} = (\hbar\omega_0)^{3/2}$, and a corresponding lower limit on the length:

$$l > l_{c1} = \frac{\pi}{e}\frac{\alpha}{\hbar\omega_0}\left(\frac{\kappa_d}{2}\right)^{1/2}. \tag{10}$$

The limit (10) means that there exists an upper threshold for the vibrational frequency that is estimated to be close to 1 THz [since conditions of the type (10) must hold with a certain margin]. If we wish to obtain higher vibrational frequencies, we must increase the deformation and correspondingly increase E_c above $\hbar\omega_0$, increase n_0, decrease l_c, and shorten the base. Then emission of optical phonons becomes important and the preceding estimates cannot be used. For simplicity, let us assume that scattering by phonons is described by a constant mean free path. This introduces another parameter into the criterion (9), which acquires the form

$$E_c^{3/2} > \alpha n_0^{1/2} + \beta\frac{E_c^2}{n_0^{1/2}}. \tag{11}$$

Here β is the new parameter, which characterizes the scattering by optical phonons. The condition (11), in contrast to condition (9), by no means can always be satisfied by adjusting E_c and n_0. The values of n_0 which satisfy the condition (11) can be found if the condition

$$E_c > 4\beta\alpha \tag{12}$$

is satisified and if they lie between the extreme values $n_0^{(1,2)}$ which are determined by the roots of the quadratic equation obtained by equating the left and right sides of Eq. (11):

$$(n_0^{(1,2)})^{1/2} = \frac{E_c^{3/2}}{2\alpha}\left(1 \mp \sqrt{1 - \frac{4\alpha\beta}{E_c}}\right). \tag{13}$$

When the inequality (12) holds rigorously,, these extreme values $(n_0^{(1,2)})^{1/2}$ become $E_c^{3/2}$ and $\beta E_c^{1/2}$, respectively.

In the region of emission of optical phonons (for the polarization mechanism of the electron–phonon interaction and for a weaker mechanism—deformation, which dominates in diamond-type semiconductors) the condition (12) can hold for deformations which are destructive (i.e., unrealistic in practice). The only realistic method that we can see is to weaken electron scattering by dopant ions while maintaining their average concentration at the preceding level, determined by selecting the value of l_c. This requires modulated doping of the base, which results in stratification of the base into strongly doped δ layers with acceptors (in the case of hole transport) and undoped layers between them. We have already proposed this method in order to realize other models for the formation of sections of NEM in the hole dispersion relation..[4–7] These other models were based on the possibility of growing special layered heterostructures with parallel transport, so that modulated doping in these cases was assumed to be one of the elements of the technology.

In the case of a model with uniaxial compression, the transition to layered-doped structures means that the technology becomes appreciably more complicated and much less accessible in practice.

3. OSCILLATIONS OF THE BALLISTIC-HOLE CURRENT

3.1. Equations and procedure. To calculate the hole current through the doped base of the diode $0 < x < l$, we solved Poisson's equation

$$-\kappa_d\frac{\partial^2 V}{\partial x^2} = e(P - n_0), \tag{14}$$

in which the hole density

$$P = \frac{2}{h^3}\int f(\mathbf{p},x,t)\,d^3p \tag{15}$$

is determined from the distribution function $f(\mathbf{p},x,t)$. This function can be found from Boltzmann's equation

$$\frac{\partial f}{\partial t} + v_x\frac{\partial f}{\partial x} + eF\frac{\partial f}{\partial p_x} = 0, \tag{16}$$

in which the electric field intensity $F = -\partial V/\partial x$ is determined (self-consistently with the calculation of f) from Eq. (14). The velocity v_x in Eq. (16) follows from the dispersion relation $E_1(\mathbf{p})$ [see Eq. (1)]: $v_x = \partial E_1(\mathbf{p})/\partial p_x$. The boundary conditions for Eqs. (14) and (16) are $V(0) = 0$, $V(l) = V_a$, and the prescribed distribution functions of the holes entering the base (from the p^+ contacts) is

$$f^{(+)}(\mathbf{p},0,t) = f_0[E_1(\mathbf{p}) - \mu], \quad f^{(-)}(\mathbf{p},l,t) = f_0[E_1(\mathbf{p}) - \mu], \tag{17}$$

where the indices $\pm$ are the signs of the velocity v_x of these outgoing holes. The function $f_0[E_1(\mathbf{p}) - \mu]$ is the Fermi distribution, and the values of the Fermi energy μ are identical at the cathode and anode, they are fixed, and they are determined by the prescribed equilibrium hole density at the contacts.

The system of equations (14) and (16) was integrated numerically by analogy with the preceding studies,[2–7] and the previously obtained dependences of the amplitude and frequency of the oscillations on the voltage V_a and acceptor density n_0 were obtained by the method of computer curve tracing (CT method). In this method V_a or n_0 is assumed to be slowly varying in time: $V_a = V_a(0) + V_a' t$ and $n_0 = n_0(0) + n_0' t$, so that they run through the entire range of variation, of interest to us, of these quantities. For example, in the case of the voltage the interval of variation of V_a always contained the interval (V_c, V_k). In the case of the variation of n_0 (for fixed V_a) a critical value at which the oscillations were disrupted was always found. The rates of change V_a' and n_0' of the parameters were always chosen to be low enough so that the variation process was quasiadia-

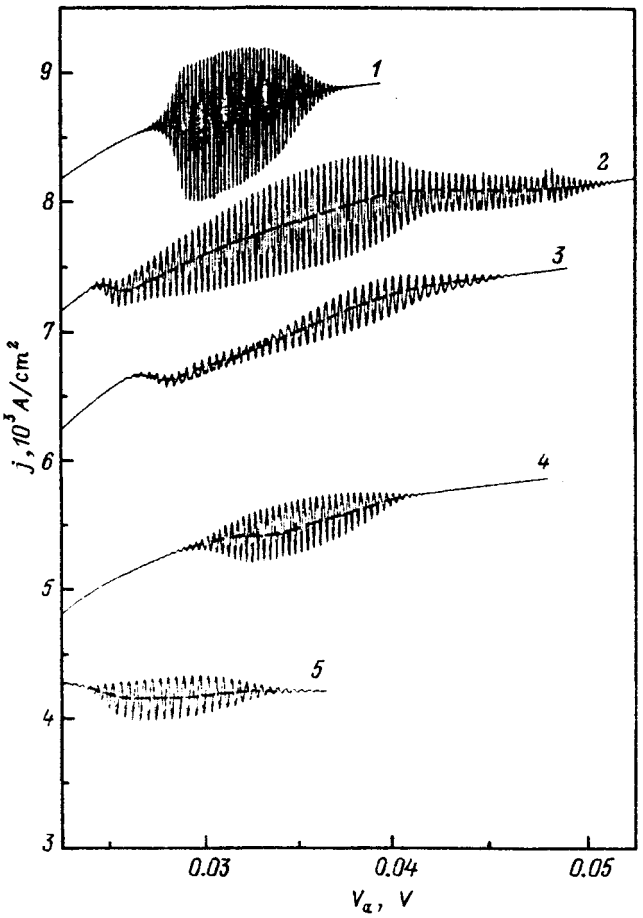

FIG. 3. The curves of $j(t)$ calculated by the computer curve tracing method. The voltage varied according to the law $V_a = V_a(0) + V_a' t$, where $V_a' = 10^{-4}$ V/ps (for curve 4—$V_a' = 2\times10^{-4}$ V/ps). The parameters of the samples correspond to p-Ge with $m = 0.043m_0$, $M = 0.34m_0$, and $T = 4.2$ K. The curves (*1, 2, 3*) correspond to samples with $l = 0.5$ (1), 1.0 (2), and 1.5 eV (3), $n_0 = 3\times10^{15}$ cm^{-3}, $\mu = 0.004$ eV (this corresponds to $p(0) = p(l) = 3\times10^{16}$ cm^{-3}), and $E_c = 0.022$ eV. The curves (*2*) and (*3*) are shifted downward on the current scale by 500 A/cm^2 (2) and 1000 A/cm^2 (3). Parameters for the curve *4*: $l = 0.5$ μm, $n_0 = 10^{16}$ cm^{-3}, $\mu = 0.0125$ eV ($p(0) \approx 2\times10^{17}$ cm^{-3}), $E_c = 0.028$ eV, the current values must be increased by a factor of 5 compared with the values shown on the axis; the parameters for curve *5*: $l = 2$ μm, $n_0 = 2\times10^{15}$ cm^{-3}, $\mu = 0.022$ eV, and $E_c = 0.022$ eV.

batic and did not affect the parameters of the oscillations (amplitude, frequency, form); this was checked by varying the rates themselves.

3.2. Results for long, weakly doped bases. Most results were obtained for a base with germanium parameters ($m = 0.034m_0$, $M = 0.34m_0$, $\hbar\omega_0 \simeq 0.036$ eV). In this material, for $E_c < \hbar\omega_0$ and $eV_a \leqslant \hbar\omega_0$ (and sufficiently low doping densities) bases with lengths l up to ~ 2 μm can be used. Figure 3 shows the current density $j(t)$ for samples with three different lengths l (0.5, 1.0, and 1.1 μm) and other parameters (curves *1, 2, 3*, respectively) equal to the values indicated in the caption. The voltages V_a, instead of time, are plotted along the abscissa, so that the dependences which are obtained are also current-voltage characteristics which inlcude simulation of the oscillation sections. The dashed lines in the oscillation sections represent the curves of the average current density, which were obtained as $j = (j_{\min} + j_{\max})/2$ (irrespective of the form of the oscillations). A general property of all three dependences $j = j(V_a)$ is the presence of sections with N-shaped features with negative differential conductivity (NDC) on the initial sections of the oscillation intervals, followed by sections where j increases with V_a. All three dependences are characterized by well-defined oscillation frequencies f, which are equal to, respectively, 500, 330, and 250 GHz and which do not depend on the voltage V_a. These frequencies satisfy the simple dependence $f \sim (l + l_1)^{-1}$, where in this case $l_1 \simeq 0.5$ μm. The voltage independence of f markedly distinguishes these results from the results described in Refs. 2, 4, and 7, where in the case of different mechanisms of the formation of NEM sections in similar situations a strong voltage dependence $f(V_a)$ was observed. Another feature of the characteristics being described is the obvious nonlinearity of the oscillations. For $l = 0.5$ μm (curve *1*) the oscillations are characterized by some ''rectification'' (asymmetry): The lower half-periods are much sharper than the upper half-periods. The same effect is observed in a more obvious form on the initial sections of the oscillations on curves *2* and *3*. These initial sections become sinusoidal sections, and the rectification then seems to change sign. In addtion, complicated variants of the nonlinear oscillations also occur on curves *2* and *3*. We note that the amplitude of the oscillations was found to be greatest for $l = 0.5$ μm, and the voltage interval was widest for $l = 1$ μm.

Two additional curves (*4* and *5*), which correspond to different parameters of the doping density (both curves) and deformation (curve *4*), are drawn in Fig. 3. An increase in the acceptor density in the base by more than a factor of 3, which is accompanied by a small increase in compression (curve *4*, $l = 0.5$ μm), did not appreciably change the from the behavior of the sample of the same length (curve *1*). The oscillation frequency f increased up to ~ 600 GHz (which corresponds to a decrease in the parameter l_1). An appreciable change in the behavior is observed on curve *5*. Here the frequency of the oscillations, ~ 250 GHz, remains the same as for a slightly shorter base (curve *3*, $l = 1.5$ μm); this also corresponds to a decrease of l_1. The scale of the section N-NDC for $j(V_a)$ increased appreciably.

The function $j(t)$ for a fixed value $V_a = 0.035$ V and for other fixed parameters, with a linear decrease in the doping density $n_0 = n_0(0) - n_0' t$ in time, is shown in Fig. 4 (curve *1*). The linear decrease of n_0 is clearly seen as a linear decrease in the average current density j. However, a decrease in n_0 by more than a factor of 3 did not cause substantial changes in either the amplitude of the oscillations or the frequency. Both quantities decreased (with decreasing n_0) only near the upper values of n_0, $n_0 \sim (3-4)\times10^{15}$ cm^{-3}. The amplitude and frequency remained constant when the nonlinear oscillations (here the degree of nonlinearity was higher for higher values of n_0) changed appreciably.

Similar results were obtained for bases with p-InAs and p-InSb, which differed in the present calculations from the p-Ge bases by the values of the masses m and M (i.e., the parameters γ_1 and γ_2 or A and B), as well as the values of the permittivity κ_d in Poisson's equation (14).

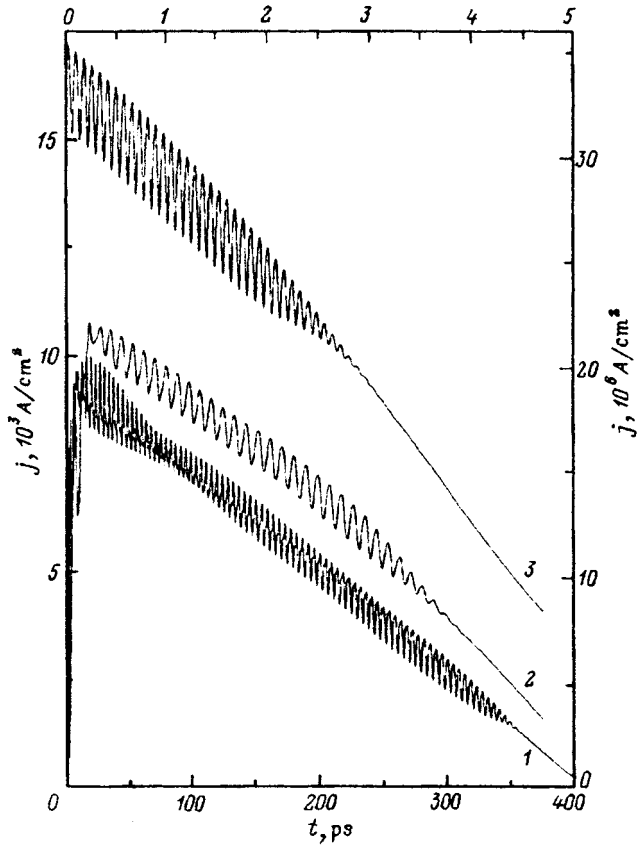

FIG. 4. The curves of $j(t)$ calculated by the computer curve tracing method with acceptor density n_0 decreasing in time according to the law *1*—$(40-0.1t)\times 10^4$ cm^{-3}, *2*—$(3-0.6t)\times 10^{18}$ cm^{-3}, *3*—$(4-0.8t)\times 10^{18}$ cm^{-3}. Here time t is measured in ps. The parameters correspond to p-Ge. Curve 1 (abscissa at the bottom and ordinate on the left): $T=4.2$ K, $l=0.9$ μm, $\mu=0.004$ eV, $E_c=0.22$ eV, $V_a=0.035$ V. Curves 2 and 3 (abscissa at the top and ordinate on the right): $T=300$ K, $l=0.1$ μm (2), 0.07 μm (3), $\mu=0.25$ eV, $E_c=0.391$ eV, $V_a=0.425$ V.

3.3. Results for short, strongly doped bases. Since the results in the preceding subsection, were obtained for small deformations ($E_c\leqslant\hbar\omega_0$), low voltages ($eV_a\leqslant\hbar\omega_0$), and low temperatures ($T\ll\hbar\omega_0$), they describe the real situation in uniformly doped p-type bases. The frequencies of the ballistic-current oscillations predicted there, however, are low (<1 THz). The increase in these frequencies, as indicated in Sec. 2, is connected with the shortening of the base when it is more strongly doped. If in the process the condition E_c, $eV_a<\hbar\omega_0$ is preserved, then the decrease in the mean free path l_b supercedes the decrease in the size l_c and the predicted generation becomes unrealistic. The way out of this situation, as indicated in the same section, is to switch to structures with modulated doping, which makes it possible to decrease the scattering by dopant ions, while maintaining constant at the same time the screening action of the dopant on the longitudinal field $F(x)$. Therefore, by using layered-doped bases instead of uniformly doped bases, we can attempt to obtain generation in the case of shortened bases with small deformations and low temperatures. For a specific assessment of the possibilities of this advance, the scattering by ionized impurity in selectively doped structures must be studied in detail, which falls outside the scope of this study.

The other way in which the scattering at a charged impuritiy can be decreased is by increasing the energy E_c and correspondingly the range of working voltages, i.e., transition into the region E_c, $eV_a<\hbar\omega_0$. In this case, the mean free path decreases sharply due to the emission of optical phonons and it is necessary to switch into a different region of base thicknesses l and therefore sharply increase the dopant density, which requires a further increase of E_c, decrease of l, and so on. Self-consistency starts at much too high values of E_c, which are unrealistic. To remain at the level $E_c\sim 0.2-0.4$ eV, the scattering by impurities must be decreased by a factor of 2–3; i.e., selective doping must also be allowed in this case.

Next, we present the results of model calculations of ballistic-current oscillations at of room temperature ($T=300$ K) for short ($l\leqslant 0.1$ μm), strongly doped ($n_0\geqslant 10^{18}$ cm^{-3}) bases. In the case of p-type Ge the base thickness $l\leqslant 0.5$ μm is sufficient for hole transport without scattering by optical phonons. In the case of materials such as p-InAs and p-InGaAs, the stricter condition $l\leqslant 0.05-0.06$ μm must be satisfied.

The function $j(t)$ for a linearly increasing voltage $V_a(t)$ is shown in the inset in Fig. 5 (for a p-Ge diode with $l=0.1$ μm and $n_0=2\times 10^{18}$ cm^{-3}). The short section of the oscillations (between values of $V_a=0.4$ and 0.5 V) resembles the analogous section of the oscillations from Fig. 3 (curve *4*). However, not only did the voltage range change, but the current density j increased sharply (in accordance with the increase in n_0) and the frequency of oscillations increased also (almost 10 THz). The increase in frequency is apparently due not only to the decrease in the length l, but also an increase in the voltages and average fields in the charged layers. Just as in the preceding cases, the direct dependence of the frequency on the voltage across the sample is not studied here.

The functions $j(t)$, calculated by the same method for five different $In_{0.6}Ga_{0.4}As$ base thicknesses ($l=0.08$, 0.07, 0.06, 0.055, and 0.0545 μm) with $n_0=2\times 10^{18}$ cm^{-3}, $E_c=0.22$ eV, and $T=300$ K are presented in Fig. 5. The parameters A and B for this alloy were found by linear interpolation of the well-known parameters for InAs and GaAs. A decrease of the length l decreases the oscillation interval and increases the oscillation frequency (8 THz for $l=0.08$ μm to 10 THz at $l=0.06$ μm). We obtain on the sample with $l=0.08$ μm (Fig. 5, curve *1*) ostensibly two ranges, merged into one another, of oscillations with different frequencies: The range of lower voltages corresponds to the frequency $f\leqslant 8$ THz and the higher voltage range corresponds to the frequency $f\geqslant 10$ THz. The curves *1–5* lie in Fig. 2 in a manner so that it is possible to construct (dashed line) the phase boundary of the region of oscillations in the (l,V_a) plane.

The two functions $j(t)$ with dopant density decreasing linearly in time in the case of short bases are presented in Fig. 4 (curves *2* and *3*). They were calculated for the same value $E_c=0.39$ eV and the same voltage $V_a=0.425$ V. The model samples are distinguished by a long base ($l=0.07$ and 0.1 μm, respectively). Since the density m_0 in the samples decreases with time according to several different laws, the

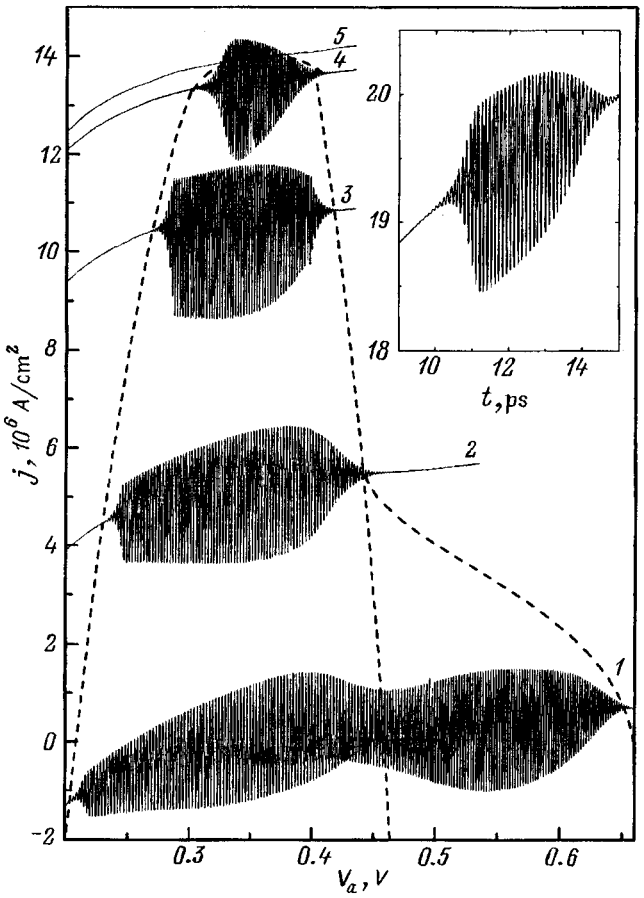

FIG. 5. The curves of $j(t)$ calculated by the computer curve tracing method with voltage increasing linearly with time ($V_a'=2\times10^{-2}$ V/ps), l, μm: *1*—0.08, *2*—0.07, *3*—0.06, *4*—0.055, *5*—0.0545; $n_0=2\times10^{18}$ cm^{-3}, $\mu=0.08$ eV ($p(0)\approx10^{19}$ cm^{-3}), $E_c=0.22$ eV, $T=300$ K, $m=0.376m_0$, $M=0.0403m_0$. The curves are shifted along the ordinate by the amount $\Delta j_i=525(0.055-l_i[\mu\text{m}])\times10^6$ A/cm^2. Inset: $j(t)$ obtained for the case p-Ge with $T=300$ K, $l=0.1$ μm, $n_0=2\times10^{18}$ cm^{-3}, $\mu=0.14$ eV ($P(0)\approx10^{19}$ cm^{-3}), $E_c=0.31$ eV, $V_a(0)=0.2$ V.

moments of equal density can be identified with the moments of equal current density. The oscillation frequency (virtually independent of n_0) in the case of a shorter base (curve *3*) is much higher than in the case of a longer base (curve *2*): 13 and 9 THz, respectively. In the shorter sample the amplitude of the oscillations is larger [also, the amplitude remains nearly constant with a large drop in the average value of $j(t)$]. Oscillations in the shorter sample ceased at a substantially higher acceptor density (in agreement with the discussion in Sec. 2).

The ballistic-current oscillations were accompanied by oscillations of the potential (and field) in the diode base (for a prescribed constant voltage on the diode) and oscillations of the hole density, which have the form of irregular plasma waves that propagate in the direction of hole transport. Since these patterns are fundamentally the same as the analogous patterns for different mechanisms of NEM, we refer the reader to Refs. 4, 6, and 7, where these patterns are presented.

4. QUASICLASSICAL HOLE APPROXIMATION UNDER UNIAXIAL COMPRESSION

4.1. Equations and procedure. In the numerical calculations in the preceding section we ignored the existence of the second hole subband with dispersion relation $E_2(\mathbf{p})$ and we assumed that holes in the subband with the relation $E_1(\mathbf{p})$ move in electric fields classically and cannot pass into the subband $E_2(\mathbf{p})$. Actually, the minimum gap between the hole subbands near the point of degeneracy is very narrow, so that tunneling between the subbands occurs in very weak fields (and at the degeneracy point itself in zero fields $p_x=\pm p_c$, $p_\perp=0$). This makes it necessary to analyze the validity of the classical approach more carefully.

In this section we examined the general approach to the problem indicated above and we obtained the required criteria. We note that hole transport, in which the interband tunneling in a prescribed spatially constant electric field **F** is taken into account, was studied a long time ago.[12,13,14–16] However, in those studies only an undeformed crystal was examined, i.e., tunneling occurred near the point $\mathbf{p}=0$; the method of analysis was based substantially on the fact that the field **F** is constant in space.

Here we employ a universal method which is applied to a wide range of problems, specifically, in Refs. 17–20 and which is based on a unitary transformation of the 4×4 Kohn–Luttinger Hamiltonian.[21] This transformation, which was proposed in Refs. 22 and 23, reduces the problem to operations with a 2×2 Hamiltonian

$$\hat H=\begin{bmatrix}\hat P+\hat Q & \overline{R}\\ \overline{R^+} & \hat P-\hat Q\end{bmatrix}+b\epsilon'\begin{bmatrix}1 & 0\\ 0 & -1\end{bmatrix}+[a\epsilon+eV(x)-E]\begin{bmatrix}1 & 0\\ 0 & 1\end{bmatrix}, \tag{18}$$

where the parameters $a\epsilon$ and $b\epsilon'$ are the same as in Eq. (1). As provided above, here only the version of isotropic (in the absence of deformation) valence bands is used: $C=0$ (i.e., $\gamma_2=\gamma_3$), although according to Ref. 19, a similar procedure can also be used in a more general formulation. In Eq. (18) we used the notation

$$\hat P=A\left(k_\perp^2-\frac{d^2}{dx^2}\right),\quad \hat Q=\frac{B}{2}\left(k_\perp^2+2\frac{d^2}{dx^2}\right),$$

$$\overline{R}=\sqrt{3}B\left(\frac{k_\perp^2}{2}-|k_\perp|\frac{d}{dx}\right),\quad \overline{R^+}=\sqrt{3}B\left(\frac{k_\perp^2}{2}+|k_\perp|\frac{d}{dx}\right),$$

$V(x)$ is the electric field potential, and E is the total hole energy. The Hamiltonian (18) operates on the two-component column wave function

$$\Psi(k_\perp,x)=\begin{bmatrix}\Psi_1(k_\perp,x)\\ \Psi_2(k_\perp,x)\end{bmatrix},$$

which gives the system of equations

$$-\hbar^2(\gamma_1+2\gamma_2)\frac{d^2\Psi_1}{dx^2}+[(\gamma_1-\gamma_2)p_\perp^2+2m_0\times(a\epsilon+b\epsilon'+eV(x)-E)]\Psi_1+\sqrt{3}\gamma_2$$

$$\times\left(p_\perp^2\Psi_2+2\hbar|p_\perp|\,\frac{d\Psi_2}{dx}\right)=0, \tag{19}$$

$$-\hbar^2(\gamma_1-2\gamma_2)\,\frac{d^2\Psi_2}{dx^2}+[(\gamma_1+\gamma_2)p_\perp^2+2m_0$$
$$\times(a\epsilon-b\epsilon'+eV(x)-E)]\Psi_2+\sqrt{3}\gamma_2$$
$$\times\left(p_\perp^2\Psi_1-2\hbar|p_\perp|\,\frac{d\Psi_1}{dx}\right)=0. \tag{20}$$

The use of the parameters $\gamma_{1,2}$ in Eqs. (19) and (20) made it possible to introduce explicitly the Planck constant $\hbar$ and then perform a quasiclassical expansion. We seek $\Psi_{1,2}(k_\perp,x)$ in the form

$$\Psi_{1,2}(x)=\exp\left[\frac{eS_0(x)}{\hbar}+iS_{1,2}(x)\right] \tag{21}$$

and we expand the functions $S_{1,2}(x)$ in quasiclassical series: $S_{1,2}(x)=S_{1,2}^{(0)}(x)+\hbar S_{1,2}^{(1)}(x)+\hbar^2 S_{1,2}^{(2)}(x)+\ldots$. Together with $S_{1,2}(x)$, we introduce the difference of these functions $T(x)=T_0(x)+\hbar T_1(x)+\hbar^2 T_2(x)+\ldots$, where $T_i(x)=S_1^{(i)}(x)-S_2^{(i)}(x)$.

After substituting the expressions (21) into Eqs. (19) and (20), the latter equations, will contain the functions $S_0(x)$ and $S_{1,2}^{(i)}(x)$, in addition to different powers of the exponential cofactors $\exp[\pm iT(x)]$. Rapid convergence of the quasiclassical series requires satisfaction of the condition

$$\hbar|T_1(x)|\ll 1, \tag{22}$$

which would make it possible to use the expansion

$$e^{\pm iT(x)}=e^{\pm iT_0(x)}[1\pm i\hbar T_1(x)+0(\hbar^2)].$$

The condition (22) is used below as a criterion for the validity of the classical approach employed in Sec. 3.

In the zeroth approximation in $\hbar$, it follows from Eqs. (19) and (20) that

$$(\gamma_1+2\gamma_2)S_0'^2+(\gamma_1-\gamma_2)p_\perp^2+2m_0[a\epsilon+b\epsilon'+eV(x)-E]$$
$$+\sqrt{3}\gamma_2(p_\perp^2+2|p_\perp|iS_0')e^{-iT_0}=0, \tag{23}$$

$$(\gamma_1-2\gamma_2)S_0'^2+(\gamma_1+\gamma_2)p_\perp^2+2m_0[a\epsilon-b\epsilon'+eV(x)-E]$$
$$+\sqrt{3}\gamma_2(p_\perp^2-2|p_\perp|iS_0')e^{iT_0}=0, \tag{24}$$

(everywhere except ϵ' the prime designates a derivative with respect to x). We thus obtain

$$S_2'^2=-p_\perp^2+f_1(x)\pm\sqrt{f_2^2(x)+f_3p_\perp^2}, \tag{25}$$

where

$$f_1(x)=-\frac{2m_0\{\gamma_1[eV(x)+a\epsilon-E]-2\gamma_2 b\epsilon'\}}{\gamma_1^2-4\gamma_2^2},$$

$$f_2(x)=-\frac{2m_0\{2\gamma_2[eV(x)+a\epsilon-E]-\gamma_1 b\epsilon'\}}{\gamma_1^2-4\gamma_2^2},$$

$$f_3(x)=-\frac{12m_0\gamma_2 b\epsilon'}{\gamma_1^2-4\gamma_2^2}.$$

We recall that we are interested in the case of compression ($b\epsilon^1<0$), so that $f_3>0$. We are also interested only in negative potentials $V(x)$. The quantity $|eV(x)+a\epsilon-E|$ is small on the hole emitter (i.e., at the anode) and increases away from it, so that the functions $f_{1,2}(x)$, which are negative at the anode, can change sign as x and $|V(x)|$ increase. The function $f_1(x)$ changes sign first as $|V(x)|$ increases, and for even larger values of $|eV(x)|$ $f_2(x)$ also changes sign and becomes positive.

In what follows, we restrict our attention only to the solution (25) with the plus sign, which corresponds to the branch $E_1(p)$, in front of the radical on the right-hand side. Classical treatment of this subband will be checked below..

Besides S_0', Eqs. (23) and (24) also make it possible to find $T_0=S_1^{(0)}-S_2^{(0)}$. In the next approximation in $\hbar$, the system of equations obtained from Eqs. (19) and (20)

$$-(\gamma_1+2\gamma_2)[iS_0''-2S_0'(S_i'^{(0)})']+2\sqrt{3}i|p_\perp|\gamma_2(S_2^{(0)})'e^{-iT_0}$$
$$-\sqrt{3}i\gamma_2(p_\perp^2+2|p_\perp|iS_0')T_1e^{-iT_0}=0, \tag{26}$$

$$-(\gamma_1-2\gamma_2)[iS_0''-2S_0'(S_2'^{(0)})']-2\sqrt{3}i|p_\perp|\gamma_2(S_1^{(0)})'e^{iT_0}$$
$$+\sqrt{3}i\gamma_2(p_\perp^2-2|p_\perp|iS_0')T_1e^{iT_0}=0, \tag{27}$$

can be used to calculate [knowing $T_0(x)$] $(S_{1,2}^{(0)})'$ and $T_1(x)$ and then to check that the condition (22) is satisfied. We have

$$T_1=\Delta_1/\Delta, \tag{28}$$

where

$$\Delta_1=2(\gamma_1^2-4\gamma_2^2)T_0'S_0'^2-6\gamma_2^2p_\perp^2T_0'-\sqrt{3}|p_\perp|\gamma_2S_0''$$
$$\times[(\gamma_1+2\gamma_2)e^{iT_0}+(\gamma_1-2\gamma_2)e^{-iT_0}],$$

$$\Delta=i\gamma_2\sqrt{3}|p_\perp|S_0'\{-4i\sqrt{3}\gamma_2|p_\perp|+(\gamma_1+2\gamma_2)$$
$$\times(|p_\perp|-2iS_0')e^{iT_0}+(\gamma_1-2\gamma_2)(|p_\perp|+2iS_0')e^{-iT_0}\}.$$

4.2. *Quasiclassicity criterion.* Let the potential $V(x)$ vary according to the law

$$V(x)=V_c-V_1e^{-\lambda x}, \tag{29}$$

where V_c is determined by the condition $f_2(x)\to 0$ as $x\to\infty$, i.e., $eV_c=a\epsilon-E-\gamma_1 b\epsilon'/2\gamma_2$, and the characteristic length λ^{-1} is estimated to be slightly lower. Then $f_2(x)$ has the form

$$f_2(x)=-F_2e^{-\lambda x}, \tag{30}$$

where $F_2=4m_0\gamma_2eV_1/(\gamma_1^2-4\gamma_2^2)$, and $f_1(x)=m_0b|\epsilon'|/\gamma_2-\gamma_1F_2e^{-\lambda s}/2\gamma_2$. The law of variation of the potential (29) presumes that in the limit $x\to\infty$ there exists a region with holes with NEM, where the potential equals V_c, and the condition (22) must be checked for the approaches to this region, where screening remains linear. The values of $p_\perp$, which must be studied, below are determined by the Fermi distribution of the injected holes. If this distribution is not too wide, then for the potentials $V_x\simeq V_c$ the condition

$$S_0'^2\gg\sqrt{f_3}|p_\perp| \tag{31}$$

holds for all values of $p_\perp$ under consideration. Under this condition we obtain $|S_0'| \simeq (m_0 b|\epsilon'|/\gamma_2)^{1/2}$, and we can also obtain the estimate

$$|e^{2iT_0}| \gg 1. \tag{32}$$

The conditions (31) and (32) make it possible to estimate

$$\Delta \simeq 2\sqrt{3}\gamma_2 |p_\perp| S_0'^2 (\gamma_1 + 2\gamma_2) e^{iT_0},$$

$$\Delta_1 \simeq 2(\gamma_1^2 - 4\gamma_2^2) T_0' S_0'^2$$

and, finally,

$$|T_1| \simeq \frac{\gamma_1 - 2\gamma_2}{\sqrt{3}\gamma_2 |p_\perp|} |T_0' e^{-iT_0}|$$

$$= \frac{(\gamma_1^2 - 4\gamma_2^2)\lambda}{6\gamma_2^2 p_\perp^2 S_0'} \cdot \left[\frac{-f_2(\sqrt{f_2^2 + f_3 p_\perp^2} + f_2)}{\sqrt{f_2^2 + f_3 p_\perp^2}} \right]. \tag{33}$$

It is easy to verify that the right side of Eq. (33) is maximum for $f_2^2 = (\sqrt{5}-1) f_3 p_\perp^2/2$. The expression in square brackets on the right side of Eq. (33) equals $\sim 0.49\sqrt{f_3}|p_\perp|$, so that

$$|T_1| \simeq 0.28 \frac{\sqrt{\gamma_1^2 - 4\gamma_2^2}}{\gamma^2} \frac{\lambda}{|p_\perp|},$$

and the condition (22) acquires the form

$$0.28\hbar \frac{\sqrt{\gamma_1^2 - 4\gamma_2^2}}{\gamma_2} \frac{\lambda}{|p_\perp|} \ll 1. \tag{34}$$

We shall apply two different estimates of λ for use in the expression (34). The first estimate is similar to that used in Ref. 7, where the screening length of the electric field screened by drifting holes with NEM in the quasineutral NEM region serves as λ^{-1}. This situation differs from that studied in Ref. 7 in that there all carriers had the same negative mass, since the dispersion relation in the x direction was uniform to a first approximation. In our case, however, the dispersion relation $E(p_x)$ near the point $p_x = p_c$ depends strongly on $|p_\perp|$, so that screening is produced by a multicomponent hole mixture. The value of λ for this mixture is calculated in the *Appendix*. The set of parameters in Fig. 1 corresponds to $\lambda \approx 100\ \mu\text{m}^{-1}$. After substituting $|p_\perp| = p_r$ and using Eqs. (A.10), (A.11), and (A.12) from the *Appendix* the condition (34) acquires the form

$$0.28\left[\frac{2(\gamma_2 - \gamma_2)^{3/4}}{\pi^{5/4} 3^{1/2} \gamma_1^{1/4} \gamma_2 (\gamma_1^2 - 4\gamma_2^2)^{1/4}} \frac{e^2 m_0 n_0^{1/4}}{\kappa_d h^{1/4} p_c^{7/4}} \right]^{1/2} \ll 1. \tag{35}$$

Substitution of the parameters from the caption in Fig. 5 gives the inequality $\hbar|T_1| = 0.1 \ll 1$. According to our estimates, the condition (35) holds satisfactorily not only in the case of large deformations ($E_c \simeq 0.3$ eV), but also in the case of small deformations ($E_x \simeq 26$ meV).

The second method of estimation consists of determining the quantity λ directly from a computational experiment, since we have at our disposal the hole density distribution along the x axis for all values of V_a. We estimate λ at the voltage $V_a \simeq V_c$, i.e., at the boundary of the transition from a stationary state into an oscillatory state. The value $\lambda \approx 150\ \mu\text{m}^{-1}$ was obtained for the concentration distributions corresponding to the model in Fig. 5; this value agrees satisfactorily with the previous estimate of λ. The quantity p_r could also be estimated from the hole distribution in the momentum space. These estimates did not refute the previous estimates. We have therefore used solely this brief information.

5. CONCLUSIONS

We examined above the previously proposed mechanism for excitation of oscillations of a ballistic current of carriers with NEM on the basis of uniaxially compressed hole semiconductors. Holes as current carriers realize best and with the largest margin the required condition $M > 2m$. Furthermore, the NEM realization studied here is of a volume character (in contrast to the contact (interface) character in the case of asymmetric double quantum wells[4,7] or composite ΓX quantum wells[7]). Accordingly, the carrier dispersion necessary for our purposes does not require in and of itself a layered structure of the base and can be realized in the homogeneous volume of a hole semiconductor. Therefore, the experimental realization of this version in the regime of low temperature ($T \ll \hbar\omega_0$), low voltages ($eV \leqslant \hbar\omega_0$), and small deformations ($E_c < \hbar\omega_0$) is most realistic (especially since the base lengths in this case are also easily accessible: $l \geqslant 0.5\ \mu$m). Unfortunately, the frequencies of the oscillations in this case are not too high (typical value ~ 0.5 THz). At the transition to the maximum admissable deformations (for which $E_c > \hbar\omega_0$) the length l must be substantially decreased and therefore n_0 must be increased in order to obtain oscillations. In this case, the scattering of holes by randomly arranged acceptors makes it impossible to satisfy the condition (12) with acceptable values of E_c. The way out of this situation can be found in modulation doping and by switching to a layered structure of the base (but preserving the volume mechanism for formation of NEM). Specifically, this could be δ-doped bases with the required period and with the required surface density of acceptors per layer. The transition to layered bases and values $l < 0.1\ \mu$m would make it possible to achieve oscillation frequencies above 10 THz, which were obtained here in Sec. 3. On the other hand, the existence of a variation of the potential in the transverse direction would result in some changes in the dispersion relations for holes, which were ignored in Sec. 3.

The transition to a layered structure of the base, however, eliminates the structural simplicity of a p^+pp^+ diode, which is the main attractive feature of the mechanism. In this case there appears an additional competing method for realizing a dispersion relation with a NEM section in hole semiconductors—quantization of holes in quantum wells;[24] here we give an extensive list of earlier studies. The application of longitudinal transport through the base in hole quantum wells makes it possible 1) to maintain a large ratio M/m; 2) to regulate the energy E_c by the width of the quantum well; 3) to combine in pseudomorphic structures (in systems Ge_xSi_{1-x} or $In_xGa_{1-x}As$) two mechanisms of formation of NEM—quantization and anisotropic deformation; and, 4) to perform modulated doping. Therefore, the analysis of such quantized hole layered bases on the basis of the problem described here is extremely urgent. We note that the problem of oscillations in layered bases was studied

previously[3] in a model version; it was found that current oscillations were present even in the case of a single layer.

As mentioned in detail in Sec. 2, the main conflict in the generator principle lies in the double role of the dopant—the dopant screens the electric field (and in this role there must be a large amount of dopant in order to realize short structures) and it scatters holes (and in this role there should not be any dopant at all). The modulated doping, which results in an unavoidable layered structure, is one method for solving this conflict.

Another possible method is to introduce a definite inhomogeneity in the distribution of impurities along the direction of the current, i.e., along the x axis, since different regions of the base play different functional roles. However, we note that such a stratification is dangerous in that it is impossible to give a systematic ballistic description. This description should not depend on any assumptions about carrier scattering in the base, for carriers entering the base from both electrodes, only in the case when a potential minimum is absent there (i.e., the potential well should be described only by a monotonic function or contain one potential barrier). Introducing layers with a high doping level, we introduce potential wells and in so doing it is necessary to describe the trapping of carriers by wells and freeing of the carriers from the wells.

The generation mechanism, which we examined above and which is based on carriers with NEM, is an analog of the well-known Gunn effect. In both cases use is made of the increase in the mass of the carriers as their kinetic energy increases. The fundamental difference between these mechanisms lies in the fact that the Gunn generation of oscillations is a typical dissipative effect with diffusion transport, intervalley transitions as a result of scattering, and an increase in of the mobility and density of states masses. In our case it is a nondissipative effect; only a single transport mass increases and only in the direction of motion. It is obvious that intermediate situations with a small number of scatterings in the base (so-called quasiballistic transport), which combines the particular features of each mechanism (see, for example, Ref. 25), are possible.

The quasiclassical approach used by us requires that another criterion be satisfied [in addtion to the condition (22)]—the frequency of the current oscillations $2\pi f$ must be small compared with the minimum quantum frequency, $\omega=[E_2(k_c)-E_1(k_c)]/\hbar$. This condition cannot be satisfied for $p_\perp=0$ when $\omega=0$; but it will hold for most holes participating in the current flow if ω is assumed to be the value at $p_\perp=p_r$,:

$$\omega(p_r)=\frac{2}{\hbar}\sqrt{\frac{2\gamma_2}{\gamma_1-\gamma_2}\mu|b\epsilon'|}. \tag{36}$$

Let us estimate the corresponding frequency $f(p_r)=\omega(p_r)/2\pi$ for $|b\epsilon'|=2\times10^{-2}$ eV and $\mu=4\times10^{-3}$ eV. The result is $f(p_r)\sim7$ THz, which is more than an order of magnitude higher than the frequency found in Sec. 3 for the current oscillations. The estimates are just as favorable in the other cases.

This work was performed with the partial financial support of the Joint Fund of the Ukrainian Government, the International Science Foundation (Grant N K5D100), and the Fund for Fundamental Research of the Ukrainian State Committee on Science and Technology (Grant 2.3/23 ''Ballista'').

6. APPENDIX

A. Calculation of the effective screening radius of holes with negative effective mass

In Sec. 5 we employed the parameter, λ which determines the decay of the electric field in the quasilinear NEM region and which has the physical meaning of the reciprocal of the screening radius of the electric charge. We recall that in the NEM region the charge of the acceptors is neutralized by the charge of the drifting NEM holes, so that the neutrality condition $P=n_0$ holds. Here the hole density P is given by Eq. (15), which we rewrite in the form

$$P=\frac{4\pi}{h^3}\int p_\perp dp_\perp dp_x f(x,p_x,p_\perp). \tag{A.1}$$

Let us assume that the effective anode (the anode is the hole injector) lies in the plane $x=0$. The holes entering the anode are described by the Fermi distribution

$$f(0,p_x,p_\perp)=\begin{cases}1, & \text{for } \mu>\widetilde{E}_1(p_x,p_\perp)>0,\\ & \text{and } p_x>0;\\ 0, & \text{for } \mu<\widetilde{E}_1(p_x,p_\perp)\\ & \text{or } p_x<0.\end{cases} \tag{A.2}$$

We note that the parameter μ on the effective anode is not a constant of this contact, but rather it depends on the flowing current, and the potential of the effective anode, in contrast to the potential of a metallurgical anode, varies with the current. Using Eq. (A.2) and the condition for a ballistic hole current, we write the hole distribution function for arbitrary values of x (ignoring, on the other hand, the reverse flow of holes that leave the anode) in the form

$$f(x,p_x,p_\perp)=\begin{cases}1, & \text{for } \mu-eV(x)>\widetilde{E}_1(p_x,p_\perp)>-eV(x)\\ & \text{and } p_x>0;\\ 0, & \text{for } \widetilde{E}_1(p_x,p_\perp)<-eV(x),\\ & \widetilde{E}_1(p_x,p_\perp)>-eV(x)+\mu \text{ or } p_x<0.\end{cases} \tag{A.3}$$

We introduce for prescribed values of x and $p_\perp$ the two maximum values of p_x, which are denoted as $p_x^{(1)}=p_x^{(1)}\times(p_\perp,x)$ and $p_x^{(2)}(p_\perp,x)$ and which are determined by the formulas

$$\widetilde{E}_1(p_x^{(1)},p_\perp)=-eV(x),\quad \widetilde{E}_1(p_x^{(2)},p_\perp)=-eV(x)+\mu. \tag{A.4}$$

We recall that $V(x)<0$ and that $\widetilde{E}_1(p_x,p_\perp)$ is measured from the bottom of the band $E_1(p_x,p_\perp)$; i.e., $\widetilde{E}_1(p_x,p_\perp)=E_1(p_x,p_\perp)-a\epsilon+Bk_c^2$ is the kinetic energy in the bottom subband. Using Eq. (A.3) and the definitions (A.4), we have

$$P=\frac{4\pi}{h^3}\int_0^{p_r} p_\perp dp_\perp(p_x^{(2)}-p_x^{(1)}), \tag{A.5}$$

where p_r is the highest value of $p_\perp$ determined by the condition

$$\widetilde{E}_1(0,p_r)=\mu. \tag{A.6}$$

The problem now is to obtain an explicit expression for $p_x^{(2)}-p_x^{(1)}$ and to calculate the integral in Eq. (A.5). Using Eqs. (2) and (3), we have

$$p_x^2=-p_\perp^2-2\gamma_2\,\frac{\gamma_1 p_k^2+2\gamma_2 p_c^2}{\gamma_1^2-4\gamma_2^2} +2\gamma_2\,\sqrt{\frac{(\gamma_1 p_c^2+2\gamma_2 p_k^2)^2}{(\gamma_1^2-4\gamma_2^2)^2}+\frac{3p_c^2p_\perp^2}{\gamma_1^2-4\gamma_2^2}}, \tag{A.7}$$

where $p_k^2=-p_c^2-m_0E/\gamma_2$. It is easy to verify that Eq. (A.7) is a modification of Eq. (25). Substituting in Eq. (A.7) for E the right-hand sides of Eq. (A.4), we obtain expressions for $(p_x^{(1)})^2$ and $(p_x^{(2)})^2$, respectively. Substituting these expressions into Eq. (A.5), we obtain

$$P=\frac{4\pi}{h^3p_c}\left[\frac{\gamma_1 m_0\mu}{\gamma_1^2-4\gamma_2^2}\,\frac{p_r^2}{2}+\frac{\gamma_2}{3p_0^2}\,((p_r^2p_0^2+p_2^4)^{3/2} -(p_r^2p_0^2+p_1^4)^{3/2})-\frac{\gamma_2}{3p_0^2}\,(p_2^6-p_1^6)\right], \tag{A.8}$$

where

$$p_0^2=3p_c^2/(\gamma_1^2-4\gamma_2^2),\quad p_1^4=4e^2V_1^2(x)m_0^2/(\gamma_1^2-4\gamma_2^2)^2,$$
$$p_2^4=4m_0^2[eV_1(x)+\mu]^2/(\gamma_1^2-4\gamma_2^2)^2.$$

On the right side of Eq. (A.8) we assumed that $p_c\gg p_r$ and that $E_c\gg\mu$, $V(x)=V_c-V_1(x)$, where V_c is determined by analogy with to Eq. (29): $eV_c=-E_c=-(\gamma_1+2\gamma_2)p_c^2/2m_0$. Further simplification of the right side of Eq. (A.8) gives the expression

$$P\simeq\frac{4\pi}{h^3}\,\frac{m_0\mu}{\gamma_1^2-4\gamma_2^2}\,\frac{p_r}{p_c}\left[\frac{\gamma_1 p_r}{2}+\frac{4m_0eV_1\gamma_2}{p_c\sqrt{3(\gamma_1^2-4\gamma_2^2)}}\right], \tag{A.9}$$

and from Eq. (A.6) (since $p_c\gg p_r$) we have

$$p_r^2=\frac{2m_0\mu}{\gamma_1-\gamma_2}. \tag{A.10}$$

The quasineutrality condition $P=n_0$ in the volume of the NEM region ($V_1=0$) makes it possible to calculate the value of μ, which corresponds to the value of the current density $j=j_c$ at which a stationary NEM region is formed:

$$\mu=\mu_c=\frac{h^{3/2}p_c^{1/2}n_0^{1/2}}{m_0}\left[\frac{(1-\gamma_2/\gamma_1)(\gamma_1^2-4\gamma_2^2)}{4\pi}\right]^{1/2}. \tag{A.11}$$

Substituting Eq. (A.11) into Poisson's equation (14), we obtain

$$\frac{d^2V_1}{dx^2}=\lambda^2V_1,$$

where

$$\lambda^2=\frac{e^2m_0n_0^{3/4}}{\kappa_d h^{3/4}p_c^{5/4}}\left[\frac{8\pi^{1/4}}{3^{1/2}}\,\frac{\gamma_2(\gamma_1-\gamma_2)^{1/4}}{\gamma_1^{3/4}(\gamma_1^2-4\gamma_2^2)^{3/4}}\right].$$

[1] G. L. Bir and G. E. Pikus, *Symmetry and Deformation Effects in Semiconductors* [in Russian], Nauka, Moscow, 1972.
[2] N. Z. Vagidov, Z. S. Gribnikov, and A. N. Korshak, JETP Lett. **61**, 38 (1995).
[3] N. Z. Vagidov, Z. S. Gribnikov, and A. N. Korshak, Fiz. Tekh. Poluprovodn. **29**, 1944 (1995) [Semiconductors **29**, 1014 (1995)].
[4] N. Z. Vagidov, Z. S. Gribnikov, and A. N. Korshak, in *Hot Carriers in Semiconductors*, edited by K. Hess, J.-P. Leburton, and U. Ravaioli, Plenum Press, New York, 1995.
[5] A. N. Korshak, Z. S. Gribnikov, and N. Z. Vagidov in *Ibid*., 1995.
[6] Z. S. Gribnikov, A. N. Korshak, and N. Z. Vagidov, Lithuanian J. Phys. **35**, 495 (1995); N. Z. Vagidov and V. V. Mitin, in *Proceedings of the 1995 International Semiconductor Development Research Symposium*, Charlottesville, 1995, p. 451.
[7] Z. S. Gribnikov, A. N. Korshak, and N. Z. Vagidov, J. Appl. Phys.
[8] J. M. Luttinger, Phys. Rev. **102**, 1030 (1956).
[9] M. Heiblum, K. Seo, H. P. Meier, and T. W. Hickmott, Phys. Rev. Lett. **60**, 828 (1988).
[10] Z. S. Gribnikov and A. N. Korshak, Fiz. Tekh. Poluprovodn. **288**, 1445 (1994) [Semiconductors **28**, 812 (1994)].
[11] Z. S. Gribnikov and A. N. Korshak, in *Quantum confinement. Physics and Applications*, Electrochem. Soc. Inc., San Francisco, 1994, p. 34.
[12] V. Ya. Aleshkin and Yu. A. Romanov, Zh. Éksp. Teor. Fiz. **87**, 1857 (1984) [Sov. Phys. JETP **60**, 1068 (1984)].
[13] V. Ya. Aleshkin and Yu. A. Romanov, Fiz. Tekh. Poluprovodn. **20**, 281 (1986) [Sov. Phys. Semicond. **20**, 176 (1986)].
[14] A. Dargys and A. F. Rudolph, Phys. Status Solidi B **135**, 437 (1986).
[15] A. Dargys and A. F. Rudolph, Phys. Status Solidi B **140**, 535 (1987).
[16] A. Dargys, Phys. Status Solidi B **143**, 675 (1987).
[17] J.-B. Xia, Phys. Rev. B **38**, 8365 (1988).
[18] D. Ahn and S.-L. Chuang, IEEE J. **QE-24**, 2400 (1988).
[19] S.-L. Chuang, Phys. Rev. B **40**, 10379 (1989).
[20] C. Y.-P. Chao and S.-L. Chuang, Phys. Rev. B **43**, 7027 (1991).
[21] J. M. Luttinger and W. Kohn, Phys. Rev. **97**, 869 (1955).
[22] D. A. Broido and L. J. Sham, Phys. Rev. B **31**, 888 (1985).
[23] A. Twardowski and C. Herman, Phys. Rev. B **35**, 8144 (1987).
[24] G. Schechter, L. D. Shvartsman, and J. E. Golub, Phys. Rev. B **51**, 10857 (1995).
[25] V. Ryzhiĭ, N. A. Bannov, and V. A. Fedirko, Fiz. Tekh. Poluprovodn. **18**, 769 (1984) [Sov. Phys. Semicond. **18**, 481 (1984)].

Translated by M. E. Alferieff

Trapping of hot electrons at repulsive centers under transverse runaway conditions

Z. S. Kachlishvili, Kh. Z. Kachlishvili, and F. G. Chumburidze

Tbilisi State University, 380028 Tbilisi, Georgia
(Submitted October 10, 1995; accepted for publication April 18, 1996)
Fiz. Tekh. Poluprovodn. **31**, 268–270 (February 1997)

The trapping of hot electrons at repulsive centers under transverse runaway conditions is calculated. The dependence of the trapping probability on the Sommerfeld factor and the exponential dependence of the trapping probability on the energy of the tunneled electron are taken into account. It is shown that the latter dependence plays an important role near the threshold of transverse runaway of hot electrons, while far from the threshold the Bonch–Bruevich trapping probability is a good approximation. © *1997 American Institute of Physics.* [S1063-7826(97)01302-1]

The trapping of hot electrons at negatively charged centers has been studied extensively (see, for example, Refs. 1–5). It is well known that in this case the probability of passage through the Coulomb barrier plays the main role at low temperatures. Since the most important distances in these processes are much larger than the size of a trap, the trapping probability is proportional to the Sommerfeld factor and the corresponding trapping cross section is given by the standard Bonch–Bruevich expression.[1]

However, it was shown in Ref. 6 that, besides its dependence on the Sommerfeld factor, the probability P for an electron to be trapped at a negatively charged center should depend exponentially on the energy of the tunneled electron:

$$P \sim \exp\left(-\frac{2\tau_l}{\hbar} W \right), \tag{1}$$

where W is the kinetic energy which an electron must lose on being trapped, and τ_1 is the tunneling time. The trapping coefficient in the electron-temperature approximation was also calculated in this work. It was shown that when the above-noted circumstance is taken into account, the standard concept of electron temperature is replaced by an effective electron temperature which contains the parameters of the center and is of the order of the reciprocal of the phonon energy. In the case where the electron temperature is much lower than this energy, the result obtained by Abakumo *et al.*[6] is identical to the Bonch–Bruevich result.[1] In Ref. 7, the trapping coefficient was calculated, taking into account what we have said above, for a needle-shaped, hot-electron distribution. According to the results of these calculations, the effective Bonch–Bruevich cross section is a good approximation for a highly charged trapping center, while in the opposite case the exponential factor (1) must be taken into account.

In the present paper the trapping coefficient is calculated under the conditions of transverse runaway (TR) of hot electrons. As shown in Refs. 8 and 9, in the Hall regime in strong electric and magnetic fields and for some combinations of momentum and energy dissipation mechanisms, as the average energy increases, the collision frequency of the hot electrons approaches zero and, because of a sharp increase in the internal field, the current-voltage characteristic changes abruptly, the change being of a threshold nature. For one combination of dissipation mechanisms a threshold exists only with respect to the applied electric field and for the other it exists with respect to the applied electric and magnetic fields. This effect was called transverse running away.[8] According to Refs. 8 and 9, transverse running away occurs under the following conditions:

$$t>0, \quad t+s=2,$$

$$t>0, \quad 3t+s=2.$$

Here t and s are exponents in the energy dependence of the momentum and energy mean-free paths:

$$l=l_0 x^{(1+t)/2}, \quad \tilde{l}=\tilde{l}_0 x^{(1+s)/2},$$

where $x=W/k_0T$. The values of t and s for the known dissipation mechanisms are given, for example, in Ref. 10. In the case of strong heating, when

$$\alpha x^{(t+s)/2}/(1+\eta x^t) \gg 1, \tag{2}$$

the distribution functions under transverse runaway conditions have the form

$$f_{0,1}(x)=A_1 \exp(-\eta x^t/\alpha t), \tag{3}$$

$$f_{0,2}(x)=A_2 \exp[-x/(1+\alpha)]. \tag{4}$$

Here $\alpha \equiv (E/E_0)^2$, $\eta \equiv (H/H_0)^2$, A_1 and A_2 are normalization factors, $E_0 \equiv \sqrt{3}k_0T/e(l_0\tilde{l}_0)^{1/2}$, and $H_0 \equiv (2mc^2k_0T)^{1/2}/el_0$. All other notations is standard.

It should be noted that of the known energy and momentum dissipation mechanisms, the following scattering mechanisms satisfy the condition $t>0$ and $t+s=2$ (see Ref. 10):

$t=3$, $s=-1$, i.e., for the momentum—scattering by impurity ions and for the energy—scattering by the deformation potential of the acoustic phonons (DA scattering) at both high and low temperatures;

$t=1$, $s=1$, i.e., for the momentum—scattering by dipole centers, by the piezoelectric potential of the acoustic phonons (PA scattering) in the high-temperature approximation, polarization scattering by optical phonons (PO scattering); for the energy—PA scattering in the high-temperature or low-temperature approximations or deformation scattering by optical phonons.

The following dissipation mechanisms satisfy the condition $t>0$, $3t+s=2$:

 1063-7826/97/020161-03$10.00

$t=1$, $s=-1$, i.e., for the momentum—scattering by dipole centers, PA scattering in the high-temperature approximation or PO scattering; for the energy—DA scattering in both the high- and low-temperature approximations.

Using Eqs. (1) and (3), we can write the trapping coefficient for $t>0$ and $t+s=2$, in the form

$$C_n=\frac{2\sqrt{2mt}}{\Gamma(3/2t)}\,(k_0T)^{\nu_0-1/2}\left(\frac{\alpha t}{\eta}\right)^{-3/2t}\times\int\frac{x^{\nu_0}\Psi(k_0Tx)\exp(-\eta x^t/\alpha t-\gamma_0 x)}{\exp(\gamma/x^{1/2})-1}\,dx, \tag{5}$$

where $\gamma\equiv 2\pi ze^2/\varepsilon\hbar v_0$, z is the charge of the repulsive center in units of the electron charge, ε is the permittivity of the material, v_0 is the velocity, ν_0 is a parameter of order 1, Ψ is a slowly varying function of the energy (ν_0 and Ψ are taken from the Bonch–Bruevich expression for the effective cross section[1]), $\gamma_0=2\tau_1k_0T/\hbar$, and $\Gamma(x)$ is the gamma function. The integral in Eq. (5) can be calculated by the saddle-point method, taking into account that $\gamma\gg 1$ under the conditions of interest to us. Dropping the 1 in the denominator in Eq. (5), we obtain for C_n

$$C_n=\frac{4\sqrt{\pi mt}}{\Gamma(3/2t)}\,(k_0T)^{\nu_0-1/2}\left(\frac{\alpha t}{\eta}\right)^{-3/2t}\times\gamma\,\frac{\exp[\varphi_1(x_{01})]}{\sqrt{|\varphi_1''(x_{01})|}}x_{01}^{\nu_0}\Psi(k_0Tx_{01}), \tag{6}$$

where

$$\varphi_1(x)=\gamma x^{-1/2}-\gamma_0x-\frac{\eta x^t}{\alpha t}, \tag{7}$$

and x_{01} is the solution of the equation

$$\gamma/2=x^{3/2}\left(\gamma_0+\frac{\eta}{\alpha}\,x^{t-1}\right). \tag{8}$$

Expressing the internal electric field in terms of the applied field E_x, we obtain[8]

$$\alpha=\alpha_x\Big/\left\{1-\frac{\Gamma^2[(2t+3)/2t]t}{\Gamma^2[(t+3)/2t]}\,\alpha_x\right\}, \tag{9}$$

where $\alpha_x=(E_x/E_0)^2$. Near the transverse runaway threshold

$$E_x\lesssim E_0\Gamma\left(\frac{t+3}{2t}\right)\Big/\,\Gamma\left(\frac{2t+3}{2t}\right)t$$

the condition (2) also holds well and the solution of Eq. (8) has the form $x_{01}=(\gamma/2\gamma_0)^{2/3}$. For the trapping coefficient we have

$$\frac{C_n}{C_{n1}^0}=\frac{(\alpha/\eta)^{3/2t}}{\sqrt{(t-1)\,(\eta/\alpha)\,(\gamma/2\gamma_0)^{(2t+1)/3}+\frac{3}{4}\,\gamma}}\times\exp\left[-\left(\frac{\gamma}{2\gamma_0}\right)^{2t/3}\frac{\eta}{\alpha t}\right], \tag{10}$$

where α is given by expression (9) and

$$C_{n1}^0=\frac{4\sqrt{\pi m}}{\Gamma(3/2t)}\,t^{(2t-3)/2t}(k_0T)^{\nu_0-1/2}\left(\frac{\gamma}{2\gamma_0}\right)^{(4\nu_0+5)/6}\times\Psi\left[k_0T\left(\frac{\gamma}{2\gamma_0}\right)^{2/3}\right]\exp\left[-3\left(\frac{\gamma}{2}\right)^{2/3}\gamma_0^{1/3}\right]. \tag{11}$$

Far from threshold, when the inequalities

$$\gamma_0\ll\frac{\Gamma^{t-1}(5/2t)t^{(t-1)/t}}{\Gamma^{t-1}(3/2t)}\left(\frac{\eta}{\alpha_x}\right)^{1/t}\ll 1, \tag{12}$$

$$\alpha_x\ll\left(\frac{2t+1}{2}\right)^{2t+1}\left(\frac{\gamma}{2}\right)^{2t}\eta, \tag{12a}$$

hold, the solution of Eq. (8) can be represented as $x_{02}=(\alpha\gamma/2\eta)^{2/(2t+1)}$ and the trapping coefficient has the form

$$\frac{C_n}{C_{n2}^0}=\left(\frac{\alpha}{\eta}\right)^{\frac{(4\nu_0t-t-3)}{2t(2t+1)}}\Psi(k_0Tx_{02})\exp\left\{-\left(\frac{\gamma}{2}\right)^{\frac{2}{(2t+1)}}\left(\frac{\alpha}{\eta}\right)^{\frac{2t}{(2t+1)}}\times\left[\gamma_0+\left(\frac{\alpha}{\eta}\right)^{\frac{-3}{(2t+1)}}\left(\frac{\gamma}{2}\right)^{\frac{2(t-1)}{(2t+1)}}\frac{2t+1}{2t}\right]\right\}. \tag{13}$$

Here

$$C_{n2}^0=\frac{4}{\Gamma(3/2t)}\left(\frac{2\pi m}{2t+1}\right)^{1/2}\left(\frac{\gamma}{2}\right)^{\frac{(2\nu_0+2-t)}{2t+1}}, \tag{14}$$

$$\alpha\simeq\alpha_x\left[1+\alpha_xt\Gamma^2\left(\frac{2t+3}{2t}\right)\Big/\,\Gamma^2\left(\frac{t+3}{2t}\right)\right]. \tag{14a}$$

We note that the inequalities (12) and (12a) can always be made compatible by varying the field and taking into account the large value of the numerical coefficient $[(2t+1)/2]^{2t+1}(\gamma/2)^{2t}$.

If $\gamma_0=0$, the expression (13) is identical to the expression obtained in Ref. 5 using the effective Bonch–Bruevich cross section.[1]

In the case $t>0$ and $3t+s=2$, using the saddle-point method, we obtain for the trapping coefficient

$$\frac{C_n}{C_{n3}^0}=(1+\alpha)^{-3/2}\left(\frac{1+\alpha}{1+(1+\alpha)\gamma_0}\right)^{(4\nu_0+s)/3}\Psi(k_0Tx_{03})\times\exp\left\{-3\left(\frac{\gamma}{2}\right)^{2/3}\left[\frac{1+\gamma_0(1+\alpha)}{1+\alpha}\right]^{-1/3}\right\}. \tag{15}$$

Here

$$C_{n3}^0=8\left(\frac{2m}{3}\right)^{1/2}(k_0T)^{\nu_0-1/2}\left(\frac{\gamma}{2}\right)^{(2\nu_0+1)/3}, \tag{15a}$$

$$L=L_x\left[1+2.76\left(\frac{H}{H_0}\right)^2\right]\left[1-2.76\left(\frac{H}{H_0}\right)^2\alpha_x\right]^{-1}, \tag{16}$$

$$x_{03}=\left(\frac{\gamma}{2}\right)^{2/3}\left(\frac{1+\alpha}{1+(1+\alpha)\gamma_0}\right)^{2/3}. \quad (17)$$

As in the first case, near the threshold of transverse runaway of hot electrons, the exponential factor (1) in the effective trapping cross section plays an important role, while far from the runaway threshold the effective Bonch–Bruevich cross section is a good approximation.

[1] V. L. Bonch-Bruevich, Fiz. Tverd. Tela (Leningrad) **6**, 2047 (1964) [Sov. Phys. Solid State **6**, 1615 (1964)].
[2] V. L. Bonch-Bruevich and S. G. Kalashnikov, Fiz. Tverd. Tela (Leningrad) **7**, 750 (1965) [Sov. Phys. Solid State **7**, 599 (1965)].
[3] V. L. Bonch-Bruevich and Z. S. Kachlishvili, Vestn. MGU. Ser. 3, Fizika, astronimiya, No. 5, 580 (1974).
[4] Kh. Z. Kachlishvili and A. G. Mironov, Tr. TGU **291**, 37 (1989).
[5] D. P. Bkhattachariya and Z. S. Kachlishvili, Fiz. Tverd. Tela (Leningrad) **19**, 2117 (1977) [Sov. Phys. Solid State **19**, 1238 (1977)].
[6] V. M. Abakumov, V. Karpus, V. I. Perel', and I. N. Yassievich, Fiz. Tekh. Poluprovodn. **22**, 262 (1988) [Sov. Phys. Semicond. **22**, 159 (1988)].
[7] Kh. Z. Kachlishvili and Z. S. Kachlishvili, Solid State Commun.
[8] Z. S. Kachlishvili, Zh. Éksp. Teor. Fiz. **78**, 1955 (1980) [Sov. Phys. JETP **51**, 982 (1980)].
[9] Z. S. Kachlishvili and F. G. Chumburidze, Zh. Éksp. Teor. Fiz. **87**, 1834 (1984) [Sov. Phys. JETP **60**, 1055 (1984)].
[10] Z. S. Kachlishvili, Phys. Status Solidi A **33**, 15 (1976).

Translated by M. E. Alferieff

Characteristic features of electron photoemission from the metal in SiC-based Schottky diodes

L. A. Kosyachenko, V. M. Sklyarchuk, and E. F. Sklyarchuk

Chernovtsy State University, 274012 Chernovtsy, Ukraine
(Submitted October 24, 1995; accepted for publication April 18, 1996)
Fiz. Tekh. Poluprovodn. **31**, 271–276 (February 1997)

The photosensitivity of an Al–SiC Schottky diode in the range of photon energies less than the band gap of the semiconductor and the height of the potential barrier at the contact with the metal has been investigated. The observed characteristic features of the photon energy and applied voltage dependences of the photocurrent are interpreted in a model that takes into account the photoexcitation of electrons in the metal and their subsequent above-barrier passage and tunneling into the semiconductors. © *1997 American Institute of Physics.*
[S1063-7826(97)01402-6]

1. INTRODUCTION

The photosensitivity of a Schottky diode is determined mainly by electron–hole pair production in the space-charge region as well as in the adjoining semiconductor layer by photons whose energy $h\nu$ is greater than the band gap E_g in the semiconductor. However, in contrast to a p–n junction, charge carriers excited in the metal by photons also participate in the formation of the photocurrent in the Schottky diode. Photoemission from the metal extends the photosensitivity into the long-wavelength region, and its spectral dependence is often used to find the height of the potential barrier at the metal–semiconductor contact.[1] In what follows, the properties of Al–SiC diodes that reveal a number of characteristic features of the electron photoemission from the metal ($h\nu < E_g$) are described and a theoretical interpretation of these features is presented.

2. SAMPLES

Single-crystalline wafers of n-type SiC–6H, doped with nitrogen up to uncompensated donor density $N_d - N_a = 10^{17} - 10^{19}$ cm^{-3}, were used to prepare the photodiode structures. After mechanical grinding and polishing, the wafers were chemically etched in molten KOH:KNO_3 for 30 min at 850–900 °C. Next, the wafers were washed in deionized water using ultrasound. Aluminum, which was deposited in vacuum (10^{-6} Torr) at a substrate temperature of the order of 450 °C, was employed as the metal for preparing the Schottky barrier. Electron-beam evaporation from a water-cooled copper crucible was used to deposit a 10 to 15-μm-thick Al layer. An important stage in obtaining these samples was vacuum annealing of the Al–SiC structures at a temperature of the order of 900 °C for 10–20 s. An ohmic contact to the substrate was produced by vacuum sputtering of Al followed by brazing it to the substrate with short pulses from a solid-state laser ($\lambda = 1.06$ μm). With sufficiently strong reverse biases, white-blue luminescence is observed over the entire area of the rectifying Al–SiC contact. Diodes for which brighter spots (microplasmas) were observed against the background of uniform luminescence were not used for these investigations.

Analysis of the electrical properties of the diodes shows that the influence of the intermediate layer (between the metal and the semiconductor) is negligible.[2] With sufficiently high forward biases the current-voltage characteristic is determined by above-barrier transmission of electrons from the conduction band of the semiconductor into the metal [for high currents the dependence of the current I on the voltage U deviates from the law $I \sim \exp(eU/kT)$ because of the voltage drop across the serial resistance of the crystal]. For low U, when the thermionic current is weak, the forward current is determined by tunneling of electrons from the conduction band of the semiconductor into the metal through the barrier.[2] Tunneling also determines the reverse current through the diode, even at the lowest voltages U. Furthemore, for strong reverse biases an additional increase of the current as a result of carrier multiplication in the barrier region of the structure is observed; this is indicated by photoelectric measurements (see below). Naturally, the reverse currents, just as the forward currents with low U, are lower when SiC with lower values of $N_d - N_a$ is used.

The height φ_0 of the potential barrier of the experimental diodes, which was found from capacitive measurements, increases from 1.75 to 1.85 eV as a result of a displacement of the Fermi level into the volume of the semiconductor as the doping level of the SiC wafer increases. We note that an appreciably greater barrier height, as compared with the results of Ref. 2 (where $\varphi_0 = 1.3$ eV), is achieved as a result of the described technology for obtaining rectifying contacts, especially, etching of SiC wafers in molten KOH:KNO_3 and vacuum annealing of the Al–SiC structures.

The uniform prebreakdown luminescence, which is observed over the entire area of the Al contact, and the high rectification coefficient (10^4–10^5 at 2 eV) attest to the high quality of the diode structures.

3. PHOTOELECTRIC MEASUREMENTS

The excitation of a photocurrent I_p in the experimental structures with a nontransparent Al layer is possible under illumination only from the substrate side. For a substrate thickness of the order of 400 μm, photons with energy $h\nu$ greater than the band gap in the semiconductor $E_g \simeq 3$ eV do

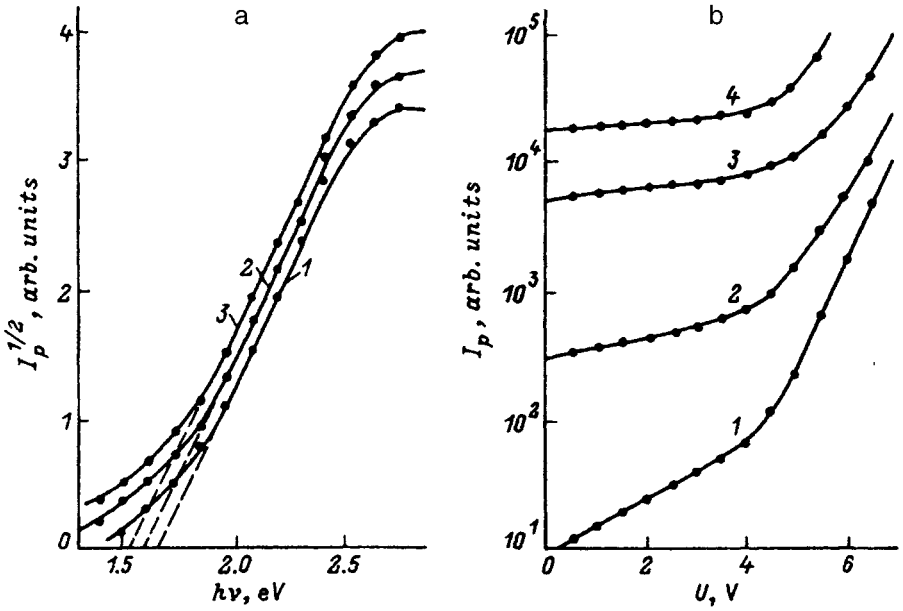

FIG. 1. Curves of the photocurrent of the Al–SiC diode ($N_d-N_a=5\times10^{17}$ cm^{-3}) in the region $h\nu<E_g$ at room temperature: a — versus photon energy $h\nu$ with reverse bias U,V: *1* — 0.45, *2* — 1.45, *3* — 2; b — versus the reverse voltage U with photon energy $h\nu$, eV: *1* — 1.5, *2* — 1.8, *3* — 2.2, *4* — 2.8.

not reach the barrier region, so that the diodes are photosensitive only in the spectral region $h\nu<E_g$, which corresponds to electron photoemission from the metal. According to Fowler's theory[7] applied to a metal–semiconductor contact,[1] in the region $\varphi_0+\Delta\mu<h\nu<E_g$ ($\Delta\mu$ is the distance of the Fermi energy from the bottom of the conduction band in the volume of the semiconductor)

$$I_p\sim[h\nu-(\varphi_0+\Delta\mu)]^2, \tag{1}$$

which makes it possible to identify immediately the mechanism of the observed photocurrent and to find φ_0 by constructing the curve of $\sqrt{I_p}$ versus $h\nu$. The results of such a construction for one diode are illustrated in Fig. 1a. As one can see, the curves measured for different reverse biases contain rectilinear sections, where I_p changes by approximately an order of magnitude. For $h\nu>2.5$ eV the observed deviation from straight lines is explained by the decrease in the optical transmission of the substrate, through which the rectifying Al–SiC contact is illuminated. Indeed, our measurements show that the transmission of Al-doped SiC–6*H* starts to decrease at $h\nu\simeq2.5$ eV as the absorption edge is approached and drops to zero for $h\nu>E_g=2.96$ eV. A more important feature of the results shown in Fig. 1a is that the spectral variation of the photocurrent depends on the voltage applied to the diode. Extrapolation of the linear curves $\sqrt{I_p}$ versus $h\nu$ to the photon energy axis gives a value of $\varphi_0+\Delta\mu$ close to the barrier height obtained from capacitive measurements, but only if the dependence $I_p(h\nu)$ is measured with the minimum values of U. As U is increased, the photoelectric measurements give increasingly underestimated values of the barrier height. Another feature which we discovered is that the photodiode is photosensitive in the region of $h\nu$ appreciably below $\varphi_0+\Delta\mu$, down to 1.4–1.5 eV. This region does not fit into the Fowler theory, in accordance with which I_p decreases rapidly ($\sim\exp(h\nu/kT)$) for $h\nu<\varphi_0+\Delta\mu$.

Curves of I_p versus the reverse voltage U are shown in Fig. 1b for different values of the energy of the exciting photons. A section of relatively slow change of the current, which is replaced by a section with a sharp increase in current above some value of U, is present on all curves for low values of U. The latter feature is due to the impact ionization of the atoms of the crystal lattice by charge carriers accelerated by a strong electric field in the space-charge region (see, for example, Ref. 2). The associated photocurrent multiplication will not be studied below. The curves $I_p(U)$ with $U=4-5$ V presented in Fig. 1b reflect the behavior of the current due to the electron photoemission from the metal into the barrier region of the semiconductor (in all cases $h\nu<E_g$). According to the diode theory of charge transport in the barrier region, the current does not depend on U, and it should increase as $\sqrt{\varphi_0-eU}$ only for the diffusion mechanism.[4] As one can see from Fig. 1b, the behavior of the photocurrent for low biases is more complicated: The current increases with the voltage more rapid than $I_p\sim\sqrt{\varphi_0-eU}$, and the growth rate depends on the energy of the exciting photons. For example, for $h\nu=1.5$ eV, as U increases from 0 to 5 V, the current increases approximately by an order of magnitude, while $\sqrt{\varphi_0-eU}$ increases by only a factor of 1.9.

Another feature of photoemission in the diode studied by us concerns the temperature dependences of the photocurrent. In contradistinction to Fowler's theory, which assumes that photoemission is insensitive to a change in temperature, the measured currents grow appreciably with increasing temperature. The temperature dependence intensifies as $h\nu$ decreases, especially in the region $h\nu<\varphi_0$. Under otherwise the same conditions, the dependence of I_p on T increases with decreasing voltage at which the spectrum is measured.

4. INTERPRETATION OF THE RESULTS

A distinguishing feature of our experimental diodes is the high doping level of SiC, as a result of which the barrier

region at the contact with the metal is narrow and the intensity of the electric field there is high. For $N_d-N_a=10^{18}$ cm^{-3}, $\varepsilon=10.2$, $\varphi_0=1.8$ eV, and a reverse bias of 1 V the width of the barrier region is $d=[2\varepsilon\varepsilon_0(\varphi_0-eU)/e^2(N_d-N_a)]^{1/2}\simeq 5\times10^{-6}$ cm, and the intensity of the field in the semiconductor near the interface is $F_{\max}=2(\varphi_0-eU)/ed\simeq10^6$ V/cm. In discussing charge transport under such conditions, we take into account the action of two factors — lowering of the barrier height by the mirror image force (Schottky effect) and tunneling processes.

We start the quantitative description of the effect of these factors with the expression for the decrease of the barrier by the mirror image force[1] $\Delta\varphi=e(eF/4\varepsilon\varepsilon_0)^{1/2}$. Substituting for F the expression for the maximum intensity of the electric field in the barrier, we obtain

$$\Delta\varphi=\beta(\varphi_0-eU)^{1/4}, \tag{2}$$

where $\beta=e^{3/2}(N_d-N_a)^{1/4}/\pi^{1/2}(2\varepsilon\varepsilon_0)^{3/4}$. Substituting $N_d-N_a=10^{18}$ cm^{-3} gives $\beta=0.1$ (eV)$^{3/4}$. This means that as U increases from 0 to 5 V, the barrier decreases approximately by 0.13 eV. For $N_d-N_a=10^{19}$ and 10^{17} cm^{-3} the barrier $\Delta\varphi$ correspondingly increases or decreases approximately by a factor of 1.8. Such changes in the barrier height are comparable to a shift in φ_0, which follows from Fig. 1a.

In studying electron photoemission from a metal into the semiconductor, it is convenient to measure the electron energy from the Fermi level in the metal. In this reference system, the probability of finding in the metal an electron with energy components E_x, E_y, E_z is

$$f(E_x,E_y,E_z)=\{\exp[(E_x+E_y+E_z)/kT]+1\}^{-1}. \tag{3}$$

For an electron to pass through a barrier oriented in the yz plane, the x component of the energy is important, and the y and z components can be arbitrary. After integrating the expression (3) over E_y and E_z from 0 to ∞, we obtain the following expression for the number of electrons with energy $E=E_x$ which are approaching the barrier:[5]

$$n(E)=(mkT/2\pi^2\hbar^3)\ln[1+\exp(-E/kT)]. \tag{4}$$

Integrating $n(E)$ over E from $\varphi_0+\Delta\mu-\Delta\varphi$ to ∞, it is easy to obtain the standard formula for the density of the reverse thermionic emission current through the Schottky diode {in this case $\ln[1+\exp(-E/kT)]\simeq\exp(-E/kT)$}. To calculate the above-barrier photoemission current, it is necessary to take into account in Eq. (4) the fact that an electron with energy E, which passes through the barrier, has energy $E-h\nu$ upon absorbing a photon. Furthermore, it is necessary to introduce coefficients which take into account the reflection of light at the interface, the absorption depth of the photons in the metal, and other factors. However, the effects considered here correspond to a narrow spectral interval, so that it can be assumed that these coefficients are virtually independent of $h\nu$. Therefore, we can write the following expression for the above-barrier photoemission current:

$$I_{p0}=I_0\int_{\varphi_0+\Delta\mu-\Delta\varphi}^{\infty} n(E-h\nu)dE, \tag{5}$$

where I_0 is a constant. For $h\nu$ exceeding the barrier height by several kT, the integration region $E<h\nu$ makes the main contribution in calculating I_{p0}. In this case $\ln\{1+\exp[(h\nu-E)/kT]\}\simeq(h\nu-E)/kT$ and, ignoring the participation of electrons with energy above the Fermi energy, the upper limit of integration can be set equal to $h\nu$. As a result,

$$I_{p0}=(I_0m/2\pi^2\hbar^3)\int_{\varphi_0+\Delta\mu-\Delta\varphi}^{h\nu}(h\nu-E)dE$$
$$=(I_0m/4\pi^2\hbar^3)[h\nu-(\varphi_0+\Delta\mu-\Delta\varphi)]^2. \tag{6}$$

In other words, we obtain Fowler's formula (1), which contains a weak dependence of I_{p0} on U (in terms of $\Delta\varphi$). The results of an exact calculation using Eq. (5) with the same values of the photon energy as in Fig. 1b are presented in Fig. 2. One can see from Fig. 2 that the present model results in behavior which resembles the experimental dependences, but only with respect to the general features. For $h\nu>\varphi_0+\Delta\mu-\Delta\varphi$ the computed photocurrent is virtually independent of U, while the measured photocurrent increases by a factor of 1.5–2 as U increases from 0 to 5 V. Conversely, for $h\nu<\varphi_0+\Delta\mu-\Delta\varphi$ the computed dependence of I_{p0} on U becomes stronger and for fixed U the computed current decreases much more rapidly than the experimentally measured current as $h\nu$ decreases (by six orders of magnitude instead of three as $h\nu$ decreases from 2.8 to 1.5 eV). We note that the only adjustable parameter in calculating I_{p0} is the quantity ε, which can differ from the static permittivity of the semiconductor. However, its effective value, which is manifested in the Schottky effect, can be only smaller than the static permittivity.[1] Taking this fact into account would give an even larger discrepancy between the computational and experimental results.

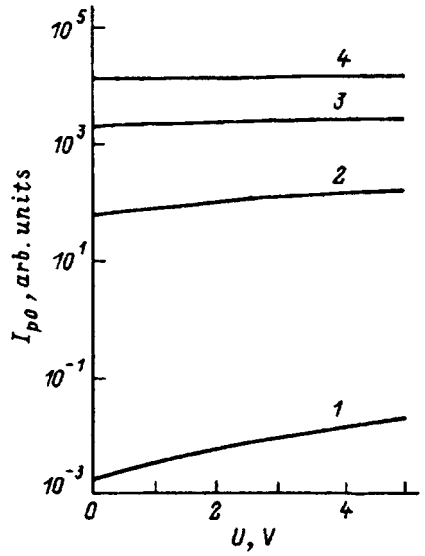

FIG. 2. Computed curves of the above-barrier photoemission current taking account of the mirror image force with exciting photon energies $h\nu$, eV: *1* — 1.5, *2* — 1.8, *3* — 2.2, *4* — 2.8. Room temperature.

We now give a quantitative description of electron photoemission from the metal with participation of tunneling. For an electron with energy E_0, which moves along the x direction, the tunneling transmission coefficient is

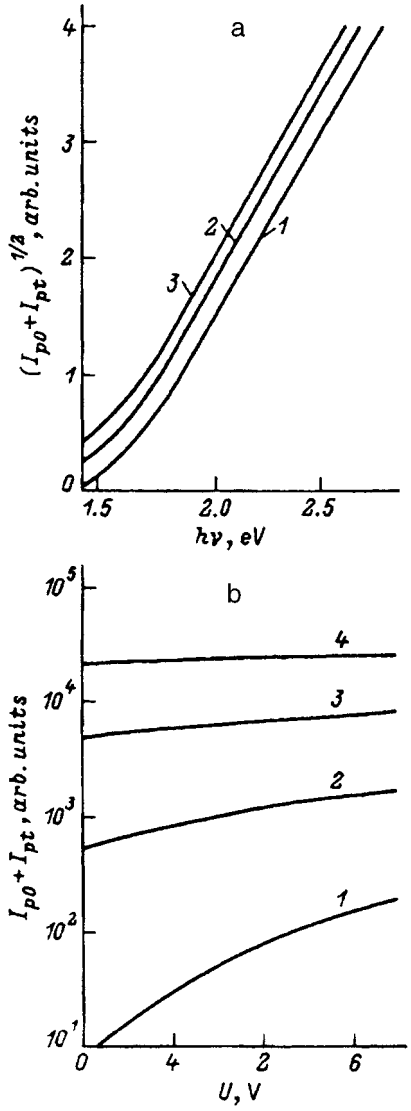

FIG. 3. Computed curves of the sum of the above-barrier and tunneling photocurrents $I_{p0}+I_{pt}$ taking account of the mirror image force under the same conditions as in Fig. 1.

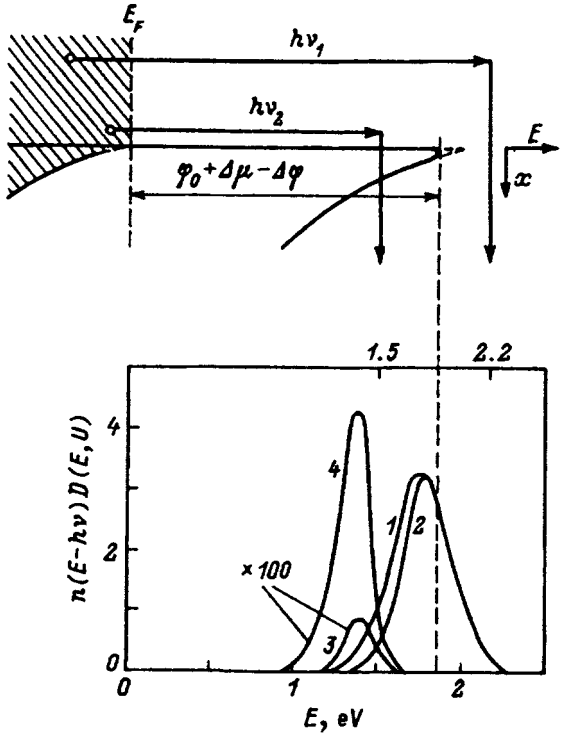

FIG. 4. Energy diagram of an Al–SiC contact, illustrating photoemission from the metal with subbarrier electron transmission into the semiconductor ($h\nu_1=1.5$ eV) and with the participation of tunneling ($h\nu_2=2.2$ eV). Bottom: Computed distribution of electrons emitted from the metal into the semiconductor. The electrons absorbed photons with energy $h\nu_1$ (curves *3*, *4*) and $h\nu_2$ (curves *1*, *2*) with reverse voltage U,V: *2*, *3* — 1, *1*, *4* — 3. The position of the Fermi level in the metal corresponds to $E=0$; for above-barrier photoemission $D(E,\ U)=1$. Room temperature.

$$D(E_0,\ U)=\exp\left[-2\sqrt{2m}/\hbar\int_{x_1}^{x_2}\sqrt{\varphi(x)-E_0}\,dx\right], \quad (7)$$

where x_1 and x_2 are the turning points, and $\varphi(x)$ is the variation of the potential in the barrier; the remaining notation is standard. If the energy is measured, just as $\varphi(x)$, from the bottom of the conduction band in the volume of the semiconductor and x is measured from the interface,[2] we have

$$\varphi(x)=(\varphi_0-\Delta\varphi-eU)(1-x/d)^2. \quad (8)$$

In this case $x_1=0$ and x_2 is determined by the equality $\varphi(x)-E_0=0$. After integration, it follows[2] from Eq. (7) that

$$D(E_0,U)=\exp[-(\sqrt{2m}\ d_1/\hbar)([\varphi_0-\Delta\varphi-eU)(\varphi_0-\Delta\varphi-E_0)]^{1/2}+E_0\ \ln\{\sqrt{E_0}/[(\varphi_0-\Delta\varphi-eU)^{1/2}+(\varphi_0-\Delta\varphi-eU-E_0)^{1/2}]\})], \quad (9)$$

where $d_1=[2\varepsilon\varepsilon_0/e^2(N_d-N_a)]^{1/2}$. If the energy E is measured not from the bottom of the conduction band of the semiconductor but from the Fermi level in the metal [as in Eqs. (3)–(6)], we obtain an expression for $D(E,\ U)$ by replacing in Eq. (9) E_0 by $E-\Delta\mu-eU$. Integrating the product $n(E)D(E,U)$, we obtain for large reverse biases ($|\varphi_0-eU|\gg\varphi_0$) an analytic expression for the current[6] which is similar to the Fowler–Nordheim formula.[7] Expression (9) for $D(E_0,\ U)$ and the corresponding expression for $D(E,U)$ are good in that they are applicable not only for large voltages but also for the actual voltages, which in this case are low voltages.

To calculate the photoemission current I_{pt} associated with tunneling, it is necessary, just as in calculating the above-barrier photoemission current I_{p0}, to replace in the expression for the number of electrons approaching the barrier E by $E-h\nu$ and to introduce the coefficient I_0:

$$I_{pt}=I_0\int_{E_{\min}}^{\varphi_0+\Delta\mu-\Delta\varphi}n(E-h\nu)D(E,U)dE. \quad (10)$$

The lower limit of integration $E_{\min}$ must be such that it would encompass the entire tunneling region. In practice, it is sufficient to set $E_{\min}$ at a value equal to several tenths of an electron-volt lower than either the upper limit of integration if $h\nu>\varphi_0+\Delta\mu-\Delta\varphi$ or slightly lower than $h\nu$ if $h\nu<\varphi_0+\Delta\mu-\Delta\varphi$.

According to the model employed by us, the electron photoemission current from the metal is a sum of the above-

barrier current I_{p0} and the tunneling current I_{pt}. The results of a computer calculation according to Eqs. (5) and (10) of the photosensitivity spectra in the Fowler coordinates are presented in Fig. 3 for different voltages, together with curves of the photocurrent versus the voltage for different exciting photon energies (of course, the curves do not take into account the effect of absorption of light in the substrate and avalanche processes). Comparing the results obtained by us with those presented in Fig. 1 shows that the proposed model satisfactorily describes the experimental data.

The processes occuring in the diodes invesetigated are explained and the energy distribution of the electrons emitted from the metal into the semiconductor is illustrated with the aid of Fig. 4; the latter distribution is described by the function $n(E-h\nu)$ for above-barrier photoemission and by the function $n(E-h\nu)D(E,\ U)$ for tunneling photoemission. We see from the figure that for 2.2-eV photons, i.e., for $h\nu>\varphi_0-\Delta\varphi+\Delta\mu$, only a small part of the photoexcited electrons penetrates into the semiconductor above the barrier and most electrons tunnel through the barrier; in addition, as the voltage increases, the fraction of tunneling electrons increases appreciably. If the photon energy is 1.5 eV, i.e., $h\nu<\varphi_0-\Delta\varphi+\Delta\mu$, virtually all electrons excited by the light enter the semiconductor by tunneling through the barrier. As the voltage increases, the tunneling region shifts in the direction of lower electron energies, and the electron flux from the metal increases sharply. Therefore, it follows clearly from Fig. 4 that tunneling can explain the observed features of electron photoemission from the metal in the experimental diodes. To achieve quantitative agreement between the computational and experimental results, it is necessary to take into account the lowering of the barrier by the mirror image forces.

5. CONCLUSIONS

Study of the photoelectric properties of Al–SiC Schottky diodes reveals characteristic features of electron photoemission from the metal (in the region $h\nu<E_g$) that do not fit into the standard idealized model. Allowance for the lowering of the barrier by the mirror image force gives dependences of the photocurrent on the photon energy and voltage that are quantitatively different from the experimentally observed dependences and makes it impossible to explain the photosensitivity of a diode for photon energies below the barrier height. The quantitative and qualitative agreement between theory and experiment can be achieved by using a combined photoemission mechanism, which includes, in addition to the above-barrier photoemission, photoabsorption of photons by electrons in the metal and subsequent tunneling of the electrons into the conduction band of the semiconductor.

We wish to thank V. V. Guts for assistance in the preparation of this paper.

[1] S. Sze, *Physics of Semiconductor Devices*, Wiley, N. Y., 1981, 2nd edition [Russian translation, Mir, Moscow, 1984].
[2] L. A. Kosyachenko, N. M. Pan'kiv, A. V. Pivorar, and V. M. Sklyarchuk, Ukr. Fiz. Zh. **27**, 101 (1982).
[3] R. H. Fowler, Phys. Rev. **38**, 45 (1931).
[4] G. E. Pikus, *Theory of Semiconductor Devices* [in Russian], Nauka, Moscow, 1965.
[5] R. J. Archer and T. O. Yep, J. Appl. Phys. **41**, 303 (1970).
[6] I. S. Kabanova, L. A. Kosyachenko, and V. P. Mikhniĭ, Fiz. Tekh. Poluprovodn. **21**, 2087 (1987) [Sov. Phys. Semicond. **21**, 1265 (1987)].
[7] R. H. Fowler and L. Nordheim, Proc. Roy. Soc. A **119**, 173 (1928).

Translated by M. E. Alferieff

Breakdown electroluminescence spectra of silicon carbide p–n junctions

M. V. Belous, A. M. Genkin, V. K. Genkina, and O. A. Guseva

Kiev Polytechnical Institute, Ukrainian National Academy of Sciences, 252056 Kiev, Ukraine
(Submitted October 17, 1995; accepted for publication April 23, 1996)
Fiz. Tekh. Poluprovodn. **31**, 277–280 (February 1997)

The breakdown electroluminescence spectra of p–n junctions with uniform and microplasma breakdown, which were prepared on SiC–3*C* crystals, have been investigated. A distinct periodic structure of an oscillatory nature with oscillation periods of 0.1–0.5 eV was observed in the room-temperature emission spectra of individual microplasmas. The amplitude of the bands increases with the period, and at maximum period it exceeds the amplitude of the background radiation. A similar structure was also observed in the spectra of individual microplasmas on SiC–6*H*. It is assumed that the structure is due to the action of a strong electric field in the region of radiation formation. © *1997 American Institute of Physics.* [S1063-7826(97)01502-0]

The breakdown electroluminescence of silicon carbide p–n junctions has been under investigation for many years because of its possible applications in the production of highly stable wideband emitters. Attempts have been made to explain the spectral features of the radiation,[1–3] but there is sitill no general agreement about the mechanism of the breakdown radiation. Among other reasons, this is apparently due to the lack of reliably established parameters of the band structure for the most common polytypes of silicon carbide (SiC–6*H*, 15*R*). At the same time, in view of its simpler crystal structure, the band structure parameters of the less common cubic modification SiC–3*C* have been determined much more reliably, and this has already made it possible to interpret one of the breakdown electroluminescence bands.[1] It is of special interest in this connection to investigate SiC–3*C* in order to determine the breakdown electroluminescence mechanisms in silicon carbide.

In the present paper we present the results of an experimental study of the breakdown electroluminescence spectra of uniform and microplasma breakdown in SiC–3*C* based structures and of the new phenomena, which have also been observed in SiC–6*H*, and which were discovered in the process.

We investigated p–n junctions prepared by alloying Silumin in the *B* face of SiC–3*C* crystals grown by the method of thermal decomposition of methyltrichlorosilane and doped with nitrogen during the growth process. The p–n junctions possessed an area of the order of 10^{-2} cm^2. Samples with breakdown voltages of 6–30 V were chosen.

Microplasma breakdown was observed in most p–n junctions, but in a several samples, as the current increased, the entire area of the p–n junctions was filled with luminescence, which, when observed under microscope with a magnification of about 100, looked to be completely uniform. Some samples emitted uniformly with no microplasmas.

Investigation of the emission from samples with microplasma breakdown revealed that, in addition to the properties described in the literature, the spectra are also characterized by other features. To study these features, it was necessary to separate the radiation from small sections of the p–n junction (with dimensions of less than 50 μm), which contained a single microplasma or a region of uniform luminescence. Accordingly, we covered the entire crystal, except the measuring section, with light-absorbing paint.

A high-power EMR-3 monochromator was used to record the spectra of weak radiation fluxes (with integrated power 10^{-10}–10^{-9} W) from the experimental samples. The detector consisted of a specially selected FÉU-79 photomultiplier, employed in the single-electron mode. To ensure maximum sensitivity with adequate spectral resolution, the sample being measured was placed directly in the plane of the input slit of the monochromator. The statistical error in signal detection within the working photon energy range (1.8–4.0 eV) did not exceed 1% at the ends of the spectrum and 0.5% at the center of the spectrum; the confidence probability was equal to 0.99. The instability of the sensitivity of the photodetecting channel did not exceed 1% per hour. The signal strength was measured with a step of 0.02 eV.

The typical emission spectra of p–n junctions with uniform luminescence, which differed in the magnitude of the working voltage of the sample, and in the excitation level and which were measured at room temperature, are presented in Fig. 1. As one can see from the figure, the spectrum of

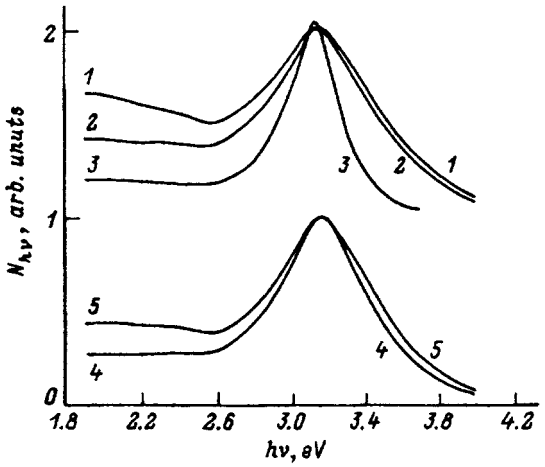

FIG. 1. Breakdown electroluminescence spectra of SiC–3*C* p–n junctions with uniform luminescence. Samples: *1*—(3), *2*—(16–2), *3*—(9), *4,5*—(16–1). Powering regime: *1*—30 mA, 30 V; *2*—100 mA, 9.6 V; *3*—100 mA, 8,3 V; *4*—15 mA, 8.25 V; *5*—60 mA, 10 V.

samples exhibiting uniform breakdown electroluminescence contains a band with a maximum near 3.1 eV against the background of the wideband radiation.

The wideband background is very weakly expressed in the spectra of the low-voltage p–n junctions with a breakdown voltage of less than 10 V. This contrasts with p–n junctions whose breakdown voltage exceeds 20 V, for which the wideband background makes the main contribution to the radiation. The fraction of the wideband background also increases as the excitation level increases. It was established that the dependence of the form of the spectrum on the excitation level is much stronger in samples with low-voltage breakdown.

The standard interpretation of the 3.1-eV band as radiation associated with direct transitions of hot electrons in the conduction band ($X_{3c}-X_{1c}$) (Ref. 1) is consistent with the latest data on the energy band structure of SiC–3C.[4,5] Detailed analysis of the form of the spectrum, taking into account the different types of electronic transitions (performed, for example, for Si (Ref. 6), is impossible at present, because the quantitative parameters of the band structure of SiC–3C have not been reliably determined. However, there is virtually no doubt that the radiation in the 3.1-eV band is related to electronic transitions. In this connection, an important difference in the behavior of the 3.1-eV band and the wideband background accompanying a change in the excitation conditions of the breakdown electroluminescence suggests that hole transitions participate in the formation of the wideband radiation. A good correlation is observed between the fraction of the wideband radiation and the probable changes in the number of free holes in the region of the p–n junction. Similar behavior has been described in Refs. 2 and 3.

A distinct structure, of an oscillatory nature, with the oscillations superimposed on the standard spectrum, has been observed in the room-temperature spectra of some p–n junctions with microplasma breakdown. These junctions are characterized by comparatively low working voltages (in most cases less than 18 V). The amplitude and energy position of the oscillations differs substantially from sample to sample. The indicated structure is virtually independent of the temperature of the sample in the range 77–400 K. The ratio of the bands changes in a complicated manner as the excitation level changes. An attempt to determine the emission regions of the p–n junction which are responsible for structure manifestation led to the need to separate small sections of the junction on which, according to a visual assessment, radiation of one luminescing ''dot'' was present (we call such an object an individual microplasma). The spectra of such sections have a very simple shape.

A series of typical room-temperature spectra of individual microplasmas is shown in Fig. 2a. Differentiation of the spectra with a step of 0.02 eV was performed for additional analysis of the oscillatory structure. The relative magnitude of the change in the spectral density of the radiation was determined for each photon energy. The corresponding curves are presented in Fig. 2b.

As one can see from the figures, the bands of the oscillatory structure cover virtually the entire spectral range, they have an almost uniform energy spacing, and the period of the

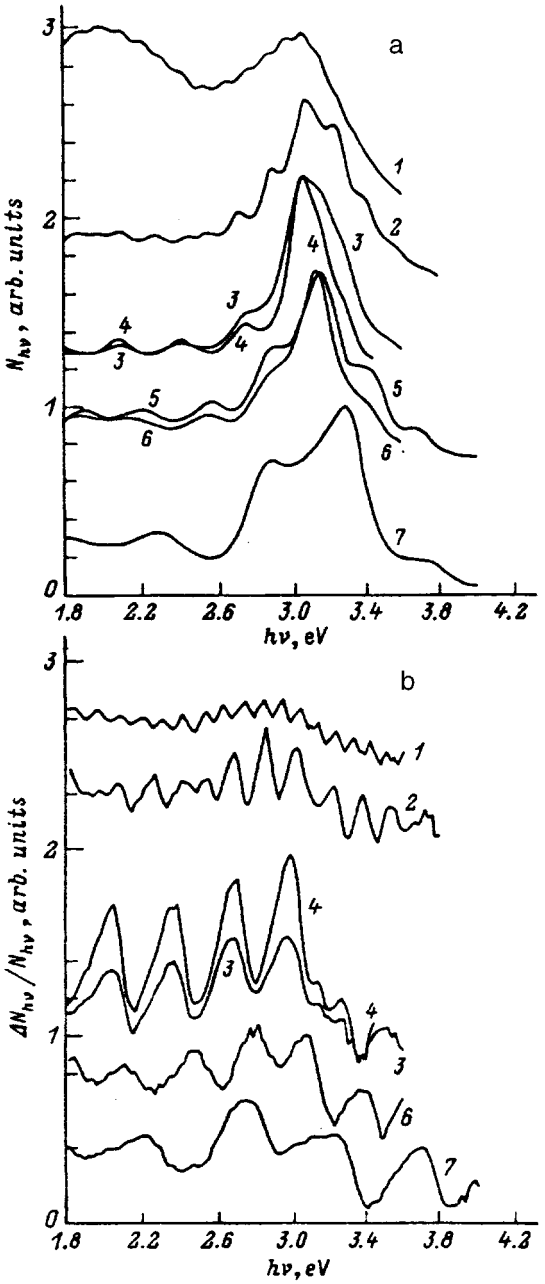

FIG. 2. Emission spectra of individual microplasmas in SiC–3C p–n junctions (a) and differentiated spectra (b). Samples: *1*—(135–1), *2*—(135–2), *3*, *4*—(11–4), *5*, *6*—(11–10), *7*—(11–6). Voltage on a sample, V: *1*, *2*—18, *3*—11.83, *4*—6.64, *5*, *6*—14.3, *7*—18. Operating time of a sample, h: *5*—0, *6*—8.

structure is substantially different (0.1–0.5 eV) in different microplasmas. The amplitude of the oscillations with respect to the background radiation is approximately the same in all sections of the spectrum. A correlation is observed between the period and the average amplitude of the bands. This correlation increases markedly as the amplitude of the bands increases. The radiation spectra with a large period of oscillations always have the 3.1-eV band as the dominant contribution against the background of the weak wideband radiation.

No definite correlation between the period of the structure and the working voltage of the p–n junction was found.

For example, the spectra of microplasmas present on one $p-n$ junction with the powering regime are presented in Fig. 2 (curves *1* and *2*). However, it was noted that structure with the maximum period and amplitude is most likely to be present in the case of samples obtained on crystals with a higher doping level and, correspondingly, lower breakdown voltage. For such samples, a stronger electric field can be expected in the microplasmas.

As the excitation level of the $p-n$ junction changes, despite the substantial change in the general character of the spectrum, virtually no energy shift of the bands of the oscillatory structure is observed (Fig. 2, curves *3* and *4*).

The bands of the oscillatory structure are subject to substantial, very rapid degradation (substantial degradation is observed over the operating time, measured in hours). The degradation is maximum for microplasmas with high-intensity bands with a long period. The background radiation goes out together with the bands with the oscillatory structure but more slowly. The voltage on the $p-n$ junction decreases at constant current synchronously with the decrease in the quantum radiation yield. The degradation rate decreases substantially, as a rule, when the samples are powered in a regime in which the voltage rather than the current is stabilized. The typical character of the change in the emission spectrum of a microplasma during operation is shown in Fig. 2 (curves *5* and *6*). More complicated cases of the variation of the spectrum structure during the operation of a $p-n$ junction, which are characteristic for microplasmas with a longer period of the structure, are also encountered. In these cases a change in the energy position and a redistribution of the relative intensity of the bands are observed. Virtually no degradation occurs when the samples are in storage.

It should be noted that we observed a periodic structure of the breakdown electroluminescence spectra only in the radiation of some low-voltage microplasmas. Many attempts to observe this structure in the radiation of $p-n$ junctions with uniform luminescence, including with current density exceeding 10^5 A/cm^2 when the sample is powered in the pulsed regime, as well as in the radiation of microplasmas with breakdown voltages exceeding 20 V were not successful.

The observation of such a periodic structure in the spectra of $p-n$ junctions prepared using other SiC polytypes is noteworthy. We observed such a structure in the emission spectra of individual microplasmas in alloyed $p-n$ junctions based on SiC–6*H*. The samples were produced from SiC–6*H* wafers, grown by Lely's method, and doped with nitrogen during growth to uncompensated donor density above 10^{19} cm^{-3}. The $p-n$ junctions were produced on the faces perpendicular to the crystallographic **C** axis. The breakdown voltage of the samples did not exceed 10 V and apparently corresponded to the region of tunneling breakdown.[7]

Room-temperature spectra, of two microplasmas, differing in the structural period, in SiC–6*H* $p-n$ junctions are shown in Fig. 3. As one can see from the figure, the basic features of the structure in SiC–6*H* and SiC–3*C* are similar.

We know of no examples of oscillations, similar to those which we observed, in the emission spectra of semiconductor

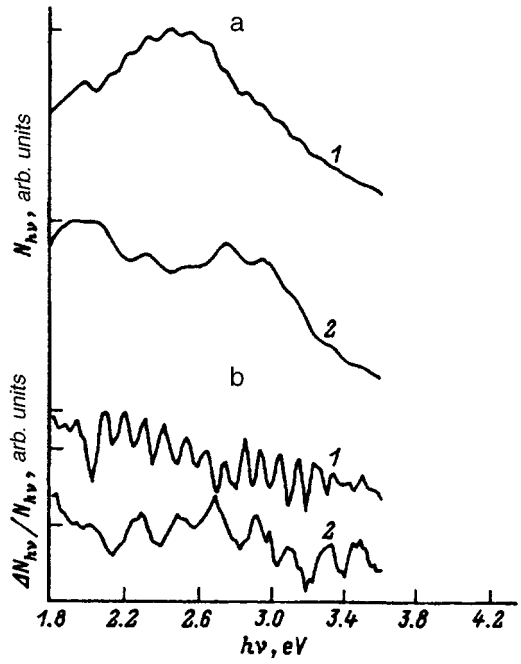

FIG. 3. Emission spectra of individual microplasmas in SiC–6*H* $p-n$ junctions (a) and differentiated spectra (b). Samples: *1*—(209), *2*—(107). Voltage on a sample, V: *1*—14.3, *2*—8.8.

structures. According to a number of qualitative features — weak temperature dependence, energy periodicity, and correlation between period and amplitude — these oscillations are most like the oscillations observed in near-edge absorption spectra of CdS (Ref. 8) and GaAs (Refs. 9 and 10) in the presence of a uniform electric field. The possibility of interpreting them as a manifestation of the Wannier–Stark levels was discussed. The question of the nature of these oscillations apparently remained open, while later theoretical and experimental investigations of the manifestation of Wannier–Stark levels were concerned mainly with artificial periodic structures (for example, Refs. 11 and 12).

While there is a qualitative similarity, the oscillations which we observed also exhibit fundamental quantitative differences — order-of-magnitude longer periods, larger amplitude, and, most importantly, they cover a very wide spectral range.

Nonetheless, it is helpful to estimate the magnitude of the electric field that would correspond in the Wannier–Stark model to the observed oscillations. The electric field intensity $E=\Delta h\nu/a$, where $\Delta h\nu$ is the period of the oscillations, and a are the lattice constants, should reach values of $(2-10)\times10^6$ V/cm in SiC–3*C* and $(3-7)\times10^6$ V/cm in SiC–6*H*. Taking into account the data for $E_{\max}$ in SiC–6*H*,[13] we see that such fields are realistic. It is also possible to explain in this case the rapid degradation of the junction in microplasmas with the longest oscillation periods and hence with the maximum fields.

However, such a model must be based on the assumption that all radiation is formed in a region of an almost uniform field, which seems unlikely. From our point of view, the assumption that a strong electric field in the region of radiation formation influences the structure of the states cannot be

rejected in and of itself, especially since in SiC the fields in the region of the junction reach strengths which are an order of magnitude greater than in known experiments on electroabsorption and electroreflection, where such an influence is well known (Franz–Keldysh effect, Wannier–Stark levels).

In any case, it is obvious that the investigation of the emission spectra of individual microplasmas and the oscillatory structure observed in them is of interest in itself, and it can also yield new information about the structure of the junctions and the mechanisms of the breakdown radiation.

[1] A. M. Genkin and V. N. Rodionov, Fiz. Tekh. Poluprovodn. **13**, 789 (1979) [Sov. Phys. Semicond. **13**, 463 (1979)].
[2] A. O. Konstantinov, Fiz. Tekh. Poluprovodn. **21**, 670 (1987) [Sov. Phys. Semicond. **21**, 410 (1987)].
[3] L. A. Kosyachenko, A. V. Pivovar, and V. M. Sklyarchuk, Zh. Prikl. Spektrosk. **36**, 236 (1982).
[4] W. R. L. Lambrecht, W. R. Segall, and W. Suttrop, Appl. Phys. Lett. **63**, 2747 (1993).
[5] M. Rohlfing, P. Kruger, and J. Pollmann, Phys. Rev. B **45**, 17791 (1992).
[6] J. Bude, N. Sanco, and A. Yoshii, Phys. Rev. B **45**, 5848 (1992).
[7] Yu. M. Altaĭskiĭ, A. M. Genkin, V. K. Genkina, and L. G. Ogneva, Électron. Tekhn. Ser. 2, No. 4(190), 76 (1987).
[8] V. S. Vavilov, V. B. Stopachinskiĭ, and V. Sh. Chanbarisov, Fiz. Tverd. Tela (Leningrad) **8**, 2660 (1965) [Sov. Phys. Solid State **8**, 2126 (1965)].
[9] B. T. French, Phys. Rev. **174**, 991 (1968).
[10] R. W. Koss and L. M. Lambert, Phys. Rev. B **5**, 1479 (1973).
[11] K. Gibb, M. M. Dignam, J. E. Sipe *et al.*, Phys. Rev. B **48**, 8156 (1993).
[12] K. Niizeki and A. Matsumura, Phys. Rev. B **48**, 4126 (1993).
[13] Yu. A. Vodakov, A. O. Konstantinov, D. P. Litvin, and V. I. Sankin, Pis'ma Zh. Tekh. Fiz. **7**, 705 (1981) [Tech. Phys. Lett. **7**, 301 (1981)].

Translated by M. E. Alferieff

The dominant mechanisms of charge-carrier scattering in lead telluride

D. M. Zayachuk

Chernovtsy State University, 274012 Chernovtsy, Ukraine
(Submitted January 30, 1995; accepted for publication April 24, 1996)
Fiz. Tekh. Poluprovodn. **31**, 281–284 (February 1997)

The present status of the dominant mechanisms of charge-carrier scattering in lead telluride is analyzed critically. It is shown that the role of the Coulomb potential of the vacancies and the role of the deformation potential of acoustic phonons in carrier scattering in PbTe has been strongly overestimated in most existing studies. Futhermore, the role of optical phonons at high temperatures has been unjustifiably reduced to a polar component only. It is shown that, in addition to this mechanism, the deformation potential due to optical phonons, whose greatest contribution is at high carrier densities, also plays an important role in carrier scattering processes at temperatures in the range of room temperature. © *1997 American Institute of Physics.* [S1063-7826(97)01602-5]

The dominant mechanisms for scattering of free charge carriers in lead telluride have been discussed and analyzed for a long time (see Refs. 1–7). It has been established that carrier scattering by characteristic point defects and by thermal phonons are such mechanisms. Their relative role in scattering processes reduces to the following.

At low temperatures, of the order of the liquid-helium temperatures, charge carriers are scattered predominantly by charged vacancies. At high carrier densities, of the order of 10^{19} cm^{-3} and higher, the scattering by the short-range potential of the vacancies predominates; at low densities, of the order of 5×10^{18} cm^{-3} and lower, scattering by the Coulomb potential of the vacancies predominates. In our analysis the charge of the vacancies was assumed to be equal to $\pm e$ or $\pm 2e$, where e is the electron charge.

As the temperature increases, the role of the vacancy mechanisms of charge-carrier scattering decreases and the role of scattering by thermal phonons increases. The latter processes dominate at temperatures of the order of room temperature, and scattering by the deformation potential of acoustic phonons and polarization scattering by optical phonons make the main contribution. The constant of the acoustic deformation potential is estimated to be 24 eV for electrons and 27 eV for holes.[1–7]

However, the present concept, formulated at the beginning of the 1970s, concerning the dominant charge-scattering mechanisms in PbTe requires a substantial correction. It does not answer the question of why the electron mobility in PbTe is more than two times higher than the hole mobility. According to present theory, the valence band (v band) and the conduction band (c band) in PbTe are mirror images of one another, and the electron and hole effective masses are nearly identical at the band extrema (see, for example, Ref. 5). If under such conditions the scattering of charge carriers by the Coulomb potential of the vacancies dominates at low charge-carrier densities, then the electron and hole mobilities should also be equal, because the electron and hole masses are equal. This implies that the role of the Coulomb potential of the vacancies in charge-carrier scattering processes in PbTe must be reexamined. Furthermore, apparently, the approach to estimating the role of optical phonons in these processes, specifically, the question of the deformation potential of optical phonons, must also be reinterpreted.

On this basis, an attempt was made to reanalyze the dominant mechanisms of charge-carrier scattering in PbTe proceeding from the present level of knowledge. The analysis made below is based on Kane's band model

$$\varepsilon(1+\varepsilon/\varepsilon_g)=\hbar^2k_t^2/2m_t+\hbar^2k_l^2/2m_l \tag{1}$$

and the well-known experimental dependences of the Hall mobility of charge carriers on their density. The analysis is made at room temperature and liquid-helium temperatures, at which all scattering mechanisms which are important in PbTe can be described in the relaxation-time approximation. In this approximation, the Hall mobility μ_H of the charge carriers, with arbitrary degeneracy of the charge carriers, can be calculated as[8]

$$\mu_H=e\langle[\tau(\varepsilon)/m_0(\varepsilon)]^2\rangle/\langle\tau(\varepsilon)/m_0(\varepsilon)\rangle, \tag{2}$$

where the brackets indicate averaging

$$\langle A(\varepsilon)\rangle=\int_0^\infty(-\partial f_0/\partial\varepsilon)k^3(\varepsilon)A(\varepsilon)d\varepsilon/\int_0^\infty(-\partial f_0/\partial\varepsilon)k^3(\varepsilon)d\varepsilon,$$

$f_0(\varepsilon)$ is the Fermi–Dirac distribution function, and $m_0=3m_tm_l/(2m_l+m_t)$. The dependences of the relaxation time τ on the reduced energy $x=\varepsilon/k_0T$ for the scattering mechanisms which are assumed to be dominant mechanisms in PbTe, have the following forms:[2,8]

a) Coulomb potential of the vacancies:

$$\tau_C(x)=\frac{\varepsilon_0^2(2m_n)^{1/2}(k_0T)^{3/2}(x+\beta x^2)^{3/2}}{\pi(Ze^2)^2N_v[\ln(1+\xi)-\xi/(1+\xi)](1+2\beta x)}, \tag{3}$$

where $\xi=(2kr_v)^2$, k is the carrier wave vector, and r_v is the screening radius of the vacancy potential;

b) polarization scattering by optical phonons ($T\gg\theta$):

$$\tau_{PO}(x)=\frac{\hbar^2(x+\beta x^2)^{1/2}F^{-1}}{e^2(2m_nk_0T)^{1/2}(\varepsilon_\infty^{-1}-\varepsilon_0^{-1})(1+2\beta x)}, \tag{4}$$

 1063-7826/97/020173-04$10.00

where

$$F=1-\delta\ln(1+\delta^{-1})-\frac{2\beta x(1+\beta x)}{(1+2\beta x)^2}$$

$$\times[1-2\delta+2\delta^2\ln(1+\delta^{-1})],$$

$\delta=(2kr_0)^{-2}$, and r_0 is the screening length of the optical phonons;

c) short-range potential of the vacancies and the deformation potential of the acoustic phonons:

$$\tau_m(x)=\frac{\tau_{0,m}(T)(x+\beta x^2)^{-1/2}}{(1+2\beta x)[(1-A)^2-B]},$$

$$A=Bx(1-K_m)/(1+2\beta x),$$

$$B=8\beta x(1+\beta x)K_m/3(1+2\beta x)^2, \qquad (5)$$

where for the short-range potential of the vacancies $m=v$ and

$$\tau_{0,v}=\pi\hbar^4/m_n(2m_nk_0T)^{1/2}U_{vc}^2N_v, \quad K_v=U_{vv}/U_{vc}, \qquad (6)$$

for the deformation potential of the acoustic phonons $m=a$ and

$$\tau_{0,a}=2\pi\hbar^4C_l/E_{ac}^2(2m_nk_0T)^{3/2}, \quad K_a=E_{av}/E_{ac}. \qquad (7)$$

In Eqs. (3)–(7) m_n is the effective density-of-states mass in one ellipsoid at the band edge; ε_0 and ε_∞ are the static and high-frequency permittivities, respectively; Ze is the vacancy charge; $U_{vc,vv}$ and $E_{ac,av}$ are, respectively, the short-range potential of the vacancies and the deformation potential for the c and v bands; N_v is the vacancy density; and C_l is a combination of elastic constants. In the case of mixed scattering the total relaxation time was calculated in the usual manner[8]

$$\tau_\Sigma^{-1}=\sum_i \tau_i^{-1}. \qquad (8)$$

The main PbTe crystal parameters employed for calculating μ_H are presented in Table I.

The parameters E_{ac} and U_{vc} are adjustable parameters and their values were determined so as to obtain the best agreement between the computed and experimental dependences of the electron mobility on the electron density. If the c and v bands of PbTe are mirror images of one another, then the ratio of the values of these parameters for the indicated bands should give, in the simplest variant, a difference in the electron and hole mobilities in the investigated material. As the zeroth-order approximation, it was assumed that this quantity is the same and equals 1.5 for both the short-range potential of the vacancies and the acoustic deformation potential; this agrees with the published data[2] and gives the required value of the ratio of the electron and hole mobilities in PbTe.

The experimental results on $\mu_H(n)$ at 4.2 and 300 K, which are to be analyzed and are generalized according to existing published data, are shown in Figs. 1 and 2. It was first necessary to estimate the possible role of the long-wavelength acoustic phonons in the formation of the electron mobility at 4.2 K. We have accordingly compared the maximum experimental values of the electron mobility with the values computed from Eqs. (2), (5), and (7) for different values of E_{ac} (see Fig. 3). We see that E_{ac} in PbTe cannot exceed 19 eV, since otherwise the electron mobility at 4.2 K could not reach the experimentally observed value of the order of 5.6×10^6 cm^2/(V·s).

TABLE I. Basic parameters of PbTe which were employed for calculating the electron Hall mobility.

Parameter	4.2 K	300 K	References
ε_g, eV	0.19	0.315	
m_t/m_0	0.026	0.0453	Refs. 10–12
m_l/m_0	0.24	0.24	
ε_0	1470	400	Refs. 2, and 13
ε_∞	38.5	32.6	Ref. 14
C_l, dynes/cm^2	8.1×10^{11}	7.1×10^{11}	Refs. 2, 5, and 15
$\hbar\omega_0$, eV		0.0136	Ref. 2
a, Å		6.461	Ref. 5
ρ, g/cm^2		8.24	Ref. 5
Z	0.14		Ref. 9
E_{ac}, eV	15	15	Our data
E_{oc}, eV		26	
U_{vc}, ergs/cm^3	3×10^{-34}	3×10^{-34}	
$K_{v,a,o}$	1.5	1.5	

The results of the latest theoretical investigations of the character of the localization of electric charge on vacancies were taken into account in the analysis of the possible contribution of the Coulomb potential of the vacancies to the charge-carrier scattering processes in PbTe.[9] According to this work, a charge of $0.14e$ is localized on a vacancy giving two free carriers, as happens in PbTe.[10] The remaining excess charge is spread over the crystal. Therefore, the quantity Z in the expression (3) for the relaxation time must be set equal to 0.14 and not 1 or 2, as previously assumed. As a

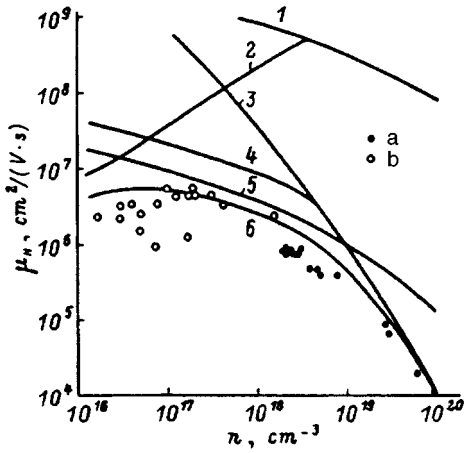

FIG. 1. Electron Hall mobility μ_H versus electron density n ($T=4.2$ K) according to the data from Ref. 2 (a) and Ref. 6 (b). Lines—Calculation for the scattering mechanisms: *1, 2*—Scattering by the Coulomb potential of the vacancies, *3, 4*—scattering by the short-range potential of the vacancies, *5*—scattering by the deformation potential of the acoustic phonons; *6*—total scattering according to Eq. (8) for the dependences *2,4,5*. Values of the parameters used in the calculation: *1,3*—$N_v=n/2$, *2,4*—$N_v=2\times10^{18}$ cm^{-3} for $n<4\times10^{18}$ cm^{-3} and $N_v=n/2$ for $n\geq4\times10^{18}$ cm^{-3}, *5*—$E_{ac}=15$ eV.

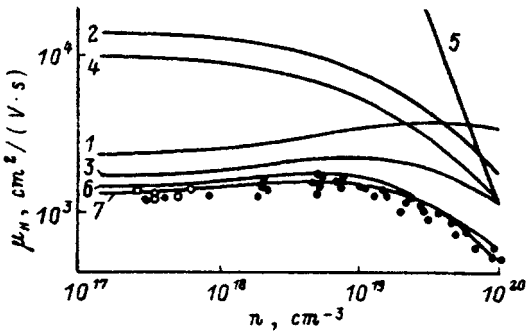

FIG. 2. Electron Hall mobility μ_H versus electron density n ($T=300$ K) according to the data in Ref. 2 (a) and our data (b). Lines—Calculation for scattering mechanisms: *1*—Polarization scattering by optical phonons (PO); *2*—scattering by the deformation potential of the acoustic phonons (DA);*3*—$PO+DA$; *4*—scattering by the deformation potential of optical phonons (DO) according to Eqs. (5) and (9); *5*—DO according to Eq. (10); *6*—$PO+DA+DO$, DO—according to Eq. (10); *7*—$PO+DA+DO$, DO—according to Eqs. (5) and (9).

result of the smallness of the charge localized on the vacancies and the high permittivity of PbTe, the Coulomb potential of the vacancies plays a secondary role in the charge-carrier scattering in the entire range of vacancy densities (Fig. 1, curve *1*), if one adheres closely to the idea that one vacancy gives two free carriers,[10,11] i.e., $N_v=n/2$. Our calculations show that the role of the Coulomb potential of the vacancies in charge-carrier scattering in PbTe can become appreciable only in strongly compensated crystals, when the total vacancy density is much higher than the densities of free charge carriers (Fig. 1, curve *2*). In this connection, to give a satisfactory quantitative explanation of the experimental results at low electron densities (mainly, the pronounced tendency for μ_H to decrease somewhat as n decreases below the level 10^{17} cm^{-3}), it is necessary to assume that the one-to-one relation between the carrier and vacancy densities is strongly violated. The best agreement between the computational and experimental results was obtained under the condition that for $n<4\times10^{18}$ cm^{-3} the density N_v stabilizes at the level 2×10^{18} cm^{-3}, and for the values of the parameters $U_{vc}=3\times10^{-34}$ ergs/cm^3 and $E_{ac}=15$ eV (Fig. 1, curve *6*). It is interesting to note that the minimum defect density of the order of 2×10^{18} cm^{-3} in PbTe crystals, which follows from the analysis made above, correlates very well with the

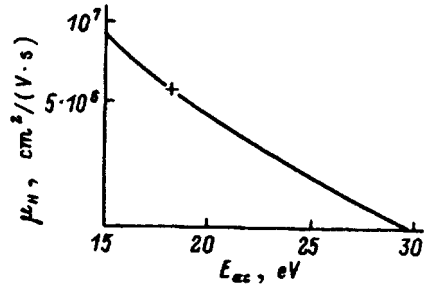

FIG. 3. Calculation of the electron Hall mobility at 4.2 K and $n=1.5\times10^{17}$ cm^{-3} for electron scattering by the deformation potential of acoustic phonons as a function of E_{ac}. The cross indicates the maximum experimental value of the electron mobility in PbTe at 4.2 K.

typical hole density in crystals grown from melt.[1,16–18] It should be noted that the quantity $E_{ac}=15$ eV, which we proposed on the basis of an analysis of the low-temperature electron mobility, is much smaller than the standard value $E_{ac}=24$ eV, which was found by analyzing the high-temperature mobility.[1–6] This means that the role of the acoustic deformation potential in charge-scattering processes in PbTe has been systematically overestimated.

At 300 K the simplest approach is to estimate the contribution of polar optical phonons to the scattering processes, since the mobility which they produce can be calculated without any adjustable parameters. As one can see from Fig. 2 (curve *1*), this contribution is rather large at low carrier densities, which agrees with the known results (Refs. 1–5).

Under the combined action of polar optical phonons and the acoustic deformation potential, the computed values of the mobility for $E_{ac}=15$ eV are much higher than the experimental values (Fig. 2, curve *3*). They can be formally matched by setting E_{ac} equal to 24 eV, as done previously.[1–7] However, it is difficult to explain satisfactorily such a large increase in the constant of the deformation potential with increasing T, since it is usually assumed to be temperature-independent.[1–5] More likely, the estimates presented indicate that these two scattering mechanisms are insufficient to explain correctly the formation of charge-carrier mobility in PbTe at high temperatures. It would be more logical to conclude that under these conditions scattering by the optical deformation potential is also important.

To take account of the possible role of this scattering, different expressions were used for the relaxation time: the standard expression (5), in which according to Ref. 8 (setting $m=0$), we have

$$\tau_{0,o}=2\hbar^2a^2\rho(\hbar\omega_0)^2/\pi(2m_nk_0T)^{3/2}E_{oc}^2,$$
$$K_o=E_{ov}/E_{oc}, \tag{9}$$

and the expression obtained in Ref. 19

$$\tau_l^{-1}=(2m_n)^{3/2}\Omega k_0T\varepsilon^{3/2}(1+\varepsilon/\varepsilon_g)^{3/2}$$
$$\times C^2/\pi M\hbar^4\omega_0^2\varepsilon_g(1+2\varepsilon/\varepsilon_g), \tag{10}$$

where a is the lattice constant, ρ is the density of the crystal, ω_0 is the frequency of the optical phonon, M is the reduced mass of the ions, E_{oc} and E_{ov} are the constants in the optical deformation potential for the c and v bands, C is a matrix element with respect to the wave functions of the c and v bands, and Ω is the unit-cell volume.

The use of expressions (9) and (10) for the relaxation time considered here, in combination with the polar optical phonons and acoustic deformation potential, yields satisfactory agreement between theory and experiment (Fig. 2, curves *6* and *7*). Accordingly, when expressions (5) and (9) are used for $\tau_0(x)$, the quantity E_{oc} should be set equal to 26 eV (Fig. 2, curve *7*), and when expression (10) is issued, the quantity C should be set equal to 4×10^8 eV/cm (Fig. 2, curve *6*). In either case, in the temperature range investigated, the contribution of the optical deformation potential to the formation of charge-carrier mobility, when the charge-carrier density is high, turned out to be the dominant contribution (see Fig. 2, curves *1, 2 4*, and *5*).

CONCLUSIONS

The dominant charge-carrier scattering mechanisms in PbTe are scattering by vacancies and scattering by thermal phonons.

The vacancy mechanism of scattering is realized mainly through scattering by the short-range potential of the vacancies, which dominates at low temperatures and high charge-carrier densities. Its component associated with the Coulomb potential is suppressed because of the strong delocalization of the vacancy-related electric charge and the high permittivity, and has virtually no effect on the scattering of carriers in uncompensated crystals.

The role of acoustic phonons in the charge-carrier scattering processes is large at 4.2 and 300 K. At temperatures close to room temperature, optical phonons also make a large contribution to the processes investigated. At low carrier densities these vibrations influence the carrier-scattering processes predominantly through the polar component and at high densities through the optical deformation potential, which assumes the dominant role in the total carrier scattering.

[1] Yu. I. Ravich, B. A. Efimova, and I. A. Smirnov, *Methods for Investigating Semiconductors in Application to the Lead Chalcogenides PbTe, PbSe, and PbS* [in Russian], Nauka, Moscow, 1968.

[2] Yu. I. Ravich, B. A. Efimova, and V. I. Tamarchenko, Phys. Status Solidi B **43**, 11 (1971); **43**, 453 (1971).

[3] W. Szymanska, Postepy Fizyki **26**, 5 (1975).

[4] L. Palmetshofer, K. H. Gresslehuer, L. Ratschbacher, and A. Lopez-Otero, Lect. Not. Phys. **152**, 391 (1982).

[5] G. Nimtz and B. Schlicht, *Narrow-Gap Semiconductors*, Berlin, 1985, p. 1.

[6] R. Granger, A. Lasbley, C. M. Pelletier, and S. Rolland, J. Physique **46**, 1185 (1985).

[7] N. P. Gavaleshko, P. N. Gorleĭ, and V. A. Shenderovskiĭ, *Narrow-Gap Semiconductors: Preparation and Physical Properties* [in Russian], Naukova dumka, Diev, 1984.

[8] B. M. Askerov, *Electronic Transport Phenomena in Semiconductors* [in Russian], Nauka, Moscow, 1985.

[9] O. A. Pankratov and P. P. Povarov, Solid State Commun. **66**, 847 (1988).

[10] K. Cuff, M. Ellet, C. Kuglin, and C. Williams, in *Proceedings of the International Conference on Physics of Semiconductors*, Paris, 1964, p. 690.

[11] E. Palik, D. Mitchell, and J. Zemel, Phys. Rev. A **135**, 763 (1964).

[12] D. M. Zayachuk, V. I. Mikityuk, and P. M. Starik, Fiz. Tekh. Poluprovodn. **20**, 1679 (1986) [Sov. Phys. Semicond. **20**, 1051 (1986)].

[13] H. Kawamura, Lect. Not. Phys. **150**, 470 (1980).

[14] G. Dionne and J. C. Wooley, Phys. Rev. B **6**, 3898 (1972).

[15] B. Houston, R. E. Strakna, and H. S. Belson, J. Appl. Phys. **39**, 3913 (1968).

[16] N. J. Parada and G. W. Pratt, Phys. Rev. Lett. **22**, 180 (1969).

[17] B. A. Volkov and O. A. Pankratov, Zh. Éksp. Teor. Fiz. **88**, 280 (1985) [Sov. Phys. JETP **61**, 165 (1985)].

[18] D. M. Zayachuk, V. I. Mikityuk, and V. A. Shenderovskiĭ, Dopovidi Akad. Nauk USSR, Ser. A No. 8, 57 (1990).

[19] L. Ya. Morgovskiĭ and Yu. I. Ravich, Fiz. Tekh. Poluprovodn. **5**, 974 (1971) [Sov. Phys. Semicond. **5**, 860 (1971)].

Translated by M. E. Alferieff

Formation of order in a system of localized charges in disordered layers of solid solutions of cadmium telluride and cadmium sulfide

A. P. Belyaev, V. P. Rubets, and I. P. Kalinkin

St. Petersburg Technological Institute, 198013 St. Petersburg, Russia
(Submitted February 19, 1996; accepted for publication April 24, 1996)
Fiz. Tekh. Poluprovodn. **31**, 286–290 (February 1997)

Relaxation processes stimulated in layers of the solid solutions $CdTe_xS_{1-x}$ ($x<0.2$) by a change in an external electric field, temperature, and illumination have been studied. Polarization effects and maxima of the inversion current of photostimulated and thermally stimulated polarization were found. It is shown that all characteristic features of the relaxation processes can be explained in a quasidipole model, and the inversion maxima of the current can be interpreted as being due to a photostimulated and thermally stimulated order–disorder transition. © *1997 American Institute of Physics.* [S1063-7826(97)01702-X]

The observation of inversion maxima of the thermally stimulated current and polarization in disordered layers of solid solutions (SSs) of cadmium selenide and telluride was reported in Ref. 1. These effects were not explained properly. Later we observed similar phenomena in layers of solid solutions of cadmium telluride and cadmium sulfide. In the present paper we attempt to describe in detail and explain these phenomena.

1. EXPERIMENTAL SAMPLES AND EXPERIMENTAL PROCEDURE

We investigated $CdTe_xS_{1-x}$ ($x<0.2$) layers, synthesized on a mica substrate by the method of vacuum thermal vaporization and condensation of a mechanical mixture from a reactor with a ''thermal screen.'' According to x-ray phase and electron-diffraction analysis the layers possess a polycrystalline structure with average crystallite size of 10^{-2} μm. The layers were approximately 1 μm thick. To stabilize the electrical properties, before the measurements the layers were annealed in a 10^{-3} Pa vacuum for 2 h. After annealing, 0.5-cm-wide silver contacts, separated by a distance of 0.1 cm, were deposited on the samples. The resistivity of the contacts was checked on the initial sections of the current-voltage characteristic. X-Ray analysis was used to determine the composition of the solid solutions.

The electrical characteristics of the samples were measured in a current regime using a V7-30 electrometer. To take into account the parasitic capacitances, prior to the measurements, the experimental stand was checked using standards consisting of active resistances, whose values were close to that of the experimental samples. A quantitative estimate of the magnitude of the relaxing charges was made by integrating the corresponding currents in time.

All measurements of the electric and photoelectric characteristics of the samples were made in a vacuum of 10^{-3} Pa. A special constant-temperature chamber was used to maintain the temperature of the samples within 0.1 K. The photoelectric parameters of the layers were investigated under illumination with a 90-W incandescent lamp.

2. EXPERIMENTAL RESULTS

The electric, photoelectric, photoluminescence, and relaxation properties were investigated. The electric and photoluminescence measurements revealed the following characteristics: high conduction activation energy (greater than 0.7 eV) and high resistivity ($10^{10}-10^{11}$ $\Omega\cdot$cm at room temperature), a complicated temperature dependence of the conductivity, presence of relaxations, and a large half-width of the photoluminescence bands (0.3–0.5 eV), i.e., a combination of properties which are characteristic of disordered semiconductors.[2]

The amplitude of the fluctuations of the potential of the random field, estimated according to the photoluminescence measurements, was equal to 0.3–0.5 eV. It increased with increasing cadmium telluride content in the solid solution.

The basic results of the investigations of the relaxation properties are presented in Figs. 1–3. The curve of the relaxation of the current in the external circuit of the sample with the external emf source switched on (at time $t=0$) and off ($t=15$ s) is represented qualitatively in Fig. 1 (curve *1*). It is evident from the figure that when the external field is switched on, decreasing current relaxations occurred. After equilibrium was established, the samples became polarized. The surface charge density Q_p accumulated during polarization was equal to $10^{-7}-10^{-5}$ C/cm^2. The value of the surface polarization depended on the illumination of the sample and the magnitude of the external field. It increased together with these actions, but sublinearly.

The characteristic time for establishing a stationary value of the polarization depended on the temperature and amplitude of the fluctuations of the random potential in the sample (Fig. 2). An increase in the amplitude of the nonuniformity of the potential caused, the characteristic time to increase.

The sample was polarized only at relatively low temperatures. As the temperature increased (slightly above room temperature), the polarization vanished. The vanishing of polarization changed the shape of the current relaxation curve. After an external electric field was switched on, the current

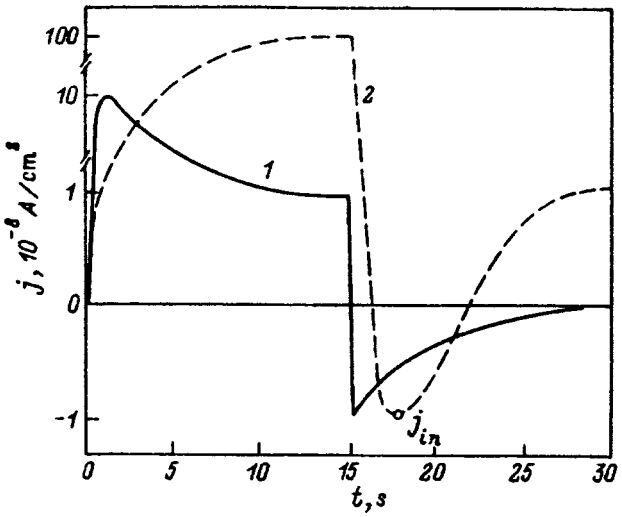

FIG. 1. Curves of current relaxation in a layer of the solid solution $CdTe_xS_{1-x}$ ($x=0.1$) with the amplitude of the fluctuations of the potential energy of the electrons $\gamma=0.3$ eV; $T=300$ K; with the external field switched on (*1*) and with illumination switched on (*2*) at time $t=0$ and with both switched off at $t=15$ s.

increased monotonically up to a stationary value. The specific value of the temperature at which the polarizing of the sample ceased depended on the magnitude of the external field. As the magnitude of the external field increased, the limit shifted into a higher-temperature region.

Curve *2* in Fig. 1 represents qualitatively the current relaxation under strong illumination ($t=0$) and with dark screening ($t=15$ s) of the layers in an electric field. As one can see from the figure, after the sample is screened, the relaxation is characterized by the formation of an inversion maximum j_{in}, which precedes a stationary value of the direct current. Such maxima could be observed with rapid heating of the polarized sample (Fig. 3, curve *1*). For comparison, the behavior of the current when the heated sample

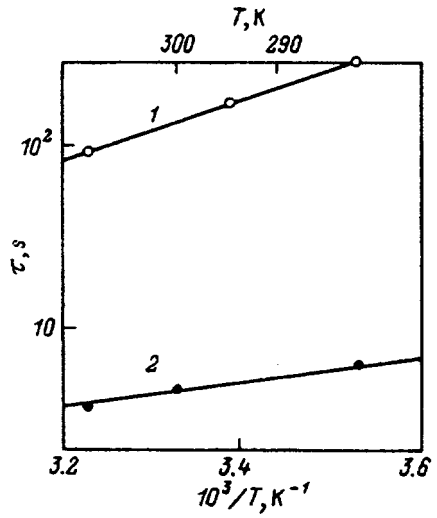

FIG. 2. Temperature dependences of the characteristic polarization time of layers of the solid solutions $CdTe_xS_{1-x}$ with the amplitude of the fluctuations of the potential energy of the electrons γ, eV: *1* — 0.42 ($x=0.15$), *2* — 0.1 ($x=0.1$).

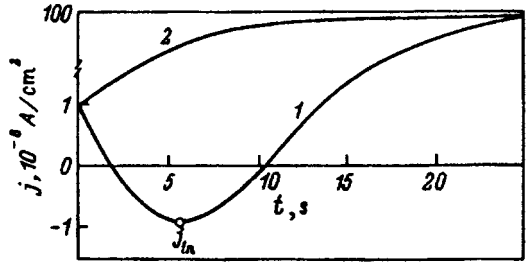

FIG. 3. Relaxation curves of the thermally stimulated polarization current in a layer of the solid solution $CdTe_xS_{1-x}$ with heating (*1*) and cooling (*2*) of the sample.

is cooled is also shown in the figure (curve *2*). The current j_{in} depends on the heating rate. The inversion maximum vanishes completely with slow heating.

The relaxation curves described above are complex curves. They could be represented by a simple exponential on the initial sections only in some cases. We took advantage of this circumstance to determine the characteristic polarization time.

Without the action of an external electric field no polarization of the samples was observed.

3. DISCUSSION

The random potential in disordered systems based on II–VI solid solutions is mainly formed by composition fluctuations over the volume.[3] Charged impurities together with the majority carriers — electrons in the layers investigated — perform the function of screening. As follows from the low conductivity of the samples, at the experimental temperatures most electrons are localized either in the tail of the density of states of the conduction band or in donor levels. They can move only by thermal activation on delocalized states or by thermally activated hops along localized states. To distinguish electron motion along the conduction band and along donor levels, we call a free donor a hole and, correspondingly, we call electron motion along the impurity band hole motion. As they move, electrons and holes are distributed according to states in such a way as to minimize the potential energy. The electron and hole densities can be assumed, to a first approximation, to be identical and the layer of the solid solution can be represented as a volume with a nonuniform electron-hole quasiplasma in a random field formed by the composition fluctuations of the solid solution. In addition, the possible configuration states of the charges in the quasiplasma are limited by the particular arrangement of the impurities in the volume.

An external voltage applied to a nonuniform system is distributed nonuniformly. According to Shklovskiĭ,[4] most of the voltage is applied across the regions where the potential energy is close to the mobility edge. In $CdTe_xS_{1-x}$ layers, these are regions depleted of free carriers and enriched with localized carriers. Such regions are separated from one another by distances which are much greater than the average spatial size of the nonuniformities. Correspondingly, the voltage drop across them is much larger than the average. As a result, a high electric field capable of redistributing carriers

in localized states is produced in these regions even with weak external biases. As a result, the dynamic equilibrium between individual components of the quasiplasma is destroyed. Experimental observation of this phenomenon in a film of II–VI solid solutions was reported in Ref. 5. A nonuniform quasiplasma in an external field must arrive in a new equilibrium state, which must necessarily be nonuniform.

It can be assumed that this state contains regions of spatially separated, localized charges of opposite sign — quasidipoles. A necessary condition for the formation of quasidipoles is that the thermal energy must be comparable to the change in the energy caused by the external electric field on atypical[4] regions (system must be driven out of equilibrium). The fact that polarization effects in films of the solid solutions $CdTe_xS_{1-x}$ appear only at low temperatures and that the limiting temperature increases together with the external field are evidence in support of the proposed model.

To make a systematic calculation of the conditions of formation of quasidipoles, it is necessary to solve simultaneously the continuity and Poisson equations with boundary conditions that do not admit solutions in terms of elementary functions.[6] However, calculations performed for simpler initial conditions (neglecting the conduction current and the nonuniformity of the sample) revealed a distinguishing feature, due to quasidipoles, of the temperature dependence of the thermally stimulated polarization current. According to Refs. 7 and 8, current inversion should occur in an external circuit of the sample heated by the voltage; we observed such a current inversion in the $CdTe_xS_{1-x}$ layers.

In our view, the inversion maximum of the current in the external circuit containing a $CdTe_xS_{1-x}$ sample is due to the relaxation of charge which accumulates on the electrodes and becomes excess charge by virtue of the temperature disorientation of the quasidipoles. An order–disorder transition occurs in the $CdTe_xS_{1-x}$ layers under the influence of the temperature.

Another argument in support of the quasidipole model of polarization is the inversion maximum of the current which arises as a result of intense screening of the layers (Fig. 1, curve *2*). It necessarily follows from the proposed model. Once light gives rise to polarization, switching off the light should result in the appearance of excess charge on the electrodes. This charge is induced by virtue of the low conductivity of the sample and relaxes mainly through the external circuit.

The increase in polarizability of the sample under the action of the light is due to the increase in the charge of the quasidipoles, and the rapidity of the charge recombination after screening is due to the character of the potential barrier. The potential barrier in the $CdTe_xS_{1-x}$ layers is formed mainly as a result of fluctuations of the composition of the solid solution; in this case the potential wells for the holes and electrons of the main bands coincide spatially.

Qualitative agreement between the experiment and the quasidipole model can be also seen in the field relaxations of the current (Fig. 1, curve *1*). The decreasing current relaxations are explained by the increase in the opposing field in the process of orientation of the quasidipoles; the exponential temperature dependence of the characteristic polarization time τ (Fig. 2) is due to the potential barrier which carriers must overcome in order to form oriented quasidipoles. This follows from almost all existing quasidipole models of relaxation oscillators, since their polarization time is determined by the expression[9]

$$\tau = \frac{1}{2\nu} \exp \frac{W}{kT}, \tag{1}$$

where ν is the frequency factor of the system, and W is the height of the potential barrier, which a quasidipole must overcome in order to become oriented. The values of W calculated on the basis of Fig. 2 to within hundredths of an eV agree with the estimates of the amplitude γ of the nonuniformity potential of the corresponding $CdTe_xS_{1-x}$ samples from photoluminescence measurements. This agreement can be interpreted as additional evidence for the formation of oriented quasidipoles in the random field of the experimental samples.

We shall present some quantitative assessments of the model. First, let us determine whether or not the minimum field at which polarization was observed is indeed capable of driving the system of localized and free carriers out of equilibrium. We observed polarization effect at room temperature in an electric field of not less that $E \simeq 100$ V/cm. Since the random field in the experimental solid solutions is due mainly to composition fluctuations of the solid solution and according to Ref. 10 the composition of a phase of the solid solution depends on the size of the region where this phase is formed, it can be assumed that the external voltage falls mainly on the interphase regions (different regions will possess a different composition and therefore a different band gap) and according to Shklovskiĭ[4] mainly atypical regions. Since there are no other alternatives, let us assume that one of the hundreds of interphase regions is atypical. Then, for an average size of the regions in the $CdTe_xS_{1-x}$ layers equal to 10^{-2} μm, we obtain the energy change produced by a field of the order of 100 V/cm to be 10^{-2} eV, which is comparable to the thermal energy and hence sufficient to destroy the dynamic equilibrium in the system of localized and free charges. Second, let us see how realistic the volume density of polarizing charges required by the model is.

It is well known that

$$\rho = -\operatorname{div} \cdot \mathbf{P}, \tag{2}$$

$$Q_p = P_n, \tag{3}$$

where ρ is the charge density, $\mathbf{P}$ and P_n are, respectively, the polarization vector in the sample and its normal projection, and Q_p is the surface charge density. Then, interpreting div $\mathbf{P}$ as the increment to P_n as a result of the displacement of carriers from one electrode to another and using the experimental data $Q_p = 10^{-7} - 10^{-5}$ C/cm^2, we obtain the charge density $\rho = 10^{13} - 10^{15}$cm^{-3}. This value with impurity density $10^{17} - 10^{19}$ cm^{-3} (Ref. 3) is completely realistic.

In conclusion, we note that the appearance of polarization in layers has also been observed by other authors. Specifically, polarization of doped layers of II–VI compounds

was reported in Ref. 10. The data reported by the authors are completely explained on the basis of the model proposed above.

4. CONCLUSIONS

The following conclusions can be drawn on the basis of the results presented above.

1. Under certain conditions order in the distribution of charges localized in a volume — quasidipoles — can appear in inhomogeneous layers of cadmium telluride and cadmium sulfide under the influence of an external field.

2. A decrease of the temperature and an increase of the external field and illumination of the sample give rise to the formation of quasidipoles in the disordered system $CdTe_xS_{1-x}$.

3. An external manifestation of order in the distribution of localized charge in the disordered system $CdTe_xS_{1-x}$ is polarization of the sample.

4. A sharp increase in temperature or illumination of a polarized disordered system can result in the appearance of an inversion maximum of the current as a result of an order–disorder transition in the system of localized charges.

5. The characteristic time for establishing order in an experiment depends on the temperature with activation energy determined by the amplitude of the fluctuations of the potential energy of the electrons in the random field of the disordered system.

This work was performed with the support of the Russian Fund for Fundamental Research (Grant 96-02-19138).

[1] A. P. Belyaev, I. P. Kalinkin, and V. A. Sanitarov, Fiz. Tekh. Poluprovodn. **17**, 1337 (1983) [Sov. Phys. Semicond. **17**, 848 (1983)].
[2] A. Ya. Shik, *Inhomogeneous and Impurity Semiconductors in External Fields* [in Russian], Shtiintsa, Kishinev, 1979, p. 22.
[3] A. P. Belyaev and I. P. Kalinkin, Thin Sol. Films **158**, 25 (1988).
[4] B. I. Shklovskiĭ, Fiz. Tekh. Poluprovodn. **13**, 93 (1979) [Sov. Phys. Semicond. **13**, 53 (1979)].
[5] A. P. Belyaev, I. P. Kalinkin, and V. A. Sanitarov, Fiz. Tekh. Poluprovodn. **19**, 154 (1985) [Sov. Phys. Semicond. **19**, 95 (1985)].
[6] R. M. Ramoviĉ, D. A. Tjapkin, and I. P. Marinoviĉ, in *Proceedings of the Seventh Yugoslavian Symposium on Physics of Condensed Matter*, Ohrid, 1980, p. 50.
[7] P. Miller, Phys. Status Solidi A **67**, 11 (1981).
[8] I. Vanderschueren, A. Linkens, and I. Gosiot, J. Appl. Phys. **51**, 4967 (1980).
[9] Yu. A. Gorokhovatskiĭ and G. A. Bordovskiĭ, *Thermally Activated Current Spectroscopy of High-Resistivity Semiconductors and Dielectrics* [in Russian], Nauka, Moscow, 1991.
[10] S. A. Kukushkin and V. V. Slezov, Fiz. Tverd. Tela (Leningrad) **29**, 3657 (1987) [Sov. Phys. Solid State **29**, 2092 (1987)].
[11] O. V. Snitko, *Physical Principles of Semiconductor Electronics* [in Russian], Naukova dumka, Kiev, 1985.

Translated by M. E. Alferieff

Two-electron tin centers with negative correlation energy in lead chalcogenides. Determination of the Hubbard energy

V. F. Masterov, F. S. Nasredinov, S. A. Nemov, and P. P. Seregin

St. Petersburg State Technical University, 195251 St. Petersburg, Russia
(Submitted March 5, 1996; accepted for publication April 24, 1996)
Fiz. Tekh. Poluprovodn. **31**, 291–295 (February 1997)

It is shown using Mössbauer spectroscopy on the isotope ^{119}Sn that an isovalent tin impurity in the solid solutions $PbS_{1-z}Se_z$ is a two-electron donor with negative correlation energy. The energy levels associated with the tin impurity are found in the lower half of the band gap for $z<0.7$ and are found among the allowed states of the valence band for $z>0.7$. We have demonstrated electron transfer between neutral and ionized tin centers. The activation energy E_o of this process decreases monotonically as z is increased, which reflects the fact that the tin energy levels move toward the top of the valence band, and for $z>0.7$ the activation energy is $E_o=U/2$, where U is the Hubbard energy. © *1997 American Institute of Physics.* [S1063-7826(97)01802-4]

1. INTRODUCTION

Lead and tin chalcogenides form solid substitution solutions ($Pb_{1-x}Sn_xS$, $Pb_{1-x}Sn_xSe$, $Pb_{1-x}Sn_xTe$) and, according to Mössbauer spectroscopic data for the tin isotope ^{119}Sn, tin is an electrically active impurity of donor type in PbS and PbSe.[1,2] However, efforts to explain the temperature dependence of the electrical conductivity, thermal voltage, and Hall coefficient of the solutions $Pb_{1-x-y}Sn_xA_yS$ and $Pb_{1-x-y}Sn_xA_ySe$ (A=Na, Tl) the framework of a single-level model were not successful.[3] According to the picture developed in Ref. 3, tin exhibits donor activity only at low temperatures (e.g., for PbSe at $T<200$ K), whereas when the temperature is increased, tin begins to play the role of an acceptor. Obviously, this picture can be realized if at low temperatures neutral (Sn^{2+}) and ionized (Sn^{4+}) tin centers in the PbS (PbSe) lattices are found at different sites: e.g., the Sn^{4+} ion can strongly deform its immediate environment with the formation of associates with vacancies or ionized acceptors.[3] When the temperature is raised, the stability of the deformed local environment of the Sn^{4+} ions is lowered and the tendency for the formation of Sn^{2+} ions grows. At some critical temperature (according to Ref. 3, at $T>200$ K for PbSe) the nonequivalence of the sites of the Sn^{2+} and Sn^{4+} centers disappears and this promotes the localization of electrons at the Sn^{4+} centers, changing them into Sn^{2+} centers. A substantial shortcoming of the picture developed in Ref. 3 is the absence of any proof of the existence of such associates, not only in the Mössbauer spectra,[4,5] but also in the optical absorption spectra of the solid solutions $Pb_{1-x-y}Sn_xA_yS$ and $Pb_{1-x-y}Sn_xA_ySe$.[6,7]

This paper presents a model that allows one to describe an isovalent (isoelectronic) tin impurity in the lead chalcogenides PbS and PbSe and the solid solutions based on them $PbS_{1-z}Se_z$ as a two-electron donor with negative correlation energy. It is shown that an analysis of the Mössbauer spectroscopic data within the framework of such a model allows one to experimentally determine the Hubbard energy.

Synthesis of samples and the technique used for measuring the Mössbauer spectra of ^{119}Sn are described in Ref. 8.

2. EXPERIMENTAL RESULTS AND DISCUSSION

Figure 1 shows Mössbauer spectra of ^{119}Sn at 80 K for the solid solutions $Pb_{1-x-y}Sn_xA_yS$ with different ratios of the tin and acceptor concentrations N_{Sn} and N_A. For compositions with acceptor content $0<y<2x$ the spectra consist of a superposition of two lines whose isomeric shifts correspond to Sn^{2+} and Sn^{4+}. The fraction of Sn^{4+} centers,

$$P=N_{Sn^{4+}}/(N_{Sn^{2+}}+N_{Sn^{4+}}),$$

(here $N_{Sn^{2+}}$ and $N_{Sn^{4+}}$ are the concentrations of the Sn^{2+} and Sn^{4+} centers) is directly proportional to the acceptor concentration, and the proportionality coefficient is equal to 2 (see Fig. 2). Thus, tin in PbS is a two-electron donor: the Sn^{2+} and Sn^{4+} ions correspond to neutral ($[Sn]^0$) and doubly ionized ($[Sn]^{2+}$) tin centers. The electrical neutrality equation has the form

$$2N_{Sn^{4+}}=N_A-p, \tag{1}$$

and the hole concentration p can be ignored since at 80 K, $N_{Sn}\gg p$ for all of the investigated samples. Since all of the samples with composition $0<y\ll 2x$ are hole-type and the hole concentration depends on the temperature ($p=6\times10^{13}$ cm^{-3} at 80 K and $p=10^{19}$ cm^{-3} at 300 K), the Fermi level E_F associated with the partially ionized tin donor-level is situated in the lower half of the band gap. Such a picture of the behavior of tin is found to be in agreement with the temperature data on the electrical conductivity, thermal voltage, and Hall coefficient for the solid solutions $Pb_{1-x-y}Sn_xA_yS$ (Ref. 9).

Theoretical analysis of the behavior of impurity atoms capable of giving up (accepting) two electrons (''two-electron centers'') was carried out for the first time by Hubbard.[10] Two bands of localized states, which are separated by the intratomic energy (the Hubbard energy or correlation energy)[11], are formed in the band gap of a semiconductor in this case[11]

$$U=E_2-E_1, \tag{2}$$

 1063-7826/97/020181-05$10.00

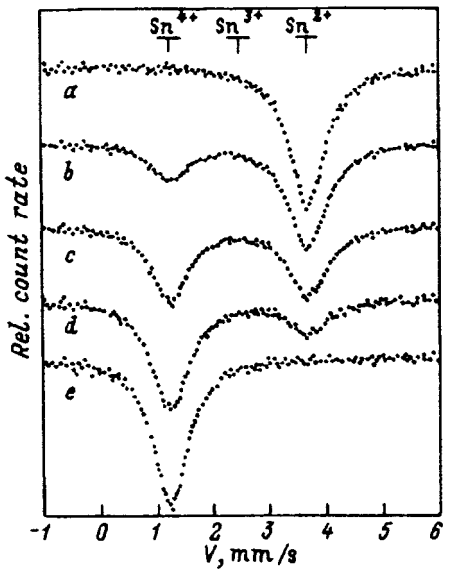

FIG. 1. Mössbauer spectra in ^{119}Sn of the solid solutions $Pb_{0.99-x}Sn_{0.01}A_yS$ at 80 K for $y=0$ (a), 0.005 (b), 0.01 (c), 0.015 (d), 0.02 (e). The positions of the spectral lines of the spectra for the Sn^{4+}, Sn^{3+}, and Sn^{2+} centers are shown.

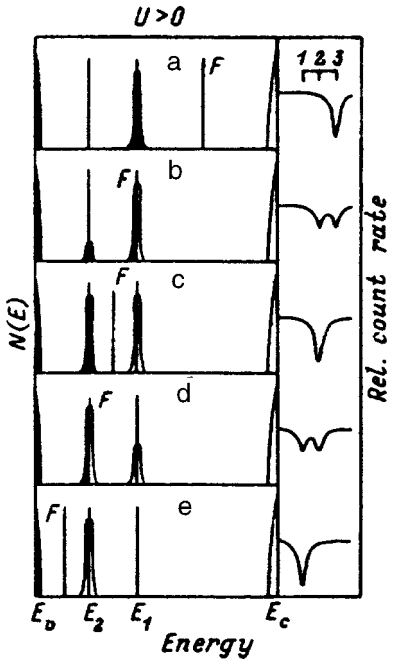

FIG. 3. Density of states for $Pb_{1-x-y}Sn_xA_yS$ in the case $U>0$. $N_A=0$ (a), $0.5N_{Sn}$ (b), N_{Sn} (c), $1.5N_{Sn}$ (d), and $2N_{Sn}$ (e). The hatched and unhatched regions of the E_1 band correspond, respectively, to the neutral (i.e., Sn^{2+}) and the singly ionized (i.e., Sn^{3+}) tin centers (denoted as $[Sn]^0$ and $[Sn]^+$, respectively). The hatched and unhatched regions of the E_2 band correspond, respectively, to the singly ionized and doubly ionized (i.e., Sn^{4+}) tin centers (denoted as $[Sn]^{2+}$). The expected forms of the Mössbauer spectra are shown on the right; the line positions corresponding to the ions are shown above: *1*—Sn^{4+}, *2*—Sn^{3+}, and *3*—Sn^{2+}.

where E_1 and E_2 are the first and second ionization energies of the center.

The distribution of the density of states as a function of degree of compensation for the solid solution $Pb_{1-x-y}Sn_xA_yS$ is given in Refs. 3 and 4 for $U>0$ and $U<0$ (we have used the results of Ref. 11 here). These figures show the expected shapes of the Mössbauer spectra of ^{119}Sn. Comparison of the experimental (Fig. 1) and theoretical (Figs. 3 and 4) Mössbauer spectra unmistakably indicates that $U<0$ for two-electron tin centers in PbS.

The situation is not radically altered for the solid solutions $Pb_{1-x-y}Sn_xA_ySe$: for partially compensated samples

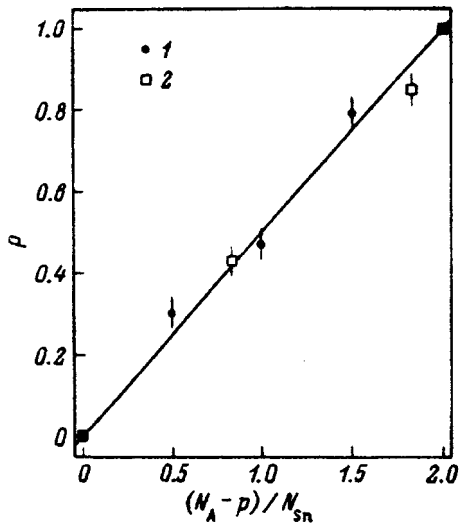

FIG. 2. Dependence of the fraction P of Sn^{4+} centers at 80 K on the acceptor concentration for the solid solutions $Pb_{10.99-x}Sn_{0.01}A_yS$ (*1*) and $Pb_{10.99-x}Sn_{0.01}A_ySe$ (*2*). In the determination from the Mössbauer spectra of the Sn^{2+} and Sn^{4+} center concentrations the ratio of the Mössbauer coefficients for these centers was assumed to be equal to 0.93(1).[8]

$(0<y<2x)$ the Mössbauer spectra of ^{119}Sn at 80 K consist of a superposition of Sn^{2+} and Sn^{4+} lines (Fig. 5); however, the fraction of Sn^{4+} centers is proportional to N_A-p (Fig. 2). This is explained by the fact that in PbSe the Fermi level associated with the partially ionized tin donor-level is located below the top of the valence band (all samples with $0<y<2x$ were hole-type and degenerate with $p\approx10^{19}$ cm^{-3} at 80 K and 295 K) and in the electrical neutrality equation it is necessary to allow for the hole concentration, which is comparable to the tin concentration.

Thus, in PbSe the parameter $U<0$ and the tin centers are two-electron centers. However, the tin energy levels are found among the allowed states of the valence band. Note that this conclusion is in agreement with the temperature data on the electrical conductivity, thermal voltage, and Hall coefficient for the solid solutions $Pb_{1-x-y}Sn_xA_ySe$.[3,9] Figure 6 shows the distribution of the density of states for partially compensated $Pb_{1-x-y}Sn_xA_ySe$.

Figure 7 plots P as a function of z for the solid solutions $Pb_{1-x-y}Sn_xA_yS_{1-z}Se_z$ which contain identical concentrations of tin and the acceptor impurity $(x=y)$. It can be seen that for $z<0.7$ we have $N_{Sn^{2+}}=N_{Sn^{4+}}$, whereas for the compositions with $z>0.7$ we have $N_{Sn^{2+}}>N_{Sn^{4+}}$. Since all samples were hole-type, we may conclude that for the solid solutions with $z>0.7$ we must allow for the hole concentration in the electrical neutrality equation since the Fermi level associated with the partially ionized tin level lies below the top of the valence band.

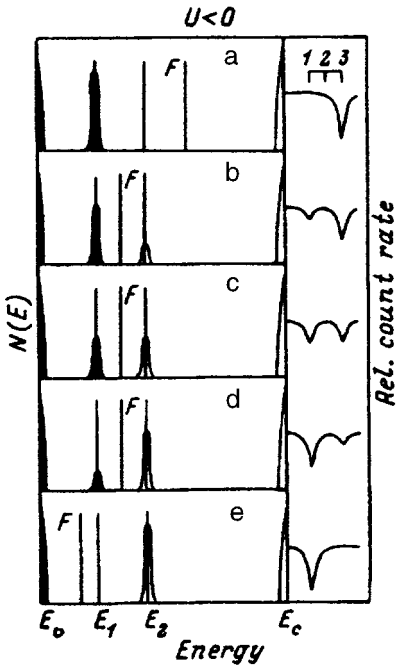

FIG. 4. Density of states for $Pb_{1-x-y}Sn_xA_yS$ in the case $U<0$. $N_A=0$ (a), $0.5N_{Sn}$ (b), N_{Sn} (c), $1.5N_{Sn}$ (d), and $2N_{Sn}$ (e). The hatched regions of the E_1 band correspond to the neutral (i.e., Sn^{2+}) tin centers (denoted as $[Sn]^0$), and the unhatched regions of the E_2 band correspond to the doubly ionized (i.e., Sn^{4+}) tin centers (denoted as $[Sn]^{2+}$). The expected forms of the Mössbauer spectra in ^{119}Sn are shown on the right; the line positions corresponding to the ions are shown above: *1*—Sn^{4+}, *2*—Sn^{3+}, and *3*—Sn^{2+}.

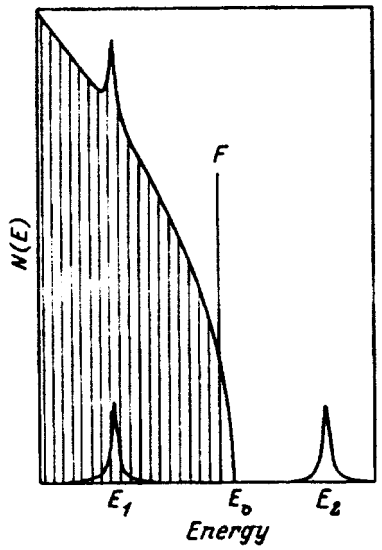

FIG. 6. Density of states for the case $Pb_{1-x-y}Sn_xA_ySe$ ($U<0$) when $x=y$. The explanation is given in the caption of Fig. 4.

It is significant that in the $Pb_{1-x-y}Sn_xA_yS$ and $Pb_{1-x-y}Sn_xA_ySe$ samples which contain only one tin state [Sn^{2+} for $y=0$ and Sn^{4+} for $y>2x$ (see Fig. 1)] the width of the Mössbauer spectra is close to the instrumental width [0.77(2) mm/s] and does not depend on either the composition of the solid solution or the measurement temperature (80–295 K). The closeness of the width of the experimental lines in the spectra of the solid solutions to the instrumental width rules out the possibility of resolving the spectra into quadrupole doublets. In other words, using Mössbauer spectroscopy, special efforts to search for differences in the symmetry of the local environment of the Sn^{2+} and Sn^{4+} centers lead to the conclusion that the local environments of the Sn^{2+} and Sn^{4+} centers are identical (the tin ions are located at the centers of regular octahedra of chalcogenide atoms) and that they do not depend on either the composition of the solid solution or the temperature. Different kinds of associates of Sn^{4+} centers with lattice defects and ionized acceptors are found only for incompletely homogenized materials,

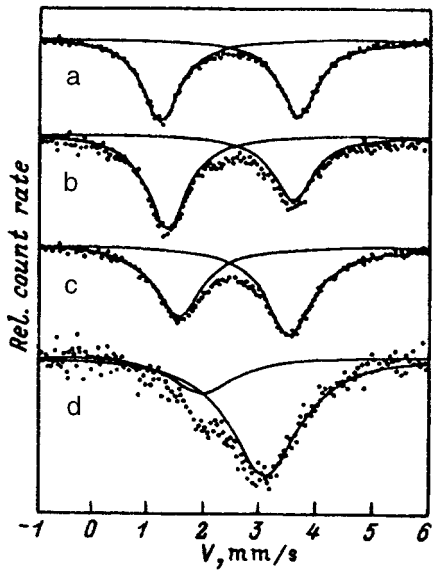

FIG. 5. Mössbauer spectra in ^{119}Sn for the solid solutions $Pb_{0.96}Sn_{0.02}Na_{0.01}Tl_{0.01}S$ (a,b) and $Pb_{0.96}Sn_{0.02}Na_{0.01}Tl_{0.01}Se$ (c,d) at 80 K (a,c) and 295 K (b,d).

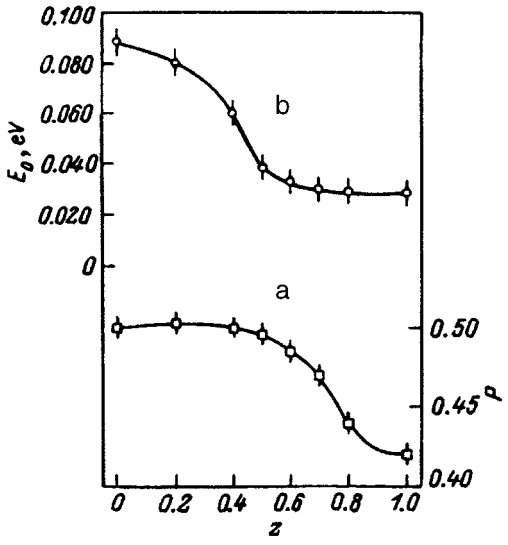

FIG. 7. Dependence of the fraction P of Sn^{4+} centers (a) and activation energy of the electron transfer between tin centers E_0 (b) on z for the solid solutions $Pb_{0.96}Sn_{0.02}Na_{0.01}Tl_{0.01}S_{1-z}Se_z$.

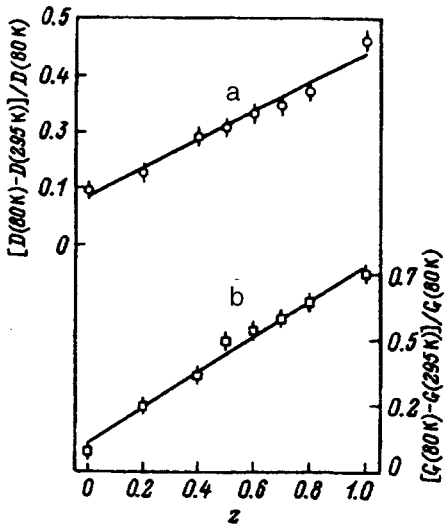

FIG. 8. The z dependence of the relative change in the distance between the Sn^{2+} and Sn^{4+} lines (a) and the widths of these lines (b) when the temperature is raised from 80 to 295 K for the solid solutions $Pb_{0.96}Sn_{0.02}Na_{0.01}Tl_{0.01}S_{1-z}Se_z$. Here $D(80\ \mathrm{K})$ and $D(295\ \mathrm{K})$ are the distances (in mm/s) between the Sn^{2+} and Sn^{4+} lines at 80 and 295 K, respectively; $G(80\ \mathrm{K})$ and $G(295\ \mathrm{K})$ are the widths (in mm/s) of the Sn^{2+} spectrum at 80 and 295 K, respectively.

but in this case they make up less than 10% of the total concentration.[12]

However, for solid solutions that contain Sn^{2+} in addition to Sn^{4+} centers, the widths and the isomeric shifts of the Sn^{2+} and Sn^{4+} spectral lines depend on the temperature at which the spectra are measured. We examined such trends for solid solutions $PbS_{1-z}Se_z$ containing identical tin and acceptor concentrations ($Pb_{0.96}Sn_{0.02}Na_{0.01}Tl_{0.01}S_{1-z}Se_z$, $0<z<1$). For all of the samples, raising the temperature from 80 to 295 K was accompanied by a convergence of the Sn^{2+} and Sn^{4+} lines (Fig. 5), and, as can be seen from Fig. 8, this convergence increases with increasing z. We see that the widths of the Sn^{2+} and Sn^{4+} lines increase at the same time (Fig. 8).

Such temperature dependences of the line widths and isomeric line shifts are characteristic of the case of electron transfer between two charge states of the Mössbauer atom when the lifetime of each of the states is comparable to the lifetime of the Mössbauer level (for ^{119}Sn this time is on the order of 20 ns). We measured the frequency of electron transfer between the Sn^{2+} and Sn^{4+} states in the solid solutions $Pb_{0.96}Sn_{0.02}Na_{0.01}Tl_{0.01}S_{1-z}Se_z$ in the temperature interval 80–295 K. The activation energy of the process, E_o, is plotted as a function of z in Fig. 7. It can be seen that as the selenium content z increases, E_o at first decreases monotonically, reaching a limiting value of 0.029 eV at $z=0.7$, and then remains constant within measurement error limits. A comparison of the dependences $P(z)$ and $E_o(z)$ (Fig. 7) allows us to conclude that E_o reaches its limiting value at the same value of z at which the Fermi level enters the valence band.

Finally, it would be desirable to broaden the temperature interval of the E_o measurements. However, for the solid solution $Pb_{0.96}Sn_{0.02}Na_{0.01}Tl_{0.01}S_{1-z}Se$ a temperature increase is accompanied by an abrupt growth of the ratio R of the area under the Sn^{2+} and Sn^{4+} spectra ([$R=1.25(2)$ at 80 K and $R=3.61(5)$ at 295 K], which is linked with a growth of the depth of the tin energy levels in the valence band. Analysis shows that this should lead to an overestimate of E_o (see, for example, Ref. 13, where the temperature interval of the E_o measurements was extended up to 373 K. As a result, an exaggerated value of E_o was obtained).

Two mechanisms of electron transfer between the Sn^{2+} and Sn^{4+} centers are possible: electron tunneling transport directly between the tin ions and electron transport via the states of the valence band. The frequency of electron transfer in the first model should depend on the concentration of the tin impurity atoms, rather than on the temperature. Since the rate of convergence of the Sn^{2+} and Sn^{4+} lines in the Mössbauer spectra of $Pb_{1-x-y}Sn_xA_ySe$ was found to be independent of the tin concentration ($0.01<x<0.05$) and since the rate of convergence depends on the temperature, we can disregard the direct transfer between the tin centers.

A consideration of the density of states in Figs. 6 and 4 shows that for $z<0.7$, when the tin donor states lie in the band gap, the energy of the electron transfer process is

$$E_o=(F-E_v)+U/2 \tag{3}$$

and the decrease in E_o with growth of z in this range indicates a closing up of the gap between the Fermi level and the top of the valence band. For $z>0.7$, when the tin donor states lie in the valence band, the activation energy is

$$E_o=U/2 \tag{4}$$

and, consequently, we were able to experimentally determine the intratomic energy for the tin centers in $PbS_{1-z}Se_z$ ($z>0.7$) to be equal to 0.058(5) eV.

3. CONCLUSIONS

Using Mössbauer spectroscopy we have demonstrated that an isovalent tin impurity in the solid solutions $PbS_{1-z}Se_z$ forms two-electron donor centers with negative correlation energy, where the energy levels associated with the tin impurity are situated in the lower half of the band gap for $z<0.7$ and are set against the background of the allowed states of the valence band for $z>0.7$. We have shown that the activation energy E_o of electron transfer between the neutral and ionized tin centers decreases monotonically with growth of z, which reflects the movement of the tin energy levels toward the top of the valence band, and for $z>0.7$ $E_o=U/2$ (U is the Hubbard energy).

This work was carried out with the financial support of the Russian Fund for Fundamental Research (Grant No. 96-02-16957a).

[1] F. S. Nasredinov, L. V. Prokof'eva, and P. P. Seregin, Zh. Éksp. Teor. Fiz. **87**, 951 (1984) [Sov. Phys. JETP **60**, 542 (1984)].
[2] F. S. Nasredinov, L. V. Prokofieva, P. P. Seregin, S. V. Zarubo, A. V. Ermolaev, and A. N. Kurmantaev, Phys. Status Solidi B **130**, 727 (1985).
[3] G. T. Alekseeva, E. A. Gurieva, P. P. Konstantinov, N. V. Maksimova, and L. V. Prokof'eva, Fiz. Tekh. Poluprovodn. **29**, 1388 (1995) [Semiconductors **29**, 719 (1995)].
[4] F. S. Nasredinov, E. Yu. Turaev, P. P. Seregin, N. B. Rakhmatullaev, and M. K. Bakhadyrkhanov, Phys. Status Solidi A **121**, 571 (1990).

[5] V. F. Masterov, F. S. Nasredinov, S. A. Nemov, and P. P. Seregin, Fiz. Tekh. Poluprovodn. **30**, 840 (1996) [Semiconductors **30**, 450 (1996)].
[6] A. N. Veĭs and L. V. Prokof'eva, Fiz. Tekh. Poluprovodn. **21**, 743 (1987) [Sov. Phys. Semicond. **21**, 455 (1987)].
[7] A. N. Veĭs and N. A. Suvorova, Fiz. Tekh. Poluprovodn. **29**, 278 (1995) [Semiconductors **29**, 138 (1995)].
[8] V. F. Masterov, F. S. Nasredinov, S. A. Nemov, and P. P. Seregin, Fiz. Tekh. Poluprovodn. **30**, 884 (1996) [Semiconductors **30**, 472 (1996)].
[9] L. V. Prokof'eva, S. V. Zarubo, M. N. Vinogradova, Yu. A. Nikulin, and K. G. Gartsman, Fiz. Tekh. Poluprovodn. **16**, 2136 (1982) [Sov. Phys. Semicond. **16**, 1377 (1982)].
[10] J. Hubbard, Proc. R. Soc. A **276**, 238 (1963).
[11] D. Adler and E. J. Yoffa, Phys. Rev. Lett. **36**, 1197 (1976).
[12] F. S. Nasredinov, L. V. Prokov'eva, A. N. Kurmantaev, and P. P. Seregin, Fiz. Tverd. Tela **26**, 862 (1984) [Sov. Phys. Solid State **26**, 522 (1984)].
[13] B. G. Zemskov, V. S. Lyubimov, A. N. Martynyuk, A. A. Artemova, Yu. V. Permyakov, and S. P. Ionov, Fiz. Tekh. Poluprovodn. **22**, 934 (1988) [Sov. Phys. Semicond. **22**, 590 (1988)].

Translated by Paul F. Schippnick

Effect of thermal annealing on the luminescence properties of ZnCdSe/ZnSe quantum-well structures

E. M. Dianov, P. A. Trubenko, E. É. Filimonov, and E. A. Shcherbakov

Fiber-Optics Scientific Center, Institute of General Physics, Russian Academy of Sciences, 117942 Moscow, Russia

(Submitted April 8, 1996; accepted for publication April 24, 1996)
Fiz. Tekh. Poluprovodn. **31**, 296–298 (February 1997)

The thermal stability and luminescence properties of ZnCdSe/ZnSe quantum-well structures grown by molecular-beam epitaxy are investigated. A comparative analysis is made of the photoluminescence spectra of the structures before and after annealing. In the sample spectra after annealing (at 500 °C) a decrease in the intensity of the exciton luminescence line by more than two orders of magnitude, accompanied by an increase in the intensity of the deep levels, is observed. As a result of annealing at a lower temperature (about 400 °C), a narrowing of the exciton luminescence, accompanied by a shift of the maximum toward longer wavelengths, was detected. © *1997 American Institute of Physics.* [S1063-7826(97)01902-9]

1. INTRODUCTION

A large number of papers, dealing with the study of II–V materials, in particular, ZnSe and ZnCdSe, which are promising for creating blue-green semiconductor injection lasers, have recently been published.[1,2] An important consideration here is the thermal stability of such laser structures. From this point of view, a study of thermal stability and interdiffusion processes in $Zn_{1-x}Cd_xSe/ZnSe$ compounds is of great interest. It should be noted that such structures are usually grown on GaAs substrates which have the same structure and a similar lattice constant—the mismatch between GaAs and ZnSe is 0.27%. In a structure consisting of a set of $Zn_{1-x}Cd_xSe/ZnSe$ quantum wells the internal strains are associated with differences in the lattice constants. It can be assumed that annealing such structures should relax these strains, in the process altering the effective width of the superlattice band gap and decreasing the width of the exciton luminescence line. Luminescence spectra of $Zn_{0.8}Cd_{0.2}Se/ZnSe$ superlattices were obtained in Refs. 3 and 4 at 1.4 K before and after annealing in a steady flow of selenium vapor at 400 and 600 °C for 4.5 h, where the structure remained stable to the annealing process. On the other hand, high-resolution transillumination-electron-microscope data on the results of Cd diffusion during thermal annealing of CdSe/ZnSe quantum-well structures were reported in Ref. 5. The samples were annealed for one hour at temperatures in the range 340–400 °C. It was found that the cadmium diffusion coefficient $D(T)$ in ZnSe in this temperature range is equal to $1.9\times10^{-4}\ [\mathrm{cm^2/s}]\exp(-1.8[\mathrm{eV}]/kT)$. These results contradict the data of Refs. 3 and 4.

In the present paper we report the results of an experimental study of the effect of thermal annealing on the luminescence properties of $Zn_{1-x}Cd_xSe/ZnSe$ quantum-well structures.

2. EXPERIMENT

The quantum-well structures were grown by molecular-beam epitaxy. To grow these structures we used separate effusion cells for each element: Zn, Cd, Se. Growth took place on GaAs (100) substrates with a 3° de-orientation in the (011) direction. Details of the growth process are given in Ref. 6. The surface morphology of the structure during the growth process was monitored by fast-electron reflection diffraction with an accelerating voltage of 10 kV. The effect of annealing was investigated on a $Zn_{1-x}Cd_xSe/ZnSe$ quantum-well structure consisting of a buffer layer of ZnSe (156 nm) and a 90-period quantum-well structure (5.2 nm $Zn_{0.86}Cd_{0.14}S$, 5.2 nm ZnSe) and a cover layer of ZnSe (78 nm) (Fig. 1).

With the aim of investigating the thermal stability and interdiffusion processes on the luminescence properties of quantum-well structures with strained layers, the samples were subjected to ''impact'' heating to temperatures of 400 and 500 °C. The time of heating to the prescribed temperature was 50 s, and the samples were subjected to an additional anneal at 400 °C for 5 min. The structures before and after annealing were examined by the low-temperature photoluminescence method at 11 K. As the excitation source we used a mercury lamp, from the radiation spectrum of which we separated out the 3.396-eV ultraviolet line (365 nm) with irradiance 50 $\mathrm{mW/cm^2}$. The photoluminescence radiation was passed through an MDR-6 monochromator and recorded by a Spectroscopy Instruments linear diode array. The video signal so obtained was processed on an O-SMA ST-100 controller.

3. DISCUSSION OF RESULTS

The results of our study of the luminescence properties of $Zn_{1-x}Cd_xSe/ZnSe$ quantum-well structures before and after annealing are shown in Figs. 1 and 3. In the spectra of the unannealed samples we observed an intense blue line which corresponds to recombination of heavy holes and electrons in the $Zn_{1-x}Cd_xSe/ZnSe$ quantum wells. In the red region a self-activated luminescence band with a maximum at 1.95 eV, which corresponds to deep layers in the ZnSe buffer layer, is observed. This band is caused by the presence of

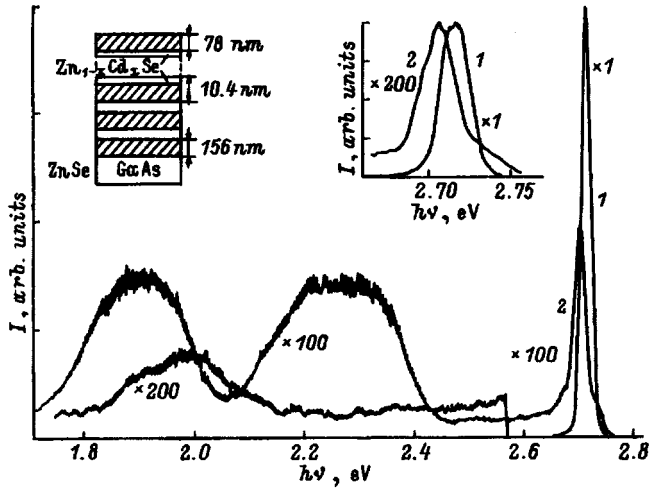

FIG. 1. Photoluminescence spectra at 11 K before annealing (*1*) and after annealing (*2*) at 500 °C, 50 s. Inset: on the left, diagram of the arrangement of layers of the quantum-well structure, on the right, photoluminescence in the region of the exciton luminescence.

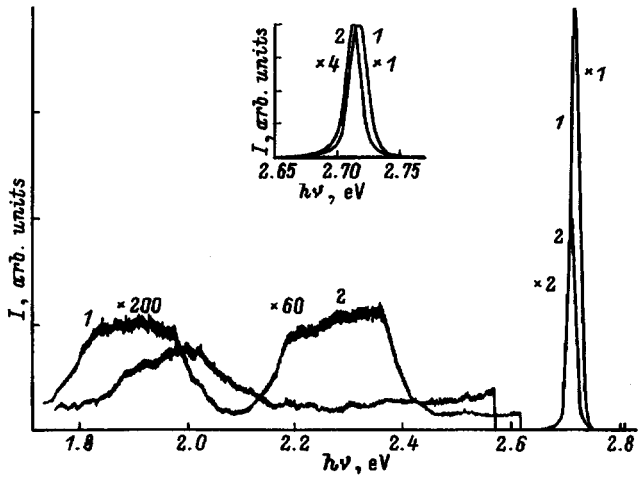

FIG. 3. Photoluminescence spectra at 11 K before annealing (*1*) and after annealing (*2*) at 400 °C, 5 min. Inset: photoluminescence in the region of the exciton luminescence.

zinc vacancies V_{Zn}^- and/or complexes of vacancies of zinc and gallium atoms $(V_{Zn}–Ga_{Zn})^-$ in the zinc sublattice.[7] During thermal annealing characteristic behavior of the intensity of the exciton luminescence line is observed. The degree to which the intensity decreases depends on the time and the annealing temperature. When the samples are annealed at 500 °C for 50 s (Fig. 1), the intensity of the exciton luminescence falls by more than two orders of magnitude. In addition, an increase in the intensity of the luminescence band of the deep levels is observed in the spectra of the annealed samples, together with the appearance of a new maximum in the lower energy region (1.89 eV). Here it is necessary to give our attention to the dynamics of the displacement of the maximum (1.89 eV) into the lower energy region as a function of temperature and anneal time. The increase in the intensity of the luminescence band of the deep levels (1.95 eV) is caused by an increase in the concentration of the zinc

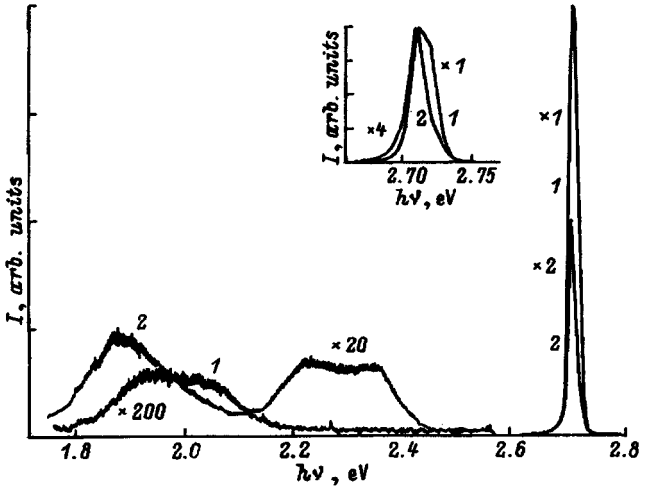

FIG. 2. Photoluminescence spectra at 11 K before annealing (*1*) and after annealing (*2*) at 400 °C, 50 s. Inset: photoluminescence in the region of the exciton luminescence.

vacancies V_{Zn}^- and/or $(V_{Zn}–Ga_{Zn})^-$ complexes in the ZnSe buffer layer. The shift of the luminescence maximum of the deep layers is apparently a manifestation of the fact that $(V_{Zn}–Ga_{Zn})^-$ complexes also arise in the $Zn_{1-x}CD_xSe$ layers as a result of gallium diffusion from the substrate. This conclusion is supported by the magnitude of the shift, which essentially coincides with the energy difference in the ZnSe and $Zn_{1-x}Cd_xSe$ band gaps. In addition, a new wide luminescence band is observed in the photoluminescence spectra of the annealed samples in the energy region 2.1–2.4 eV, whose nature is still not clear. The half-width of the exciton luminescence line was observed to decrease by 1 and 4.7 meV, respectively, when the sample was annealed at 400 °C for 50 s and 5 min (Figs. 2 and 3). The decrease in the half-width is connected with a partial relaxation of the internal strains between the ZnSe and $Zn_{1-x}Cd_xSe$ layers, which amount to $\varepsilon=0.1$ at a cadmium concentration of 14% as a result of cadmium diffusion and the formation of mismatch dislocations. In the case where the sample was annealed for 50 s at 500 °C the half-width of the exciton luminescence line increases by 6.5 eV (Fig. 1) due to processes of crystal structure degradation. A low-energy shift of the maximum of the exciton luminescence line is observed in the spectra of all the annealed samples in comparison with its position in the spectra of the same samples before annealing. The largest shift is observed for the sample annealed at 500 °C for 50 s—10 meV (Fig. 1). The shift of the maximum of the exciton luminescence line is explained by cadmium diffusion, which leads to an increase in the well width and therefore to a shift of the energy levels in the well. It should be added that due to the diffusion of cadmium, its concentration in the well decreases and a concentration profile appears across the thickness of the well, which leads to additional broadening of the line. Knowing the diffusion coefficient for cadmium in ZnSe, it is possible to estimate the amount of spreading of the well. The diffusion coefficient at 500 °C, D_{Cd}(500 °C), is approximately equal to 3.5×10^{-16} cm^2/s. The diffusion length can be estimated from the formula $l_D=\sqrt{2\cdot D(T)^*t}$. It follows that $l_D=1.17$ nm after 20 s (allowing for the fact

that considerable diffusion takes place at temperatures greater than 350 °C). Thus, the width of the quantum well after annealing should be on the order of 7.5 nm, in fairly good agreement with the value of 10 meV for the shift of the exciton luminescence peak, which corresponds to an increase of the well width by this amount.

4. CONCLUSIONS

We have presented the results of an experimental study of the luminescence properties of $Zn_{1-x}Cd_xSe$ quantum-well structures. $Zn_{1-x}Cd_xSe$/ZnSe quantum-well structures were subjected to thermal annealing and a comparative analysis of the photoluminescence spectra of the annealed and unannealed samples was carried out. The characteristic decrease in the intensity of the exciton luminescence line was observed in the spectra of the annealed samples, and an increase in the intensity of the luminescence of the deep levels. Annealing was found to result in a narrowing of the exciton luminescence line (at 400 °C) and a displacement of the maximum toward longer wavelengths, which is explained by cadmium diffusion into the ZnSe barrier layers.

[1] M. A. Haase, J. Qiu, J. M. De Puydt, and H. Cheng, Appl. Phys. Lett. **59**, 1272 (1991).
[2] G. Landwehr and D. Hommel, Phys. Status Solidi B **187**, 269 (1995).
[3] T. Yokogawa, P. D. Floyd, J. L. Merz, H. Luo, and J. K. Furdyna, J. Cryst. Growth **138**, 564 (1994).
[4] T. Yokogawa, J. L. Merz, H. Luo, J. K. Furdyna, S. Lau, M. Kuttler, and D. Bimberg, Jpn. J. Appl. Phys. **34**, 1159 (1995).
[5] A. Rosenauer, T. Reisinger, E. Steinkirchner, J. Zweck, and W. Gebhardt, J. Crystl. Growth **152**, 42 (1995).
[6] E. M. Dianov, A. M. Prokhorov, P. A. Trubenko, and E. A. Shcherbakov, Fiz. Tekh. Poluprovodn. **28**, 1278 (1994) [Semicond. **28**, 725 (1994)].
[7] J. Gutowski, N. Presser, G. Kudlek, Phys. Status Solidi A **120**, 11 (1990).

Translated by Paul F. Schippnick

Formation of radiation defects in high-resistivity silicon as a result of cyclic irradiation and annealing

E. M. Verbitskaya, V. K. Eremin, and A. M. Ivanov

A. F. Ioffe Physicotechnical Institute, Russian Academy of Sciences, 194021 St. Petersburg, Russia

Z. Li

Brookhaven National Laboratory, Upton, New York 11973, USA

B. Schmidt

Institute for the Physics of Ion Beams and Material Science, Rossendorf Research Center, D-01314 Dresden, Germany

(Submitted April 12, 1996; accepted for publication April 24, 1996)
Fiz. Tekh. Poluprovodn. **31**, 299–304 (February 1997)

Transformation of radiation-induced defects in p^+-n-n^+ structures fabricated from high-resistivity n-type silicon subjected to cyclic irradiation and annealing is investigated. The kinetic behavior of the increase in the concentration of the C_i-O_i defects is analyzed as a function of the detector fabrication process. During the second irradiation cycle a transformation of the defects, which were formed as a result of annealing of the original radiation defects, is observed. The appearance of ''hidden'' sources of deep center formation is revealed. It is established that the presence of a higher oxygen concentration, which arises in the samples as a result of the extended silicon oxidation process, results in a more active complex-formation of carbon-containing defects in comparison with samples with reduced oxygen content. © *1997 American Institute of Physics.* [S1063-7826(97)02002-4]

1. INTRODUCTION

The change in the properties of semiconductor devices exposed to radiation is without any doubt a serious problem from the point of view of practical applications. It is well known that compensation of impurities and defects in the interior of a semiconductor by radiation defects leads to an abrupt growth of its resistivity and to changes in the effective charge concentration in the space charge region. In nuclear radiation detectors based on high-resistivity silicon proposed for use in powerful radiation fields, the effect of ''reverse'' annealing arises.[1] The concept of reverse annealing includes changes in the effective charge concentration in the space-charge region during storage of a diode previously exposed to strong radiation. This effect has been studied in detail in experiments on the action of penetrating radiation (e.g., 1-MeV fast neutrons).[2,3] Reverse annealing stems from the instability of the radiation defects that arise immediately after irradiation; however, at present an unambiguous explanation is lacking.

It is well known that the most active impurities participating in the formation of radiation defects are oxygen and carbon. The latter enters into the composition of deep radiation centers which do not have a high stability and which have a metastable nature.[4,5] All these factors allow us to assume that the radiation-generated, carbon-containing centers are responsible for the changes in the characteristics of silicon devices immediately after exposure to radiation.

In earlier studies[6,7] we investigated the effect of the raw material and fabrication technology of the silicon detectors on the restructuring of the radiation defects associated with carbon. We focused our main attention on the rate of annealing of the deep centers of interstitial carbon (C_i) formed in substitution reactions with the primary radiation defect—interstitial silicon. In the present paper we analyze the behavior of the defects arising as a result of annealing of interstitial carbon at temperatures close to room temperature, and also after thermal annealing in the temperature range 250–400 °C.

2. TEST SAMPLES AND EXPERIMENTAL TECHNIQUE

We examined detectors based on p^+-n-n^+ structures made from silicon by zone melting (FZ-Si), of n-type conductivity, with resistivity $\rho=1-5$ k$\Omega\cdot$cm. The silicon sources were Wacker Chemitronics ($\rho=5$ k$\Omega\cdot$cm) and Freiberg Elektronikwerkstoffe GmbH ($\rho=1-2$ k$\Omega\cdot$cm). The area of the p^+-n junction was 25 mm^2 and the thickness of the samples was 300 μm. The detectors were fabricated by methods of planar technology. The specifications of the fabrication regimes are listed in Table I.

The samples were irradiated by α particles from the radioactive source ^{238}Pu (5.5 MeV) on the p^+-contact side. To stabilize the defects, the samples were irradiated in vacuum at reduced temperature ($\sim$180 K). Between measurements the samples were stored in a cooled state. The irradiation dose was 10^9 cm^{-2}.

To observe the changes in the radiation defects, we used a DLTS setup with a working frequency of 100 kHz and a rate window of (41.7 ms)$^{-1}$.

3. EXPERIMENTAL RESULTS AND DISCUSSION

The DLTS spectrum measured in the minority-carrier-injection regime, characteristic of detectors made from high-

 1063-7826/97/020189-05$10.00

TABLE I. The effect of exposing a sample to high temperature during oxidation.

Sample	Oxidation temperature, °C	Atmosphere	Thickness of oxide, Å	Anneal rate C_i
BNL 213	1100	O_2+TCA	4500	fast
BNL 268-A8	975	O_2	2500	intermediate
FZR 2-1	1000	O_2+3% HCl	1000	slow

Note: TCE stands for trichlorethane.

TABLE II. Parameters of the deep levels.

Type of level	Level energy	Capture cross section σ_n, σ_p, cm^{-2}
$E1$	$E_c - 0.18$ eV	2×10^{-14}
$E2$	$E_c - 0.21$ eV	5×10^{-16}
$E3$	$E_c - 0.40$ eV	2×10^{-16}
$H0$	$E_v + 0.27$ eV	7×10^{-14}
$H1$	$E_v + 0.33$ eV	9×10^{-14}
$H2$	$E_v + 0.40$ eV	3×10^{-14}
$H3$	$E_v + 0.22$ eV	7×10^{-17}

Note: The values of σ_n are given for E_1, E_2, and E_3 and the values of σ_p are given for the other quantities.

resistivity silicon which have been irradiated by α particles, is shown in Fig. 1a, and the parameters of the deep centers that are formed are listed in Table II. Here $E1$ is a center formed from two radiation defects, namely, an A center (oxygen-vacancy) and C_iC_s center (interstitial carbon–carbon at a lattice site); $E3$ is a single-charge divacancy VV^-; $H1$ is a C_i center; $H2$ is a C_i–O_i center (interstitial carbon–interstitial oxygen). As was mentioned in Ref. 7, detectors made from FZ-Si can be subdivided according to the

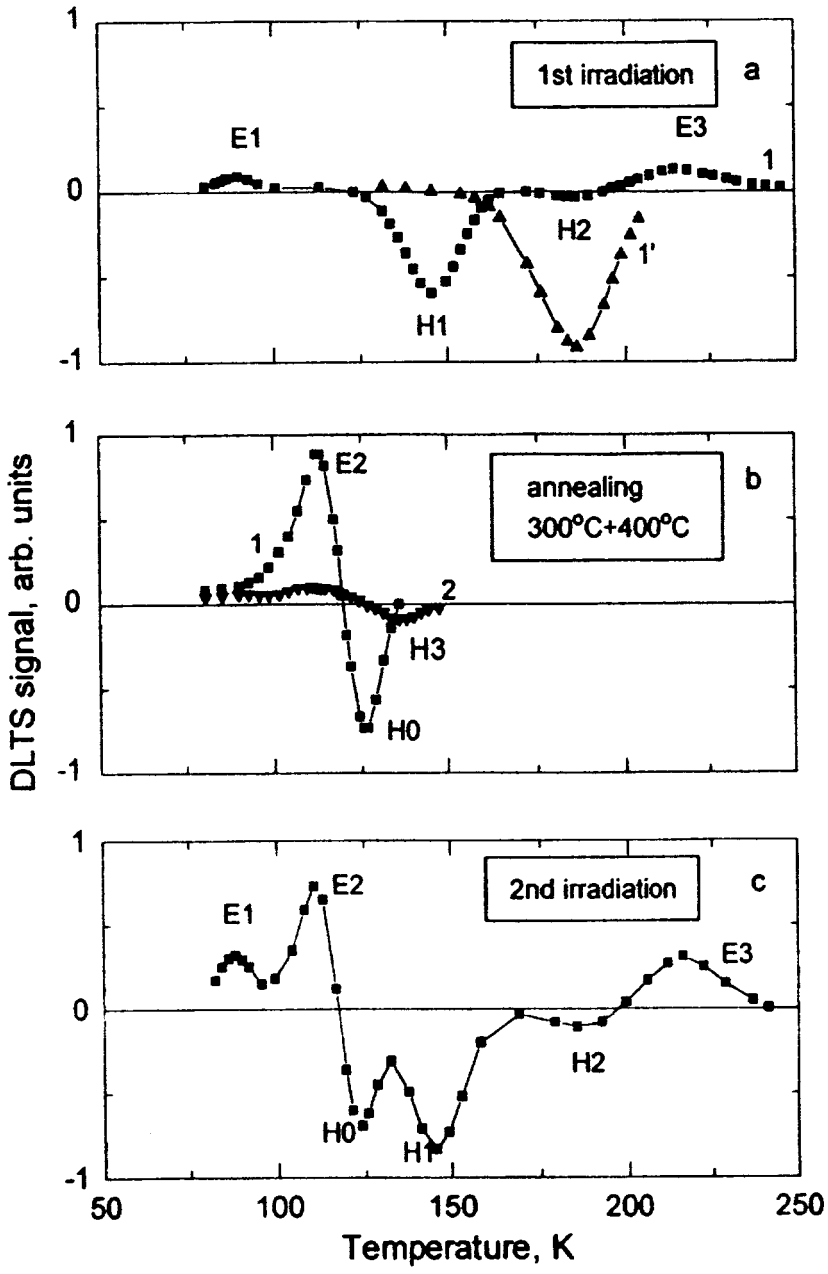

FIG. 1. DLTS spectra in the minority-carrier-injection regime, a) fast sample immediately after initial irradiation (dose 10^9 cm^{-2}) (1) and after annealing at room temperature for 15 h (1′); b) fast sample (*1*) and intermediate (*2*) sample after annealing at 300 °C for 30 min and 400 °C for 45 min; c) fast sample after annealing (see b) and repeated irradiation (dose 10^9 cm^{-2}).

rate of annealing of interstitial carbon into the categories ''fast,'' ''intermediate,'' and ''slow,'' reflecting the fabrication regimes of the devices. In particular, the fast samples are formed during prolonged oxidation at elevated temperatures ($\geqslant$1100 °C), which produces a higher oxygen content in the crystals.[8] The C_i–O_i complex (the *H*2 defect) forms at the same time as C_i is annealed. For the fast sample this process takes place at room temperature and continues even after complete disappearance of C_i. This indicates that the interstitial carbon is present in a state such that it is not observed by DLTS; however, it is capable of taking part in the formation of the C_i–O_i defect. For a better understanding of the nature of the appearance of C_i–O_i deep centers, we have analyzed the nature of the reaction that produces it.

During the annealing of interstitial carbon the following reactions take place:

$$C_i + O_i = C_i - O_i,$$

$$C_i + C_s = C_i - C_s.$$

In Ref. 4 we showed that the temporal variation of the concentration $n_x(t)$ of the C_i defects is described by the monomolecular reaction

$$\frac{dn_x(t)}{dt} = -\frac{n_x(t)}{\tau}, \quad n_x(t) = n_{x0}\exp(-t/\tau), \tag{1}$$

where τ is the time constant of annealing of interstitial carbon and n_{x0} is the initial C_i concentration. Formation of the C_i–O_i complex takes place with the participation of two atoms, whose concentrations are represented by $n_{x1} = n_x$ and n_{x2}. This process can be treated as a pseudo-monomolecular reaction,

$$N_x(t) = n_{x0}[1 - \exp(-t/\tau)], \tag{2}$$

if the concentration of the nascent complexes $N_x(t)$ is determined by the concentration of only one of the reactants, i.e., $n_{x1} \ll n_{x2}$. If the concentrations of the reactants are comparable,

$$n_{x1} = n_{x2} = n_x, \tag{3}$$

then they decrease simultaneously according to the bimolecular reaction

$$\frac{dn_x(t)}{dt} = -kn_x^2(t), \tag{4}$$

where k is the reaction rate constant. For the initial conditions $n_x(0) = n_{x0}$ the concentration increase of the C_i–O_i complexes will then be

$$N(t) = n_{x0} - n_x(t). \tag{5}$$

It is described by the relation

$$N(t) = n_{x0}\left(1 - \frac{1}{1 + kn_{x0}t}\right). \tag{6}$$

Figures 2 and 3 plot the growth of the concentration of the C_i–O_i defects for the fast samples at room temperature and the slow samples at 50 °C, and their approximation by formulas (2) and (6), which correspond respectively to a pseudo-monomolecular reaction and a bimolecular reaction.

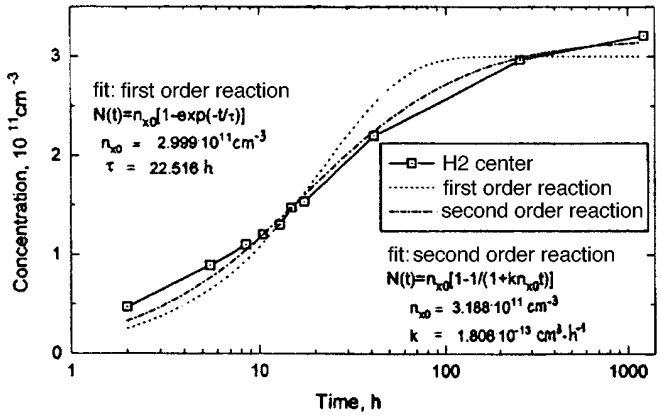

FIG. 2. Growth of C_i–O_i defect concentration in the fast sample at room temperature.

For the fast sample the experimental dependences correspond better to a bimolecular reaction (Fig. 2). Such behavior corresponds to the case in which the variation of the C_i–O_i complex concentration is controlled by both reactants, despite the fact that the interstitial oxygen content in silicon substantially exceeds the interstitial carbon content which arises only as a result of irradiation of the diode. This alows us to assume that the formation of this complex is augmented by a process involving the participation of interstitial carbon atoms not recorded in the DLTS measurements. The significant setup time for saturation of the C_i–O_i concentration and its very large value for the fast sample are apparently linked with the dominant influence of these atoms. At the same time, for the slow sample an increase in the concentration of C_i–O_i essentially ceases after the C_i defects have completely disappeared, which does not allow us to uniquely identify the formation of this complex as a bimolecular reaction (Fig. 3). This indicates the bounded nature of an additional (unrecorded) source of interstitial carbon at temperatures close to room temperature in diodes of the given type in comparison with the fast samples.

In order to investigate the reproducibility of the observed effects, a few samples previously investigated in Ref. 7 were subjected, after storage at room temperature for two years, to annealing to eliminate radiation defects. The annealing was

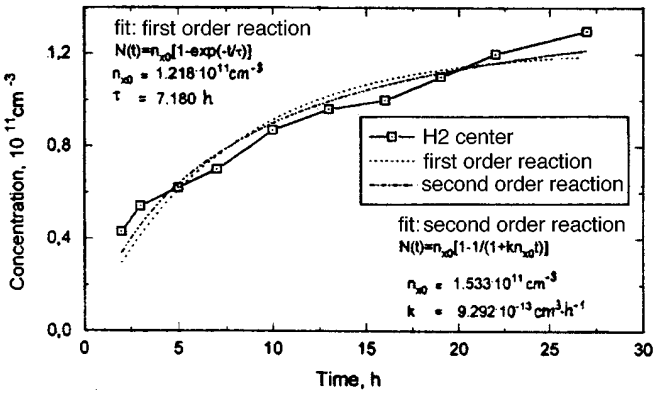

FIG. 3. Growth of C_i–O_i defect concentration in the slow sample at room temperature.

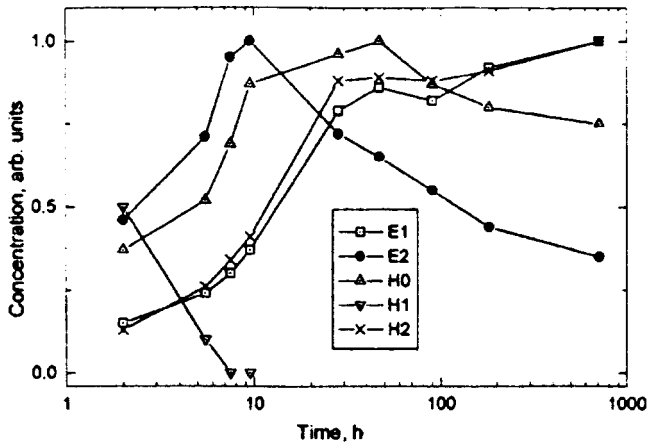

FIG. 4. Variation of the defect concentration at room temperature in the fast sample after annealing and repeated irradiation.

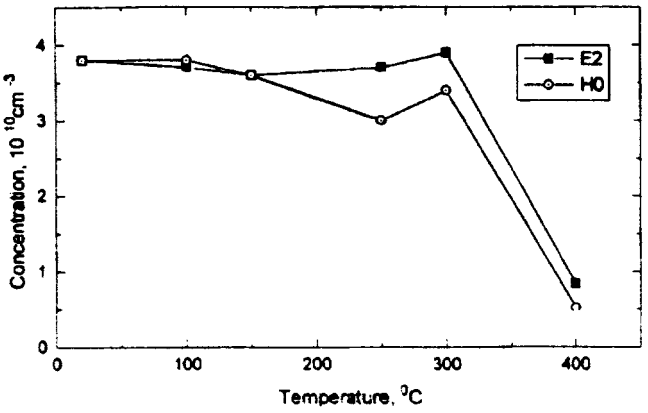

FIG. 5. Isochronous annealing of the fast sample after formation of $E2$ and $H0$ defects.

performed in two steps: at 300 °C for 30 min and at 400 °C for 45 min, after which the samples were again irradiated with α particles with a dose of 10^9 cm^{-2}. The fast, intermediate, and slow samples responded differently to this anneal. Thus, in the fast sample upon complete annealing of the radiation defects, two new defects—$E2$ and $H0$ (Fig. 1b, curve 1)—were formed, and in the intermediate sample instead of the defect $H0$ the defect $H3$ (curve 2) was formed. In both the intermediate and slow samples the defect $E2$ was formed at an insignificant concentration level, which did not vary during subsequent heat processing.

Let us examine the fast sample in greater detail since the initial material for it was silicon from Wacker Chemitronics, which is the most frequent source for fabrication of detectors. The DLTS spectrum in the minority-carrier-injection regime for the fast sample exposed to repeated irradiation is shown in Fig. 1c. Note that the concentration of the $E2$ and $H0$ centers which arose during annealing as a result of decay of the radiation defects increases as a result of the repeated irradiation.

The variation in the concentration of the deep centers during the course of isothermal annealing at room temperature after repeated irradiation of the fast sample is shown in Fig. 4. In addition to the above-mentioned growth of the concentration of the C_i–O_i defects and the $E1$ defects including the C_i–C_s complex (the latter together with the A center forms the DLTS peak), there is also a nonmonotonic variation of the concentration of the $E2$ and $H0$ centers during the annealing of C_i and after its completion: their concentration at first grows and then falls. Noting that restructuring of the carbon centers proceeds at room temperature, we may assume that carbon enters into the composition of the $E2$ and $H0$ centers. Additionally, since the given centers are more actively manifested in the fast samples, i.e., the samples having significantly higher oxygen content, oxygen probably also participates in their formation. Note that the $E2$ and $H0$ centers are very stable. Figure 5 plots data on isochronous annealing of a fast sample after the appearance of these centers. The concentration of the $E2$ and $H0$ centers remains virtually the same up to 300 °C. At the same the only concentration of note that takes place in them occurs in the presentce of the restructuring radiation defects, in particular, of those associated with oxygen, which is observed even at room temperature. The maximum growth of their concentrations coincides with annealing of the C_i centers.

Figure 6 presents results of annealing of a slow sample after repeated irradiation. At 70 °C no growth in the C_i–O_i concentration is observed after annealing of the C_i defects. However, raising the temperature to 250 °C causes an abrupt growth of the concentration of the $H2$ centers. This suggests that a ''hidden'' carbon source, which cannot be detected by the DLTS method, is present in the slow samples. In this case, however, a significantly larger energy is required to free it so that it can participate in the formation of complexes.

4. CONCLUSIONS

Our results confirm the idea that the restructuring of radiation defects depends on the source material and the fabrication technology of silicon diodes. The presence of a higher

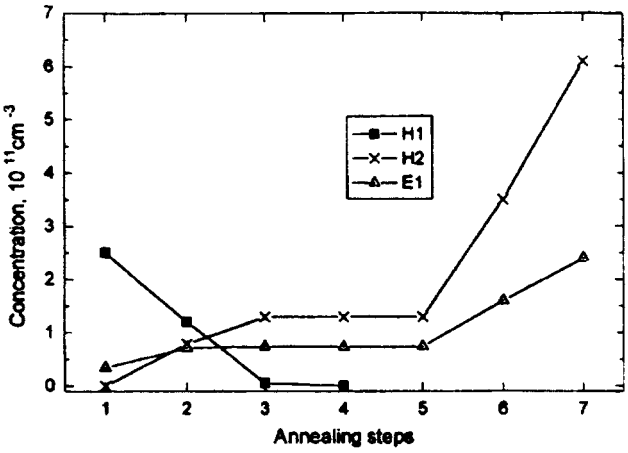

FIG. 6. Annealing of carbon-containing defects in the slow sample after repeated irradiation. Labeling of the abscissa corresponds to the sample immediately after irradiation (*1*) and the stages that follow the annealing: *2*) 70 °C, 1 h, *3*) 70 °C, 3 h, *4*) 70 °C, 3 h, *5*) 70 °C, 2 h, *6*) 250 °C, 1 h, *7*) 300 °C, 1 h.

oxygen concentration arising as a result of prolonged oxidation, even in detectors based on *FZ*-Si, promotes more active complex-formation in comparison with samples with a reduced oxygen content. This alters the device parameters immediately after exposure to radiation. In particular, an intense growth of the C_i-O_i centers can affect the initial stage of reverse annealing. The variation of the concentration of radiation defects at room temperature and the presence of ''hidden'' sources of the formation of deep centers, one of which is interstitial carbon, makes it difficult to establish a link between the device parameters and specific defects and to predict their characteristics after extended cyclical radiation exposure.

[1] Z. Li, IEEE Trans. Nucl. Sci. **NS-42**, 224 (1995).
[2] E. Fretwurst, H. Feick, M. Glaser, C. Gobling, E. H. M. Heijline, A. Rolf, T. Schulz, and C. Soave, Nucl. Instrum. Methods A **342**, 119 (1994).
[3] Z. Li, W. Chen, L. Dou, V. Eremin, H. W. Kraner, C. J. Li, G. Lindstroem, and E. Spiriti, IEEE Trans. Nucl. Sci. **NS-42**, 219 (1995).
[4] M. T. Asom, J. L. Benson, R. Sauer, and L. C. Kimberling, Appl. Phys. Lett. **51**, 256 (1987).
[5] L. W. Song, X. D. Zhan, B. W. BEnson, and G. D. Watkins, Phys. Rev. B **42**, 5765 (1990).
[6] E. M. Verbitskaya, V. K. Eremin, A. M. Ivanov, N. B. Strokan, Z. Li, and B. Schmidt, Fiz. Tekh. Poluprovodn. **27**, 2068 (1993) [Semiconductors **27**, (1993)].
[7] B. Schmidt, V. Eremin, A. Ivanov, N. Strokan, E. Verbitskaya, and Z. Li, J. Appl. Phys. **76**, 4072 (1994).
[8] S. D. Brotherton and P. Bradley, J. Appl. Phys. **53**, 5720 (1982).

Translated by Paul F. Schippnick

Photosensitivity of InP/CdS heterostructures in linearly polarized light

V. M. Botnaryuk, L. V. Gorchak, and V. N. Pleshka

State Institute of Moldova, Kishinev, Moldova

V. Yu. Rud'

St. Petersburg State Technical University, 195254 St. Petersburg, Russia

Yu. V. Rud'

A. F. Ioffe Physicotechnical Institute, Russian Academy of Sciences, 194021 St. Petersburg, Russia
(Submitted April 15, 1996; accepted for publication April 24, 1996)
Fiz. Tekh. Poluprovodn. **31**, 305–308 (February 1997)

Measurements have been made of the photosensitivity of (p^+-p^-)-InP/n^+-CdS structures formed by the growth of indium phosphide and cadmium sulfide films on p^+-InP substrates with (100) crystallographic orientation. These structures exhibit a photosensitivity $S_i \simeq 0.13$A/W in the spectral range from 1.3 to 2.4 eV at $T=300$ K. Polarizational photosensitivity was observed for oblique incidence of linearly polarized light on the CdS surface of these structures. The induced photopleochroism of these structures is governed by the angle of incidence θ. The photopleochroism increases proportionally to θ^2 and its maximum value is found to be $\sim 50\%$ at $\theta \simeq 75-80°$. The maximum azimuthal photosensitivity was found to be ~ 0.13A/W·deg. Structures consisting of CdS deposited on InP can be used as polarimetric photodetectors. © *1997 American Institute of Physics.* [S1063-7826(97)02102-9]

Gallium-phosphide and cadmium-sulfide based heterostructures heretofore have been studied only for the purpose of creating high-efficiency solar cells. Complex physical and technological studies of the system InP/CdS have made it possible to create structures with high radiation hardness and a coefficient of useful action as high as 18%.[1–3] In the present paper we report the initial results of an experimental study of the photoelectric properties of InP/CdS structures in linearly polarized light, which have allowed us to draw conclusions regarding their potential for application in polarization photonics.

1. (p^+-p^-)-InP/n^+-CdS heterostructures were obtained as follows. In the first step, epitaxial layers of p^--InP in a chloride system In-PCl_3-H_2 were grown on zinc-doped indium-phosphide wafers [with p^+ hole concentration equal to $(3-4)\times 10^{18}$ cm^{-3} at $T=300$ K, thickness ~ 0.4 mm with orientation (100) and misorientation $\sim 4-5°$ in the (110) direction]. The epitaxial layer was doped with zinc during the growth process up to p^- hole concentrations of $10^{16}-10^{17}$ cm^{-3} with Hall mobility $\mu_p \simeq 90-120$ cm^2/(V·s). This working regime allowed us to obtain electrically homogeneous layers with thicknesses in the range $2-4$ μm. In the second step, we deposited layers of CdS onto the surface of the epitaxial layer of p^--InP in a hydrogen flow-through system without any additional processing of the epitaxial layer. The temperature in the region of the CdS source T_s was usually about 840 °C, and the temperature in the deposition zone T_0 was roughly 700–750 °C. As the measurements show, the free electron concentration in the n^+-CdS layers deposited on the p^--InP surface depends strongly on T_0. The electron concentration in the n^+-CdS layers obtained at $T_0=700-730$ °C was equal to $n \simeq (3-5)\times 10^{19}$ cm^{-3} at $T=300$ K. The indicated level of doping of the CdS layers can be explained by indium diffusion into the forming layers from the indium-phosphide substrate. No effect of the doping level of the indium-phosphide substrate on the electron concentration in the n^+-CdS layers was detected.

After formation of the n^+-CdS layers, the (p^+-p^-)-InP/n^+-CdS structures were fitted with chemical contacts. A layer of Ag + 5% Zn, roughly 0.1 mm in thickness, was deposited on the free surface of the p^+-InP substrate by thermal sputtering, and a contact grid with composition. In +5% Te was deposited through a mask on the free surface of the n^+-CdS layer. After deposition of the contacts, the structure was subjected to heat processing at ~ 250 °C for 5–10 min. The so-obtained structures were mounted on a standard crystal-holder.

The spectral dependence of the photoelectric properties of the structures was measured with the help of an SPM-2 monochromator with a quartz prism. Light having the necessary orientation of the electric vector **E** was separated from natural light by means of polarization filters with $\sim 100\%$ polarization in the investigated spectral range. To vary the angle of incidence θ of the linearly polarized light, we mounted the structures on a Fedorov table. The spectral resolution of the setup was no worse than 1 meV, and the angle of incidence was controlled with an accuracy of $\pm 1°$.

2. As measurements of the stationary current–voltage characteristics show, a distinct rectification (Fig. 1, inset) is observed in the obtained heterostructures. The direct current–voltage characteristic in the voltage range $U>0.7$ V obeys the relation

$$I=\frac{U-U_0}{R},$$

where the cutoff voltage is $U_0 \simeq 0.7-0.8$ V, and the resistance is $R \approx 10-20\ \Omega$ at $T=300$ K. The saturation current

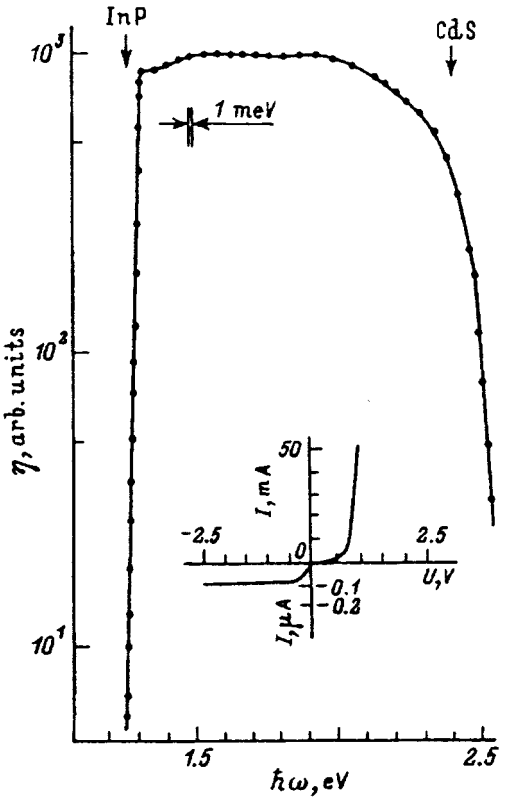

FIG. 1. Spectral dependence of the quantum efficiency of photoconversion of the (p^+-p^-)-InP/n^+-CdS heterostructure at room temperature. Sample 18-3. The arrows indicate the width of the InP and CdS band gaps. Inset: steady-state current–voltage characteristic.

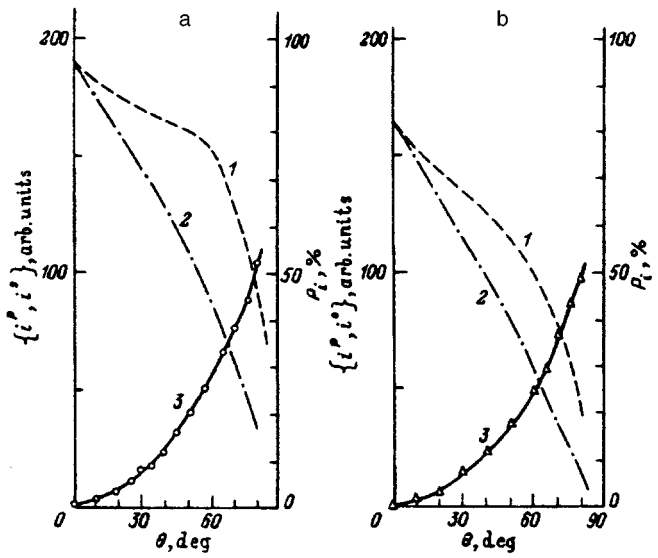

FIG. 2. Short-circuited photocurrent for $\mathbf{E} \parallel$ PI (plane of incidence) (*1*) and $\mathbf{E} \perp$ PI (*2*) and induced photopleochroism, plotted versus the angle of incidence of the illuminating light on the surface of the (p^+-p^-)-InP/n^+-CdS structure at $T=300$ °K. Sample 18-2. Wavelength, μm: a—0.92, b—0.50.

for reverse biases up to 2 V in all the structures stands at 10^{-7}A, and a sudden breakdown is observed at voltages >3 V. A typical spectral dependence of the relative quantum efficiency, calculated as the ratio of the short-circuit photocurrent to the number of incident photons, is shown in Fig. 1 for the heterostructures in natural (unpolarized) light. It can be seen that a high photosensitivity (η) is realized over a wide spectral range between the widths of the band gaps of the investigated materials. The long-wavelength edge of the photosensitivity spectrum corresponds to interband photoactive absorption in InP. It is described by an exponential and is characterized by a slope $S \simeq 80-100$ eV^{-1}, which is typical of direct interband transitions. The short-wavelength limit of the photosensitivity is caused by the appearance of interband absorption in the wideband layer when the photogeneration region is localized at its surface at distances from the active region of the heterostructure which exceed the diffusion drift length of the photoelectrons in the n^+-CdS layer. It should be stressed that the photoelectric parameters of the (p^+-p^-)-InP/n^+-CdS heterostructures proved to be reproducible when the fabrication process parameters were held constant. The maximum current photosensitivity S_i of these structures reaches a value of approximately 0.13A/W at $T=300$ K. It was possible to attain such a high photosensitivity as a result of epitaxial growth of the p^--InP layer. In the absence of this layer, also when using p-InP wafers with (111) orientation, the current photosensitivity S_i falls by at least an order of magnitude.

3. In the case where the heterostructures were illuminated by linearly polarized light normal to the CdS surface, the short-circuit photocurrent turned out to be independent of the orientation of the polarization plane of the incident light. This allows us to conclude that photoactive absorption in the region of the interband optical transitions in InP and CdS is isotropic. For indium phosphide, which has a cubic sphalerite lattice, this is an obvious result, whereas for the anisotropic semiconductor CdS, this result may be caused by either the polycrystalline structure of the layer or by the coincidence of the surface normal to the CdS symmetry axis, i.e., the [0001] direction. For deviations of the incidence angle from zero ($\theta \neq 0°$) the polarization indicatrices of the short-circuit photocurrent (i) for all the heterostructures revealed a periodic dependence on the azimuthal angle φ between the electric field vector of the wave **E** and the plane of incidence (IP). These dependences obey the relation $i_\varphi = i^p \cos^2\varphi + i^s \sin^2\varphi$, where i^p and i^s are, respectively, the photocurrent for $\mathbf{E} \parallel$ IP and $\mathbf{E} \perp$ IP. The form of the polarization indicatrices was identical over the entire range of photosensitivities of the structures, and the ratio i^p/i^s grew monotonically with θ at fixed photon energy.

Figures 2a and 2b show typical $i^p(\theta)$ and $i^s(\theta)$ curves for the heterostructures at two different wavelengths from the fundamental absorption region of InP and CdS. These curves were identical in nature for all the heterostructures and one shared peculiarity is that immediately as the angle of incidence departs from $\theta=0°$ both photocurrents i^p and i^s begin to fall. Consequently, in these structures we were not able to observe an increase in i^p. We observed growth of i^p previously in the case of structures in which the receiver surface was of high optical quality; thus, in agreement with the Fresnel relations the photocurrent for $\mathbf{E} \parallel$ IP reached its maximum in the vicinity of the pseudo-Brewster angle.[4] As the optical quality of the receiver surface deteriorated, growth of

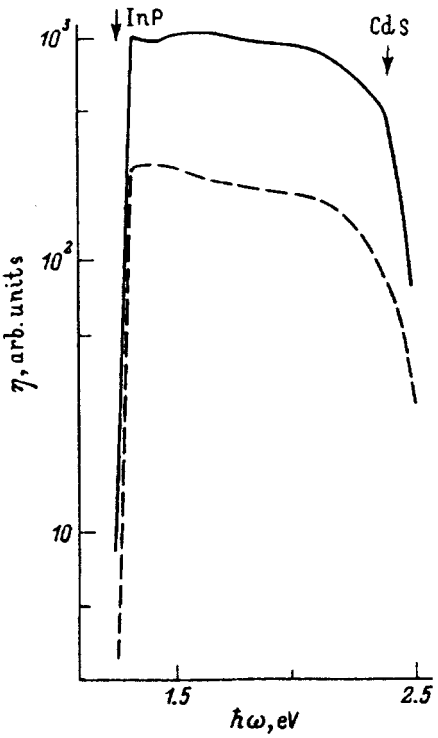

FIG. 3. Spectral dependence of the relative quantum efficiency of the (p^+-p^-)-InP/n^+-CdS heterostructure in linearly polarized light at $T=300$ K. Sample 18-3; $\theta=75°$; *1*) $\mathbf{E}\parallel$ PI, *2*) $\mathbf{E}\perp$ PI. The arrows indicate the width of the InP and CdS band gaps.

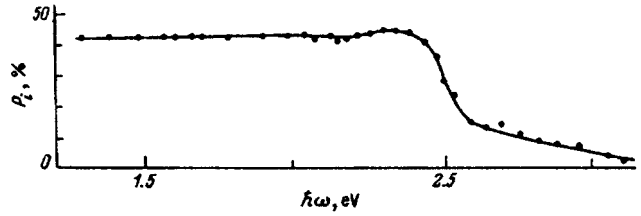

FIG. 4. Spectral dependence of the coefficient of induced photopleochroism of the (p^+-p^-)-InP/n^+-CdS heterostructure for oblique incidence of linearly polarized light, $\theta=75°$.

i^p in such structures with increase of θ disappeared.[5,6] Therefore, the features revealed in the $i^p(\theta)$ curves for the heterostructures can be immediately linked with the poor optical quality of the light-reflecting surfaces of the structures. It can be assumed that further technological efforts might afford an improvement in the quality of the layers, after which the experimental values of $i^p(\theta)$ would correspond to the Fresnel relations. In this regard, measurement of the polarization indicatrices of the photocurrent of such heterostructures could be used as express nondestructive diagnostics of the optical quality of the layers.

It also follows from Figs. 2a and 2b that the photopleochroism associated with oblique incidence of linearly polarized light,[7] $P_i=(i^p-i^s)/(i^p+i^s)$, is found to be in agreement over the entire photosensitivity range with a theoretical analysis of the phenomenon[8] and obeys the law $P_i\sim\theta^2$. It is clear from the obtained $P_i(\theta)$ curves (curve *3* in Figs. 2a and 2b) that photopleochroism arises only at $\theta\neq0°$ and grows smoothly as the angle of incidence is increased, reaching its maximum value $P_i^m\simeq50\%$ near $\theta\simeq80°$. The experimental curves of $P_i(\theta)$, according to the theoretical analysis in Ref. 8, yield the value $n\simeq2.5$ for the refractive index, which corresponds to the known value for CdS.[9] Therefore, there are grounds to assume that the main contribution to P_i comes from processes connected with the passage of linearly polarized light through the CdS surface.

4. Typical spectral curves of the relative quantum efficiency of the photopleochroism for oblique incidence of linearly polarized light onto the doped surface of one of the heterostructures are shown in Fig. 3. These curves are similar to those obtained when illuminating the structures with unpolarized light, and varying the polarization of the incident light from $\mathbf{E}\parallel$ IP to $\mathbf{E}\perp$ IP is accompanied by a downward shift of the photocurrent. This shift increases as the angle of incidence is increased; the relation $i^p>i^s$ is preserved over the entire photosensitivity range of the structures.

The coefficient of induced photopleochroism in the maximum photosensitivity region of the heterostructures remains nearly constant (Fig. 4) relative to the light intensity, and its magnitude can be easily controlled by choosing the appropriate angle of incidence. The falloff of the photopleochroism in the short-wavelength spectral region agrees with the onset of interband absorption in the wideband layer. The maximum azimuthal photosensitivity of InP/CdS heterostructures, which is realized in the vicinity of $\varphi=45°$ (Ref. 7), reaches the value $\Phi_i^m\simeq0.13\text{A/W}\cdot\text{deg}$ at $T=300$ K, which is at the record level of this parameter for semiconductor polarimetric structures.[4] The wideband nature of the quantum efficiency of photoconversion (Fig. 1) and of the photopleochroism (Fig. 4) suggest that InP/CdS heterostructures developed for solar cells can also be used as wide-range (1.3−2.4 eV), high-sensitivity photo-analyzers of linear polarized radiation. It should also be mentioned that an improvement in the optical quality of the exterior surface of the CdS layers would make it possible to increase the quantum efficiency of photoconversion near the pseudo-Brewster angle and, consequently, raise the level of azimuthal photosensitivity attained by us by approximately 30%.

[1] S. Wagner, J. L. Shay, K. J. Bachman, and E. Buchler, Appl. Phys. Lett. **20**, 220 (1976).
[2] S. Yasugawa and J. Sakai, Solid–State Electron. **20**, 133 (1977).
[3] V. M. Botnariuk, L. V. Gorchak, G. N. Grigorieva, M. B. Kagan, T. A. Kozyreva, T. L. Lybaskaya, E. V. Russu, and A. V. Simoshkevich, Solar Energy Mater. **20**, 359 (1990).
[4] S. G. Konnikov, V. Yu. Rud', Yu. V. Rud', D. M. Melebaev, A. Berveliev, M. Serginov, and S. Tilevov, Jpn. J. Appl. Phys. **32**, 515 (1993).
[5] Yu. V. Zhilyaev, N. Nazarov, V. Yu. Rud', Yu. V. Rud', and L. M. Fedorov, Fiz. Tekh. Poluprovodn. **27**, 1610 (1993) [Semiconductors **27**, 890 (1993)].
[6] D. Melebaev, V. Yu. Rud', and Yu. V. Rud', *Book of Abstracts of ICTMC-10*, Stuttgart, 1995.
[7] Yu. V. Rud', Ivz. Vuz. Fizika **29**, No. 8, 68 (1986).
[8] G. A. Medvedkin and Yu. V. Rud', Phys. Solid State A **67**, 333 (1981).
[9] *Physical-Chemical Properties of Semiconductor Materials* [in Russian], Nauka, Moscow, 1978.

Translated by Paul F. Schippnick

Photoelectric properties of porous and single-crystal silicon heterocontacts

V. Yu. Rud'

St. Petersburg State Technical University, 195251 St. Petersburg, Russia

Yu. V. Rud'

A. F. Ioffe Physicotechnical Institute, Russian Academy of Sciences, 194021 St. Petersburg, Russia
(Submitted April 15, 1996; accepted for publication April 24, 1996)
Fiz. Tekh. Poluprovodn. **31**, 309–312 (February 1997)

The polarization photosensitivity of a heterocontact of porous and single-crystal silicon is experimentally investigated. A maximum in the photosensitivity is observed at ~1 mA/W at energies in the range 1.2–2.3 eV, when linearly polarized light is obliquely incident on the surface of the porous-silicon layer. The photopleochroism of these heterostructures depends on the angle of incidence θ, varies roughly as $\sim\theta^2$, and reaches the maximum value of ~32% at $\theta\simeq 80°$. Oscillations due to interference of natural and linearly polarized light in the porous-silicon layers are observed in the photocurrent and the photopleochroism of these structures. Heterostructures consisting of a layer of porous silicon on a silicon single crystal can find application as photoconverters of natural and linearly polarized light. © *1997 American Institute of Physics.* [S1063-7826(97)02202-3]

Lowering the dimensionality in semiconductors is an effective means by which to control their fundamental parameters.[1,2] In recent years, there has been growing interest in visible radiation from porous silicon.[1–5] In the present paper we report the results of an experimental study of the polarizational aspects of the photosensitivity of the heterocontact between a silicon single crystal and the porous-silicon layer formed on it during anodic etching.

1. A typical stationary current–voltage characteristic of a heterostructure consisting of a porous-silicon layer formed on a (100)-cut p-Si (KDB-2) wafer is shown in Fig. 1. To obtain such heterostructures, we used the well-known method of subjecting p-Si wafers to anodic etching.[1,2] The thickness of the porous-silicon layers was controlled by the etching time and the magnitude of the anode current and varied from a few micrometers to tens of micrometers. The transparency direction in such structures corresponds to negative polarity of the external bias on the porous-silicon layer. At large forward biases ($U>U_c$) the current I depends linearly on the voltage and obeys the relation

$$I=(U-U_c)/R,$$

where R is the residual resistance. For heterostructures with thickness of the porous-silicon layer in the range $5-10$ μm, R usually equals $2-10$ MΩ, and the cutoff voltage in this case $U_c=1.5-1.6$ V at $T=300$ K. In the case of reverse bias up to 25 V the current saturates at the level $2–6\times10^{-8}$ A at $T=300$ K. A sudden breakdown takes place when the reverse bias reaches $30-35$ V. As the thickness of the porous-silicon layers is decreased, the residual resistance is reduced.

2. Illumination of a heterostructure gives rise to the photovoltaic effect, which is due to a separation of light-generating charge carriers in the electric field localized at the boundary of the porous and crystalline silicon layers. Irrespective of where the light probe (diameter 1 mm) is placed on the surface of the heterostructure, the porous-silicon layer is always negatively charged relative to the p-Si substrate. The photosensitivity is usually greater when these heterostructures are illuminated from the porous-silicon side and reaches a value in the range $S_i=0.5-1.0$ mA/W (the current sensitivity) or $S_u=20-50$ V/W (the voltage sensitivity) at $T=300$ K.

A typical spectral dependence of the relative quantum efficiency of photoconversion η for the obtained heterostructures, defined as the ratio of the short-circuit photocurrent to the number of incident photons, is shown in Fig. 1. When such structures are illuminated in the direction of the normal to the surface from the side of the porous-silicon layer, the window effect, typical for such heterostructures, is observed. Here the long-wavelength photosensitivity limit obeys an exponential law (Fig. 1, curve *2*) and is localized in the region of photon energies corresponding to edge absorption in a silicon single crystal. If the heterostructures are illuminated from the silicon-crystal side for substrate thicknesses of 0.4 mm and photon energies greater than 1.15 eV, the photoresponse falls nearly to zero, due to localization of the photoexcitation region at a distance exceeding the diffusion drift length of the photoelectrons. If the structures are illuminated by unpolarized light from the side of the porous-silicon layer (Fig. 1), then a wideband effect takes place, and for layer thicknesses d in the neighborhood of 10 μm the photosensitivity begins to fall abruptly in the region of photon energies $\hbar\omega\geqslant 2$ eV. The latter apparently is due to increased absorption in the porous-silicon layers as a result of switching on the interband transitions. In the energy range between the widths of the band gaps of crystalline and porous silicon, a series of nearly equidistant peaks shows up in the photosensitivity spectra of all the obtained structures with porous-silicon layers with specular face planes. In the given example (Fig. 1) for illumination by unpolarized light the number of peaks reaches 20. The distance between the peaks is ~90 meV on average. This allows us to estimate the thickness of the nascent layers from the known value of the refractive index for porous silicon:[6] we obtain $d\simeq 4-5$ μm. This esti-

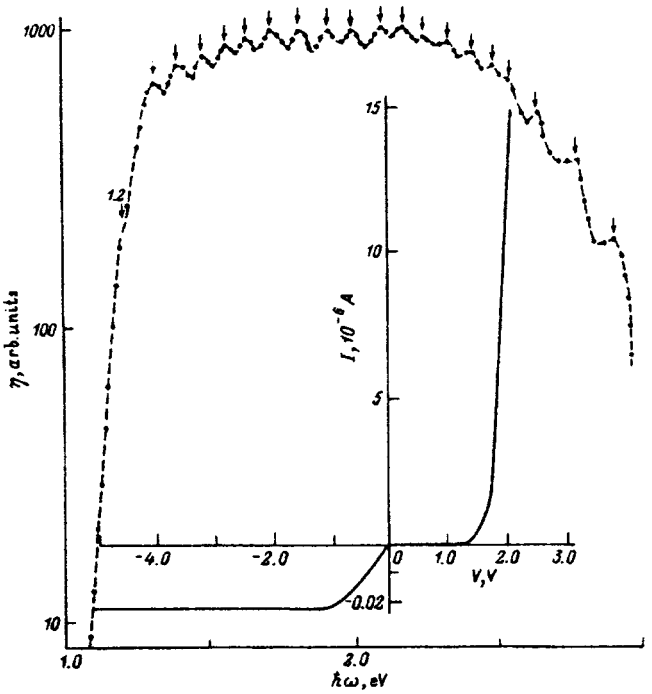

FIG. 1. Spectral dependence of the quantum efficiency of the photoresponse of a heterostructure based on porous silicon and crystalline silicon. Sample 20 A, $d=5$ μm, $T=300$ K, unpolarized radiation, angle of incidence $\theta=0°$, spectral resolution no worse than 1 meV, illumination from the porous-silicon side. Inset: steady-state current–voltage characteristic.

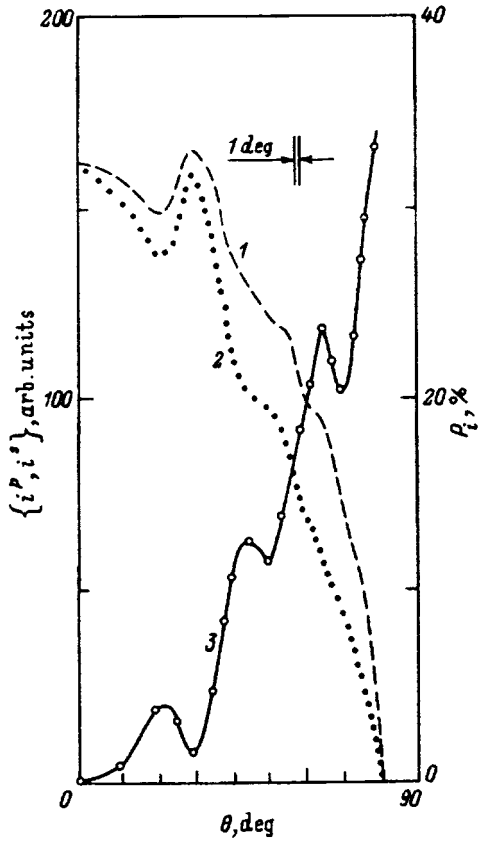

FIG. 2. i^p (*1*), i^s (*2*) and the induced photopleochroism (*3*) plotted versus the angle of incidence of the linearly polarized light incident on the porous-silicon surface. Sample 20 A, $T=300$ K.

mate of the layer thickness from the spectral distribution of the photosensitivity of the heterostructures is found to be in good agreement with the results of direct microscopic measurements. In general, the very fact that structure has been detected in the photosensitivity spectra of the heterostructures, where this structure is the result of interference of the incident radiation in the wideband material, allows us to conclude that the homogeneity of the obtained porous-silicon layers is high enough.

It should be noted that already in heterostructures with porous-silicon layer thicknesses ~ 1 μm the short-wavelength falloff in the spectral curves of $\eta(\hbar\omega)$ is essentially absent up to 3 eV.

3. When the heterostructures were illuminated with linearly polarized light normal to the porous-silicon surface, the quantum efficiency over the entire photosensitivity range turned out to be independent of the orientation of the electric vector of the light wave **E** relative to the principal crystallographic axes of the silicon substrate, i.e., photoactive absorption in both components of the heterostructure is isotropic. Consequently, natural photopleochroism in such heterostructures is absent ($P_N=0$).[6] As the angle of incidence θ becomes nonzero, the short-circuit photocurrent for the case in which **E** lies in the plane of incidence (IP), i^p, over the entire photosensitivity range begins to predominate over the photocurrent for the case in which **E** is perpendicular to the plane of incidence, i^s, and, correspondingly, for $\mathbf{E}\perp$ IP. As can be seen from Fig. 2, the dependence of i^p and i^s on the incidence angle for the heterostructures turns out to be different than expected from the Fresnel relations. Indeed, the curves obtained for $i^p(\theta)$ and $i^s(\theta)$ are nonmonotonic and have at least three peculiarities in the form of their peaks and bends (Fig. 2, curves *1* and *2*). Such curves were typical of heterostructures with a specular receiver surface. In the investigated range of angles θ the polarization dependence of the photocurrent when varying the azimuthal angle φ between **E** and the plane of incidence is periodic, with the maximum photocurrent corresponding to $\mathbf{E}\parallel$ IP and the minimum, to $\mathbf{E}\parallel$ IP. The induced photopleochroism coefficient $P_i=(i^p-i^s)/(i^p+i^s)$ was calculated on the basis of polarization measurements of the photocurrent at $\theta=$ const and $\hbar\omega=$ const.

A typical angular dependence of induced photopleochroism for the examined heterostructures is shown in Fig. 2 (curve *3*). Its main distinguishing feature is that with growth of the angle of incidence, the induced photopleochroism P_i grows according to a nearly quadratic law, which agrees with the analysis presented in Ref. 8. However, in contrast to what one might expect from Ref. 8, at certain values of the angle of incidence the experimental curves $P_i(\theta)$ undergo oscillations. Such a feature has not been previously observed (see Refs. 7–9) and may be connected with interference of linearly polarized light in the wideband layer. As can be seen from Fig. 2, the induced photopleochroism at $\theta=70°$ reaches a value of $20-25\%$ for different heterostructures, which based on the theoretical analysis in Ref. 8 yields the value $n\simeq 1.7$ for the refractive index for layers formed by anodic

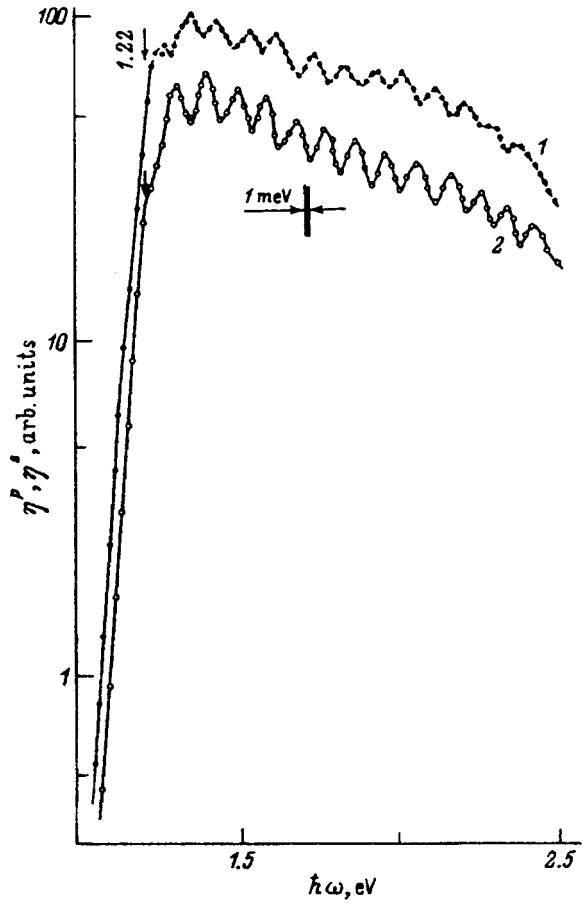

FIG. 3. Spectral dependence of the photocurrents i^p and i^s in p-polarization (η^p) (*1*) and in s-polarization (η^s) (*2*) of a heterocontact of porous and crystalline silicon. Sample 20 A, $T=300$ K, $\theta=75°$.

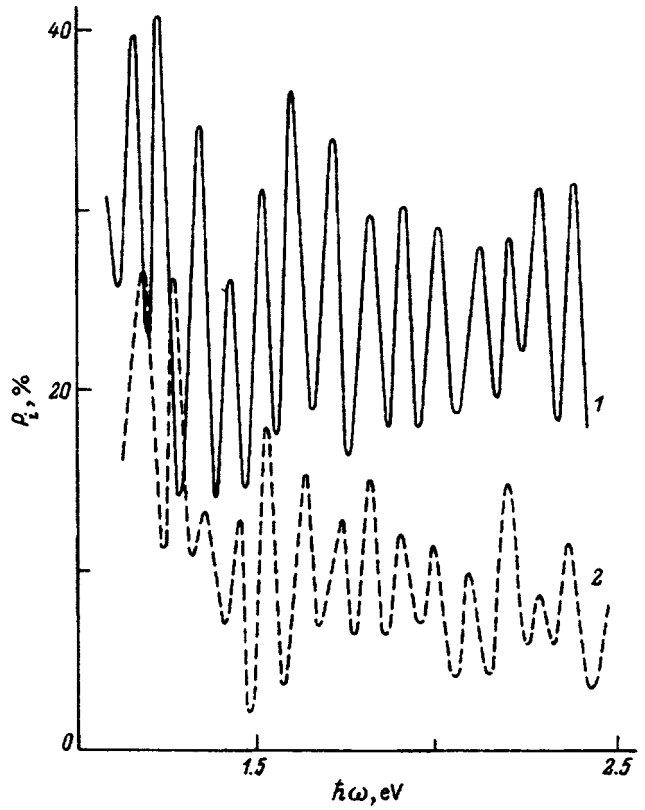

FIG. 4. Spectral dependence of the induced photopleochroism of a heterocontact of porous and crystalline silicon. Sample 20 A, $T=300$ K, $\theta=75°$ (*1*), 45° (*2*); illumination from the porous-silicon side.

etching. This value differs from known values of n for crystalline silicon, which serves to explain the polarizational photosensitivity for oblique incidence of linearly polarized light of heterostructures with phenomena at the air-porous silicon surface boundary.

Figure 3 plots typical spectral curves of the photocurrents i^p and i^s for the obtained structures. It can be seen that over the entire spectral range the photosensitivity $i^p > i^s$ and, as in the case of unpolarized radiation (Fig. 1, curve *2*) a distinct system of equidistant peaks shows up in the photocurrent spectra in the region of maximum photosensitivity for both polarizations. The number of peaks in the better structures with $d=5$ μm reaches 13–14. It is characteristic that the depth of modulation of the photocurrent is higher for i^s. It is also important to mention that the energy positions of the maxima of i^p correspond to minima of i^s and *vice versa*.

This latter feature has the result that in contrast to the known properties of induced photopleochroism in structures where interference is not observed and for which the value of P_i is nearly constant over the entire photosensitivity range,[9,10] in heterostructures of porous and crystalline silicon P_i begins to vary strongly as a function of the photon energy (Fig. 4). It follows from Fig. 4 that as the angle of incidence θ is decreased, oscillations in the spectral dependence of P_i are preserved, but the mean value of the induced photopleochroism falls according to the law $P_i \sim \theta^2$ (Fig. 2, curve *3*).

The results presented here thus show that heterostructures based on porous and crystalline silicon can find application as wideband photovoltaic converters of natural and linearly polarized light. The observed interference of light in anodized layers of silicon indicates that they have a high level of homogeneity and that polarizational photoelectric spectroscopy can be used for express diagnostics of such layers.

The authors are grateful to A. A. Lebedev for providing heterostructures and for his interest in this work.

[1] L. T. Canham, Appl. Phys. Lett. **57**, 1046 (1990).
[2] M. S. Brandt, H. D. Fuchs, and M. Stutzmann, Solid State Commun. **81**, 307 (1992).
[3] Y. Kanemitsu, H. Uto, Y. Masumoto, T. Matsumoto, T. Futagi, and H. Mimura, Phys. Rev. B **48**, 2827 (1993).
[4] L. Brus, J. Phys. Chem. **98**, 3575 (1994).
[5] E. V. Astrova, A. A. Lebedev, A. D. Remenyuk, and Yu. V. Rud', Jpn. J. Appl. Phys. **34**, 251 (1995).
[6] S. M. Prokes, Appl. Phys. Lett. **62**, 3224 (1993).
[7] Yu. V. Rud', Izv. Vuz. Fizika, No. 8, 68 (1986).
[8] G. A. Medvedkin and Yu. V. Rud', Phys. Status Solidi A **67**, 333 (1981).
[9] S. G. Konnikov, D. Melebaev, Y. Yu. Rud', Yu. V. Rud', A. Berkeliev, M. Serginov, and S. Tilevov, Jpn. J. Appl. Phys. **32**, 515 (1993).
[10] V. Yu. Rud', Candidacy Dissertation (A. F. Ioffe Physicotechnical Institute, Russian Academy of Sciences, St. Petersburg, 1995), p. 17.

Translated by Paul F. Schippnick

Photoluminescence of anodized layers of $CdSiAs_2$

A. A. Lebedev and Yu. V. Rud'

A. F. Ioffe Physicotechnical Institute, Russian Academy of Sciences, 194021 St. Petersburg, Russia

V. Yu. Rud'

St. Petersburg State Technical University, 195251 St. Petersburg, Russia
(Submitted April 22, 1996; accepted for publication April 24, 1996)
Fiz. Tekh. Poluprovodn. **31**, 313–314 (February 1997)

$CdSiAs_2$ belongs to the II–IV–V_2 group of chalcopyrite semiconductors with a direct band gap of 1.51 eV at $T=300$ K. In this paper we investigate the spectral dependence of the steady-state photoluminescence of $CdSiAs_2$ anodized layers. These layers were fabricated by electrochemical anodization of unoriented p-type $CdSiAs_2$ wafers in an solution of HF in ethanol. It is found that a broad photoluminescence band with a maximum at the photon energy $\hbar\omega=1.82$ eV at 300 K arises. This band lies deep in the fundamental absorption region of $CdSiAs_2$ crystals. The dependence of the parameters of the photoluminescence spectra of anodized Si, GaAs, and $CdSiAs_2$ layers is discussed. © *1997 American Institute of Physics.* [S1063-7826(97)02302-8]

The direct-band-gap semiconductor $CdSiAs_2$ (band gap $E_g\simeq1.51$ eV at 300 K; Refs. 1–3) is the closest ternary analog of gallium arsenide and is of interest as a material for polarization optoelectronics, solar cells, and polarized electron emitters.[4] In recent years the possibility has opened up of transforming the electron spectrum of semiconductors as a result of anodic etching.[5] In particular, efficient photoluminescence of porous silicon has been obtained in the visible spectral range. On this level, the behavior of binary and ternary analogs of elementary semiconductors resulting from anodic etching is of unquestionable interest. Recently it was found that, as in the case of silicon, anodic etching of gallium arsenide is accompanied by a flareup of strong luminescence of the anodized surface in the visible region of the spectrum.[1)] In this paper we present the results of a preliminary study of the effect of anodic etching on the photoluminescence of $CdSiAs_2$ crystals. By analogy it could be expected that ternary semiconductors II–IV–V_2 (Ref. 4), which are electron analogs of elementary semiconductors (Ge, Si) and III–V compounds, should ''react'' to the electrochemical processing of their surface similar to silicon.[5] Admittedly, the complication of the number and type of chemical bonds and, as a consequence, complications of the atomic composition of the semiconductors in the series IV→III–V to II–IV–V_2 give rise to a host of peculiarities which would be difficult to guess in advance and which could be observed only in experimental studies. Such peculiarities will be discussed below.

1. Experiments on anodic etching were carried out on electrically homogeneous wafers of p-type $CdSiAs_2$ with average dimensions $5\times5\times1$ mm^3 and arbitrary crystallographic orientation. Single crystals of p-type $CdSiAs_2$ were grown by steady-state directed crystallization from nonstoichiometric melts.[1] The free hole concentration in specially pure (dopant-free) samples was 10^{16} cm^{-3}, and the Hall mobility of the holes was 200 cm^2/(V·s) at 300 K. As the anodic etchant we used $2HF + 3C_2H_5OH + 0.1HNO_3$ (by volume). Etching was usually performed at current densities from 20 to 120 mA/cm^2 for 40–120 min at room temperature. As a result, a blackened region copying the shape of the electrical contact of the wafer with the solvent appeared on the specularly polished surface of the p-type $CdSiAs_2$ wafers. The surface of this region was diffusely scattered and resembled in its outward appearance the layer of porous silicon appearing on a silicon surface. After completion of this process, the $CdSiAs_2$ samples were carefully washed in deionized water and dried. The newly formed anodic layers preserved their good adhesion to the p-type $CdSiAs_2$ substrate even after drying.

2. Steady-state photoluminescence was excited by either an argon or helium–cadmium laser and recorded by an MDR-3 monochromator with a 600 lines/mm grating and an FZU-62 photomultiplier. The photoluminescence was analyzed from the side on which the exciting light fell. All mea-

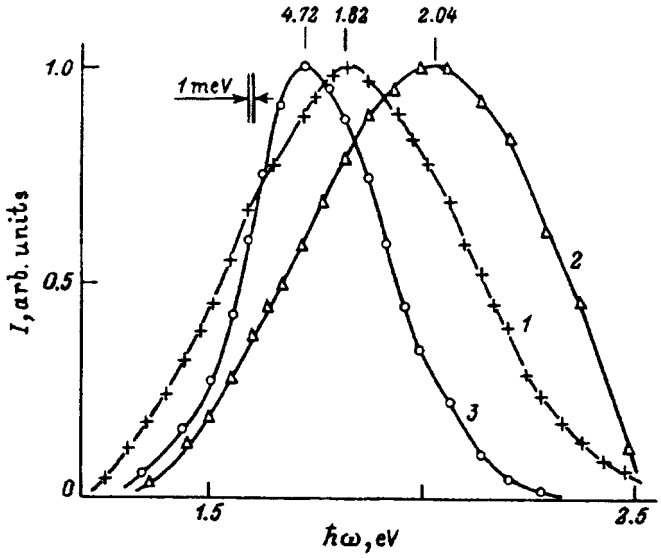

FIG. 1. Spectral dependence of the photoluminescence intensity I of anodized layers of $CdSiAs_2$ (*1*), GaAs (*2*), and Si (*3*) at $T=300$ K.

TABLE I.

Semiconductor	E_g, eV	Properties of anodized layers		
		$\hbar\omega_m$, eV	$\delta_{1/2}$, meV	$\hbar\omega_m - E_g$, eV
Si	1.1	1.72	380	0.6
GaAs	1.43	2.04	680	0.6
$CdSiAs_2$	1.51	1.82	630	0.3

surements were performed at room temperature.

Figure 1 shows typical photoluminescence spectra of the anodized layer on the p-type $CdSiAs_2$ substrate (curve *1*). For the original p-type $CdSiAs_2$ single crystals recombination radiation has been observed so far only in the spectral region $\hbar\omega \lesssim E_g$ and not one publication on this compound has so far reported the appearance of photoluminescence at energies above 1.5 eV.[1–3,6] For the anodized layers formed on p-type $CdSiAs_2$ substrates the photoluminescence, as can be seen from the figure, has the form of a wide and symmetrical enough band with absolute maximum at $\hbar\omega_m \simeq 1.82$ eV at $T=300$ K. The spectral shape of the photoluminescence is nearly the same for excitation by argon and helium–cadmium laser radiation, and varying the pump intensity showed that the intensity of the short-wavelength radiation is proportional to the intensity of the exciting light. Figure 1 also shows the spectral curves of the photoluminescence of anodized layers obtained under similar conditions on GaAs (curve *2*) and Si (curve *3*). Common to all the anodized layers of these analogs is the appearance of wideband photoluminescence in the visible spectral range, with the energy position of the maxima of these bands $\hbar\omega_m$ greater in each case than the width of the band gap of the corresponding semiconductor (see Table I). The shift of the maxima, defined as the difference $\hbar\omega_m - E_g$, for these semiconductors lies within the limits $0.3-0.5$ eV, where the value of $\hbar\omega_m$ was found to be sensitive to the conditions of anodic etching. The magnitude of the short-wavelength shift $\hbar\omega_m - E_g$ is therefore probably only a qualitative characteristic of the reconstruction of the near-surface region of the semiconductor. The photoluminescence bands in the comparison analogs appearing in the visible spectral range are characterized, as follows from Fig. 1 and Table I, by a large full width at half-maximum (FWHM) $\delta_{1/2}$, which may serve as an indication of their nonelementary nature.

In conclusion, we note that the fact of the formation of anodized wideband layers on diamond-like semiconductors can be of interest in the creation of various types of optoelectronic devices based on them.

This work was carried out within the scope of the program ''Physics of Solid-State Nanostructures.''[1)]

[1)]This result will be considered in detail in a special publication.

[1] V. D. Prochukhan and Yu. V. Rud', Fiz. Tekh. Poluprovodn. **12**, 209 (1978) [Sov. Phys. Semicond. **12**, 121 (1978)].
[2] I. A. Mal'tseva, V. D. Prochukhan, Yu. V. Rud', and M. Serginov, Fiz. Tekh. Poluprovodn. **10**, 1222 (1976) [Sov. Phys. Semicond. **10**, 727 (1976)].
[3] Yu. V. Rud', Fiz. Tekh. Poluprovodn. **17**, 2208 (1983) [Sov. Phys. Semicond. **17**, 1413 (1983)].
[4] F. P. Kesamanli and Yu. V. Rud', Fiz. Tekh. Poluprovodn. **27**, 1761 (1993) [Semiconductors **27**, 969 (1993)].
[5] L. T. Canham, Appl. Phys. Lett. **57**, 1046 (1990).
[6] J. L. Shay and J. H. Wernick, *Ternary Chalcopyrite Semiconductors* (Pergamon Press, Oxford, 1975).

Translated by Paul F. Schippnick

Photoluminescence of anodized silicon carbide

V. F. Agekyan and Yu. A. Stepanov

St. Petersburg State University, 198904 St. Petersburg, Russia

A. A. Lebedev, A. A. Lebedev, and Yu. V. Rud'

A. F. Ioffe Physicotechnical Institute, Russian Academy of Sciences, 194021 St. Petersburg, Russia
(Submitted May 15, 1996; accepted for publication May 22, 1996)
Fiz. Tekh. Poluprovodn. **31**, 315–317 (February 1997)

The luminescence of single-crystalline 6*H*-SiC plates after electrochemical etching has been investigated. The photoluminescence spectrum was found to change strongly after etching; the decay times of separate bands were determined. Just as in the case of silicon, the change in the photoluminescence could be due to the formation of nanostructures. © *1997 American Institute of Physics.* [S1063-7826(97)02502-7]

The optical properties of an anodized surface of SiC are of interest for several reasons. It was found several years ago[1] that temperature-stable luminescence consisting of wide bands in the visible region of the spectrum appears as a result of electrochemical etching of crystalline silicon. Many authors interpreted this luminescence as a spectroscopic manifestation of silicon nanostructures which form together with the porous silicon.[1–4] It has been suggested that the luminescence of wide-gap compounds which are formed during etching (silicon dioxide, amorphous silicon, siloxens, etc.) could contribute to the spectrum.[5,6] This problem is evidently common to an entire series of semiconductors, and enlarging the range of objects could help solve it. The radiative properties of an anodized silicon carbide surface[7,8] are of interest in themselves since SiC is employed as an electroluminescent material.

Silicon carbide is an indirect wide-gap semiconductor with a gap width exceeding 3 eV.[9] The edge luminescence of SiC is due to impurity states, specifically, relaxed bound excitons. In the present we paper report the results of an experimental study of the radiation from an anodized SiC surface (which we shall simply call porous silicon carbide) under excitation by a short-wavelength laser pulse. To prepare such a surface, single-crystalline silicon carbide (6*H* polytype) plates, grown by Lely's method,[10] with electron density $(1-3)\times 10^{18}$ cm^{-3} and (0001) orientation, were electrochemically etched. For anodic etching, we used the mixture $HF+C_2H_5OH+HNO_3$ in volume ratios 2:3:0.1. Etching was conducted at room temperature for 40–120 min with current densities 20–120 mA/cm^2.

The photoluminescence of porous SiC was excited with a pulsed nitrogen laser ($h\nu=3.68$ eV) with a 2-ns pulses and a pulse repetition frequency of 100 Hz. The spectra were recorded at 80 and 300 K by two methods — in a stroboscopic regime (time-resolved luminescence) with a time constant of about 5 μs and in a quasicontinuous regime. In the latter case, a recording method ordinarily employed with continuous excitation was used.

In the unetched region of the single-crystalline SiC plate, we observed at 80 K, a luminescence, which was recorded in the quasicontinuous regime with a maximum near 2.7 eV, and a structure ordinarily attributed to radiative recombination at deep aluminum acceptor levels.[11] In the stroboscopic regime with a delay $\tau=0$, the wider recorded spectrum is shifted into the short-wavelength region (Fig. 1).

Porous SiC is distinguished by a diversity of emission spectra, which is perceived visually by color ranging from blue to orange but usually nearly white, indicating a wide spectral region of luminescence. The peripheral part of the etch region (the boundary of the etched and unetched re-

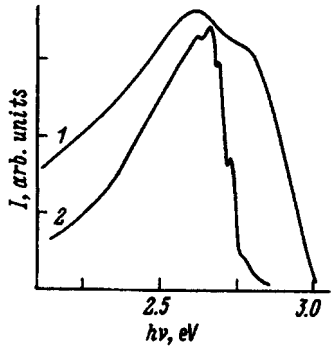

FIG. 1. Luminescence spectra of unetched 6*H*-SiC recorded in a time-resolved regime with $\tau=0$ (*1*) and in a quasicontinuous regime (*2*); $T=80$ K.

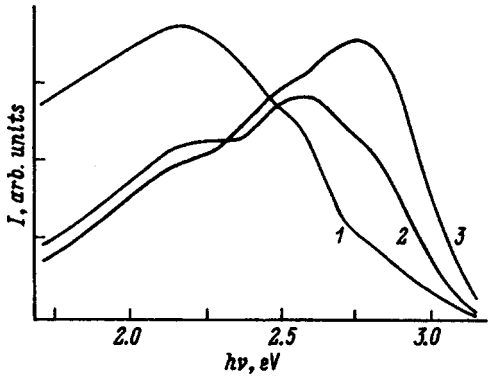

FIG. 2. Three types of luminescence spectra of porous silicon carbide (quasicontinuous recording regime); $T=80$ K.

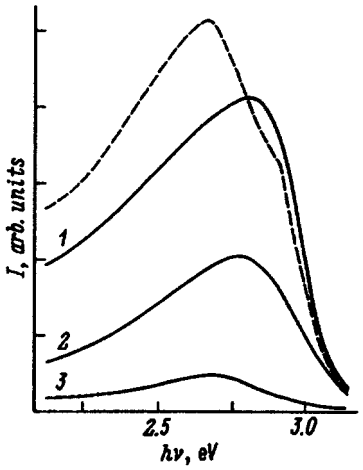

FIG. 3. Luminescence spectra of porous SiC at $T=80$ K with time delays τ (μs): *1* — 0, *2* — 8, and *3* — 30 (spectra 2 and 3 are intensified by factors of 5 and 50, respectively). Dashed line — luminescence spectrum obtained from the same point of the sample in the quasicontinuous regime.

gions) luminesces most strongly. As one can see from Fig. 2, at least three bands with maxima near 2.2, 2.6, and 2.8 eV can be distinguished. The position of the maxima of these bands correlates well with the position of the known impurity emission bands of SiC: radiative transition ⟨conduction band⟩ — ⟨deep boron acceptor level (2.2 eV)⟩;[12] donor–acceptor recombination on aluminum impurities — ⟨nitrogen(2.6eV)⟩;[13] radiative transition ⟨conduction band⟩ — ⟨aluminum acceptor level (2.8eV)⟩.[14] The association of the intensities of these three bands can differ substantially even within the etch region of the same sample (we note that spectrum 1 in Fig. 2 is atypical). All this indicates that the technology of electrochemical etching of SiC must be improved.

As τ increases, the shape of the luminescence band changes substantially and the maximum of the band shifts into the long-wavelength region (Fig. 3). This behavior corresponds to the previous results obtained from investigations of the decay time constants τ_n of impurity luminescence bands in single-crystalline SiC: τ_n for luminescence associated with impurity boron atoms is much greater than τ_n for luminescence associated with impurity aluminum atoms.[15,16] The spectrum with a temporal delay τ of about 30 μs is closest to the spectrum recorded in the continuous regime.

In contrast to the situation with ordinary and porous silicon, the spectral range of radiation from unetched silicon carbide is identical to that of porous silicon carbide. It is therefore difficult now to draw any convincing conclusions about the fundamental difference of the emission mechanisms in silicon carbide before and after anodization. The main differences in the spectra consist of the following.

1. The spectrum from porous SiC is more temperature-stable. As a result of heating from 80 to 300 K, the intensity of the luminescence decreases by more than an order of magnitude in the initial silicon carbide as compared with porous SiC.

2. Etching intensifies luminescence in the red region of the spectrum and increases the short-wavelength shift of the blue limit of the luminescence.

Finally, our results do not rule out the formation of Si- and SiC-based nanostructures, which contribute to the red and blue regions of the luminescence spectrum of porous silicon carbide during electrochemical etching (anodization) of SiC. However, the formation of compounds (oxides and siloxens), similar to the compounds to which the short-wavelength radiation of porous Si is attributed, cannot be ruled out. We note, however, that in the case of porous silicon carbide, the increase in the intensity of luminescence bands characteristic of single-crystalline SiC, just as the similarity of the properties of these bands in SiC and porous SiC, most likely indicates the formation of nanostructures rather than any new chemical compounds.

In contrast to porous Si, the radiation from porous SiC does not degrade appreciably as a result of intense, continuous laser excitation. The temperature stability of porous silicon carbide makes this material promising from the standpoint of practical applications of the electroluminescence effect.

This work was performed as part of the State program ''Physics of solid-state nanostructures'' and was partially supported by the University of Arizona (USA).

[1] L. T. Canham, Appl. Phys. Lett. **57**, 1046 (1990).
[2] J. C. Vial, A. Baisey, F. Gaspard, R. Herino, M. Ligeon, F. Muller, R. Rotestain, and R. M. MacFarlane, Phys. Rev. B **45**, 14171 (1992).
[3] M. Voos, Ph. Uzan, C. Delalande, G. Bastard, and A. Halimaoui, Appl. Phys. Lett. **61**, 1213 (1992).
[4] R. P. Vasques, R. W. Fathauer, T. George, A. Ksendzov, and T. L. Lin, Appl. Phys. Lett. **60**, 1004 (1992).
[5] M. S. Brand, H. D. Fuchs, M. Stuzmann, J. Weber, and M. Cardona, Solid State Commun. **81**, 307 (1992).
[6] H. D. Fuchs, M. Stuzmann, M. S. Brandt, M. Rosenbauer, J. Weber, A. Bretischwerdt, P. Deak, and M. Cardona, Phys. Rev. B **48**, 8172 (1993).
[7] T. Matsumoto, J. Takahashi, T. Tamaki, T. Futagi, and H. Mimura, Appl. Phys. Lett. **64**, 225 (1994).
[8] A. A. Lebedev, A. A. Lebedev, and Yu. V. Rud', Pis'ma Zh. Tekh. Fiz. **21**, 64 (1995) [Tech. Phys. Lett. **21**, 195 (1995)].
[9] P. Choyke and L. Patrick, Phys. Rev. **127**, 1868 (1962).
[10] J. A. Lely, Ber. Deut. Ceram. Ges. **32**, 229 (1995).
[11] V. I. Pavlichenko, I. V. Ryzhikov, Yu. I. Suleĭmanov, and Yu. M. Shaĭdan, Fiz. Tverd. Tela (Leningrad) **10**, 2801 (1968) [Sov. Phys. Solid State **10**, 2205 (1968)].
[12] E. E. Violin and G. F. Khbluyanov, Fiz. Tverd. Tela (Leningrad) **8**, 3395 (1966) [Sov. Phys. Solid State **8**, 2716 (1966)].
[13] M. Ikeda, U. Matsunami, and T. Tanaka, Phys. Rev. B **22**, 2842 (1980).
[14] W. von Müch and W. Kükzinder, Solid–State Electron. **21**, 1129 (1978).
[15] A. A. Lebedev, N. K. Poletaev, M. G. Rastegaeva, and N. S. Savkina, Fiz. Tekh. Poluprovodn. **28**, 1769 (1994) [Semiconductors **28**, 981 (1994)].
[16] M. M. Anikin, N. I. Kuznetsov, A. A. Lebedev, A. M. Strel'chuk, and A. L. Syrkin, Fiz. Tekh. Poluprovodn. **24**, 1384 (1990) [Sov. Phys. Semiconductors **24**, 869 (1990)].

Translated by M. E. Alferieff

Semiconductors-97: Third Russian Conference on Semiconductor Physics

1. ORGANIZERS

The OOFA of the Russian Academy of Sciences, the Scientific Council of the Russian Academy of Sciences on the problem ''Semiconductor physics,'' the P. N. Lebedev Institute of Physics of the Russian Academy of Sciences, the Institute of Radio Engineering and Electronics of the Russian Academy of Sciences, and the Department of Physics at M. V. Lomonosov Moscow State University.

2. LOCATION AND DATE

The third Russian conference on semiconductor physics will be held at the P. N. Lebedev Institute of Physics in Moscow from December 1 to December 5, 1997.

The conference chairman is L. V. Keldysh (Institute of Physics of the Russian Academy of Sciences, Moscow)

3. PROGRAM COMMITTEE

V. V. Timofeev (Chairman) — Institute of Solid-State Physics of the Russian Academy of Sciences, Chernogolovka

I. P. Akimchenko (Secretary) — Scientific Council on the problem ''Semiconductor physics''

Zh. I. Alferov — A. F. Ioffe Physicotechnical Institute, St. Petersburg

A. A. Gippius — Institute of Physics of the Russian Academy of Sciences, Moscow

A. A. Gorbatsevich — Moscow Institute of Electronics Machine Building, Zelenograd

A. G. Zabrodskiĭ — A. F. Ioffe Physicotechnical Institute, St. Petersburg

V. P. Zakharchenya — A. F. Ioffe Physicotechnical Institute, St. Petersburg

M. S. Kagan — Institute of Radio Engineering and Electronics of the Russian Academy of Sciences, Moscow

L. V. Keldysh — Institute of Physics of the Russian Academy of Sciences, Moscow

Yu. V. Kapaev — Institute of Physics of the Russian Academy of Sciences, Moscow

V. D. Kulakovskiĭ — Institute of Solid-State Physics of the Russian Academy of Sciences, Chernogolovka

M. G. Mil'vidskiĭ — State Scientific Research and Design Institute of the Rare Metals Industry, Moscow

V. I. Perel' — A. F. Ioffe Physicotechnical Institute, St. Petersburg

V. M. Pudalov — Institute of High Pressure Physics of the Russian Academy of Sciences, Troitsk

R. A. Suris — A. F. Ioffe Physicotechnical Institute, St. Petersburg

A. V. Shashkin — Institute of Metal Physics of the Russian Academy of Sciences, Nizhniĭ Novgorod

A. S. Terekhov — Institute of Semiconductor Physics of the Siberian Branch of the Russian Academy of Sciences, Novosibirsk

A. V. Chaplik — Institute of Semiconductor Physics of the Siberian Branch of the Russian Academy of Sciences, Novosibirsk

4. ORGANIZATIONAL COMMITTEE

Yu. V. Kopaev — Chairman, Institute of Physics of the Russian Academy of Sciences, Moscow

N. N. Sibel'din — Vice Chairman, Institute of Physics of the Russian Academy of Sciences, Moscow

I. V. Kucherenko — Secretary, Institute of Physics of the Russian Academy of Sciences, Moscow

Yu. A. Aleshchenko — Institute of Physics of the Russian Academy of Sciences, Moscow

V. A. Volkov — Institute of Radio Engineering and Electronics of the Russian Academy of Sciences

G. I. Galkina — Institute of Physics of the Russian Academy of Sciences, Moscow

A. A. Gippius — Institute of Physics of the Russian Academy of Sciences, Moscow

S. P. Grishechkina — Institute of Physics of the Russian Academy of Sciences, Moscow

A. G. Zabrodskiĭ — A. F. Ioffe Physicotechnical Institute, St. Petersburg

I. I. Zasavitskiĭ — Institute of Physics of the Russian Academy of Sciences, Moscow

Z. F. Krasil'nik — Institute of Metal Physics, Nizhniĭ Novgorod

V. A. Kurbatov — Institute of Physics of the Russian Academy of Sciences, Moscow

Yu. A. Mityagin — Institute of Physics of the Russian Academy of Sciences, Moscow

V. N. Murzin — Institute of Physics of the Russian Academy of Sciences, Moscow

S. T. Pavlov — Institute of Physics of the Russian Academy of Sciences, Moscow

D. R. Khokhlov — Moscow State University, Moscow

5. PROGRAM

The conference program includes current topics in semiconductor physics. The topics are grouped into three basic sections.

1. Electronic properties of semiconductors (electronic transport, optical properties, nonlinear optical effects, hot charge carriers, tunneling phenomena, fast electronic processes, mesoscopics).

2. Low-dimension semiconductor structures and nanostructures (superlattices and quantum wells, quantum wires and dots, interfaces) and their properties.

 1063-7826/97/020204-02$10.00

3. New technologies and methods for investigating semiconductor structures.

6. ABSTRACTS

The report abstracts (original and six copies) must be submitted no later than June 3, 1997 to the Scientific Council of the Russian Academy of Sciences on the problem ''Semiconductor physics'' at the following address:

117333 Moscow, Leninskiĭ Prospekt, 53, I. P. Akimchenko.

Improperly formatted abstracts will not be considered.

7. FORMAT OF ABSTRACTS

Camera ready abstracts must follow the following format:

THE TITLE OF THE REPORT IS PRINTED
IN UPPERCASE LETTERS
AND CENTERED ON EACH LINE
(blank line)
I. I. Ivanov, P. P. Petrov*, S. S. Sidorov
(blank line)
Organization, City
*Organization, City
(blank line)

The text of the abstract should be placed on a single A4 page with a spacing of 1.5 lines within a 240×152 mm frame (38 lines with 60 symbols) with 30 mm margins on the left and at the top.

Just as the title, the authors' names and organizations should be centered on each line. Abstracts should be printed with a good quality black ribbon or a high-quality printer. Formulas should be composed on a computer or written out by hand using India ink, black ink, or black printer's paste and arranged symmetrically on a line and separated from the text by blank lines at the top and bottom.

The list of references is separated from the text by a blank line. The word ''References'' should be omitted.

1. Citations to the literature are designated in the text by numbers in brackets [1], [2], etc.

2. Ivanov I. I. Pis'ma Zh. Éksp. Teor. Fiz. **58**, 108 (1993).

The number of the corresponding section of the program (1–3) should be inserted in pencil in the upper right-hand corner of each copy.

8. SECOND NOTICE AND INVITATION

The second notice and invitation to conference participants will be sent out at the end of September 1997. The organizing committee requests authors of accepted papers also to submit abstracts in electronic form (ASCII, TeX or LaTeX codes). They should be sent by e-mail to the secretary of the organizing committee: kucheren@sci.lpi.msk.su.

Photovoltaic effect in a *p*-type $CuInSe_2$/green leaf heterojunction

V. Yu. Rud',* Yu. V. Rud', and V. Kh. Shpunt

A. F. Ioffe Physicotechnical Institute, Russian Academy of Sciences, 194021 St. Petersburg, Russia

(Submitted October 16, 1995; accepted for publication October 19, 1995)
Fiz. Tekh. Poluprovodn. **31**, 193–196 (February 1997)

Photosensitive *p*-type $CuInSe_2$/green leaf heterojunctions are fabricated. The photocurrent polarization indicatrix, as well as the spectral dependences of the quantum efficiencies for photoconversion and of the natural photopleochroism of the heterojunctions, are measured. The polarization dependence of the photosensitivity suggests that the upper valence band in $CuInSe_2$ is of type Γ_7. A window effect is observed in the sensitivity ratio and these heterojunctions may find applications as photoconverters for the intensity and polarization of light. © *1997 American Institute of Physics.* [S1063-7826(97)00102-6]

The ternary compound $CuInSe_2$ crystallizes in a chalcopyrite structure and, in terms of its fundamental parameters, currently has the status of an elite material for creating highly efficient and cheap thin film devices for the conversion of solar into electrical energy.[1,2] It has already been used to fabricate heterojunction photoconverters with an efficiency of up to 17%.[2–6] Almost all of the techniques presently available to semiconductor materials science have been used to obtain these structures.[1] This proceeds in parallel with an unceasing search for new heterojunction components based on $CuInSe_2$ which might reduce the cost of photoconverters, improve their ecological parameters, and enhance their efficiencies. Some of these studies include natural materials[7] and the possibility of getting away from the use of cadmium, which is employed in $CuInSe_2$/CdS structures and is regarded as an ecologically dangerous element. In this material, where the highest efficiency has been realized, interdiffusion of Cu into the CdS has been observed and this causes a reduction in the photoconversion quantum efficiency in the photoactive absorption region of the $CuInSe_2$.[8] Accordingly, we have undertaken a study of the possible use of green leaves as a wide band component for heterojunctions based on $CuInSe_2$, as we have proposed earlier.[9] The use of green leaves in photoconverters will obviously solve the ecological and economic aspects of this problem.

The heterojunctions were fabricated using electrically uniform single crystals of *p*-type $CuInSe_2$ with a hole concentration $p \simeq 5\times10^{16}$ cm^{-3} at $T=300$ K grown by directed crystallization of a near stoichiometric $CuInSe_2$ melt. In a number of cases wafers with (100) and (001) orientations and average sizes of $5\times5\times1$ mm^3 were used. The surface of the wafers was subjected to mechanical and, then, chemical polishing. The ohmic contacts were layers of gold thermally sputtered in vacuum, to which current leads were attached by soldering with pure indium. Leaves of *Syringa L.*, which we denote by *L* for brevity, were mostly used as green leaves. The heterojunction was created by placing an *L* leaf on a $CuInSe_2$ surface. A semitransparent layer of metal (Mo, Ni, Au) deposited on the surface of a glass plate was used as an ohmic contact on the leaf. Besides providing an electrical contact, this plate provided a uniform mechanical *p*-$CuInSe_2/L$ contact over the area of the green leaf. As the steady-state current-voltage characteristic shows, in these structures reproducible rectification is observed with a coefficient of 2–3 at biases of 2–5 V, which for the range of mechanical stresses used to press the contact surfaces had no effect on the electrical parameters of the $CuInSe_2/L$ junction. The forward direction of these structures corresponds to a negative polarity for the external bias on the leaf.

When the $CuInSe_2/L$ junctions were illuminated, a photovoltage developed with a negative charge on the leaf relative to the $CuInSe_2$ and the polarity did not vary as the wavelength of the light was changed or the light probe was focussed onto the structure itself. This suggests that only a single energy barrier is involved in the separation of the photoinduced carriers resulting from the contact between the $CuInSe_2$ and green leaf surfaces. Thus, a green leaf can be similar to the CdS, electrolytes, etc., that are used to create an energy barrier on $CuInSe_2$.[1,10,11]

A typical plot of the relative quantum efficiency η of a $CuInSe_2/L$ heterojunction illuminated on the green leaf side as a function of photon energy is shown in Fig. 1. This curve has the shape characteristic of semiconducting heterojunctions. The long wavelength edge of the photosensitivity for these heterojunctions is exponential with a slope of ~ 40 eV^{-1}. The discontinuity in η at $\hbar\omega=1.02$ eV and the spectral position of the long wavelength edge in the photosensitivity indicate that these features are attributable to photoactive absorption in the $CuInSe_2$. In this case the slope of the long wavelength photosensitivity edge for the heterojunction is consistent with a direct interband transition for $CuInSe_2$. The short wavelength drop in the photosensitivity of the $CuInSe_2/L$ heterojunction for $\hbar\omega \gtrsim 1.65$ eV, as well as the rise in photosensitivity at $\hbar\omega > 1.8$ eV, are in qualitative agreement with the wavelength dependence of the optical transmission for a green leaf (Fig. 1). For this reason, the short wavelength drop in η can be related to the absorption of radiation in a wide band component of the heterojunction through which the radiation enters the active region of the structure. For absorbed photon energies of 1.02–1.85 eV the quantum efficiency of the heterojunction is essentially constant and this is evidence of rather efficient separation of photoinduced pairs in these structures. When these hetero-

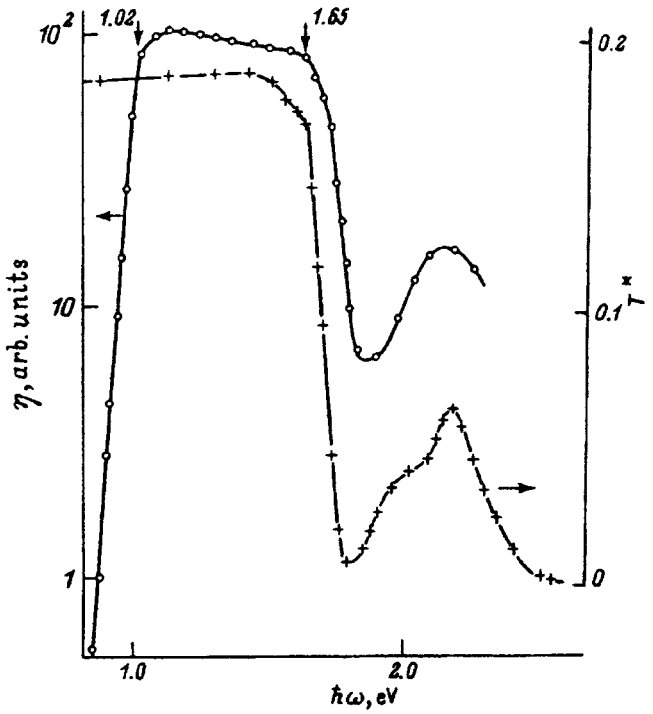

FIG. 1. Spectral dependences of the relative quantum efficiency η of a p-type $CuInSe_2/L$ heterojunction (*1*) and the optical transmission T^* of a green leaf used to fabricate the heterojunction (*2*) in unpolarized light. $T=300$ K, illumination from the green leaf side.

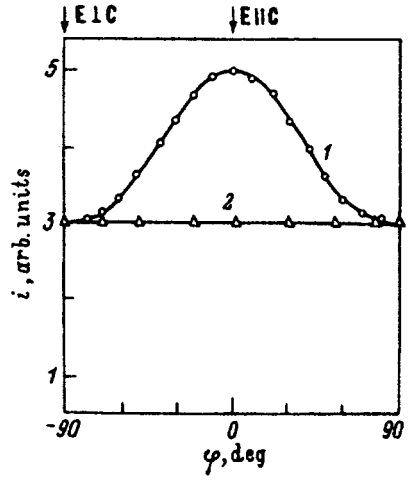

FIG. 2. Polarization indicatrix of the short circuit photocurrent of a p-type $CuInSe_2/L$ heterojunction. $T=300$ K; illumination from the green leaf side; $\hbar\omega=1.02$ eV; $\varphi=0°$ for $\mathbf{E}\|\mathbf{C}$; crystallographic orientation of the $CuInSe_2$ wafers: *1*—(100), *2*—(001).

structures are illuminated from the side of the narrow band component, $CuInSe_2$, the photoconversion efficiency falls off significantly and has a narrowly selective variation with a maximum near the width of the band gap of $CuInSe_2$. This is explained by absorption of light in the surface layer of the crystal.

When linearly polarized light acts on heterojunctions formed by contacts between oriented wafers of $CuInSe_2$ and green leaves, the photosensitivity behaves in a way characteristic of a uniaxial medium. Thus, when the $CuInSe_2$ wafer is oriented in the (100) plane (Fig. 2, curve *1*), the polarization indicatrix of the photocurrent varies periodically; i.e., $i=i^{\|}\cos^2\varphi+i^{\perp}\sin^2\varphi$, where $i^{\|}$ and $i^{\perp}$ are the photocurrents when the electric vector **E** of the light wave is, respectively, parallel and perpendicular to the tetragonal axis **C** of the crystal, and φ is the azimuthal angle between **E** and **C**, with $\varphi=0°$ when $\mathbf{E}\|\mathbf{C}$. It is important to emphasize that the polarization ratio $i^{\|}/i^{\perp}>1$, which suggests that the upper valence band in $CuInSe_2$ has symmetry Γ_7, so that the direct *A*-transitions with the lowest energies are predominantly resolved in the $\mathbf{E}\|\mathbf{C}$ polarization, as in the case of tetragonally compressed semiconductors.[12] For heterojunctions based on wafers of $CuInSe_2$ oriented in the (001) plane, the polarization indicatrices degenerate into a straight line (Fig. 2, curve *2*), which should occur for light propagating along the tetragonal **C** axis.

The photocurrent polarization indicatrices of the heterojunction were the same as for single crystal $CuInSe_2$. Thus, the presence of a ''broad band'' component in the heterojunction has no effect on the state of linearly polarized light that penetrates into the active region of these structures through the leaf layer.

Figure 3 shows a typical spectral variation in the natural photopleochroism, $\mathcal{P}_i^N=(i^{\|}-i^{\perp})/(i^{\|}+i^{\perp})$, for a heterostructure based on a wafer of p-type $CuInSe_2$ oriented in the (100) plane. The positive sign and the magnitude of this coefficient are consistent with those obtained for $n-p$-$CuInSe_2$ homojunctions.[13] The maximum in the positive photopleochroism occurs at the energy of the *A*-transition, while its low value is caused by the weak tetragonal deformation of the crystal lattice of $CuInSe_2$. Here it should be emphasized that a positive sign for the natural photopleochroism does not correspond to that predicted by a quasicubic model[12] including the stretching of the $CuInSe_2$ crystal lattice along the [001] direction. The latter may be caused by the fact that the influence of other components of the noncubic potential such as anion displacement plays a dominant role in this case, so that the selection rules for interband transitions are the same as in semiconductors with a chalcopyrite lattice that have been compressed along the [001] direction.[14]

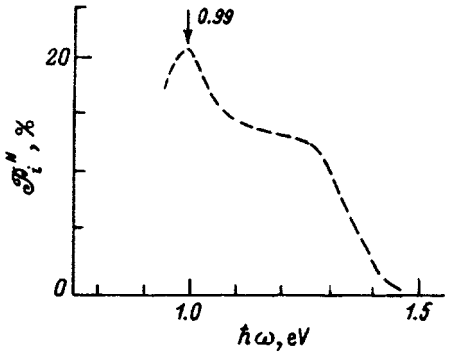

FIG. 3. Spectral variation in the natural photopleochroism of a p-type $CuInSe_2/L$ heterojunction. $T=300$ K; illumination from the green leaf side; wafer oriented in the (100) plane.

These studies, therefore, show that a contact of $CuInSe_2$ with a green leaf can be used to create wide band photoconverters for natural and linearly polarized light. Based on a comparison of the these spectral curves with published curves for a $CuInSe_2$/liquid electrolyte contact,[10] we may assume that a green leaf serves as a liquid electrolyte in the structures studied here. It should be emphasized that in the case of $CuInSe_2/L$ heterojunctions there is no need to make a cell for holding the liquid. As our measurements showed, degradation of the photocurrent was not observed in the $CuInSe_2/L$ structures over 2–3 days, when a leaf was removed from the plant and pressed to the $CuInSe_2$ surface with glass. Evidently, if this sort of heterojunction were formed on a leaf still attached to the plant, then the photoconversion process in time would be determined only by the life processes of the plant and there would be no degradation. Our studies have also shown that the properties of the heterojunctions are insensitive to whether the upper or lower surface of the leaf is in contact with the crystal. Thus, if the heteroboundary is taken to be the lower surface of the leaf, then its outer surface will be oriented toward the light source (sun, lamp, etc.) by the plant and there is no need to create special systems for orienting the photosensitive surface toward the source of light energy. This last feature of the new photoconverter, which originates in the contact between a synthetic material and one which participates in the viability of a biological object (a green leaf), may play a decisive role under certain conditions.

The authors thank Prof. H.-W. Schock and the participants in the INTAS Seminar (Stuttgart, October 26, 1995) for discussions and for their interest in this work.

This work was supported by the INTAS-94-3998 project.

*St. Petersburg State Technical University, 195251 St. Petersburg, Russia

[1] T. J. Coutts, L. L. Kazmerskii, and S. Wagner, Eds., *Copper Indium Diselenide for Photovoltaic Applications*, Elsevier, Amsterdam (1986).
[2] J. Hedstrom, H. Olsen, M. Bodegard, A. Kylner, L. Stolt, D. Hariskos, M. Ruckh, and H. W. Schock, in *Proceedings of the 23rd IEEE Photovoltaic Specialists Conf.* (1993), p. 364.
[3] N. Kohara, T. Negami, N. Nishitani, and T. Wada, Japan. J. Appl. Phys. **34**, L1141 (1995).
[4] T. Wada, *ICTMC-10, Abstracts*, Stuttgart (1995), p. 4.
[5] L. Stolt, *ICTMC-10, Abstracts*, Stuttgart (1995), p. 5.
[6] T. Walter, M. Ruckh, K. O. Velthaus, and H. W. Schock, *Proceedings of the Eleventh Photovoltaic Solar Energy Conf.*, Montreux, Switzerland (1992), p. 124.
[7] H. Dittrich, D. J. Vanghan, R. A. Pattric, S. Graeser, E. Makovicky, M. Lux-Steiner, R. Kunst, and D. Lincol, *ICTMC-10, Abstracts*, Stuttgart (1995), p. 10.
[8] N. N. Konstantiova, Yu. V. Rud', and T. N. Ushakova, *ICTMC- 10, Abstracts*, Stuttgart (1995).
[9] V. Yu. Rud', Yu. V. Rud', and V. Kh. Shpunt, Fiz. Tekh. Poluprovodn. **29**, 438 (1995). [Semiconductors **29**, 225 (1995)].
[10] N. N. Konstantinova, M. A. Magomedov, V. Yu. Rud', and Yu. V. Rud', Fiz. Tekh. Poluprovodn. **26**, 558 (1992). [Sov. Phys. Semicond. **26**, 317 (1992)].
[11] N. N. Konstantinova, V. D. Prochukhan, Yu. V. Rud', and M. A. Tairov, Fiz. Tekh. Poluprovodn. **22**, 3584 (1988). [*sic*].
[12] J. L. Shay and J. H. Wernick, in *Ternary Chalcopyrite Semiconductors*, Pergamon Press, N. Y. (1975), p. 244.
[13] I. B. Bodnar', A. A. Vaipolin, V. Yu. Rud', and Yu. V. Rud', Fiz. Tekh. Poluprovodn. **28**, 1322 (1994). [Semiconductors **28**, 748 (1994)].
[14] Yu. V. Rud', Japan. J. Appl. Phys. **30**, 512 (1994).

Translated by D. H. McNeill